Quantized vortices in a Bose-Einstein condensate: thermal activation and dynamic nucleation

Sabine Stock

Sabine Stock. Quantized vortices in a Bose-Einstein condensate: thermal activation and dynamic nucleation. Atomic Physics [physics.atom-ph]. Université Pierre et Marie Curie - Paris VI, 2006. English. NNT : . tel-00012211

THÈSE de DOCTORAT de l'UNIVERSITÉ PARIS 6

Spécialité :
Physique Quantique

présentée par

Sabine STOCK

pour obtenir le grade de DOCTEUR de l'UNIVERSITÉ PARIS 6

Sujet de la thèse :

Quantized vortices in a Bose-Einstein condensate: thermal activation and dynamic nucleation

---

Soutenue le 13 Janvier 2006
devant le jury composé de :

M.	**Claude Cohen-Tannoudji**	Examinateur
Mme	**Claire L'Huillier**	Présidente
Mme	**Hélène Perrin**	Rapporteur
M.	**Klaus Sengstock**	Rapporteur
M.	**Jean Dalibard**	Directeur de thèse

> “Cold atoms?
> That sounds like a poetry cycle of Gottfried Benn...”

Meinen Eltern und meiner Großmutter
To my parents and my grandmother

Thanks...

This thesis was carried out at Laboratoire Kastler Brossel, which is a part of the physics department of Ecole Normal Supérieure Paris. The atmosphere at this institute is inspiring and extraordinarily motivating, and I thank the institute's director, Frank Laloë, for having accepted me there.

I also thank the members of my jury, Claire Lhuillier, Claude Cohen-Tannoudji, Hélene Perrin and Klaus Sengstock for the interest they showed in my work. I am especially grateful for the attention with which they read this manuscript, and for their suggestions to improve it.

My thesis supervisor Jean Dalibard certainly played the most important role during my years at LKB. A single discussion with him at the end of 2001 was sufficient to convince me that I certainly wanted to work in the field of cold atoms - and I have to admit that I was strongly opposed to this idea until even a day before. This is only said to supply evidence for his extraordinary passion not only for his subject, but also for teaching it (...and by the way, I have never regretted my decision for rotating BECs!). His great knowledge of the field of (not only atomic) physics, his curiosity whenever he comes across a new problem, his optimism and readiness to give a helping hand in everyday lab work are already legendary (and "have been described in great detail in [7–10]"), so nothing more about this here... What I thank Jean particularly for, is for his gift to find the very specific qualities of every new member of the group. With a great patience (well, most of the time...) he lets young PhD students explore and use their specific capacities, so that they can be useful team members from the very beginning.

In my first year of thesis I mainly worked with Vincent Bretin. During this year he taught me the basics of the experiment and the physics behind. My memory of this year contains only great moments, of constantly learning and experiencing new things, as well as of a steadily growing friendship (which I hope will survive the distance to Vienna!). During this first year at LKB I also had the chance to work for a few months with Peter Rosenbusch and Yannick Seurin. They both contributed enormously to the great atmosphere in the group, and I am happy to have got to known them - let alone that they taught me a lot of things...

In my second year of thesis, Zoran Hadzibabic and Baptiste Battelier joined the group. Zoran is certainly one of the best physics teachers I ever had. His enthusiasm never lets him end a discussion before he is sure that everybody got the point (may the subject be physics or foie gras...), and I truly admire his capacity for explaining complicated physics in simple words. Baptiste, who joined the group a few months later, was a very motivated and patient partner on the experiment from the moment of his arrival. Since he joined the team the experiment would always be running already when I arrived in the morning (which is a great luxury...). He even kept that habit after his somehow crazy neighbour had moved out...
Thanks to both of you!

During the last year of my thesis, Marc Cheneau joined the group as a new “stagiaire du DEA”. His good humour made him a great person to work with down in the lab. Marc, Baptiste and Zoran now form the new team together with Peter and Patrick (who both arrived too late for me to have a chance to work with them), and they already achieved a bunch of great new results. I wish them good luck for their future work and careers.

My thanks also go to the entire cold atoms group, which provides an extraordinarily stimulating environment for all its members. An important tradition in this group is the internal seminary every Friday, where the work of everybody is challenged by thorough inquiries of everybody else... This weekly meeting as well as the summer lunches in the garden, when up to 15 people gather on the grass, will stay a precious memory. The most frequent contact I had with the people from the “mezzanines”, and I thank everybody who was present there during the last three years for contributing to the extraordinary atmosphere. Some of the group members also became an important part of my social life, and made me feel at home in Paris very soon. A very special thanks in this respect goes to to Jérémie Léonard, Julien Cubizolles, Thierry Lahaye and Frédéric Chevy. Speaking of social life in and out of the lab, I should certainly not forget our neighbours from S12 and S15 - thanks a lot for friendship, coffee chats and after-work beers to Paolo, Tristan, Salima, Julie, Philippe and Sébastien.

During the years at LKB I often took advantage of the institute’s great facilities. I would especially like to thank the people who help us with all administrative issues: Linda Krikorian, Vera da Costa and Thierry Tardieu, and most notably Nicole Neveux, who not only makes virtually everything possible, but also provided me with her great smile and some friendly words in my rather desperate moments in the lab... Thank you also to the technicians and electricians of LKB, of which I most worked with Yvon Cabirou, Lionel “Yo” Perennes and Patrick Giron. I always felt welcome in their workshops, and have to admit that sometimes my visits were much more motivated by a need for a little chat, than by my actual technical problem to be solved. A great thank you also to the people of the physics department of ENS, and here most notably to M. et Mme Guérard, Anne-France Seyer, Jack Olejnik, Jean-François Point, Didier Courtiade, Bruno Fabre and Denis Jaggi, to our basement-neighbours: Robert Dalais, Jean-Marc Jusseau, Philippe Rousseau and Franck Bouchereau, and for the help with all kinds of “computer questions” to Zaïre Dissi, Xavier Monnin, Francis Hulin-Hubard and Daniel Lemoal.

Finally my warmest gratitude goes to those whose presence in my life have also contributed a great deal to the success of this work. Without my friends - those I knew before coming to France, and those I made in Paris - my life would be much less complete. The relations I have to people all over Europe are the most important part of my life, and I thank them all for not giving up on me during the times when my conversation became rather monothematic for several weeks (the lasers!, the lattice!, the writing!, ...respectively).

For the same patience I thank the members of my family, who have always provided me with love and care (and German goodies of course, sometimes so desperately needed). Without their support I would not have had neither the moral nor simply the means to carry out my studies as free of any worries as I did.

Thank you, Thorsten.

Contents

III Fast rotating condensates in quartic potentials

Introduction

Bose-Einstein condensates in dilute atomic gases are macroscopic quantum objects, and for this reason they are interesting for physicists of different communities. Even more, BECs are *easily accessible* and *manipulable* quantum objects, which makes them an unique play- and testing ground for different theories related to more complicated and less accessible systems - like the electron gas in a solid. Indeed since the first production of BECs in dilute atomic gases by Cornell, Ketterle and Wieman in 1995 [11–14] a great interest has developed in the comparability of gaseous BECs and solid state systems.

A BEC in a dilute gas can be produced in principle in nearly arbitrary geometries. The most common trap shape consists of a 3-dimensional harmonic trapping potential with cylindrical symmetry, but also more complicated geometries, like 2- and 1-dimensional traps [15–27], double wells [28–30] and ring shaped traps [31] have been produced. Especially prominent examples are BECs trapped in the sites of periodic potentials [32, 33], as such systems are a good analogue to the electrons trapped in the periodic ion lattice in a crystal. The properties of such artificial crystals can be tuned nearly at will - which is an important difference compared to their conventional counterparts. The tunable parameters are the lattice spacing and the potential height, and thus also the tunneling between the individual sites. Tuning these parameters one can for example explore the crossover from a superfluid to an isolating system, and in a famous experiment with atomic BECs the Mott-insulator transition could be observed [34], which occurs when the tunneling energy between lattice sites becomes of the order of the on-site interactions.

The properties of the various regimes of gaseous BECs are also probed in a relatively simple manner. As gaseous BECs are trapped in magnetic and electric fields, the optical access to these systems is in principle limited only by the resolution of the imaging system. The typical size of a BEC being of the order of $100\,\mu$m, this means that measurements are performed by simply photographing the atomic cloud, and extracting the desired quantity from the density profile or its dynamical changes.

After the first production of BECs in dilute gases of various atomic species, most of the experimental research concerned the study of their specific properties. Especially the question of phase coherence of a macroscopic matter wave was of immediate interest, and through experimental and theoretical study of matter wave interference it could be confirmed that BECs possess this property [35,36]. A second important property of interacting BECs is their superfluidity, of which an especially stunning effect is that rotation of the system can only occur through the nucleation of quantized vortices. Such vortices are an analogue to the lines of magnetic flux in type-II superconductors when placed in a magnetic field [37].

From the beginning the study of the properties of gaseous BECs has thus been related to the properties of condensed matter systems, and during the last years the focus of experimental interest has shifted even more to the realization of regimes that have an equivalent in conventional condensed matter systems. Some of these regimes are related to the dimensionality of the system, and consequently the research on such low dimensional systems is another focus in the cold atoms community today. The dimensionality thereby already has an important influence on the occurrence of the BEC-transition itself. For low-dimensional homogeneous gases no Bose-Einstein condensation occurs at finite temperatures. If the system is interacting, however other interesting regimes can be explored.

An example of such low-dimensional physics is the Kosterlitz-Thouless (KT) transition [38, 39] from the normal to the superfluid phase in a 2-dimensional interacting gas. Another is a bosonic analogue to the fractional quantum Hall effect (FQHE) regime, which is predicted to exist in fast rotating Bose gases [40, 41]. A third example is the case of 1D systems, where the transition to the Tonks gas in a strongly interacting system was observed recently [22, 23]. In this regime strong interactions lead to an effective "fermionization" of the system.

The explorations of two of these regimes represented a strong motivation for the work presented in this thesis: the KT-transition in an interacting 2D trapped gas, and the transition to the FQHE-regime in fast rotating bosonic gases. In both of these regimes quantized vortices play an important role.

- The **Kosterlitz-Thouless** (KT) transition in an interacting 2D homogeneous gas is related to the unbinding of vortex-antivortex pairs. The cold temperature phase of this system is superfluid, but not a true BEC, as at finite temperatures long wavelength phase fluctuations destroy the long range order. Beside these long-wavelength excitations also bound vortex-antivortex pairs are present in the system. On the high-temperature side of the KT-transition these pairs unbind, and the free vortices destroy superfluidity. The mechanism of this phase transition was predicted in 1973 by Kosterlitz and Thouless [38, 39], and a phase transition to a superfluid phase was observed already in two systems, in 1978 in a 2-dimensional ^{4}He film [42], and in 1998 in a thin layer of spin-polarized atomic hydrogen [43]. In these systems it is however not possible to directly observe a possible emergence of vortices or vortex pairs. In dilute atomic gases this would in principle be possible, and these systems might thus allow to directly prove the importance of vortices in this phase transition.

- For the **Fractional Quantum Hall effect** (FQHE)-regime known from some 2D - semiconductors when placed in a perpendicular magnetic field [44, 45], a bosonic analog is predicted to exist in rotating neutral gases [40, 41]. This analogy is due to a similarity in the theoretical description of charged particles in a magnetic field and rotating neutral particles in a harmonic trap. If the rotation frequency is equal to the harmonic trapping frequency, the eigenstates of the rotating bosons organize in highly degenerate Landau levels, and the bosonic FQHE-regime is expected for a fractional filling of the lowest Landau level, as in the "traditional" quantum Hall effect.

Approaching these two regimes requires different experimental tools, which are added to the experimental setup for the respective experiments. This manuscript is organized along these specific tools, and consist of three parts:

I. Bose-Einstein condensates: Properties and realization. The first part is a general introduction to the phenomenon of Bose-Einstein condensation and to the experimental setup used for their production. Except for small modifications this setup represents the basis for the experiments presented in the following parts.

II. 2-dimensional condensates. In part II a 1-dimensional lattice is added to the experimental setup, to create arrays of 2-dimensional condensates. The phase coherence properties of the 2D systems are explored through interference experiments with small arrays of BECs. In these experiments nontrivial phase defects are detected, which are probably due to thermally induced vortices in the 2D BECs. As a second topic the interference of large periodic arrays of condensates is studied.

III. Fast rotating condensates in anharmonic traps. Part III presents experiments where two optical potentials are used: a gaussian beam adds a quartic term to the harmonic magnetic trap, and with a “spoon potential” the condensates are stirred to fast rotation. The steep walls of the quartic potentials thereby allow for rotating frequencies higher than the harmonic trapping frequency. This setup allowed to reach the “LLL”-regime and study the properties of fast rotating condensates in nonharmonic traps.

Each of the parts contains an introduction giving an overview on the addressed topics. The first chapter of each part is dedicated to a summary of the theoretical basics needed for the understanding of the respective part. This allows that parts II and III of this manuscript can be read independently.

Part I

Bose-Einstein condensates: Properties and realization

Contents

Introduction

The first theoretical description of Bose-Einstein condensation in ideal gases dates already from 1924, when Einstein published his articles concerning the "Quantum theory of ideal gases" [46–48]. London used this theory in 1938 to explain the superfluidity of liquid ^{4}He [49], which thus represented the first experimental realization of a Bose-Einstein condensate (BEC). Liquid Helium is however strongly interacting, which makes its theoretical description a difficult task. One of the important consequences of the interactions is that in liquid Helium only about 8 % of the particles occupy the ground state at zero temperature, while in an ideal gas the occupation is 100 %.

The problems due to interactions are much less pronounced in Bose-Einstein condensates in dilute atomic gases. In those weakly interacting systems the first BECs were realized in 1995 by Eric Cornell, Wolfgang Ketterle and Carl Wieman [13, 14], an experimental success that was rewarded by the Nobel prize in 2001. Since then the realization of gaseous BECs was achieved in a large number of experiments, and a increasing number of different atomic species. Recently the first groups were able to achieve condensation of bosonic dipolar molecules [50–53].

The most prominent features that are common to all these condensates, rely on the fact that a BEC is described by a macroscopic wave function. From this function it can be deduced that BECs are phase coherent. If the particles are interacting, one can also show that a BEC is a superfluid. A number of interesting phenomena arise due to these basic properties, as for example the constraints on the velocity field of a BEC, which allow rotation only through the nucleation of quantized vortices.

The tools to probe the properties of atomic BECs, as well as the tools to fabricate them, are very similar for most of the used atomic species. They all make use of the permanent magnetic dipole moments of the atoms, or induced magnetic and electric dipole moments. The experimental cycles also are very similar for most of the atomic species (excepting atomic Hydrogen): nearly all experiments use a phase of magneto-optical trapping and cooling [54–56] before the atoms are transferred to a purely magnetic or far detuned optical trap, where condensation is reached through evaporative cooling [57–60].

This first part of the manuscript gives a short introduction to the most important properties of BECs in cold atomic gases, as well as the production cycle of our experimental setup.

The chapters of part I

- **Chapter 1** gives an introduction to the theoretical concept and the properties of the BEC phase transition.
- **Chapter 2** describes the experimental methods and setup with which Bose-Einstein condensates are produced in our group. Except for small modifications the same setup is used for all experiments presented in parts II and III of this manuscript.

Chapter 1

Bose-Einstein condensation in harmonic traps

Bose-Einstein condensation is a quantum phase transition in bosonic gases, which leads to a macroscopic population of the ground state of a system, the Bose-Einstein condensate (BEC). In this chapter the theory of the condensation transition in trapped dilute gases and the properties of BECs are briefly outlined. A more detailed approach to all topics addressed in this chapter can be found in the existing literature, e.g. in [61] or [62].

1.1 The BEC phase transition in ideal gases

1.1.1 The harmonic oscillator ground state

The theoretical description of Bose-Einstein condensation does not need a special trapping geometry. It was in fact formulated first for uniform systems [46–48]. For dilute atomic gases in practice however some kind of trap is needed, to keep the atoms thermally isolated from their environment. In this case, the trapping scheme generally relies on the magnetic interaction of the atom's magnetic moment with an external magnetic field. Most of these traps provide harmonic confinement with axial symmetry. This introductory overview will thus be restricted to harmonic traps with axial symmetry[1]. The potential of these traps can be written as:

$$U(\mathbf{r}) = \frac{m}{2}\left(\omega_\perp^2 r^2 + \omega_z^2 z^2\right), \tag{1.1}$$

where m is the atomic mass, $r^2 = x^2 + y^2$, and ω_z and $\omega_\perp = \omega_x = \omega_y$ are the axial and radial trapping frequencies.

For non-interacting atoms the many body hamiltonian consists of the sum of the single particle hamiltonians, which in a harmonic potential have the energies

$$\epsilon_{n_x,n_y,n_z} = \sum_{i=x,y,z}\left(n_i + \frac{1}{2}\right)\hbar\omega_i. \tag{1.2}$$

The ground state of a single particle in the harmonic potential is

$$\phi_0(\mathbf{r}) = \left(\frac{m\omega_{\text{ho}}}{\pi\hbar}\right)^{3/4} \exp\left(-\frac{m}{2\hbar}\left(\sum_{i=x,y,z}\omega_i\, i^2\right)\right) \tag{1.3}$$

---

[1] In part III of this manuscript a different trap geometry, including a radial quartic term, is introduced. The properties of the BEC-transition in this case are discussed in chapter 9.

where ω_{ho} is the geometric mean of the harmonic frequencies

$$\omega_{\text{ho}} = (\omega_x \omega_y \omega_z)^{1/3} = (\omega_\perp^2 \omega_z)^{1/3}.$$

The *harmonic oscillator length* is defined through the root mean square (rms) value of the Gauss function in equation (1.3), and gives a measure for the geometric mean of the ground state's size:

$$a_{\text{ho}} = \sqrt{\frac{\hbar}{m\omega_{\text{ho}}}}.$$

The ground state of N noninteracting bosons in the harmonic potential is the product state of all single particle ground states $\phi(\mathbf{r}_1, ..., \mathbf{r}_N) = \prod_i \phi_0(\mathbf{r}_i)$.

1.1.2 Saturation of the excited states

Ideal bosonic gases are described by the Bose-Einstein statistics. From this statistics one can derive that for a given temperature T exists a maximal number of atoms in the excited states of the system, which decreases with T. For small enough temperatures the population of the excited states will thus "saturate" at the maximal population and all additional atoms populate the ground state. Depending on the total atom number the ground state population can thus become macroscopic. This macroscopic ground state population is called a Bose-Einstein condensate.

Excited state population in a harmonic trap

The Bose-Einstein statistic [62] gives the probability that in a system of temperature T a particle populates a state of energy ϵ:

$$n(\epsilon) = \frac{1}{e^{\beta(\epsilon-\mu)} - 1} \qquad \text{with} \qquad \beta = \frac{1}{k_{\text{B}}T},$$

where k_{B} is Boltzmann's constant and μ the chemical potential. In the case of an ideal gas μ is negative and tends to zero for $T \to 0$.

In a harmonic trap one can write explicitly the energy dependance of the density of states, which for a 3-dimensional (3D) system with axial symmetry is

$$\rho(\epsilon) = \frac{\epsilon^2}{2\hbar^3 \omega_\perp^2 \omega_z}\,.$$

For temperatures $k_{\text{B}}T \gg \epsilon$ one can replace the sum over the excited states by an integral (this approximation is called the semi-classical approximation), and as $\rho(\epsilon) = 0$ for $\epsilon = 0$, one can take this integral from 0 to ∞. The population of the excited states then is:

$$N_{\text{exc}} = \int_0^\infty \rho(\epsilon)\, n(\epsilon)\, d\epsilon = \int_0^\infty \frac{\rho(\epsilon)}{e^{\beta(\epsilon-\mu)} - 1}\, d\epsilon.$$

This integral can be evaluated as:

$$N_{\text{exc}} = \left(\frac{k_{\text{B}}T}{\hbar\omega_{\text{ho}}}\right)^3 g_3(e^{\beta\mu}), \tag{1.4}$$

where $g_3(z)$ is a polylogarithm function defined by:

$$g_3(z) = \sum_n \frac{z^n}{n^3}.$$

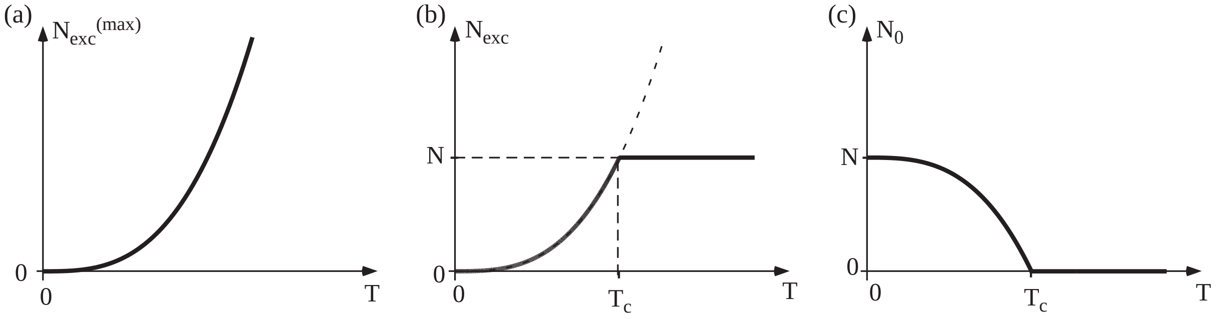

Figure 1.1: Bose-Einstein condensation in a system of N atoms: (a) The largest allowed number of atoms in the excited states decreases with T as $N_{\text{exc}}^{(\text{max})} \propto T^3$. (b) The population of the excited states has thus a upper bound, which is $N_{\text{exc}}^{(\text{max})}$ for $T < T_c$. (c) For $N > N_{\text{exc}}^{(\text{max})}$ the ground state population becomes macroscopic.

As μ is negative for all $T \neq 0$, $e^{\beta\mu}$ is smaller than 1 and $g_3(e^{\beta\mu})$ smaller than $g_3(1) \approx 1.202$. This means that the population of the excited states N_{exc} has an upper bound:

$$N_{\text{exc}}^{(\text{max})} = 1.202 \left(\frac{k_B T}{\hbar\omega_{\text{ho}}} \right)^3 \geq N_{\text{exc}}. \tag{1.5}$$

This is the maximal population of the excited states for a given temperature T.

Phase transition for a given atom number N

The best known representation of the Bose-Einstein condensation phase transition is that of a system with a large (i.e. macroscopic) but fixed atom number N, where the temperature and thus $N_{\text{exc}}^{(\text{max})}$ decreases.

As long as $N < N_{\text{exc}}^{(\text{max})}$, the distribution of the population numbers is similar to the thermal Boltzmann-distribution. However, as the maximum population of the excited states decreases with T^3, at a given temperature T_c this number $N_{\text{exc}}^{(\text{max})}$ becomes smaller than N. For temperatures lower than T_c the ground state population must thus become macroscopic, as it must at least contain the atoms that cannot populate the excited states, and the atom number in the ground state is thus larger than $N - N_{\text{exc}}^{(\text{max})}$. The ground state population N_0 thus grows with decreasing temperature, and becomes $N_0 = N$ for $T = 0$. This behavior is illustrated in figure 1.1. T_c is the critical temperature of the phase transition: below T_c the macroscopic population of the ground state forms the so called Bose-Einstein condensate (BEC).

To obtain the critical temperature T_c in a system with atom number N one simply has to set $N_{\text{exc}}^{(\text{max})} = N$ in equation (1.5), which leads to:

$$T_c = 0.94 \frac{\hbar\omega_{\text{ho}}}{k_{\text{B}}} N^{1/3} \tag{1.6}$$

To give a sense of scale for the needed temperatures, one can calculate T_c for typical parameters in experiments with dilute atomic gases, e.g. $N = 10^5$ and $\omega_{\text{ho}} = 2\pi \cdot 50\,\text{Hz}$. This gives $T_c \sim 100\,\text{nK}$.

1.1.3 Bose-Einstein condensation and the phase space density

The description of Bose-Einstein condensation in a system with a constant atom number is not valid for the experimental situation in systems of cold atomic gases. In these systems the

BEC transition temperature is reached trough evaporative cooling (see chapter 2), and the atom number decreases with decreasing temperature. To describe Bose-Einstein condensation in such a system, one has to look at a criterion for the phase-space density. To this end, the thermal de-Broglie wavelength is introduced:

$$\Lambda_{\mathrm{dB}} = \frac{h}{\sqrt{2\pi m k_{\mathrm{B}} T}}, \tag{1.7}$$

and one finds as criterion for Bose-Einstein-condensation [63]:

$$n(\mathbf{0})\Lambda_{\mathrm{dB}}^3 = g_{3/2}(1) \simeq 2.612, \tag{1.8}$$

where $n(\mathbf{0})$ is the density in the trap center. This criterion is equivalent to a quite intuitive explanation of the phenomenon: Bose-Einstein condensation occurs for a phase space density, where the wave packets of the atoms overlap.

1.2 Bose-Einstein condensation in interacting gases

While the processus of Bose-Einstein condensation was described above for noninteracting particles, Bose-Einstein condensation is also possible in the presence of atomic interactions. The role of interactions generally becomes more important with increasing atomic density. While interactions can be neglected in a thermal gas with low atomic density, they cannot be neglected in a BEC. In a BEC all atoms populate the same quantum state, which leads to a high atomic density in the trap center[2]. In this case interactions visibly modify the equilibrium properties of the condensates.

1.2.1 The scattering length

Interactions between two particles are generally described by a scattering potential. If this potential is radially symmetric, the scattering process can be treated with the partial wave expansion [64]. For collisions of low energy, already the first term of this expansion, the s-wave scattering potential, describes the scattering process accurately. This potential is characterized by a single parameter, the *s-wave scattering length a*.

Using this approximation the interatomic interaction potential $V(\mathbf{r}-\mathbf{r}')$ can be described with an effective interaction potential:

$$V(\mathbf{r}'-\mathbf{r}) = \frac{4\pi\hbar^2 a}{m}\,\delta(\mathbf{r}'-\mathbf{r}) = g\,\delta(\mathbf{r}'-\mathbf{r}), \tag{1.9}$$

where g is called the *coupling constant.*

This approximation of the interaction potential is valid for interatomic distances much larger than the scattering length. The atoms used in our experiments, ^{87}Rb in the Zeeman state $F = m_F = 2$, have a scattering length of $a = 5.2\,\mathrm{nm}$. The maximal atom densities are of the order of $n = 10^{15}\,\mathrm{cm}^{-3}$. The relation $na^3 \ll 1$ is thus verified for our experimental parameters.

1.2.2 The Gross-Pitaevskii equation

The hamiltonian for N interacting particles in an external potential $U_{\mathrm{ext}}(\boldsymbol{r})$ is in second quantification

$$\hat{H} = \int \left[\frac{\hbar^2}{2m}\boldsymbol{\nabla}\hat{\Psi}^\dagger\boldsymbol{\nabla}\hat{\Psi} + U(\boldsymbol{r})\hat{\Psi}^\dagger\hat{\Psi}\right]\mathrm{d}\boldsymbol{r} + \frac{1}{2}\int \hat{\Psi}^\dagger(\boldsymbol{r})\hat{\Psi}^\dagger(\boldsymbol{r}')V(\boldsymbol{r}'-\boldsymbol{r})\hat{\Psi}(\boldsymbol{r})\hat{\Psi}(\boldsymbol{r}')\mathrm{d}\boldsymbol{r}\mathrm{d}\boldsymbol{r}', \tag{1.10}$$

---

[2] In the case of noninteracting atoms the atom density of a BEC is proportional to the atom number, $n(\mathbf{r}) = N|\phi_0(\mathbf{r})|^2$.

where $V(\mathbf{r}-\mathbf{r}')$ is the interatomic interaction potential, and $U(\boldsymbol{r})$ the trapping potential. $\hat{\Psi}$ and $\hat{\Psi}^\dagger$ are the bosonic annihilation and creation operators in $\boldsymbol{r}$, which are constituted by the sum over the field operators of the single particle states:

$$\hat{\Psi} = \phi_0 \hat{a}_0 + \sum_{i\neq 0} \phi_i \hat{a}_i,$$

where $\hat{a}_i$ are the annihilation operators of a particle in the single-particle state ϕ_i.

In 1947 Bogoliubov formulated the basis for a mean-field treatment of dilute atomic gases [65], by replacing the operators of the ground state, $\hat{a}_0$ and $\hat{a}_0^\dagger$, by the complex number $\sqrt{N_0}$, where N_0 is the atom number in the ground state. This approximation is equivalent to treating the macroscopic component as a classical field, and it is valid for large N_0, i.e. $N_0 \approx N_0 + 1$, which is the case for a BEC. The so-called Bogoliubov-approximation thus consists in the separation

$$\hat{\Psi} = \Psi(\mathbf{r}, t) + \delta\hat{\Psi}(\mathbf{r}, t) \tag{1.11}$$

where the complex wave function $\Psi(\mathbf{r}, t)$ describes the condensate, and the field operator $\delta\hat{\Psi}^{(\dagger)}(\mathbf{r}, t) = \sum_{i\neq 0} \phi_i \hat{a}_i^{(\dagger)}$ describes the condensate depletion, which is the component of the system that is not in the ground state. In cold atomic gases well below the critical temperature T_c the condensate depletion is of the order of $8\sqrt{na^3}/(3\sqrt{\pi})$ [66]. With the typical parameters of a cold atomic Rb gas, $a \sim 5\,\text{nm}$ and $n \sim 10^{15}\,\text{cm}^{-3}$, the condensate depletion is of the order of 1%, and can thus be treated as a perturbative term.

Treating the condensate depletion as a perturbative term one obtains the Gross-Pitaevskii (GP) equation for the classical field Ψ:

$$i\hbar \frac{\partial}{\partial t}\Psi = \left[\frac{-\hbar^2\nabla^2}{2m} + U(\boldsymbol{r}) + g|\Psi|^2\right]\Psi. \tag{1.12}$$

The condensate wave function

The Gross-Pitaevskii equation is a nonlinear differential equation for a classical field Ψ. This classical field is called the order parameter of the system, or the condensate wave function, because the GP-equation has the form of a nonlinear Schrödinger equation. The condensate wave function is normalized by the BEC atom number:

$$\int |\Psi(\boldsymbol{r})|^2 d^3r = \int |\phi_0(\boldsymbol{r}) a_0|^2 d^3r = N_0,$$

and the density of the condensate is:

$$n(\mathbf{r}) = |\Psi(\mathbf{r})|^2.$$

The BEC wave function can be written as

$$\Psi(\boldsymbol{r}, t) = \sqrt{n(\boldsymbol{r}, t)}\, e^{i\varphi(\mathbf{r},t)}, \tag{1.13}$$

where $\varphi(\boldsymbol{r}, t)$ is the phase of the order parameter. The BEC can thus be characterized by two macroscopic parameters: its density $n(\boldsymbol{r}, t)$ and phase $\varphi(\mathbf{r}, t)$.

The stationary Gross-Pitaevskii equation

To obtain the equilibrium properties of a Bose-Einstein condensate it is useful to look for the stationary solutions of the GP-equation. Those can be found by separating the time-dependant solutions in a time-independent part and a time evolution term:

$$\Psi(\boldsymbol{r}, t) = \Psi(\boldsymbol{r}) e^{-i\mu t/\hbar},$$

where the temporal evolution is fixed by the chemical potential.
The stationary GP-equation for the wave function $\Psi(\mathbf{r})$ then reads:

$$\left[\frac{-\hbar^2\nabla^2}{2m} + U(\boldsymbol{r}) + g|\Psi(\mathbf{r})|^2\right]\Psi(\mathbf{r}) = \mu\Psi(\mathbf{r}). \tag{1.14}$$

1.2.3 The Thomas-Fermi approximation

For many properties of BECs it is useful to examine the possible approximations of the GP-equation. To do so, one has to look at the different parts of the total energy of the system. It can be distinguished in three parts: the kinetic, the potential and the interaction energy: $E = E_c + E_p + E_i$.
From equation (1.14), one can estimate the scale of these contributions:

$$\begin{aligned} E_c &\propto \frac{\hbar^2}{mR^2} = \hbar\omega_{\text{ho}}\frac{a_{\text{ho}}^2}{R^2} \\ E_p &\propto m\omega_{\text{ho}}^2 R^2 = \hbar\omega_{\text{ho}}\frac{R^2}{a_{\text{ho}}^2} \\ E_i &\propto g\,n(R) = \hbar\omega_{\text{ho}}\frac{a_{\text{ho}}^2}{R^2}\left(\frac{N_0 a}{R}\right), \end{aligned}$$

where R is the geometric mean of the radii of the condensate, and $a_{\text{ho}} = \sqrt{\frac{\hbar}{m\omega_{\text{ho}}}}$ the harmonic oscillator length. The assumption $E_i \gg E_c$ is valid if $(a_{\text{ho}}/R)(N_0 a/a_{\text{ho}}) \gg 1$. The dimensionless parameter $N_0 a/a_{\text{ho}}$ gives a measure of the strength of the interactions, and for typical parameters of our 3D condensates, $N_0 \sim 10^5$ and $a_{\text{ho}} \sim 1\mu$m, one gets $N_0 a/a_{\text{ho}} \sim 500$. Typical radii of the cloud are of the order of $R \sim 10\,\mu$m, and for these parameters it is thus possible to neglect E_c. This regime is called the Thomas-Fermi (TF) regime.

Within the TF regime the stationary GP-equation becomes

$$|\Psi(\boldsymbol{r})|^2 = \frac{\mu - U(\boldsymbol{r})}{g}. \tag{1.15}$$

Knowing that the condensate density is $n(\mathbf{r}) = |\Psi(\boldsymbol{r})|^2$, this equation leads to a very simple expression for the density profile. In the case of harmonic trapping the condensate profile is parabolic in all directions:

$$n(\boldsymbol{r}) = |\Psi(\boldsymbol{r})|^2 = |\Psi(0)|^2 \cdot \max\left[0\,, \left(1 - \frac{x^2+y^2}{R_\perp^2} - \frac{z^2}{R_z^2}\right)\right], \tag{1.16}$$

where $|\Psi(0)|^2 = \mu/g$ and the radii R_i in this equation are called the TF-radii of the cloud, defined by

$$\frac{1}{2}m\omega_\perp^2 R_\perp^2 = \frac{1}{2}m\omega_z^2 R_z^2 = \mu. \tag{1.17}$$

Using $N_0 = \int n(\mathbf{r})\,d\mathbf{r}$, the chemical potential in the TF-approximation can be written as a function of the atom number:

$$\mu = \frac{\hbar\omega_{\text{ho}}}{2}\left(15\frac{N_0 a}{a_{\text{ho}}}\right)^{2/5}. \tag{1.18}$$

Inserting this expression in equation (1.17) gives a relation between the TF-radii and the atom number:

$$R_\perp = a_\perp\frac{\omega_{\text{ho}}}{\omega_\perp}\left(15N_0\frac{a}{a_{\text{ho}}}\right)^{\frac{1}{5}} \qquad \text{and} \qquad R_z = a_z\frac{\omega_{\text{ho}}}{\omega_z}\left(15N_0\frac{a}{a_{\text{ho}}}\right)^{\frac{1}{5}},$$

where $a_i = \sqrt{\frac{\hbar}{m\omega_i}}$ is the length of the harmonic oscillator along the direction i ($i = r, z$).

Measuring the radii of a BEC is thus a method to determine its atom number. This method is used in our experiments, when other methods fail due to small optical densities of the cloud (see chapter 2). It is however not of high accuracy, as an error in the radius measurement is considerably amplified in the calculation of the atom number, due to the R^5-dependence.

The above equations rely on the TF-approximation and are valid for all experiments with 3D condensates described in this thesis. Part II of this thesis is however dedicated to the description of quasi-2D BECs. In this case the axial trapping frequency in z-direction is larger than $\mu/\hbar$. The axial profile of the cloud is then well approximated by a gaussian, as only the ground state of the motion along z is populated (see chapter 3).

1.3 The hydrodynamic approach

The dynamic properties of BECs can in principle be derived from the time-dependent GP-equation (equation (1.12)). It exists however a more intuitive approach, which directly uses the velocity field as a variable. This hydrodynamic approach is presented in the following.

The condensate wave function is fully described by the two macroscopic parameters $n(\boldsymbol{r}, t)$ and $\varphi(\boldsymbol{r}, t)$, the density and the phase of the condensates:

$$\Psi(\boldsymbol{r}, t) = \sqrt{n(\boldsymbol{r}, t)}e^{i\varphi(\boldsymbol{r}, t)}.$$

When looking for the current density of the wave function Ψ, one finds:

$$\boldsymbol{j} = \frac{i\hbar}{2m}[\Psi\boldsymbol{\nabla}\Psi^* - \Psi^*\boldsymbol{\nabla}\Psi] = n\frac{\hbar}{m}\boldsymbol{\nabla}\varphi \tag{1.19}$$

In this equation we can identify the velocity field $\boldsymbol{v}$, by setting $\boldsymbol{j} = n\boldsymbol{v}$:

$$\boldsymbol{v} = \frac{\hbar}{m}\boldsymbol{\nabla}\varphi. \tag{1.20}$$

1.3.1 Irrotational flow and hydrodynamic equations

According to equation (1.20) the motion of the condensate corresponds to a potential flow; the velocity field being the gradient of the scalar velocity potential $\hbar\varphi/m$. If φ is not singular, the motion of the condensate must be irrotational, that is

$$\boldsymbol{\nabla} \times \boldsymbol{v} = \frac{\hbar}{m}\boldsymbol{\nabla} \times \boldsymbol{\nabla}\varphi = 0.$$

The possible motions of a condensate are thus more restricted than those of a classical fluid. The only rotational motion is in fact induced by quantized vortices, as introduced in part III of this thesis.

To obtain the hydrodynamic equations of a BEC one inserts the condensate wave function in the time-dependent GP-equation (equation (1.12)), which leads to a system of coupled equations for n and $\boldsymbol{v}$:

$$m\frac{\partial \boldsymbol{v}}{\partial t} + \boldsymbol{\nabla}\left(-\frac{\hbar^2}{2m}\frac{\nabla^2\sqrt{n}}{\sqrt{n}} + \frac{1}{2}m\boldsymbol{v}^2 + U + gn\right) = 0 \tag{1.21}$$

$$\frac{\partial n}{\partial t} + \boldsymbol{\nabla}\cdot(n\boldsymbol{v}) = 0. \tag{1.22}$$

The first equation has the form of the Euler equation, and the second is a continuity equation. Two terms can be interpreted as a pressure:

$$P_{\text{mf}} = \frac{1}{2}gn^2 \text{ and } P_q = -\int n\boldsymbol{\nabla}\frac{\hbar^2}{2m}\frac{\nabla^2\sqrt{n}}{\sqrt{n}}.$$

The term P_{mf} depends only on the density and the coupling constant g, and thus only on mean-field parameters. The term P_q is the so-called "quantum pressure". The Thomas-Fermi approximation within the hydrodynamic approach consists in neglecting the term of the quantum pressure. Doing so, one gets the hydrodynamic equations in the Thomas-Fermi approximation:

$$\begin{aligned} m\frac{\partial \boldsymbol{v}}{\partial t} + \boldsymbol{\nabla}\left(\frac{1}{2}m\boldsymbol{v}^2 + U + gn\right) &= 0 \qquad (1.23)\\ \frac{\partial n}{\partial t} + \boldsymbol{\nabla}\cdot(n\boldsymbol{v}) &= 0. \qquad (1.24) \end{aligned}$$

In these equations no viscosity term arises. Also the only pressure terms appearing relies only on the cloud's density, the fluid is thus baroscopic. As derived above, it also is irrotational. These attributes are the signatures of a very prominent property of an interacting condensate: its superfluidity [61].

1.3.2 The healing length

As was discussed in this section, the Thomas-Fermi approximation corresponds to neglecting the quantum pressure term. For a condensate of radius R the quantum pressure scales as $\frac{\boldsymbol{\nabla}^2\sqrt{n}}{\sqrt{n}} \sim R^{-2}$. As can be seen from equation (1.21) it can be neglected in comparison with the interaction term, if

$$gn \gg \frac{\hbar^2}{mR^2} \qquad \Leftrightarrow \qquad R \gg \xi \ , \quad \text{where} \ \ \xi = \frac{\hbar}{\sqrt{mgn}} \ ,$$

and ξ is the so-called *healing length* of the condensate. It is the length scale on which the density recovers the TF-profile next to a defect in the wave function. Such a defect can e.g. be a quantized vortex: at the exact vortex position the density is zero. The size of the vortex core is then the distance on which the profile recovers the TF-density, and this distance is of the order of the healing length.

1.4 Dynamics of a condensate

The time-dependent behavior of a condensed cloud is an important source of information about its physical nature. One can for example understand the phenomenon of superfluidity in a BEC from the structure of its excitation spectrum.

This section contains a brief presentation of the methods to derive the excitation spectrum. The most complete approach follows the theory of Bogoliubov. This approach allows in principle to derive the excitations spectrum under arbitrary conditions. In most cases it does however not lead to analytic calculations.

In a second section an especially simple case is thus presented in more detail: the case of a trapped condensate at zero temperature. This section is based on the hydrodynamic treatment of a condensate, as presented in section 1.3. Within this approach some of the most studied modes of BECs are derived: the collective excitations of low energy (see e.g. [67–69] for theory, and [70, 71] for experiments). These low-lying surface modes are also of some relevance in the experimental parts of this thesis.

1.4.1 The Bogoliubov approach

For the derivation of the Gross-Pitaevskii equation (equation (1.12)), the ansatz

$$\hat{\Psi} = \Psi + \delta\hat{\Psi} \qquad \text{with} \qquad \Psi = \sqrt{N_0}\phi_0 \qquad (1.25)$$

had been introduced, where Ψ is the condensate wave function, and $\delta\hat{\Psi}$ the condensate depletion. The condensate depletion was then neglected, which is in general a reasonable approximation for Bose-Einstein condensates in atomic gases.

For a more complete description of Bose-Einstein condensates at temperatures $T \neq 0$ the condensate depletion must however be taken in to account. The expansion of the Heisenberg equation must thus be taken out to a superior order. This approach was developed by Bogoliubov [65] and is given in great detail in [62] and [8], and here only its general approach is briefly sketched out.

Inserting the ansatz (1.25) in the Heisenberg equation leads to a system of coupled linear equations for $\delta\hat{\Psi}$ and $\delta\hat{\Psi}^\dagger$. The field operator can be then be rewritten using the eigenmodes of the system:

$$\hat{\Psi}(\boldsymbol{r},t) = \sum_k \left(u_k(\boldsymbol{r})\hat{b}_k e^{-i\omega_k t} + v_k^*(\boldsymbol{r})\hat{b}_k^\dagger e^{i\omega_k t} \right) e^{i\mu t/\hbar}, \tag{1.26}$$

where k is the quantum number of the eigenmode with frequency ω_k and $\hat{b}_k^\dagger$ and $\hat{b}_k$ are its creation and annihilation operators. This change from $\hat{\Psi}$ to $\hat{b}$ is called *Bogoliubov transformation.*

When expanding the hamiltonian to second order in $\delta\hat{\Psi}$, and rewriting it in terms of $\hat{b}$ and $\hat{b}^\dagger$, one gets

$$\hat{H} = E_0 + \sum_k \hbar\omega_k \hat{b}_k^\dagger \hat{b}_k \tag{1.27}$$

The system is thus fully described in terms of its excitations. The vacuum of excitations is defined by $\hat{b}_k|0\rangle = 0$ for all k. It does however not corresponds to a pure BEC, due to the quantum depletion. The hamiltonian of equation (1.27) is equivalent to that of noninteracting particles in a harmonic oscillator and the number of excitation quanta is given by the Bose-Einstein statistics for an ideal gas: at temperature T the number of excitation quanta in a mode k is given by

$$\langle \hat{b}_k^\dagger \hat{b}_k \rangle = \frac{1}{e^{\hbar\omega_k/(k_\mathrm{B}T)} - 1}, \tag{1.28}$$

where $\langle\,\rangle$ indicates the thermodynamic mean.

Under typical experimental conditions the temperature is of the order of $k_\mathrm{B}T \sim \mu \sim 10\,\hbar\omega_\perp$, and a large number of Bogoliubov excitations ω_k is populated. For some selected trap geometries the spectrum of the eigenmodes can be calculated analytically, and the solutions are presented in the following.

- **Homogeneous case:** For a homogenous BEC k corresponds to the wave vector of the excitations, and the Bogoliubov spectrum is

  $$\hbar\omega_k = \sqrt{\frac{\hbar^2k^2}{2m}\left(\frac{\hbar^2k^2}{2m} + \mu\right)}.$$

  The spectrum of small energy modes with $\hbar^2k^2/(2m) \ll \mu$ corresponds to a phonon spectrum linear in k, while the high energy modes ($\hbar^2k^2/(2m) \gg \mu$) have an energy quadratic in k and correspond to free particles.

- **Harmonic trap:** For a condensate in a harmonic trap the modes are quantized in energy. For modes with a wavelength much smaller than the size of the cloud, the spectrum is similar to that of the homogenous case. For modes with a wavelength that is similar to the size of the condensate, some normal modes corresponding to shape oscillations of the condensate can be identified [67]. A description of these modes within the hydrodynamic approach is given in section 1.4.2.

1.4.2 Collective modes: the hydrodynamic approach

To investigate elementary excitations within the hydrodynamic approach, one considers small deviations from the equilibrium density of the gas: $n = n_{\mathrm{eq}} + \delta n$, where n_{eq} is the equilibrium density. This ansatz is inserted in the hydrodynamic equations in the TF-limit (equations (1.23)), which are then linearized by treating δn as a small quantity. If the initial velocity field is zero, this leads to the set of equations:

$$\begin{aligned} \frac{\partial \delta n}{\partial t} &= -\boldsymbol{\nabla}\left(n_{\mathrm{eq}}\boldsymbol{v}\right) &\quad (1.29)\\ m\,\frac{\partial \boldsymbol{v}}{\partial t} &= -\boldsymbol{\nabla}\delta n &\quad (1.30) \end{aligned}$$

Taking the time derivative of equation (1.29) and eliminating $\boldsymbol{v}$ from the set of equations, one gets the equation of motion for the density deviation δn in a potential U (which enters the equation through the equilibrium density n_{eq} as given in equation (1.15)):

$$m\,\frac{\partial^2}{\partial t^2}\,\delta n = g\boldsymbol{\nabla}\,\left(n_{\mathrm{eq}}\boldsymbol{\nabla}\delta n\right). \tag{1.31}$$

If we consider oscillations with time dependance $\delta n \propto e^{i\omega t}$, and use $n_{\mathrm{eq}}(\boldsymbol{r}) = (\mu - U(\boldsymbol{r}))/g$ (equation (1.15)), this simplifies to

$$\omega^2\delta n = \frac{1}{m}\left(\boldsymbol{\nabla}U\,\boldsymbol{\nabla}\delta n - \left[\mu - U(\boldsymbol{r})\right]\nabla^2\delta n\right). \tag{1.32}$$

The solutions of this differential equation are the eigenmodes of the condensate in the trapping potential $U(\boldsymbol{r})$. In the following this equation will be analyzed for the specific case of a cigar shaped harmonic trap.

Surface modes in a cigar shaped trap

The potential of a cigar shaped trap has axial symmetry:

$$U = \frac{m}{2}\omega_\perp^2 r^2 + \frac{m}{2}\omega_z^2 z^2 = \frac{m}{2}\omega_\perp^2(r^2 + \lambda^2 z^2)$$

where $\lambda = \omega_z/\omega_\perp$ is the anisotropy parameter of the trap, and $r = (x^2+y^2)^{1/2}$. Inserting this potential into equation (1.32) one gets:

$$\omega^2\delta n = \omega_\perp^2\left(r\frac{\partial}{\partial r} + \lambda^2 z\frac{\partial}{\partial z}\right)\delta n - \frac{\omega_\perp^2}{2}\left(R_\perp^2 - r^2 - \lambda^2 z^2\right)\nabla^2\delta n, \tag{1.33}$$

where $R_\perp = 2\mu/(m\omega_\perp^2)$ is the radial Thomas-Fermi radius of the cloud.

Due to the axial symmetry of the problem, functions proportional to $e^{im\phi}$ (where m is an integer), are solutions to equation (1.33) [67]. Classes of exact solutions are e.g. functions with $l > 0$, $m = \pm l$ and $m = \pm(l-1)$ and the form:

$$\delta n = r^l Y_{l,m}(\theta,\phi), \tag{1.34}$$

where Y_{lm} is a spherical harmonic. Due to the dependence of the density variation on the radius, $\delta n \propto r^l$, they become more and more localized at the surface of the cloud with increasing l, while the density in the cloud's center does not change: this is why they are called the *surface modes* of the condensate [61].

The corresponding dispersion laws for these solutions are [67]:

$$\begin{aligned} \omega^2 &= l\omega_\perp^2 &\qquad \text{for} \qquad m = \pm l &\quad (1.35)\\ \omega^2 &= (l-1)\omega_\perp^2 + \omega_z^2 &\qquad \text{for} \qquad m = \pm(l-1) &\quad (1.36) \end{aligned}$$

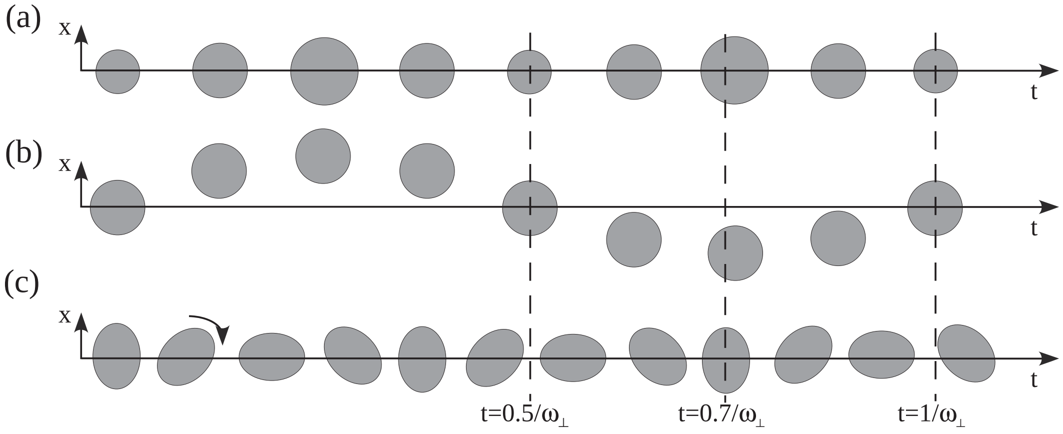

Figure 1.2: Surface modes of a Bose-Einstein condensate: (a) The monopole mode (or breathing mode), with frequency $\omega = 2\omega_\perp$, (b) the dipole modes, with frequency $\omega = \omega_\perp$, and (c) the quadrupole modes with frequency $\omega = \sqrt{2}\omega_\perp$.

Some low-lying modes

Equations (1.35) and (1.36) provide a description of the following modes, which are of some importance in our experiment:

- **The dipole modes:** The dipole modes correspond to $l = 1$, and its frequencies coincide to the harmonic oscillator frequencies:

  $$\omega(m = \pm 1) = \omega_\perp, \qquad \text{and} \qquad \omega(m = 0) = \omega_z.$$

  These modes correspond to pure center-of-mass motions of the cloud along the two radial ($m = \pm 1$) or the axial ($m = 0$) direction respectively (figure 1.2(b)).

- **The quadrupole modes:** The quadrupole modes correspond to $l = 2$, and equations (1.35) and (1.36) account for the $m = \pm 2$ and $m = \pm 1$ components, with the respective frequencies

  $$\omega(m = \pm 2) = \sqrt{2}\omega_\perp, \qquad \text{and} \qquad \omega(m = \pm 1) = \sqrt{\omega_\perp^2 + \omega_z^2}.$$

  The $m = \pm 2$ modes correspond to an elliptic deformation of the condensate, with the ellipses main axes rotating with angular frequency $\omega = \sqrt{2}\omega_\perp$ in the xy-plane (figure 1.2(c)), in opposite directions for $m = 2$ and $m = -2$.

A third quadrupole mode, with $l = 2$ and $m = 0$ is not described by the above equations. Neither is the lowest $l = m = 0$ mode, the so-called breathing mode, which mixes with the $m = 0$ quadrupole mode in case of an anharmonic trap. One can find these modes by inserting the polynomial ansatz

$$\delta n = a + br^2 + cz^2$$

into equation 1.33. This gives a system of three linear equations for a, b and c, which can be written as a matrix equation. The condition for the existence of nontrivial solutions is that the determinant of the matrix vanishes. This leads to the dispersion law of the two decoupled modes [67]:

$$\omega^2 = \omega_\perp^2 \left(2 + \frac{3}{2}\lambda^2 \pm \frac{1}{2}\sqrt{16 - 16\lambda^2 + 9\lambda^4} \right).$$

In a strongly cigar-shaped trap $\lambda \ll 1$, and the corresponding solutions are

$$\omega_- \approx \sqrt{5/2}\,\omega_z \qquad \text{and} \qquad \omega_+ \approx 2\omega_\perp \left(1 + \frac{\lambda^2}{16}\right).$$

The mode ω_+ corresponds to the $l = m = 0$ monopole mode, which is of some importance in our experiments. It is radially symmetric, and corresponds to a periodic increase and decrease of the cloud's diameter (figure 1.2(a)). For a 2D gas in a harmonic potential the breathing mode has a frequency of exactly $2\omega_\perp$, and for the case of hard core interactions it was shown by Pitaevskii and Rosch [72] that this solution is "universal", i.e. not dependent on other properties of the trapped gas.

The low-lying eigenmodes of atomic BECs have been studied thoroughly in harmonic traps with various geometries (see e.g. [70,71]). As their properties are thus well known, they are used for several purposes in the experiments: to measure the frequencies of the magnetic or optic traps (usually through the frequency of the monopole or dipole mode), or to set the condensate into rotation (by resonantly exciting the quadrupole mode). In this thesis only in one case an eigenmode is explicitly studied: chapter 10 describes an experimental study of the monopole-oscillation of a fast rotating gas in a quadratic+quartic potential.

1.5 Coherence properties of Bose-Einstein condensates

For the experiments described in this manuscript especially two notions play an important role: phase coherence and superfluidity. While superfluidity manifests itself in the excitation spectrum and the rotational properties of the BEC, phase coherence properties are especially well illustrated in interference experiments. Such experiments constitute the main experimental tool of part II of this manuscript. In the following the notion of phase coherence is briefly introduced.

1.5.1 The coherence length

The Gross-Pitaevskii equation is a non-linear differential equation for a classical field, the condensate wave function. This has some analogy to a classical light field, governed by the Maxwell-equations. Indeed a Bose-Einstein condensate without interactions can be understood as the matter equivalent to a laser. This equivalence inspired various experiments with BECs, which all have their analog in optics: interference experiments [3,35,73], bosonic amplification [74,75] and the construction of continuous atom lasers [76–78]. The notion of coherence thereby is associated with the variations of the phase φ of the condensate wave function and is crucial to the understanding of interference.

The first order correlation function

An important function for the description of interference experiments, and thus for the description of phase coherence is the first order correlation function (or one-body density matrix) [62]:

$$g^{(1)}(\boldsymbol{r}, \boldsymbol{r'}) = \langle \hat{\Psi}^\dagger(\boldsymbol{r}) \hat{\Psi}(\boldsymbol{r'}) \rangle$$

This function quantifies how well the phase relation between two points $\boldsymbol{r}, \boldsymbol{r'}$ stays defined, when the distance $\boldsymbol{s} = \boldsymbol{r} - \boldsymbol{r'}$ between these points increases. In an interference experiment, this function gives the expectation value of the fringe contrast.

For a uniform system $g^{(1)}$ depends only on the distance $\boldsymbol{s}$, due to the translational invariance. For a nonuniform system $g^{(1)}$ depends explicitly on $\boldsymbol{r}$ and $\boldsymbol{r'}$. To characterize the coherence of

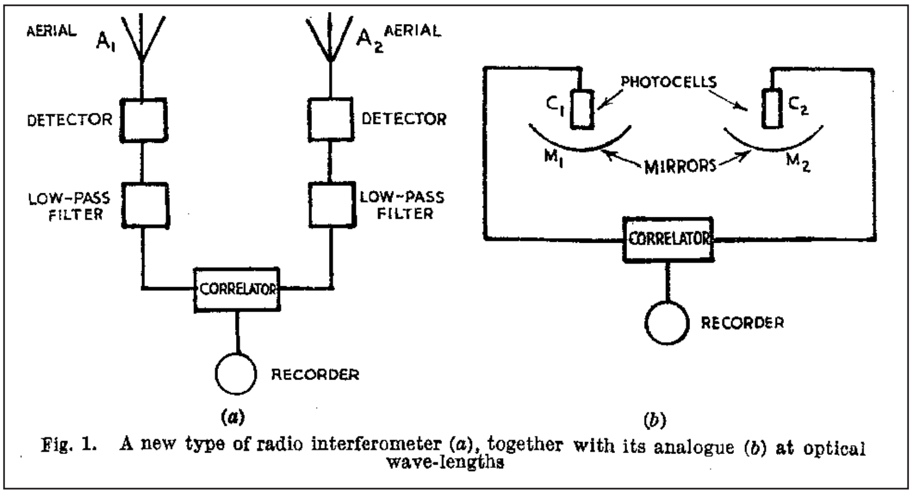

Figure 1.3: The Hanbury-Brown Twiss experiment (the figure is taken from reference [81]): (a) The signals from two photon sources (in this case aerials transmitting the signals from radio stars) are measured independently, and the correlation in the intensity fluctuations of the two sources is measured. The distance between the aerials can be varied, which allows to measure the angular diameter of the star. (b) The analogous setup for optical wavelengths.

a nonuniform cloud, one thus introduces the spatial correlation function:

$$g^{(1)}(\boldsymbol{s}) = \int g^{(1)}(\boldsymbol{r} + \frac{\boldsymbol{s}}{2}, \boldsymbol{r} - \frac{\boldsymbol{s}}{2})\, d\boldsymbol{r}.$$

The coherence length L_c of the system is then defined as the half width at half maximum value of $g^{(1)}$. One can compare L_c to the size L of the system, and one speaks of a “fully coherent” system if $L_c \sim L$.

Condensates and quasi-condensates

A condensate that is fully described by the condensate wave function of equation (1.13), has a well defined phase $\varphi(\boldsymbol{r}, t)$. This situation has been implicitly assumed so far. In this case all atoms occupy the same single-particle state ϕ_0, and the one-body correlation function of the ground state can be written as

$$g^{(1)}(\boldsymbol{r}, \boldsymbol{r}') = \sqrt{n(\boldsymbol{r})n(\boldsymbol{r}')}.$$

In this case $L_c = L$, and the system is fully coherent.

For most 3D condensates this description works very well. Some references use this relation as a necessary condition to call a system a Bose-Einstein condensate [79, 80]. In 2 dimensions however exists a superfluid phase at low temperatures [79], for which the condition $L_c = L$ is not fulfilled. Such systems are called “quasi-condensates” in the notation of [79]. The phase properties of such 2D quasi-condensates are described in chapter 3. For the sake of readability the use of the prefix will however not be strictly persevered throughout this manuscript; in all cases the significance of the word “condensate” should be clear from the context.

1.5.2 Pair correlation function

The coherence length is a function of the first order correlation function, also called the one particle density matrix. If one now wants to go a step further, one has to look at the second order correlation function, which gives the probability to find a boson at a position $\boldsymbol{r}$, given that one was already found at the position $\boldsymbol{r'}$. The second order correlation function (or two body density matrix) is defined by [62]:

$$g^{(2)}(\boldsymbol{r},\boldsymbol{r'}) = \langle \hat{\Psi}^{\dagger}(\boldsymbol{r})\hat{\Psi}^{\dagger}(\boldsymbol{r'})\hat{\Psi}(\boldsymbol{r})\hat{\Psi}(\boldsymbol{r'})\rangle = \langle : \hat{n}(\boldsymbol{r})\hat{n}(\boldsymbol{r'}) : \rangle \ , \tag{1.37}$$

where : ... : indicates that the operators have to be written in normal order.

The Hanbury-Brown Twiss experiment The second order correlation function for photons describes the fluctuations of the light field. In the case of a thermal light source, which consists of many independent (i.e. incoherent with respect to each other) elementary light sources, the temporal statistics of the radiation is gaussian. The (temporal) second order correlation function in this case is such that $g^{(2)}(|t-t'| \to 0) \approx 2$, and $g^{(2)}(|t-t'| \to \infty) \approx 1$. This signifies that when detecting an emitted photon, the probability to find a second photon at the same time is twice as high as the probability to find a second photon after a long time $|t-t'|$. This (quite counterintuitive) effect was discovered in the 1950's by Hanbury-Brown and Twiss [81,82]. Figure 1.3 shows their experimental setup, which was in fact designed to measure the angular diameter of radio stars, before also being applied to optical wavelengths. Recent interference experiments with arrays of independent BECs trapped in the sites of an optical lattice [3, 83] show the analogous effect for independent atom sources. Such experiments and a theoretical analysis of their results are presented in chapter 6.

1.5.3 Bose-Einstein condensation, superfluidity and coherence

With the concepts of superfluidity and coherence the most prominent properties of atomic Bose-Einstein condensates are now introduced. But even if pure BECs of interacting atoms are both superfluid and coherent, one should not take these three terms as equivalents. This section gives a few examples of systems exhibiting not all of these distinct properties.

- **Superfluidity** describes the capacity of a system for flow without viscosity, as defined by the celebrated Landau criterion [62]. This phenomenon was first observed in liquid Helium in 1937 [84, 85]. In 1938 London proposed that the observed superfluidity was a consequence of Bose-Einstein condensation [86]. Until today however this link could not be formally proven [87].

- **Noninteracting BECs** are fully coherent but not superfluid, the phenomenon of superfluidity relying on particle interactions. This is due to the dispersion relations of elementary excitations. In a system without interactions, the spectrum of elementary excitation is quadratic ($E(\boldsymbol{p}) = p^2/(2m)$), while it is linear for phonons ($E(\boldsymbol{p}) = c|\boldsymbol{p}|$), which are the excitations of lowest energy in an interacting BEC (see section 1.4.1 and [62]). It can be easily shown that an object which is drawn through a superfluid at $T = 0$ with a velocity smaller than the sound velocity c can not be decelerated by exciting a phonon, as the total energy and momentum have to be conserved. In contrast there always is a solution for the excitation of a free particle in an ideal gas, and thus there is no frictionless flow.

- **In two dimensions** exists a phase transition to a superfluid gas, if the system is interacting. The system is however not fully coherent below the transition temperature, but has a fluctuating phase. Such a system without true long range order is often called a *quasi-condensate* [79]. In a homogenous 2D system the transition to the superfluid phase is called Kosterlitz-Thouless transition [38, 79], and it is discussed in some detail in part II of this thesis.

1.6 Conclusion

The formalisms and results presented in this chapter represent the foundation for the theoretical treatment of the results of this thesis. Most often the experimental results can be treated in the frame of a mean-field theory, under the assumption that the Thomas-Fermi approximation is valid. The Thomas-Fermi equation (equation (1.15)) is thus the base for most fitting routines to our experimental results, which for example give access to the condensed atom number through a fit of the cloud's radius. For typical experimental parameters, $\omega_{\rm ho}/(2\pi) = 50\,\rm Hz$, and $N = 3\cdot 10^5$, the most important length scales presented in this chapter are summarized in the following table:

healing length	$\xi = \hbar/\sqrt{mgn}$	$0.1\,\mu\rm m$
length of the harmonic oscillator	$a_{\rm ho} = \sqrt{\hbar/(m\omega_{\rm ho})}$	$1.5\,\mu\rm m$
Thomas-Fermi radius	$R = \sqrt{2\mu/(m\omega_{\rm ho}^2)}$	$10\,\mu\rm m$,

The TF-approach is however not valid in the case of 2-dimensional condensates, as presented in part II, where in one spatial direction only the ground state of the harmonic trap is populated. In this case the density profiles are well approximated by those of a non-interacting gas in the lowest bound state of the harmonic oscillator, as discussed in section 1.1.1.

The foundations for the main experimental themes were also laid out in this chapter: the coherence properties of a condensate, as discussed in section 1.5.1, are important for the understanding of part II, which discusses interference experiments involving between 2 and 30 2D condensates. The superfluid characteristic of irrotational motion, as presented in section 1.3, plays an important role in part III, in which experiments with rotating condensates are presented.

Chapter 2

Experimental realization of a BEC

For our experiments with Bose-Einstein condensates (BECs) we have chosen to work with ^{87}Rb atoms. This atom is the most commonly used in cold atom experiments, due to the position of its optical resonances, which allow for the use of laser diodes in the processus of optical cooling [88]. Furthermore its collision properties are well adapted for evaporative cooling[1], by which Bose-Einstein condensation is attained.

The experimental setup with which the results of this thesis were obtained exists since 1998. For each of the presented experiments it was subject of several minor modifications, which will be detailed in the respective chapters. The parts which are necessary for the production of the condensate itself have however not qualitatively changed since the first building of the setup. Consequently they are described in great detail in the PhD theses of my predecessors, David Guéry-Odelin, Frédéric Chevy and Vincent Bretin [7–9]. This chapter will thus give only a very brief overview over the main steps necessary to obtain Bose-Einstein condensation. More detailed sections are dedicated to the experimental parts that play an important role in the experiments presented in parts II and III: the magnetic trap, the radio frequency (rf) field used for evaporation, and the imaging system.

2.1 Experimental cycle: brief overview

- **Magneto-optical trapping.** Our experimental setup is based on a vacuum system of two glass cells, vertically separated by a distance of $\sim 50\,\mathrm{cm}$, and a glass tube connecting the two cells. The upper of the cells contains ^{87}Rb vapor with a pressure of $\sim 10^{-8}$ mbar, of which is loaded a magneto-optical trap (MOT) [54–56]. As cooling transition for the MOT we use the D_2-line, with the transition wavelength $\lambda_0 = 780\,\mathrm{nm}$.

  From the upper MOT the atoms are continuously pushed down through the glass tube with a "pusher beam". When they arrive in the center of the lower cell they are retrapped by a second MOT. The pressure in the lower cell is $\lesssim 10^{-11}$ mbar, which is achieved through differential pumping between the two cells. Due to the better vacuum the "lower" MOT has a lifetime of $\gtrsim 60\,\mathrm{s}$, which is nearly a factor 100 longer than the life time of the MOT in the upper cell.

  The magnetic field of both MOTs is turned off after $\sim 15\,\mathrm{s}$, when the continuous pushing has lead to a trapped cloud of $\sim 10^9$ atoms. A short time of typically 10 ms of optical molasses follows, where the MOT beams are detuned to $\sim 80\,\mathrm{MHz}$ from the atomic reso-

---

[1] The experimental setup was initially built in 1995 to realize a Cesium (Cs) BEC. The collision properties of Cs however made this task difficult [89]. Bose-Einstein condensation in Cs was achieved only in 2002, using special evaporation methods to avoid inelastic collisions [90].

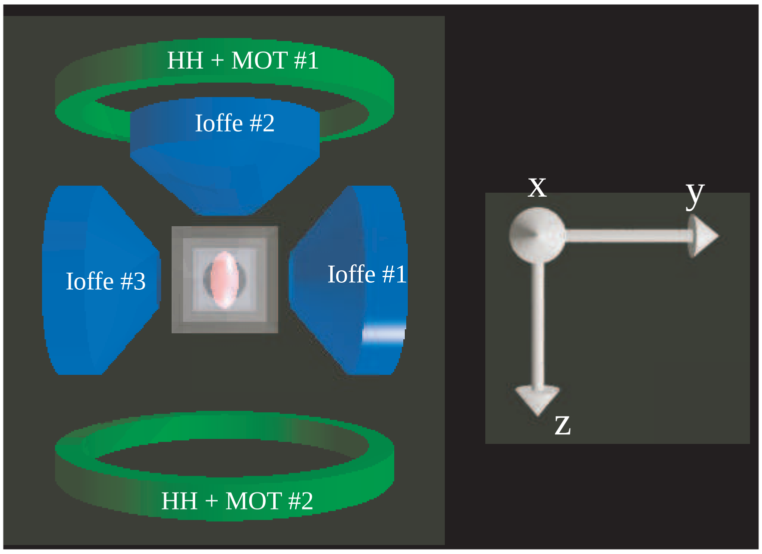

Figure 2.1: Magnetic field coils: view from above. Shown are the coils of the magneto-optical trap (“MOT 1” and “MOT 2”) and the Ioffe-Pritchard trap (“Ioffe 1”, “Ioffe 2”, “Ioffe 3”, with the pair of Helmholtz-coils “HH”). The MOT coils and the Helmholtz coil pair are mounted on the same mechanical support, which also contains a pair of coils in Helmholtz-configuration for the creation of the optical pumping field (not shown in the figure). Around each of the waterproof shells of the three Ioffe-coils, a coil of only a few turns is mounted. These coils provide the horizontal mode matching along the y- and the $z-$direction. Under the cell a fourth coil serves for vertical mode matching (none of the mode matching coils is shown).

nance. Due to Sisyphus cooling [91] the temperature of the cloud decreases to 20-30 μK during the molasses phase.

- **Magnetic trapping and evaporative cooling.** After the end of the molasses phase follows a short phase of optical pumping, during which the atoms are pumped into the Zeeman state $|F=2, m_F=2\rangle$. The polarized atoms are then trapped in a Ioffe-Pritchard (IP) trap, consisting of three conical water cooled coils (denoted as “Ioffe #1,2,3” in figure 2.1) and a pair of coils in Helmholtz configuration (“HH” in figure 2.1).

  Ideally the center of the IP should have the same position as the MOT in the lower cell, so that the atoms are not heated during the transfer to the magnetic trap. The geometry of the respective coils is organized in this way, with the pair of coils creating the quadrupole field of the lower MOT hold by the same support as the three Ioffe-coils and the pair of Helmholtz coils, as shown in figure 2.1. Due to imperfections of the mechanical setup, the two centers are however usually slightly separated by a distance of typically 0.3 mm in the horizontal directions. In vertical direction the gravitational sag of the magnetic trap (see section 2.2) dominates the center separation. This sag depends on the parameters of the magnetic trap, and is of the order of 2.5 mm for a non-compressed trap, which is the case when the atoms are loaded into the magnetic trap. Short magnetic field pulses after the optical pumping are used to bring the atoms to the center of the magnetic trap; this procedure is called *center matching.*

  Once the atoms are trapped purely magnetically, the magnetic trap is compressed radially, and the routine for evaporation cooling starts. This procedure consists in a scan of a radiofrequency (rf) field, with a frequency $\nu_{\mathrm{rf}}(t)$ starting at ~ 30 MHz above the bottom of the magnetic trap, and ending at ≈ 10 kHz above the trap bottom, which corresponds to a rf-frequency of typically ~ 1 MHz. The rf field couples different Zeeman levels on the energy surface $\mu|\boldsymbol{B}| = h\nu_{\mathrm{rf}}(t)$. The atoms that are hot enough to cross this surface are transferred to the untrapped Zeeman states and leave the trap. The rest of the atoms rethermalise at a lower temperature. If $\nu_{\mathrm{rf}}(t)$ is ramped slowly enough, evaporative cooling does not only lead to a decrease in atom number and temperature, but to an increase in phase space density. This regime is called "runaway" evaporation. To reach it, one needs a high initial atom density and a carefully designed rf ramp. At the end of evaporative cooling stands the phase transition to a BEC at a temperature of the order of 100 nK. The rf frequency is then usually kept at a frequency of 10 kHz above trap bottom, to keep the temperature of the cloud constant during the specific experimental cycles.

- **Time of flight and imaging:** After achieving Bose-Einstein condensation, the atoms are held in the magnetic trap, and different experiments are performed. At the end of these cycles, the magnetic trap is shut off abruptly and the atoms are let free to expand. After a variable time of free fall and expansion (0 to 30 ms) the cloud can be visualized by absorption imaging. We can perform absorption imaging simultaneously from two horizontal directions, along the radial direction y and the axial direction z.

2.2 The magnetic trap

When trapping neutral atoms with electromagnetic fields, one can make use either of their permanent magnetic momentum or an induced electric dipole moment. In most experiments magnetic trapping is used to obtain Bose-Einstein condensation. For our experiments we have chosen a magnetic Ioffe-Pritchard trap to obtain the initial condensates, which will be described in the following.

Later in the manuscript I will also present experiments where the condensates are manipulated with optical dipole potentials, which allow for a larger variety of potential shapes. The specific dipole potentials used are presented in the corresponding chapters of part II and III.

2.2.1 Magnetic trapping

The interaction energy of an atom with magnetic momentum $\boldsymbol{\mu}$ and a magnetic field $\boldsymbol{B}(\boldsymbol{r})$ is

$$E_{\mathrm{mag}} = -\boldsymbol{\mu} \cdot \boldsymbol{B}(\boldsymbol{r}). \tag{2.1}$$

It is thus minimal for a parallel magnetic moment in a magnetic field maximum. As can however be shown from the Maxwell-equations, a static magnetic field cannot have a local maximum $|\boldsymbol{B}|$ in vacuum (Wing-theorem, see e.g. [92]). This constraint can be overcome by using dynamic fields (a famous example for this kind of potential is the Paul trap for electric dipole moments [93]). Another possibility is to work with magnetic field *minima*: atoms polarized antiparallel to the magnetic field are "low field seekers" so that they are trapped in the minima of a magnetic field. This is the approach used for most experiments with trapped neutral atoms, including ours, where the atoms are polarized in the $|F = m_F = 2\rangle$ Zeeman state.

The second constraint in the construction of a magnetic trap is that the minimum should not be of value $B = 0$. At this value all Zeeman states have the same magnetic energy, and nothing prevents the atoms from changing from one state to another (these spin flips are called Majorana transitions). As atoms in the Zeeman levels $m_F = 0, -1, -2$ are not trapped in magnetic field minima, they leave the trap. Spin flips thus lead to considerable atom losses.

2.2.2 Geometry of the Ioffe-Pritchard trap

A magnetic field minimum with $B \neq 0$ can be constructed in different ways. The method we have chosen is the so called Ioffe-Pritchard (IP) trap, which we construct with three identical

”Ioffe” coils, as shown in figure 2.1. In second order expansion this configuration leads to a 3D harmonic potential. The three Ioffe coils are connected in series with a pair of coils in Helmholtz-configuration, which adds a homogenous magnetic field $\boldsymbol{B}_{\mathrm{HH}}$ at the position of the atoms. In our setup the Helmholtz coils are connected in a way, that $\boldsymbol{B}_{\mathrm{HH}}$ is antiparallel to the field created by the Ioffe coils, and of the same order. When taking into account terms up to the second order, the field created by this combination of coils is

$$\mathbf{B}(x,y,z) = B_0 \begin{pmatrix} 0 \\ 0 \\ 1 \end{pmatrix} + B' \begin{pmatrix} -x \\ y \\ 0 \end{pmatrix} + \frac{B''}{2} \begin{pmatrix} -xz \\ -yz \\ z^2 - \frac{1}{2}(x^2+y^2), \end{pmatrix} \tag{2.2}$$

where B_0 is a magnetic field, B' a magnetic field gradient, and B'' a magnetic field curvature. Expanding this field to the second order and using equation 2.1, one gets the following expression for the magnetic potential:

$$U(x,y,z) = U_0 + \frac{1}{2} m\omega_\perp^2 (x^2+y^2) + \frac{1}{2} m\omega_z z^2, \tag{2.3}$$

with the harmonic trapping frequencies:

$$\omega_z = \sqrt{\frac{\mu B''}{m}} \qquad \text{and} \qquad \omega_\perp = \sqrt{\frac{\mu}{m}\left(\frac{B'^2}{B_0} - \frac{B''}{2}\right)}. \tag{2.4}$$

The current sent through the Ioffe- and Helmholtz-coils is $\approx 45\,\mathrm{A}$, leading to $B_0 \approx 1\,\mathrm{G}$, $B' \approx 130\,\mathrm{G/cm}$ and $B'' \approx 80\,\mathrm{G/cm^2}$. As one can see from equation 2.4, the axial trapping frequency ω_z depends only on B'', while the radial trapping frequency $\omega_\perp$ depends on B_0, B' and B''. The addition of the Helmholtz coils, which leads to a decrease in B_0, thus increases the radial frequency, while it leaves the axial frequency unchanged: the trap changes from nearly isotropic to cigar shaped. The aspect ratio of the cigar shaped trap is ~ 10, with the harmonic trapping frequencies $\omega_z = 2\pi\,11\,\mathrm{Hz}$ and $\omega_\perp \sim 2\pi\,100\,\mathrm{Hz}$.

Tunability of the trapping frequencies

For small bias fields of $B_0 \sim 1\,\mathrm{G}$, typical field gradients of $B' \sim 100\,\mathrm{G/cm^2}$, and field curvatures of $B'' \sim 80\,\mathrm{G/cm^2}$, the last term in the equation for the radial trapping frequency (eq. (2.4)) becomes negligible. A good approximation for $\omega_\perp$ is thus given by $\omega_\perp^2 = \mu B'^2/(mB_0)$, and the addition of a homogenous field at the trap center modifies the radial trapping frequency as $\omega_\perp \propto B_0^{-1/2}$. This frequency is thus easily tunable. To this purpose a second pair of Helmholtz coils is mounted onto the same mechanical support as the first one. This Helmholtz pair is connected to an independent power supply. Due to the independent current in these coils, the field at the position of the atoms can be tuned typically from 0 to 5 G. We can thus achieve radial trap frequencies down to $\omega_\perp/(2\pi) \approx 70\,\mathrm{Hz}$ without changing the axial confinement.

2.2.3 Influence of gravity on the trap geometry

Gravity plays a relatively important role in our experiment, where it has to be taken into account when calculating the trap geometry and the evaporation efficiency (for the latter see section 2.3.2). The size of these effects can be easily calculated, as the gravitational force on the atoms is well known. The effects on the trap geometry are [8]:

1. a displacement of the trap center along x (the *gravitational sag*):

$$\Delta x = -\frac{g}{\omega_\perp^2}$$

2. a decrease of the harmonic trapping frequency along x:

$$\frac{\Delta\omega_x}{\omega_\perp} = -\frac{3}{4}\left(\frac{mg^2}{\mu B_0 \omega_\perp^2}\right) = -\frac{3}{4}\left(\frac{mg}{\mu B'}\right)^2$$

The importance of these modifications depends on the experimental aim: the gravitational sag becomes of some importance in chapter 4, because it limits the addressability of individual sites in the experiments including an optical lattice. As the gravitational sag decreases with the increasing radial trapping frequency, it can be reduced by using steep traps and small bias fields B_0.

The slight asymmetry of the trap, due to the decrease of the vertical trapping frequency ω_x (which is of the order of 1%) is of some importance in the experiments with rotating condensates (see part III): it breaks the rotational symmetry, which leads to a loss in angular momentum of the rotating cloud. As $\omega_\perp^2 \propto B_0^{-1}$, the asymmetry $\Delta\omega_x/\omega_\perp$ does not depend on B_0 and can thus not be reduced by application of an additional bias field.

2.3 Evaporative cooling

When the cloud is loaded into the magnetic trap, it still has a temperature of typically $\sim 30\,\mu$K. To obtain Bose-Einstein condensation, temperatures of some 100 nK are needed. In chapter 1 the processus of Bose-Einstein condensation was described for a fixed atom number and decreasing temperature. Experimentally it is however not a simple task to reduce the temperature to values of the order of 100 nK. The method with which this is generally achieved is the so called evaporative cooling [57]: in several steps the respectively most energetic atoms are removed from the trap, followed from an equilibration time, where the remaining atom cloud equilibrates to its new (and lower) temperature.

In the processus of evaporative cooling the atom number decreases thus continuously with the temperature, and it is not a priori sure that Bose-Einstein condensation at finite T can be reached in such a system. In can however be shown that a constant collision rate during evaporation is a sufficient condition for condensation [92].

2.3.1 The phase space density during evaporative cooling

In cold atom experiments the evaporation of the hottest atoms is generally realized with the help of a rf field of frequency ν_{rf}, that couples the Zeeman levels. This principle is illustrated in figure 2.2. Atoms with an energy larger than $E_c = 2h(\nu_{\mathrm{rf}} - \nu_0)$ are coupled to the untrapped Zeeman levels and leave the trap. The energy $2h\nu_0$ associated to the frequency which couples the Zeeman levels in the trap center is called the *trap bottom.*

To obtain Bose-Einstein condensation the rf frequency ν_{rf} is ramped down slowly. This must happen slowly enough, so that the remaining atoms have the time to thermalize, and the cloud is permanently in a quasi-equilibrium state. If this is the case, one can define the *evaporation parameter* η:

$$\eta = \frac{E_c}{k_{\mathrm{B}}T} = \frac{2h(\nu_{\mathrm{rf}} - \nu_0)}{k_{\mathrm{B}}T}. \tag{2.5}$$

This parameter gives the ratio between the energy of the evaporation surface to the temperature of the cloud.

One can show [92] that for high initial collision rates a regime exits where η stays constant, while the phase space density diverges during the rf sweep. Therefore Bose-Einstein condensation can be reached in spite of decreasing atom number. To achieve this “runaway” regime, a sufficient initial density and collision rate, and a quasi-adiabatic rf ramp are needed. In our experiment

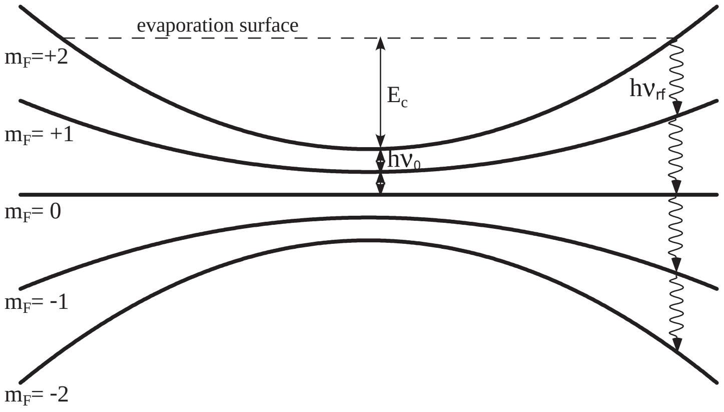

Figure 2.2: Principle of evaporative cooling: atoms with an energy larger than E_c cross the evaporation surface and are coupled to untrapped Zeeman states.

the two first conditions rely mostly on an efficient molasses phase and exact center matching (see section 2.1). The condition of quasi-adiabaticity is matched by an exponential ramp of $\nu_{\rm rf}$ with a duration of 25 to 45 s, depending on $\omega_\perp$ and the initial collision rate. The phase of evaporative cooling is thus the longest of the experiment, and determines the duration of the experimental cycle.

For the experimental conditions which lead to Bose-Einstein condensation in our experiment, the evaporation parameter η is of the order of 5 to 10.

2.3.2 Influence of gravity on evaporative cooling

One-dimensional evaporation

The gravitational sag has a direct influence on evaporation: due to the mismatch between the magnetic trap center and the center of the atomic cloud, the evaporation surfaces are not concentric around the cloud (for an illustration see figure 4.7). This effect becomes important mostly at the end of evaporation, when the radius of the evaporation surface becomes of the order of the gravitational sag. Evaporation becomes then 1-dimensional, which means that only atoms from the bottom of the cloud get evaporated. In our experiment this effect happens for $T \sim 200\,\mathrm{nK}$ and merely leads to a less efficient evaporation.

Energy of the evaporation surface

As a second effect of the gravitational sag the energy of the evaporation surface E_c has to be recalculated. When no sag is present, the energy of the atoms that cross the evaporation surface is given by $E_c = 2h(\nu_{\rm rf} - \nu_0) = 2h\Delta\nu$, where ν_0 is the resonant rf frequency at the trap bottom (see figure 2.2). In the presence of the gravitational sag this picture changes, due to the additional gradient that represents gravity[2]. In figure 2.3 a scheme of the levels $m_F = 0$ and $m_F = 2$ is shown, including the effect of gravity. The energy between the levels at $x = 0$ (corresponding to the position of the trap center) is $E_0 = 2h\nu_0$. To calculate the effect of a rf knife of frequency $\nu_{\rm rf}$, one has to take into account that the evaporation is 1-dimensional, which means that the atoms are only coupled out of the trap at the lower edge. For an evaporation surface at energy E_c from the trap bottom, the lower edge of the cloud is at $x_0 = -\sqrt{2E_c/(m\omega_x^2)}$.

---

[2] For ^{87}Rb atoms in the $m_F = 2$ Zeeman state gravity corresponds to a gradient of $\approx 15\,\mathrm{G/cm}$ in x-direction.

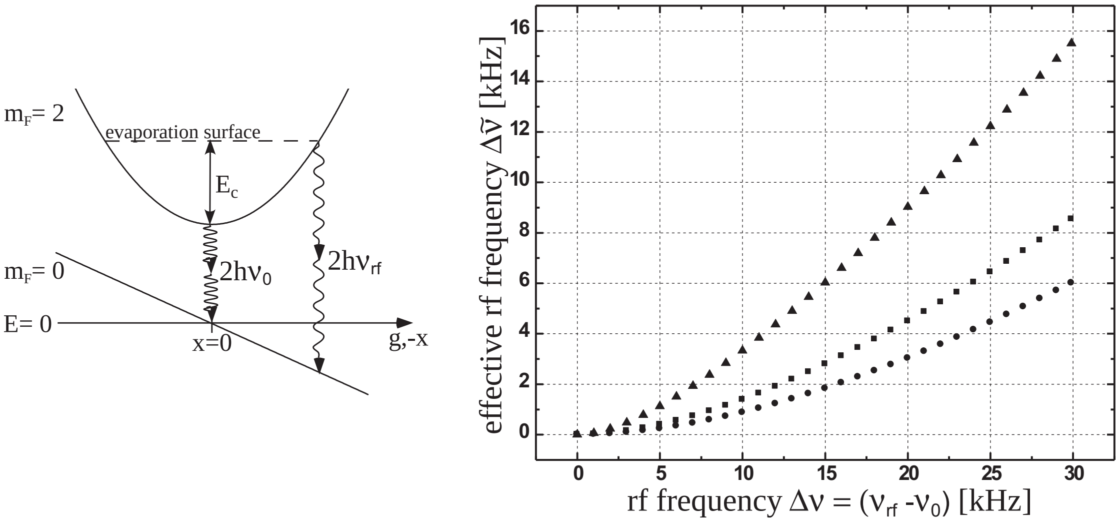

Figure 2.3: Influence of gravitation on the evaporation parameter η. Left: Schematic view of the Zeeman levels $m_F = 0$ and $m_F = 2$ as a function of the vertical coordinate x. Due to gravity evaporation is 1-dimensional, and only at the lower edge of the cloud the atoms are coupled to the untrapped levels. Right: The effective rf frequency $\Delta\tilde{\nu} = E_c/(2h)$ corresponding to the evaporation surface of energy E_c with respect to the trap bottom is given as a function of the rf frequency $\Delta\nu$. The radial trap frequency is $\omega_x/(2\pi) = 75\,\mathrm{Hz}$ (circles), $100\,\mathrm{Hz}$ (squares) and $200\,\mathrm{Hz}$ (diamonds), corresponding to $\zeta \approx 49\,\mathrm{kHz}$, $\approx 28\,\mathrm{kHz}$ and $\approx 7\,\mathrm{kHz}$.

The energy difference between the $m_F = 0$ and $m_F = 2$ states at this position is

$$E_x = E_c + E_0 - mgx_0 = E_c + E_0 + \frac{g}{\omega_x}\sqrt{2mE_c}.$$

Inserting $E_x = 2h\nu_{\mathrm{rf}}$ into this equation leads to:

$$\Delta\nu = \nu_{\mathrm{rf}} - \nu_0 = \frac{E_x - E_0}{2h} = \frac{1}{2h}\left(E_c + \frac{g}{\omega_x}\sqrt{2mE_c}\right). \tag{2.6}$$

For very steep traps $\omega_x \to \infty$ this results tends to the result without gravity, $2h\Delta\nu = E_c$. Resolving equation (2.6) for E_c one gets:

$$\Delta\tilde{\nu} \equiv \frac{E_c}{2h} = \Delta\nu + \zeta - \sqrt{2\Delta\nu\zeta + \zeta^2}, \qquad \text{where} \qquad \zeta = \frac{mg^2}{2h\omega_x^2}. \tag{2.7}$$

The effective energy distance of the rf-knife from the trap bottom is $E_c = 2h\Delta\tilde{\nu}$, and $\Delta\tilde{\nu} < \Delta\nu$ for all ω_x. In the graph of figure 2.3 $\Delta\tilde{\nu}$ is plotted as a function of $\Delta\nu$ for three different trap frequencies. As expected the influence of the gravitational sag diminishes with increasing steepness of the trap. It can however not be neglected in any of our experiments, where the steepest traps have radial frequencies of the order of $\omega_\perp/(2\pi) \sim 200\,\mathrm{Hz}$. For our smallest radial trap frequency, which is of the order of $\omega_\perp/(2\pi) \sim 75\,\mathrm{Hz}$, the difference is considerable: when using a rf knife of $\Delta\nu = 30\,\mathrm{kHz}$, the effective difference in rf frequencies is only $\Delta\tilde{\nu} \approx 6\,\mathrm{kHz}$, and is thus by a factor 5 smaller. Correspondingly the energy difference between the evaporation surface and the trap bottom is $E_c/h = 12\,\mathrm{kHz}$ instead of $E_c/h = 60\,\mathrm{kHz}$.

This difference has to be taken into account when estimating the temperatures of the trapped cloud from the formula for the evaporation parameter η. Knowing that the typical value of η in our system is between 5 and 10 [7], we often use the relation

$$k_{\mathrm{B}}T = \frac{E_c}{\eta}$$

as an estimate of the temperature. It is thus important to know the value of E_c.

2.4 The imaging system

One of the advantages of BEC experiments is the direct access to the experimental results: one simply takes a photograph of the atomic cloud. This can be done by different methods, relying on absorption or dispersion of photons (for an overview see [66]). Our experimental approach is based on the absorption of a quasi-resonant laser beam. A camera collects the remaining light, and from the missing photons the density profile of the atomic cloud is reconstructed. The images can be taken in situ or after a variable time of free expansion, up to 30 ms. In the following this time is called the time of flight (ToF) duration.

2.4.1 Principle of absorption imaging

To obtain an image of the atomic cloud, a beam centered on the atoms, and with a diameter much larger than that of the cloud, is turned on during a short time of typically 20 to 100 μs. The atoms absorb the light, which leads to a hole in the light beam. The profile[3] of this beam $I(x, y)$, is recorded by a CCD-camera. It is then compared to a reference image of the beam $I_{\mathrm{ref}}(x, y)$, taken with no atoms present. The optical density $\rho(x, y)$ of the cloud corresponds to

$$\rho(x, y) = -\ln\left(\frac{I(x, y)}{I_{\mathrm{ref}}(x, y)}\right).$$

From this profile one can conclude on the density profile of the cloud, as the optical density ρ is derived from the density profile n by

$$\rho(x, y) = \sigma \int n(x, y, z)\, dz, \qquad \text{with} \qquad \sigma = \frac{7}{15}\frac{3\lambda^2}{2\pi},$$

where σ is the atomic cross section for resonant light, under the assumption of a dilute and nonpolarized atomic cloud, and the factor 7/15 comes from the average of the squared Clebsch-Gordan coefficients for a transition $F = 2 \rightarrow F' = 3$, assuming linearly polarized light.

The peak optical density ρ_0 of a BEC in situ, axially imaged, is

$$\rho_0 = \sigma \cdot \int n(0, 0, z)\, dz \qquad \text{where} \qquad n(0, 0, z) = n_0\left(1 - \frac{z^2}{R_z^2}\right) \tag{2.8}$$

For a peak density of $n_0 = 10^{13}\,\mathrm{cm}^{-3}$ and an axial TF-radius of $R_z = 50\,\mu$m, which are typical values of our Rb condensates, the peak optical density is of the order of 100. When probing such a dense cloud with resonant light the image is easily "blacked out", making it very difficult to extract the density profile. Furthermore the radial size of the cloud is only of the order of $10\,\mu$m, and especially interesting features, vortices in rotating condensates, have a size of the order of the healing length. This is beyond the resolution of our imaging system, which is of the order of $\sim 5\,\mu$m [9].

---

[3] With our experimental setup we can take images from the radial direction y and the axial direction z. In this section the imaging direction will be denoted as z.

Most of our images are thus taken after ToF durations of the order of 20 ms, during which the clouds' radii grow to $\sim 200\,\mu$m and the optical density decreases to $\lesssim 3$. To obtain the cloud's in situ properties from the density profile after expansion, one has to know how BECs and thermal clouds expand. This question is discussed in the following section.

2.4.2 Time of flight of a BEC and a thermal cloud

Expansion of a BEC released from a harmonic trap

Within the Thomas-Fermi approximation a BEC trapped in a harmonic potential has a parabolic density profile. One can show that it keeps the harmonic profile, even after the trap has been turned off and the condensate is allowed to expand[4] [94, 95]. The evolution of the condensate can thus be described by simple scaling laws, with the TF-radii R_i evolving in time with the scaling parameters λ_i:

$$R_i(t) = \lambda_i(t) R_i(0).$$

Injecting the TF-profile of a condensate with axial symmetry in the hydrodynamic equations (1.23) gives a system of coupled equations for the scaling parameters λ_i [94]:

$$\ddot{\lambda}_i = \frac{\omega_i^2(0)}{\lambda_\perp^2 \lambda_z \lambda_i}, \tag{2.9}$$

where i stands for the radial or axial direction. For very asymmetric traps with $\omega_\perp \gg \omega_z$ one can perform some approximations which lead to analytic solutions for the scaling parameters [94]:

$$\lambda_\perp(t) = \sqrt{1+\omega_\perp^2 t^2} \tag{2.10}$$

$$\lambda_z(t) = 1 + \frac{\omega_z^2}{\omega_\perp^2}\left((\omega_\perp t)\arctan(\omega_\perp t) - \ln\sqrt{1+\omega_\perp^2 t^2}\right). \tag{2.11}$$

As $\omega_z/\omega_\perp \ll 1$ was assumed to obtain these equations, one gets $\lambda_z = 1$ in first order approximation. This means that the cloud expands only radially, and a cigar shaped cloud becomes pancake shaped during long expansions. This is the famous *inversion of ellipticity*, which is often used to distinguish a BEC from a thermal cloud. To derive the necessary ToF duration for the inversion, one has to verify the condition $R_\perp(t) = R_z(0)$. With $R_\perp(t) = \sqrt{1+\omega_\perp^2 t^2} \cdot R_\perp(0)$ this leads to

$$t_0 \approx \omega_z^{-1}$$

The cloud is thus cigar shaped for $t < t_0$, round for $t = t_0$ and pancake shaped for $t > t_0$. Note that the value of t_0 does not depend on the radial frequency. In our case $\omega_z = 2\pi\,11\,$Hz, and $t_0 = 14.5\,$ms.

The inversion of ellipticity of a condensate can be understood in terms of repartition of the cloud's total energy. In the limit of the TF-approximation, the interaction energy is the dominating term of the total energy. It is transformed into kinetic energy when the trap is shut down. The radial oscillation frequency being much faster than the axial oscillation frequency, most of the interaction energy is transformed in radial kinetic energy.

---

[4] The following analysis was actually derived for all temporal evolutions of the harmonic trapping frequencies $\omega_i(t)$, the ToF evolution being a limiting case, where $\omega_i(t) = 0$ for all $t \neq 0$.

Exploitation of the images

In a thermal cloud the interaction between particles can be neglected, and the kinetic energy is equally distributed between the spatial directions. The thermal cloud thus expands in all directions with the same velocity and becomes more and more round during ToF. Its size gives direct access to the temperature of the system.

In long time of flights a BEC can be distinguished from a thermal cloud not only due to their exact density profiles, which are respectively parabolic or gaussian, but also from the sense of their ellipticity, which has the initial sense in the case of the thermal cloud, and a inversed ellipticity in case of a BEC.

In general we use "bimodal" fits to extract the relevant data from an image. These fits assume a thermal and a condensed fraction. The fitting function thus consists of the sum of the two expected profiles (for details see [8]). The most important parameters that can be derived from these fits are the atom number and temperature of the thermal cloud and the atom number of the condensate. Also note that imaging after ToF expansion is necessarily destructive, because for each image the atoms have to be released from the trap.

2.5 Conclusion

The presentation of the experimental methods in this chapter allow for a general understanding of the production process of our Bose-Einstein condensates. Even more important, this chapter also laid out the foundations for the understanding of the specific experimental tools used for the experiments presented in this thesis, where the BECs are manipulated with the help of additional magnetic and optical potentials.

Part II

2-dimensional condensates

Contents

Introduction

The distinct properties of low-dimensional systems have been of great interest in the field of condensed matter physics. Several effects rely strongly on the dimensionality of the system, and new phenomena were observed since it is possible to create systems of reduced dimensionality. An interesting subject is the BEC-transition itself, which in homogenous ideal gases occurs only in 3-dimensional systems at nonzero temperature, while in lower dimensions BEC cannot exist at finite temperatures. Examples of other interesting regimes are the integer and fractional Quantum Hall effect, or the Kosterlitz-Thouless transition in 2D systems, or the Tonks-gas in 1D systems.

In the field of dilute atomic gases the study of low-dimensional systems is an active research domain, since it was first possible to create low-dimensional BECs experimentally [16]. Especially the phase properties of 1D or strongly elongated 3D quasi-condensate were studied thoroughly. Such systems show strong spatial and temporal fluctuations of the phase, which is different from the 3D case, where the coherence length is of the order of the condensate size. The distinct phase properties of elongated quasi-BECs were studied making use of the formation of density modulations during time-of-flight expansion [17] or the modified momentum distribution measured by Bragg-spectroscopy [19]. In other studies the spatial correlation function of two interfering copies of the quasi-condensate was determined [96], and the nonequilibrium properties of elongated BECs were studied using a condensate focusing technique [18].

The experimental study of the properties of 2-dimensional BECs has developed slower. In homogeneous interacting systems the transition from the superfluid to the normal phase is the so-called Kosterlitz-Thouless transition [38], which is associated to the unbinding of vortex-antivortex pairs. In trapped systems it is not completely clear how the transition to the superfluid phase is obtained. Since a few years individual 2D condensates or cold atomic clouds can be produced [5,16,25,26,97], and several experiments aim to study their specific phase properties [5, 25, 26]. The second part of this manuscript is focused on the realization and study of such systems. In our experiments 2D BECs are produced in the sites of a 1-dimensional optical lattice, and a wanted number of BECs is then separated from the array by selectively evaporating individual clouds.

After a small number of 2D BECs are obtained, their properties are studied mainly through interference experiments. These experiments can be divided into two groups. In a first series of experiments small arrays of clouds are allowed to overlap and interfere, to test the phase properties of individual clouds. In a second series the interference of large arrays of independent condensates is studied.

The chapters of part II

- **Chapter 3** gives a short introduction to the phase properties of 2-dimensional Bose gases. The overview treats ideal and interacting gases, for the homogeneous case and for harmonic trapping. The main focus is the introduction of the Kosterlitz-Thouless transition in interacting homogeneous systems. The topics treated in this chapter constitute the motivation for the following chapters, as well as the base to the understanding of the results presented in chapter 5.

- **Chapter 4** describes in detail the experimental setup used for the realization of periodic arrays of 2D condensates as well as single 2D BECs. All important parameters of the experimental routine and of the produced clouds are introduced in this chapter.

- **Chapter 5** presents the experimental routine and the results of the detection of non-trivial phase defects in 2-dimensional quasicondensates. The experimental method relies on interferometric detection of the phase differences between several clouds, and does not allow to unambiguously attribute a single phase configuration to the observed interference patterns. The most probable explanation of the observed patterns is however the presence of vortices in some of the observed 2D condensates. This argumentation is discussed in detail.

- **Chapter 6** studies the interference of periodic arrays of independent condensates. In a series of experiments it was found that the contrast of the obtained interference patterns can be high even for large numbers of condensates. A simple analytic analysis of this experimental result is given.

Chapter 3

2-dimensional Bose gases

The coherence properties of cold dilute gases depend strongly on the dimensionality of the system. In this chapter the possible phase transitions in 2-dimensional (2D) ultra-cold atomic gases are discussed, where in the uniform case a BEC can only exist at zero temperature. In this situation long-wavelength phase fluctuations destroy the long range order at any finite temperature[1]. In interacting gases, the system can however undergo a transition to a superfluid phase at a finite temperature. This was first pointed out by Kane and Kadanoff [101], and then proven by Berezinskii [102, 103]. Kosterlitz and Thouless found that this transition is associated with the unbinding of vortex-antivortex pairs [38], and the transition is commonly called Kosterlitz-Thouless (KT) transition. In the low temperature phase of the KT transition, the system is superfluid, but its phase shows fluctuations. These phase fluctuations consist of long-wavelength fluctuations, i.e. phonons, and bound vortex-antivortex pairs. Above the KT transition temperature the unbinding of the vortex-antivortex pairs becomes favorable and the system enters the normal state. In homogeneous systems evidence for the KT-transition was obtained in 2D layers of liquid helium [42] and, more recently, in a gas of spin-polarized hydrogen [43].

In a harmonically trapped gas the situation is different: in ideal gases a 2D BEC can exist at finite temperatures due to the modified density of states. In general the low-T divergence of the phase fluctuations is suppressed in all finite 2D systems, as the maximum wavelength of the phase fluctuations is limited due to the finite size of the trap [79, 104]. For these reasons it is not a priori sure if in harmonically trapped interacting gases the transition to the condensed phase is a KT-type transition, with a phase-fluctuating quasi-condensate for intermediate temperatures, or an “ordinary” BEC-type phase transition. This situation is illustrated in figure 3.1.

In the course of this chapter the properties of 2D gases are briefly summarized, starting with the case of an ideal gas (section 3.1). The properties of interacting gases at low temperatures are then discussed in a second section, where the notion of a quasicondensate is introduced (section 3.2). This description follows the outline of the first chapters of [80]. The third section presents the notions of the Kosterlitz-Thouless transition, where part of the quasi-condensate’s phase fluctuations are described as bound vortex-antivortex pairs (section 3.3).

3.1 Ideal Bose gases in 2D

3.1.1 Homogeneous case

The exploration of the BEC phase transition in a 2D ideal bosonic gas is very similar to that in a 3D gas, as presented in chapter 1.1.2.

---

[1] The impossibility of long range order in such infinite systems was proven rigorously by Mermin, Wagner, and Hohenberg [98–100].

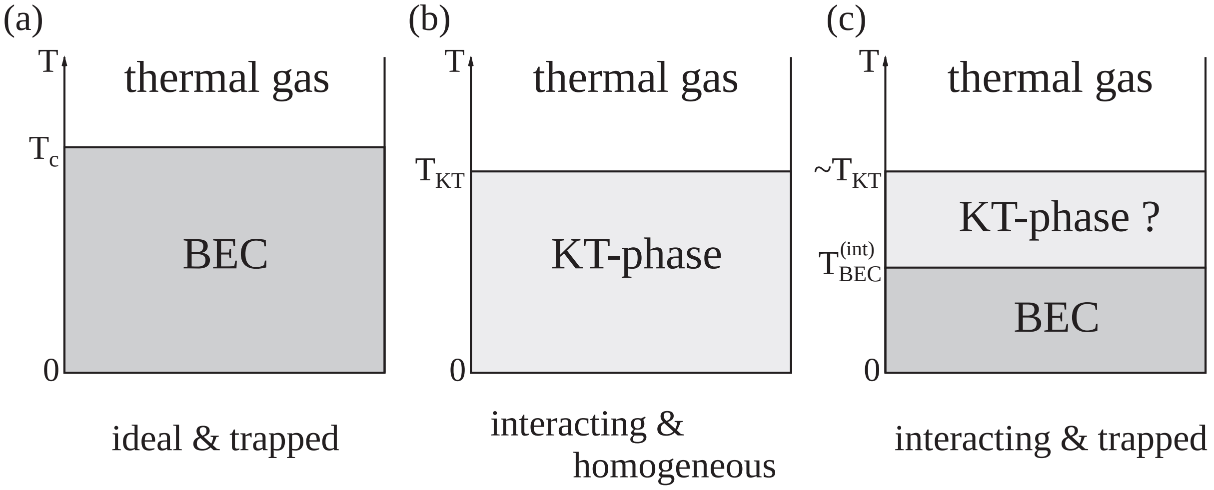

Figure 3.1: 2-dimensional bosonic gases. (a) In ideal gases trapped in harmonic potentials a true BEC exists for $T < T_c$. (b) In the homogeneous case BECs can only exist at $T = 0$, but for interacting gases there is a phase-transition to a superfluid phase at $T = T_{\mathrm{KT}}$. (c) In interacting gases trapped in harmonic potentials a KT-phase might exist in addition to a true BEC phase.

As in the 3D case it is useful to define the *degeneracy temperature* for the 2D gas

$$T_d = \frac{2\pi\hbar^2}{mk_{\mathrm{B}}}n, \tag{3.1}$$

where the 2D particle density n is the number of particles per unit area in the xy-plane. At $T = T_d$ the thermal de-Broglie wavelength of the particles, $\Lambda_{\mathrm{dB}} = \sqrt{2\pi\hbar^2/(mk_{\mathrm{B}}T)}$, is equal to the interparticle separation $n^{-1/2}$.

In the 3D regime the Bose-Einstein condensation temperature is of the order of the 3D degeneracy temperature T_d^{3D}. In 2 dimensions the situation is different, due to the difference in the density of states between the two cases. In a uniform system the density of states $\rho(\epsilon)$ is

$$\rho(\epsilon) \propto \epsilon^{d/2-1}, \tag{3.2}$$

where d is the dimensionality of the system. While in 3D $\rho(\epsilon)$ tends to 0 for $\epsilon \to 0$, it is constant in the 2D case, and diverges for $d = 1$. Following the argument given in chapter 1, for $d = 1, 2$ no saturation of the excited states exists at temperatures $T \neq 0$. The population of the ground state stays thus microscopic at finite T and a Bose-Einstein condensate occurs only for $T = 0$.

3.1.2 Harmonically trapped gases

The density of states in a harmonic confining potential is $\rho(\epsilon) \propto \epsilon^{d-1}$. For a 2D gas trapped in a potential

$$U(\mathbf{r}) = \frac{1}{2}m\omega_\perp^2(x^2 + y^2),$$

the density of states grows linearly with the energy: $\rho(\epsilon) = \epsilon/(\hbar^2\omega_\perp^2)$. In this case the excited states population saturates, and the population of the ground state N_0 becomes macroscopic for small temperatures. The relation between N_0, the total atom number N, and the temperature can be calculated to [80]:

$$N\left[1 - \left(\frac{T}{T_c}\right)^2\right] = N_0 - \left(\frac{k_{\mathrm{B}}T}{\hbar\omega_\perp}\right)^2 \frac{1 + \ln N_0}{N_0}, \tag{3.3}$$

where

$$k_{\mathrm{B}}T_c = \sqrt{\frac{6N}{\pi^2}}\hbar\omega_\perp.$$

At T_c the 2D particle density is $n \approx Nm\omega_\perp^2/(2\pi k_{\mathrm{B}}T_c)$, and T_c is of the order of T_d.
For a large number of particles, equation (3.3) indicates the presence of a sharp crossover to the BEC regime at $T = T_c$, and below T_c the population of the ground state can be approximated to

$$N_0 \approx N\left[1 - \left(\frac{T}{T_c}\right)^2\right], \tag{3.4}$$

which is similar to the 3D case.
Above T_c the ground state population is microscopic, and one can omit the first term on the right hand side of equation (3.3). The width of the crossover region, where both terms are equally important, is given by [80]

$$\frac{\Delta T}{T_c} \sim \sqrt{\frac{\ln N}{N}}.$$

For large atom numbers N this region is very narrow, and one might speak of an “ordinary” BEC transition in the ideal harmonically trapped 2D gas.

3.2 Interacting gases: Condensates and quasicondensates

As mentioned in the introduction to this chapter, in homogeneous interacting gases a transition to a superfluid phase exists at a finite temperature, even if a true condensate exists only at $T = 0$. The low temperature phase of this transition is a condensate with a fluctuating phase, which some authors refer to as a *quasicondensate* [79]. This quasicondensate can be divided into blocks corresponding to true condensates, while the phases of different blocks are not correlated with each other. This description is in the focus of section 3.2.2, while the case of a harmonic trap, in which a true BEC phase and a quasicondensate phase exist, is treated in section 3.2.3. The Kosterlitz-Thouless description of the phase fluctuations as bound vortex-antivortex pairs is presented in section 3.3.

3.2.1 The 2D regime and the quasi-2D regime

In the case of an interacting gas, an important distinction needs to be made between two different regimes, which are both commonly referred to as “2D”. In the first case, the system is truly 2D, including the collisional properties of the gas. This regime is reached, when the size of the sample in the strongly confined direction is smaller than the 3D s-wave scattering length a of the atoms. In the case of a cold ^{87}Rb gas, $a \approx 5\,\mathrm{nm}$, and a correspondingly strong confinement is not reached in most experiments.

The experimentally more common case is the so-called “quasi-2D”-regime. In the case of harmonic confinement along z, with the potential $U(z) = m\omega_z^2 z^2/2$, this regime is classified by $\mu < \hbar\omega_z$. This means that in the strongly confined direction z only the ground state of the trap is populated. The gas is confined to zero point oscillations in the z-direction and is *kinematically* 2D. The scattering properties stay however 3-dimensional, if $a \ll a_z$, where $a_z = (\hbar/(m\omega_z))^{1/2}$ is the harmonic oscillator length along z. This inequality is true in all 2D experiments referred to in this thesis, which are thus all in a “quasi-2D”-situation. Therefore no ambiguity should arise, if for simplicity this regime is in general referred to as “2D-regime” throughout this manuscript.

The coupling constant in the quasi-2D regime

In the quasi-2D regime, the gas is confined to zero point oscillations by the harmonic confinement along z, satisfies the inequalities $\hbar\omega_z > \mu$ and $\hbar\omega_z > k_\mathrm{B}T$, and the density distribution in the z-direction is

$$n(z) \approx \frac{n}{\sqrt{\pi a_z^2}}\, e^{-z^2/a_z^2},$$

where n is the 2D density, and $a_z = (\hbar/(m\omega_z))^{1/2}$ is the harmonic oscillator length along z. In this case the effective coupling constant can be calculated to be [80]

$$g = \frac{2\sqrt{2\pi}\hbar^2}{m}\frac{a}{a_z}. \tag{3.5}$$

This equation is valid in the weakly interacting regime, which is equivalent to the condition $|a| \ll a_z$. It is useful to introduce a dimensionless coupling constant,

$$\tilde{g} = \frac{mg}{4\pi\hbar^2} = \sqrt{\frac{2}{\pi}}\frac{a}{a_z}, \tag{3.6}$$

which is a small number in the case of 3D collisions $a \ll a_z$.
This is the case for all experiments presented in this thesis, where a_z is of the order of 100 nm, and the scattering length is $a \approx 5\,\mathrm{nm}$ for ^{87}Rb. In the following only repulsive interactions, i.e. $a > 0$, are considered.

3.2.2 Homogeneous interacting gases

BEC at $T = 0$

In the case of an interacting homogeneous 2D gas, a true condensate exists at $T = 0$. The phase coherence of this condensate can be verified with the following approach:

One assumes a priori the existence of a true condensate at $T = 0$. In this case the field operator can be approximated by the sum of the non-condensed part $\delta\hat{\Psi}$ and the condensate wavefunction $\Psi_0 \propto \sqrt{n_0}$, where n_0 is the density of the condensate (see chapter 1):

$$\hat{\Psi} = \delta\hat{\Psi} + \Psi_0. \tag{3.7}$$

With a Bogoliubov approach one can then express $\delta\hat{\Psi}$ through the eigenmodes of the elementary excitations, and calculate the density of the noncondensed particles to [80]

$$n' = \langle \delta\hat{\Psi}^\dagger(\mathbf{r})\delta\hat{\Psi}(\mathbf{r})\rangle \approx \tilde{g}n_0. \tag{3.8}$$

As $\tilde{g}$ is a small number in the case of 3D collisions (equation (3.6)), one finds that the density of the non-condensed particles is much smaller than the condensate density.

The phase coherence is expressed through the first order correlation function $g^{(1)}(r)$, where $r = |\boldsymbol{r_1} - \boldsymbol{r_2}|$ is the distance between two points of the system. For distances $r \gg \xi$, where $\xi = \hbar/(m\mu)^{1/2}$ is the healing length, the first order correlation function can be calculated to [80]

$$g^{(1)}(r) = \left(n_0 + \frac{\xi}{r}n'\right).$$

For distances of the order of the healing length, the correlation function has the value $g^{(1)}(r) \approx n = n_0 + n'$. For very large distances, $r \to \infty$, the correlation function tends to n_0. As $n' \ll n_0$, this means that long range order exists in the system, and the initial assumption of a true condensate at $T = 0$ is justified.

Quasicondensate at finite temperature

At temperatures $T \neq 0$ the density of the noncondensed particles is calculated as in the $T = 0$ case, that is assuming the existence of a true condensate, and using the Bogoliubov approach. The density of the non-condensed particles can be expressed as a sum of two terms,

$$n' = n'_V + n'_T,$$

where $n'_V = \tilde{g} n_0$ is the *vacuum contribution* (corresponding to $T = 0$), and n'_T the *thermal contribution.* The latter can be expressed by the elementary excitations, as [80]

$$n'_T = \frac{1}{(2\pi)^2} \int \left(\frac{E_k + \mu}{\epsilon_k} \right) N_k \, d^2k, \tag{3.9}$$

where $\epsilon_k = \sqrt{E_k^2 + 2\mu E_k}$ is the energy of an excitation with wave vector k in the Bogoliubov approach, $E_k = \hbar^2 k^2/(2m)$ is the energy of a free particle with momentum k, and $N_k = [\exp(\epsilon_k/(k_\mathrm{B}T)) - 1]^{-1}$ are the equilibrium occupation numbers of the excitations. For $k \to 0$, the occupation numbers are $N_k \approx k_\mathrm{B}T/\epsilon_k$, and the excitation energy is $\epsilon_k \propto k$. The integrand in equation (3.9) then behaves as d^2k/k^2, and the integral diverges.

The thermal contribution of the particle density thus diverges for small k, which contradicts the initial assumption (3.7) of the existence of a true condensate at $T \neq 0$. The origin of this impossibility lies in the long wave (i.e. small k) phase fluctuations in a homogeneous gas. This corresponds to the result of Hohenberg, Mermin and Wagner [98–100].

To calculate the first order correlation function the field operator $\hat{\Psi}$ is then used in the density-phase representation

$$\hat{\Psi} = \exp(i\hat{\phi}) \sqrt{\hat{n}}, \qquad \hat{\Psi}^\dagger = \sqrt{\hat{n}} \exp(-i\hat{\phi}),$$

where density and phase operator are real and satisfy the commutation relation $[\hat{n}(\boldsymbol{r}), \hat{\phi}(\boldsymbol{r'})] = i\delta(\boldsymbol{r} - \boldsymbol{r'})$.

The density operator can be expressed as $\hat{n} = n + \delta\hat{n}$, so that the stationary solution of the system is given by $\hat{n} = n$, which is the mean density, and $\nabla\hat{\phi} = 0$. The operators of the density and phase fluctuations, $\delta\hat{n}$ and $\hat{\phi}$ can then be expressed in terms of the elementary excitations, and be separated in a high-energy and a low-energy part, corresponding to phonons (for $\epsilon_k < \mu$) and free particles ($\epsilon_k > \mu$) respectively [80]:

$$\delta\hat{n} = \delta\hat{n}_p + \delta\hat{n}_f\,, \qquad \hat{\phi} = \hat{\phi}_p + \hat{\phi}_f,$$

where the indices p and f correspond to the phonon part (p) and the free-particle part (f). In zero order perturbation theory the small high-energy fluctuations can be omitted, as well as small low-energy fluctuations of the density[2] [80]. The single-particle correlation function is then found using the field operator in the approximation

$$\hat{\Psi} = \sqrt{n} e^{i\hat{\phi}_p}.$$

For $T \ll T_d$, the first order correlation function is:

$$g^{(1)}(r) = \langle \hat{\Psi}^\dagger(\mathbf{r}) \hat{\Psi}(0) \rangle = n \exp\left(-\frac{1}{2} \left\langle (\hat{\phi}_p(0) - \hat{\phi}_p(\mathbf{r}))^2 \right\rangle \right).$$

---

[2] An approach which treats the density fluctuations exactly can be found in [105].

The mean square phase fluctuations can be evaluated for the asymptotic case $r \gg \lambda_T$, where λ_T is equal to the healing length for $k_\mathrm{B}T \gg \mu$, and to the thermal de-Broglie wavelength of phonons, $\hbar c_s/(k_\mathrm{B}T)$ (with the velocity of sound c_s) for $k_\mathrm{B}T \ll \mu$ [80]:

$$\left\langle (\hat{\phi}_p(0) - \hat{\phi}_p(\mathbf{r}))^2 \right\rangle_T \approx \frac{2T}{T_d} \ln\left(\frac{r}{\lambda_T}\right). \tag{3.10}$$

For the first order correlation function this result leads to:

$$g^{(1)}(r) = n \left(\frac{\lambda_T}{r}\right)^{T/T_d}, \tag{3.11}$$

which shows for all temperatures $T \neq 0$ an algebraic decay to 0 for $r \to \infty$. The thermal fluctuations thus destroy the long-range order of the gas, and do not allow for a true BEC. This behavior at low temperatures was first found by Kane and Kadanoff [101].

The distance r at which the mean square fluctuations (equation 3.10) become of the order of unity, is called the phase coherence length L_c:

$$L_c = \lambda_T \exp\left(\frac{T_d}{2T}\right).$$

For $T \ll T_d$ the phase coherence length is much larger than the healing length ξ. The system can then be divided into blocks of a size $\tilde{L}$, with $\tilde{L} \sim L_c$. Inside each block $g^{(1)} \approx n$, which is the result for a true BEC. However, the phases of the blocks are independent from each other, due to the long-range phase fluctuations.

3.2.3 Interacting gases in harmonic traps

In the case of a trapped gas the confining potential introduces a finite size of the sample. This sets a lower bound to the momentum of the elementary excitations, and reduces the phase fluctuations. For this reason a true BEC can exist in a trapped system even at nonzero temperature.

For a trapped 2D BEC the Thomas-Fermi (TF) approach (see chapter 1.2.3) can be used for the radial direction $r = (x^2 + y^2)^{1/2}$, and allows to write the 2D condensate density as:

$$n_0(\boldsymbol{r}) = \frac{\mu}{g}\left(1 - \frac{r^2}{R_\perp^2}\right),$$

where the size of the system in the xy-plane is given by the radial Thomas-Fermi radius, $R_\perp = (2\mu/m\omega_\perp^2)^{1/2}$. As in the 3D case one can derive a relation between the chemical potential and the number of particles N, by integrating n_0 over the spatial volume of the gas:

$$\mu = 2\sqrt{N\tilde{g}}\ \hbar\omega_\perp. \tag{3.12}$$

In this case the spectrum and the wave functions of low energy excitations can be found analytically [69, 106]. As in the uniform case it can then be shown that the fluctuations of the density are small for $T \ll T_d$, where T_d is the degeneracy temperature.

Under the assumption of small density fluctuations the quasicondensate density can be approximated by n_0, and the first order correlation function generalized to a trapped system is

$$g^{(1)}(\boldsymbol{r}) = \langle \hat{\Psi}^\dagger(\mathbf{r})\hat{\Psi}(0)\rangle = \sqrt{n_0(\mathbf{r})n_0(0)}\ \exp\left(-\frac{1}{2}\left\langle (\hat{\phi}_p(0) - \hat{\phi}_p(\mathbf{r}))^2 \right\rangle\right),$$

where $\boldsymbol{r} = 0$ is the trap center.
The mean square phase fluctuations can then be approximated for $k_\mathrm{B}T > \mu$ and $r \gg \xi(0)$, where $\xi(0)$ is the healing length at $\boldsymbol{r} = 0$ [80]:

$$(\delta\phi(r))^2 \equiv \langle (\hat{\phi}_p(0) - \hat{\phi}_p(\mathbf{r}))^2 \rangle \approx \frac{\tilde{g}}{4}\frac{k_\mathrm{B}T}{\mu} \ln\left(\frac{r}{\xi}\right), \tag{3.13}$$

and as in the homogeneous system one can derive a coherence length L_c, for which the mean square fluctuations are of the order 1:

$$L_c = \xi \ \exp\left(\frac{\pi\hbar^2 n_0(0)}{mk_\mathrm{B}T}\right) = \xi \ \exp\left(\frac{n_0(0)\Lambda_\mathrm{dB}^2}{2}\right),$$

where $n_0(0) = \mu/g$ is the maximum density in the trap center. For small temperatures L_c becomes of the order of the system's size, which means that the gas is a true BEC. For higher temperatures, and $L_c < R_\perp$ the gas is a quasicondensate.

3.3 Phase-fluctuations and vortex-antivortex pairs: The KT-transition

3.3.1 A topological phase transition

The Kosterlitz-Thouless transition was first explored theoretically in the planar xy-model [38,39]. This model is a system of spins $\boldsymbol{s}_i$ of absolute value $|\boldsymbol{s}_i| = 1$ on the sites of a square lattice with spacing d. The spins are confined to rotate in the plane of the lattice, and their angles ϕ_i in the plane can vary continuously[3]. This system is described by the Hamiltonian

$$H_0 = -J\sum_{(i,j)} \boldsymbol{s}_i \cdot \boldsymbol{s}_j = -J\sum_{(i,j)} \cos(\phi_i - \phi_j), \tag{3.14}$$

where the sum is taken over all nearest-neighbor pairs (i, j) and $J > 0$ is a constant. The spin correlation function is then

$$\langle \boldsymbol{s}_0 \cdot \boldsymbol{s}_{\boldsymbol{r}} \rangle = \langle \cos(\phi_0 - \phi_{\boldsymbol{r}}) \rangle = \langle e^{i(\phi_0 - \phi_{\boldsymbol{r}})} \rangle,$$

where the last equality is due to the invariance of the Hamiltonian with respect to the transformation $\phi_i \to -\phi_i$. For the exploration of the long range order in the system, this correlation function is estimated for the high and the low temperature limit.

For a high temperature estimate, the spin correlation function is constructed from

$$\langle \boldsymbol{s}_0 \cdot \boldsymbol{s}_{\boldsymbol{r}} \rangle = \langle \cos(\phi_0 - \phi_{\boldsymbol{r}}) \rangle = \frac{1}{Z} \int_0^{2\pi} \prod_k d\phi_k \left(\cos(\phi_0 - \phi_{\boldsymbol{r}})\, e^{J/(k_\mathrm{B}T)\sum_{(i,j)} \cos(\phi_i - \phi_j)} \right) \tag{3.15}$$

with the partition function

$$Z = \sum_{[\phi_i]} e^{J/(k_\mathrm{B}T)\sum_{(i,j)} \cos(\phi_i - \phi_j)} = \int_0^{2\pi} \prod_k d\phi_k \left(e^{J/(k_\mathrm{B}T)\sum_{(i,j)} \cos(\phi_i - \phi_j)} \right),$$

where the sum over $[\phi_i]$ denotes the sum over all possible spin configurations.
For large T the exponentials in equation (3.15) are expanded in powers of $J/(k_\mathrm{B}T)$, and the terms of lowest order are identified. This leads to [107, 108]

$$\langle \boldsymbol{s}_0 \cdot \boldsymbol{s}_{\boldsymbol{r}} \rangle = \langle \cos(\phi_0 - \phi_{\boldsymbol{r}}) \rangle \approx e^{-r/\zeta}, \qquad \text{where} \qquad \zeta \approx \frac{d}{\ln(2k_\mathrm{B}T/J)},$$

and $r = |\boldsymbol{r}|$ is the distance separating the site $\boldsymbol{r}$ from the origin 0. The disordered high temperature phase is thus characterized by an exponential decay of correlations.

---

[3] The spin orientation at a given point corresponds to the direction of the velocity field in a continuous system.

At low temperatures only the lowest lying excitations around the ground state of energy $E_0 = -\sum_{(i,j)} J$ need to be taken into account. These are long-wavelength modes, which modify the spin orientation only gradually and over large distances. The energy cost of these modes is obtained by a quadratic expansion[4] of the Hamiltonian in the continuum limit (for $r \gg d$):

$$H_0 - E_0 \approx J \sum_{(i,j)} \frac{1}{2} \left(\phi_i - \phi_j\right)^2 \approx J \int \frac{1}{2} \left(\nabla\phi\right)^2 d^2 r. \tag{3.16}$$

The spin correlation function is then obtained by calculating

$$\langle e^{i(\phi_0 - \phi_{\boldsymbol{r}})} \rangle = \frac{1}{Z} \int_{-\infty}^{\infty} \prod_i d\phi_i \ \exp\left[i(\phi_0 - \phi_{\boldsymbol{r}}) - \frac{J}{k_{\mathrm{B}} T} \int \frac{1}{2} (\nabla\phi)^2 \, d^2 r \right]. \tag{3.17}$$

The evaluation of the Gaussian integral leads to the spin correlation function [107, 108]

$$\langle \boldsymbol{s_0} \cdot \boldsymbol{s_r} \rangle = \langle e^{i(\phi_0 - \phi_{\boldsymbol{r}})} \rangle \approx \left(\frac{d}{r} \right)^{\frac{k_{\mathrm{B}} T}{2\pi J}} .$$

The decay of the correlation function is thus algebraic (rather than exponential) in the low temperature regime. Note that this result for a xy-lattice is equivalent to that for the phase correlation function in a cold bosonic gas, as given in equation (3.11).

The distinct behavior at high and low temperature allows for the possibility of a finite temperature phase transition separating the two regimes. The question of interest is why the low-temperature argument breaks down for higher temperatures. To answer this question, one might look back to the ansatz for the spin correlation function in the low-temperature limit. In equation (3.17), the integration over the angle is taken from $-\infty$ to ∞. In the high temperature limit the periodicity of ϕ might thus play an important role. This is indeed the solution that was suggested to this question by Kosterlitz and Thouless [38]. They found the disordering to be caused by excitations with the character of *topological defects*, and which introduce the periodicity of the phase to the problem. These topological defects are *vortices*, which are spin configurations for which the angle rotates by $2\pi q$ when going around a closed path. Here q is an integer, and represents the *topological charge* or *vorticity* enclosed by the path. The elementary defect of lowest energy has a charge $q = \pm 1$.

Such vortices cannot be regarded as simple deformations of the ground state (and neither be described by a gradient expansion), as due to the discrete nature of the charge it is impossible to continuously deform the state to the uniformly ordered state in which the charge is zero.

The phase transition from the high temperature to the low temperature phase can then be described as the binding of vortex-antivortex pairs. These pairs consist of a vortex with charge $q = 1$ and another with $q = -1$, with the minimal distance d between them. Compared to single vortices they have only a small influence on the long-wavelength fluctuations, as they seem "neutral" from distances much larger than the size of the pair. Consequently the creation of such pairs costs also much less energy than that of a single vortex, and they can also exist at low temperatures.

To calculate the properties of the phase transition, one must calculate the free energy of single vortices as well as bound vortex-antivortex pairs as a function of J, the size of the system L and the smallest possible size for bound vortex antivortex pairs, which is given by the lattice spacing d. For the planar xy-model these calculations were first performed by Kosterlitz and Thouless, in [38, 39].

In the following the free energy for vortices and bound vortex-antivortex pairs is calculated not on a discrete lattice, but for a superfluid atomic gas. In this discusion the notations as introduced in section 3.2 are used, except that the 2D superfluid density n_s is introduced for the superfluid (or (quasi-)condensate) phase below the transition temperature.

---

[4] It can be shown that the higher order terms do not modify the behavior of the spin correlation function [108].

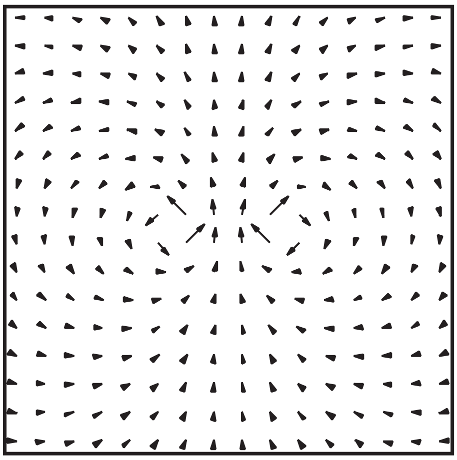

Figure 3.2: Velocity field of a bound vortex-antivortex pair.

3.3.2 Excitation probability of vortices and vortex-antivortex pairs

The KT description of the superfluid to normal phase transition involves the unbinding of tightly bound vortex-antivortex pairs. As the probability for a free vortex to occur is proportional to $e^{-F_{vx}/k_\mathrm{B}T}$, where F_{vx} is the free energy of such an excitation, the temperature of the transition can be estimated through the free energy of the first appearing single vortex. This estimate is given in the following (a), as well as the free energy of a tightly bound vortex-antivortex pair (b). In a homogeneous system the free energy of the pairs is negative for all finite T, which is the reason for their presence at all finite temperatures. The presence of such pairs will lower the excitation energy of single vortices through screening; this effect is described in (c).

a) Free energy of a single vortex

In a superfluid the vortex core is of the order of the healing length ξ, and the energy cost for the excitation of a vortex can be separated in contributions from the core region and the distortions of the wave function away from the vortex center. In a homogeneous 2D superfluid of density n_s and size $\pi R_\perp^2$ the kinetic energy of a single vortex located at the center can be approximated by neglecting the energy of the atoms in the vortex core[5]:

$$E_{vx} \approx \int_\xi^{R_\perp} n_s \frac{mv^2}{2}(2\pi r)\, dr. \tag{3.18}$$

The velocity field $v(r)$ of a singly charged vortex is $v(r) = \frac{\hbar}{mr}$ (see chapter 7), which leads to

$$E_{vx} \approx n_s \left(\frac{\pi\hbar^2}{m}\right) \ln\left(\frac{R_\perp}{\xi}\right) = \frac{1}{2}(k_\mathrm{B}T)\; n_s \Lambda_\mathrm{dB}^2 \ln\left(\frac{R_\perp}{\xi}\right), \tag{3.19}$$

where $\Lambda_\mathrm{dB} = h/\sqrt{2\pi m k_\mathrm{B} T}$ is the thermal de-Broglie wavelength.
For the calculation of the entropy, one has to estimate the number of distinguishable positions of the vortex in the system. For a vortex core area of $\sim \pi\xi^2$, the number of distinguishable positions is $R_\perp^2/\xi^2$, which leads to the entropy

$$S_{vx} = 2k_\mathrm{B} \ln\left(\frac{R_\perp}{\xi}\right). \tag{3.20}$$

---

[5] The exact calculation for a harmonically trapped Bose gas can be found in [109]

The free energy of a single vortex, $F_{vx} = E_{vx} - TS_{vx}$, is thus

$$F_{vx}/(k_{\mathrm{B}}T) = \frac{1}{2}\left(n_s\Lambda_{\mathrm{dB}}^2 - 4\right)\ln\left(\frac{R_\perp}{\xi}\right). \tag{3.21}$$

The free energy F_{vx} vanishes for $n_s\Lambda_{\mathrm{dB}}^2 = 4$, which gives a transition temperature

$$k_{\mathrm{B}}T_{\mathrm{KT}} = \frac{\pi}{2}\frac{\hbar^2}{m}n_s, \tag{3.22}$$

and n_s is the superfluid density just below the transition temperature. For $T < T_{\mathrm{KT}}$, the free energy is positive, and tends to $+\infty$ in the thermodynamic limit $R_\perp \to \infty$. This phase is thus classified by the absence of single vortices. For temperatures $T > T_{\mathrm{KT}}$ the free energy is negative and tends to $-\infty$ in the thermodynamic limit. This phase is classified by a proliferation of free vortices, which destroy the condensate.

b) Free energy of a vortex-antivortex pair

A tightly bound vortex-antivortex pair costs much less energy than a free vortex, as its velocity field decreases with r^2 instead of r at infinity. Thermal excitation of a tightly bound vortex-antivortex pair occurs thus at lower temperatures than the excitation of a single vortex [38,39].

The velocity field of a vortex-antivortex pair with a distance ξ between the cores is obtained by adding the velocity fields of the two counterrotating vortices, and is for $r \gg \xi$

$$v(r) \approx \frac{\hbar}{m}\frac{\xi}{r^2}.$$

In the homogeneous system of superfluid density n_s and radius $R_\perp$, the energy of a vortex-antivortex pair located at the cloud's center is then (again the energy of the vortex cores is neglected):

$$E_{vp} \approx \int_\xi^{R_\perp} n_s\frac{mv^2}{2}(2\pi r)\,dr \approx \frac{1}{2}n_s\frac{\pi\hbar^2}{m} \tag{3.23}$$

where $\xi \ll R_\perp$ was assumed.
The entropy of a tightly bound pair S_{vp} is comparable to that of a single vortex, and the free energy is thus

$$F_{vp}/(k_{\mathrm{B}}T) \approx \frac{1}{4}n_s\Lambda_{\mathrm{dB}}^2 - 2\ln\left(\frac{R_\perp}{\xi}\right). \tag{3.24}$$

In the thermodynamic limit F_{vp} is negative for all $T \neq 0$. Tightly bound vortex-antivortex pairs are thus present even at very low temperatures. Their influence on the phase of the superfluid is partly responsible for the loss of long range correlations. Another important influence on the long range correlations lies however in their modification of the effective potential seen by the constituents of larger pairs, since the polarization of the small pairs partially screens the field created by the larger ones. This effect lowers the effective transition temperature, and it is described in more detail in the next paragraph.

c) Screening

In the estimate of the transition temperature T_{KT} as presented above, interactions between vortices have been ignored. These interactions lower the energy of free vortices, as tightly bound pairs organize in a way to screen the velocity field of the single vortex and thus to lower the total energy. This situation is illustrated in figure 3.3(a). The same effect will occur for loosely bound vortex-antivortex pairs (figure 3.3(b)).

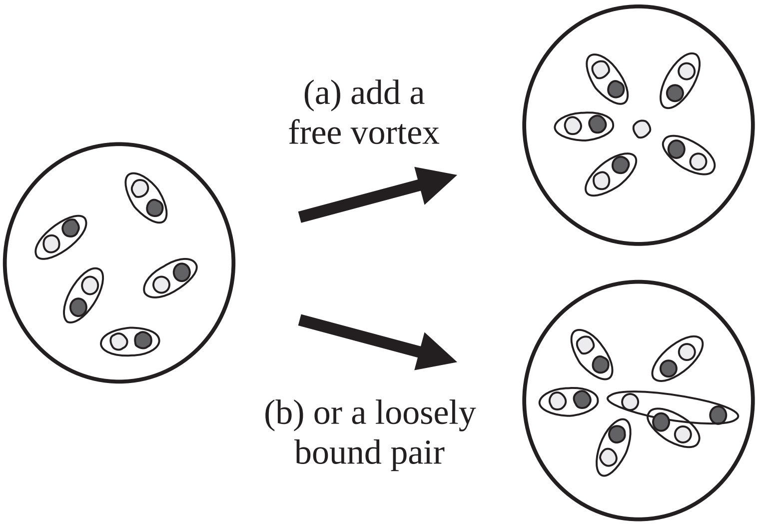

Figure 3.3: Screening of loosely bound vortex-antivortex pairs or free vortices by tightly bound pairs. The black and grey filled circles signify vortices with charge 1 and -1 respectively.

The transition temperature T_{KT} as given in the previous section is thus an upper bound, as for a more correct description vortex interactions need to be taken into account. In [39] the calculation of T_{KT} when taking into account the interactions is performed for the xy-model of spins on a lattice. Using a renormalization group approach, the author finds that the transition temperature T_{KT} is given by the solution of

$$\pi J/(k_{\mathrm{B}}T_{\mathrm{KT}}) - 1 = 2\pi\, e^{-\pi^2 J/(k_{\mathrm{B}}T_{\mathrm{KT}})},$$

instead of $k_{\mathrm{B}}T_{\mathrm{KT}} \approx \pi J$, when no interactions between the vortices are taken into account.

For weakly interacting Bose gases the dependence between the critical superfluid density n_s and the transition temperature was first calculated by Popov in 1983 [110], to

$$k_{\mathrm{B}}T_{\mathrm{KT}} = \frac{2\pi\hbar^2 n_s}{m\ \ln\left(C/\alpha\right)},$$

where C is a constant, and in the true 2D-regime the dimensionless constant α is connected to the dimensionless coupling constant by $\tilde{g} = \alpha/2$. In a more recent work, the constant C could be calculated numerically to $C \approx 380/(2\pi)$ [111].

3.3.3 Detection of the KT-regime

a) Jump in the superfluid density

The question how to detect the KT-phase was brought up soon after its prediction (see e.g. [112]). As Thouless stated, "one of the most dramatic and easily tested predictions of the theory is that the superfluid density, or corresponding other order parameter, has a definite value at the critical temperature" [113]. Approaching the KT-transition temperature from above, $T \rightarrow T_{\mathrm{KT}}^{+}$, the superfluid density n_s is zero, as any long range order is destroyed by a large number of free vortices. Approaching T_{KT} from below, $T \rightarrow T_{\mathrm{KT}}^{-}$, the superfluid density has the finite value (equation (3.22)):

$$n_s = \frac{2m}{\pi\hbar^2}\, k_{\mathrm{B}}\, T_{\mathrm{KT}}.$$

In the static KT-theory (which does not take into account vortex-vortex interactions) the value $n_s T_{\mathrm{KT}}$ is an universal quantity for a given superfluid of mass m, which does not depend on the thickness of the film or other experimental parameters.

The observation of this jump in the superfluid density was the method in the first work detecting the KT-phase in a thin film of cold ^{4}He [42]. In this work the static theory could not be tested directly, as the techniques for superfluid detection all required a nonzero superfluid velocity. However, among other parameters the dissipation associated with the vortex motion induced by the superflow could be measured with a good temperature resolution, and the estimates for n_s derived from these measurements were in good agreement with the predicted value.

b) Reduced 3-body recombination

More recently a 2D quasicondensate could be detected in a gas of spin-polarized hydrogen [43]. In these experiments a thin film of hydrogen atoms was brought on a surface of liquid ^{4}He at at temperature of $120 - 200\,\mathrm{mK}$. With increasing phase space density a strong decrease of the 3-body recombination was observed, which was attributed to the onset of local coherence in the gas, and thus to the formation of a quasicondensate. Beside the developing local coherence, this experiment could however not verify more specific properties of the KT-phase.

c) Direct observation of vortex-antivortex pairs

The recent developments in cold atomic gases gives hope for a direct observation of bound vortex-antivortex pairs, or thermally activated single vortices. This is the objective of several experiments [25, 26, 97]. A first detection of nontrivial phase defects in cold atomic gases in a quasi-2D confinement was achieved in [5]. These experiments are described in detail in chapter 5.

Cold atomic gases are however always confined in some finite trapping potential. This case is different from the homogeneous case, as in a trap also a true condensate can exist at $T \neq 0$. This situation is discussed in the following section.

3.3.4 The Kosterlitz-Thouless transition in finite trapped systems

In harmonic traps the modified density of states allows for Bose-Einstein condensation even at non-zero temperature. It is thus not a priori sure if an interacting trapped gas supports the ordinary BEC or the KT-type of a crossover to the superfluid phase. Recent studies suggest for large samples the KT-crossover [114–116], which is equivalent to the existence of a phase with tightly bound vortex-antivortex pairs.

The KT-Transition in a finite system

In a trapped system the 2D density depends on the position in the xy-plane, $n = n(\boldsymbol{r})$. The energy of single vortices as well as vortex-antivortex pairs is proportional to the particle density. Both of these excitations are thus expected to appear first on the edges of the trapped system. For low temperatures a superfluid phase in the high density center of the cloud might thus persist, even if phase coherence at the cloud's edges is already destroyed by the thermal activation of vortices [115].

As a first estimate for the temperature for which superfluidity is fully destroyed in the whole system one can thus use the result for a homogeneous gas of a density corresponding to the peak density $n_s(0)$ in the trapped system. This corresponds to the creation of a vortex in the trap center. For a homogeneous superfluid density n_s the free energy of a single vortex F_{vx} is given in equation (3.21), and it is positive for $n_s\Lambda_{\mathrm{dB}}^2 > 4$ (corresponding to $T < T_{\mathrm{KT}}$), and negative for $n_s\Lambda_{\mathrm{dB}}^2 < 4$ (corresponding to $T > T_{\mathrm{KT}}$).

This temperature estimate is lowered due to screening by bound vortex-antivortex pairs. Another important scale is thus given by the temperature above which such pairs are favorable in a finite system. The free energy of a tightly bound vortex-antivortex pair is given in equation (3.24):

$$F_{vp}/(k_{\mathrm{B}}T) \approx \frac{1}{4}n_s\Lambda_{\mathrm{dB}}^2 - 2\ln\left(\frac{R_\perp}{\xi}\right).$$

If $\ln(R_\perp/\xi)$ is finite, the pair free energy is not negative for all temperatures $T \neq 0$. The temperature associated with the disappearance is $k_{\mathrm{B}}T_{\mathrm{BEC}}^{\mathrm{int}} = \pi\hbar^2 n_s/[4m\,\ln(R_\perp/\xi)]$, and for temperatures $T < T_{\mathrm{BEC}}^{\mathrm{int}}$ the free energy of a vortex pair is positive. Note however that the existence of this temperature does not necessarily indicate a phase transition, as the value of F_{vp} stays finite on both sides of $T_{\mathrm{BEC}}^{\mathrm{int}}$ for a finite size of the system, and $T_{\mathrm{BEC}}^{\mathrm{int}} \to 0$ in the thermodynamic limit.

The KT transition in harmonically trapped, weakly interacting gases

The above given critical temperatures for the appearance of single vortices or vortex-antivortex pairs are only rough estimates to the situation in a harmonic trap. They neither take into account the specific density of states in a harmonic trap, nor the particle interactions. These subjects were addressed in recent theoretical studies [114–116].

In [116] Holzmann *et al.* explore the thermodynamic limit of a harmonically trapped system, and find that the transition temperature to the KT-phase lies below the ideal gas Bose-Einstein transition temperature. In this approach corrections in terms of the interparticle interaction are included. As a second important result they find that the jump in the superfluid density at $T = T_{\mathrm{KT}}$ is highly suppressed compared with that in a homogeneous system.

In [114] Simula *et al.* perform ab initio classical field simulations for trapped Bose gases. Their focus lies on the exploration of the transition from the pure BEC to the KT-phase (and less on the transition from the KT-phase to the thermal gas), and they argue that this is a first order phase transition.

Nature of the crossovers. The transition from the KT-phase to a pure BEC is often understood as a continuous crossover, where the two vortices of a pair merge into each other. The nature of this crossover is however not yet thoroughly studied. While all authors agree on the nature of the transition from the thermal gas to the superfluid phase (quasicondensate) to be a phase transition of infinite order in the thermodynamic limit [79, 114, 116], the nature of the transitions from the quasicondensate to a pure BEC remains indeed unclear. Most authors believe that this transition has the nature of a gradual crossover. Some authors have however suggested the existence of two distinct superfluid phases, a quasicondensate and a true BEC, separated by a first-order phase transition [114, 115].

Simulations of the KT-phase for existing experiments

As the detection of vortex-antivortex pairs in 2D quasicondensates is the goal of several experiments, the different experimental trap geometries have inspired numerical work on the possibility of such an observation. Recent results of our group strongly suggested the existence of such excitations in 2D quasicondensates (see chapter 5). These experiments have motivated numerical simulations on the KT-transition properties for our experimental parameters. Using ab initio classical field simulations the authors of [115] calculated the excitation probability for

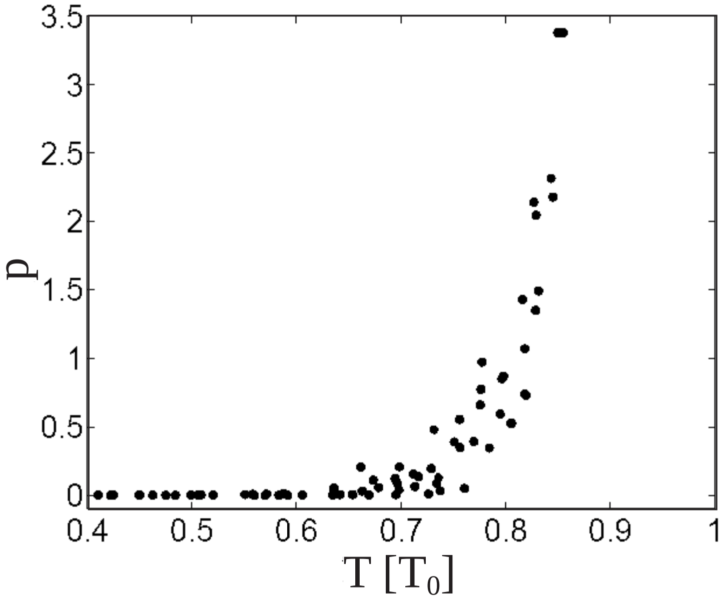

Figure 3.4: Excitation probability p (arbitrary units) for a vortex-antivortex pair as functions of the fractional temperature T/T_0, where T_0 is the critical temperature for an ideal gas to undergo Bose-Einstein condensation in the harmonic trap. Figure from reference [115].

vortex-antivortex pairs $p \propto \exp[-F_{vp}/(k_{\mathrm{B}}T)]$ as a function of the temperature, using the trap parameters of our experiment[6], as described in chapter 4. Their result is shown in figure 3.4.

---

[6] The authors used the data for the 2.7 μm period lattice.

Chapter 4

Experimental realization of 2D condensates

The condition for a trapped gas to be in the quasi-2-dimensional regime is generally formulated as $\mu < \hbar\omega_z$, which means that in the axial direction z the gas populates only the ground state of the harmonic oscillator. In the radial directions the Thomas-Fermi approximation should be valid, which means that $\mu \gg \hbar\omega_\perp$. These two conditions are fulfilled in traps with sufficiently large aspect ratios $\omega_z/\omega_\perp$. Of course the trap does not have to be harmonic (an example for a radially quartic trap is presented in part III).

Until today 2D condensates have been reached in several different setups combining magnetic and optical traps [16, 25, 26]. The 2D regime was also reached when rotating an originally 3-dimensionally BEC at a frequency Ω just below the radial trapping frequency $\omega_\perp$ [24]. In such experiments the centrifugal force weakens the effective radial trap frequency $\tilde{\omega}_\perp$ as $\tilde{\omega}_\perp = \sqrt{\omega_\perp^2 - \Omega^2}$ and thus increases the ratio $\omega_z/\tilde{\omega}_\perp$. A third method used for the creation of a 2D trap is to modify a magnetic 3D trap by dressing it with a resonant rf-field [97]. In this trap condensation could however not yet be achieved.

The sites of a 1D optical lattice usually fulfill the criteria for 2D trapping [3, 73, 117, 118]. Furthermore, the achieved potentials are generally smooth, without significant defects in the planes. One of the difficulties in these systems is to suppress tunneling between the sites. But even if tunneling is suppressed, it is not always possible to address or study the 2D clouds in the lattice sites independently [119, 120].

Our approach for the production of 2D condensates consists in the use of a 1-dimensional optical lattice with a unusually large lattice period of several micrometers, which is superposed to the magnetic trap. The two main objectives in the design of this lattice are to make the sites fully independent, and thus in principle selectively addressable, while the axial trapping frequency in each site should fulfill the 2D-criterium $\mu < \hbar\omega_z$. As the radial trapping is purely magnetic, atoms from selected sites can be removed by rf-evaporation.

4.1 The optical lattice

4.1.1 Creation of the optical lattice

To create an optical lattice we use blue-detuned laser light of wavelength $\lambda_L = 532\,\text{nm}$. This light has a shorter wavelength than the Rb transition at 780 nm and creates a repulsive optical potential. The laser is a commercially available frequency-doubled solid state laser ("verdi" [1]), which delivers a linearly polarized, single-mode beam of maximum power 2 W.

---

[1] Coherent, Model Verdi 2W, which is a frequency doubled Nd:YVO$_4$ laser.

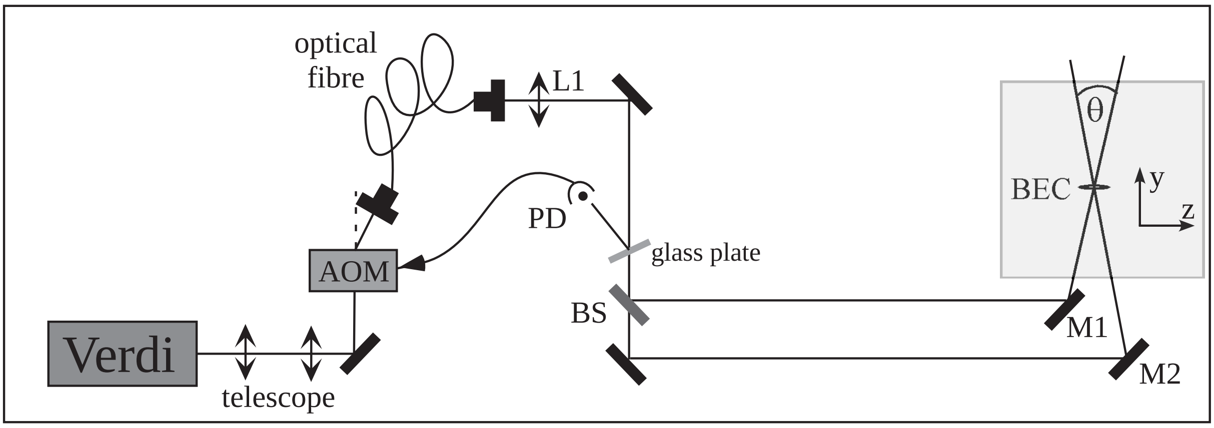

Figure 4.1: The optical lattice is created by intersecting two laser beams at the position of the BEC: a blue-detuned laser beam is spatially filtered by an optical fiber and power stabilized through a feedback loop, before being split into two beams of equal power. These beams are focused on the BEC by a lens of focal length 50 mm (L1). The grey area is shown in more detail in figure 4.2.

The beam power delivered by the verdi can not be ramped up or down on timescales faster than a few seconds. Therefore we control the beam power that arrives on the atoms by a feedback loop, consisting of an acousto-optical modulator (AOM) and a photodiode (PD) (see figure 4.1): the beam coming from the laser is sent into the AOM, where it is separated in the beams of different order. After the AOM the zero order beam is blocked, while the first order beam is sent into a fiber. After the fiber a small fraction of the beam is coupled out and sent to a photodiode (PD). The beam power measured by this photodiode is compared to the target value given by the control computer, and the difference between the two values is fed into the voltage that controls the AOM. In this way the power in the first order beam can be controlled on a sub-millisecond timescale, to between 0 and 80% of the incoming power. This setup also serves to stabilize the beam intensity after the fiber, which without stabilization fluctuates by $\approx 10\%$. As the timescale of the feedback-loop is smaller than 1 ms, all fluctuations with frequencies $\lesssim 1\,\text{kHz}$ can be eliminated.

The fiber has a core size of $3.5\,\mu$m, and after the fiber a lens of focal length 50 mm is positioned at a distance of $(50+\epsilon)$ mm, where $\epsilon \ll 50$ mm. This lens focusses the beam onto the atoms, where it has a waist of $w \approx 100\,\mu$m (and the intensity profile is $I = I_0\, e^{-2r^2/w^2}$), which is of the order of the length of the condensate. After the lens the beam is split by a non-polarizing beamsplitter (BS) into two beams of equal power and equal polarization. These beams are guided into the glass cell, with angles $\pm\theta/2$ with respect to the y-axis, and intersect at the position of the atoms with an angle θ (figure 4.2), where they create a standing wave along the z-axis with period $d = \lambda/[2\sin(\theta/2)]$. This wave creates a repulsive lattice potential for the atoms, which accumulate at the nodes of the standing wave, while the radial confinement is provided by the magnetic trap. The lattice potential along z has the shape

$$U(z) = U_0 \cos^2(\pi z/d), \tag{4.1}$$

where U_0 is the lattice height, depending on the beam power. For the work presented in this chapter, we have explored periods between $d = 2.7\,\mu$m and $d = 5.1\,\mu$m and different lattice heights U_0.

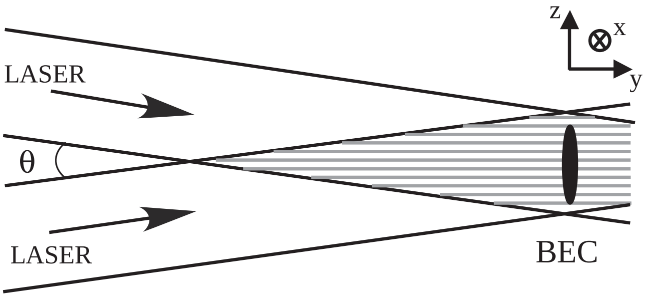

Figure 4.2: At the position of the BEC two laser beams intersect at an angle θ and create a lattice of period $d = \lambda/[2\sin(\theta/2))]$. The lattice splits the cigar-shaped condensate into an array of independent 2-dimensional pancakes.

4.1.2 Height of the lattice potential

An important parameter of the lattice is the maximal height of the lattice $U_0^{\max}$, which is the largest U_0 we can achieve with our beam parameters. It can be calculated within the model of the two-level atom from the diameter and power of the beams. This calculation is presented in the first paragraph of this section.

In a series of experiments we then used three different methods to measure the lattice height and confirm the calculation. These methods rely on a centering routine for a single beam (a), the Kapitza-Dirac effect (b), and the expansion of the atomic cloud when released from the lattice (c).

Calculation of the lattice potential: the dipole force

As described above, the beams are focussed onto the position of the atoms. Due to a slight difference in the length of their paths, they do not have exactly the same waist: beam 1 has a waist of $w_1 = 107\,\mu$m, and beam 2 a waist of $w_2 = 92\,\mu$m. The beam powers are also not exactly the same in both beams. We measured the maximal beam power directly before the beams enter the glass cell (verdi output 1.5 W and maximal output of the AOM) to $\tilde{P}_1 = 225\,\mathrm{mW}$ and $\tilde{P}_2 = 196\,\mathrm{mW}$. Taking into account that the beams have to pass through two glass surfaces of the cell (inner and outer surface of one of the walls) before arriving on the atoms, the beam powers can be estimated to $P_{1,2} = (0.96)^2\tilde{P}_{1,2}$, which gives $P_1 = 208\,\mathrm{mW}$ and $P_2 = 181\,\mathrm{mW}$.

From the measured values of the beam power and diameter one can calculate the height of the lattice potential. An easy and reliable model for our situation is the interaction of light with a 2-level atom. For far detuned light the dipole potential is [66, 121]

$$U_0 = -\frac{\hbar\Gamma^2}{8}\frac{I}{I_{\mathrm{sat}}}\left(\frac{1}{\omega_0-\omega_L} - \frac{1}{\omega_0+\omega_L}\right) \tag{4.2}$$

with the angular frequencies of the Rb-transition $\omega_0 = 2.42\cdot 10^{15}\,\mathrm{Hz}$ and the laser $\omega_L = 3.54\cdot 10^{15}\,\mathrm{Hz}$, the line width $\Gamma = 2\pi\,5.9\,\mathrm{MHz}$, and the saturation intensity $I_{sat} = 16.4\,\mathrm{W/m^2}$. The light intensity in an interference minimum is ≈ 0, while in an interference maximum it is $I_{\max} \approx 4I_0$, where $I_0 = 2P/(\pi w^2)$ is the peak intensity of a single beam with waist w and intensity profile $I = I_0 e^{-2r^2/w^2}$.

For a waist $w = \sqrt{w_1 w_2} = 100\,\mu$m and a maximal laser power $P = \sqrt{P_1 P2} = 195\,\mathrm{mW}$ (which is the average of the two beams), one gets $I_{\max} = 4.97\cdot 10^7\,\mathrm{W/m^2}$ and $U_0^{\max}/h = 60\,\mathrm{kHz}$. This value changes however fast with the waist and the exact position of the beams. Therefore we preferred to confirm this calculation using methods which measure directly the effect of the laser on the atoms.

In the following, three experimental routines are presented, which were used to measure the lattice height.

a) Centering the beams

A first method to derive the height of the lattice potential from its influence on the atomic cloud is based on the method used to center the beams onto the atoms. To this end one of the beams is blocked. The other one then splits the condensate into two halfs. If one supposes the beam to be perfectly centered on the atoms, the combined potential of the magnetic trap along the z-axis and the gaussian repulsive potential created by the beam is

$$U(z) \approx \frac{1}{2} m (\omega_z^{(0)})^2 z^2 + A_i e^{-2z^2/w_i^2},$$

where $\omega_z^{(0)}$ is the axial trapping frequency of the magnetic trap, $i = 1, 2$ and $A_{1,2}$ and $w_{1,2}$ are the amplitude and the waist of the gaussian potential, created by beam 1 or 2 respectively. The propagation axis of the beams is here supposed to be parallel to the y-axis (taking the angle into account gives corrections smaller than 0.5%). For sufficient beam power the above potential has two minima at positions $z = \pm z^{(0)} \neq 0$. For our trap parameters the distance between these minima is large enough to be well resolved by our imaging system. The experiment performed to measure the splitting is very similar to the standard production of a BEC, except that one of the beams is turned on to maximal power already during the evaporative cooling cycle. The atoms then condense directly in the combined double-well potential, and are imaged *in situ*, without ToF expansion.

This method serves well to detect misalignment of the beams along both axes: in case of misalignment along the z-axis, the two created minima are not symmetric around the position of the purely magnetic trap, while in case of misalignment along the x-axis the distance $2z^{(0)}$ between the minima becomes smaller and smaller, the more the beam is far from the trap center. By maximizing the splitting distance, and making the position of the minima symmetric around the magnetic trap center, this method permits to center each of the beams on both axes.

The largest splitting distances observed are $2z_1^{(0)} = 184\,\mu$m for beam 1 and $2z_2^{(0)} = 173\,\mu$m for beam 2. This leads to amplitudes $A_1/h = 13.1\,$kHz and $A_2/h = 13.0\,$kHz. The height of the lattice potential then is $U_0/h = 4\sqrt{A_1 A_2}/h = 52\,$kHz. This is about 15 % lower than the theoretical value calculated above from the beam parameters. As mentioned above, this mismatch is easily explained with a slight misalignment of the beams ($\leqslant 0.1\,w$), or a slightly larger waist on the atoms' position.

b) Diffraction of atoms by a standing light wave: the Kapitza-Dirac effect

The second experimental method to measure the lattice height relies on the Kapitza-Dirac (KD) effect [122, 123]. This effect describes diffraction of atoms by a light wave, and is analogue to diffraction of light waves by a matter grating. With neutral atoms the KD effect was first measured in 1986 [124].

In our experimental setup the lattice axis is parallel to the z-axis, and the lattice is turned on after a short time-of-flight of typically 6 ms, so that the atoms have acquired a velocity along the vertical x-direction. The lattice power is ramped up to maximum value U_0 by switching on the AOM (which takes $\sim 2\,\mu$s), left at this value for a variable time $t_{\mathrm{KD}} > 10\,\mu$s, and ramped down by switching off the AOM. The shape of the resulting light pulse can be approximated by a square profile.

The probability P_n that the moving atoms gain transverse momentum $n\hbar k$ from the interaction with the light wave, is obtained by expansion of the light wave in a Fourier series in z. This results in a sum of Bessel-functions, with the argument $\tau_{\mathrm{KD}} = U_0 \cdot t_{\mathrm{KD}}/(2\hbar)$ (for the exact calculation see [124]). The density distribution of the atoms is then calculated by squaring this probability, and increasing t_{KD} (and thus τ_{KD}) leads to a increasing number of well separated density maxima, which are separated in momentum by even multiples of the photon momentum.

As t_{KD} is well controlled, it is possible to estimate the lattice height U_0 by comparing the experimental density profiles with the shape of the squared Bessel-functions for different parameters τ_{KD}. The resulting estimates are given in the following table.

pulse duration t_{KD}	number of density maxima	corresponding τ_{KD}	U_0/h
12 μs	2	2.5	66 kHz
20 μs	3	4	64 kHz
32 μs	4	5.5	54 kHz
42 μs	5	7	54 kHz

The differences between the smallest and the largest estimate are of the order of $\approx 20\,\%$. The purely qualitative comparison of the expected and observed density profiles is thus not a very reliable way to measure U_0. However, the Kapitza-Dirac diffraction represents a second useful tool for the centering of the lattice, as for centered beams the argument τ_{KD} is larger than for decentered beams, if the pulse duration is kept constant.

c) Expansion dependance on the lattice potential

A third experimental method to measure the lattice potential is based on the expansion of the atomic clouds from the individual lattice sites. If the tunneling rates between the sites are negligible, the atoms form independent condensates in the individual sites of the lattice. The axial frequency of each of these traps depends on the lattice height U_0, and the larger it is, the faster the atomic clouds expand along z.

In the absence of tunneling, the kinetic energy of the atoms is the sum of the kinetic energy due to the axial magnetic confinement and the axial confinement in the individual lattice sites. This latter term depends on the harmonic trapping frequency in the wells, which is derived from the harmonic approximation of the lattice potential (equation (4.1)):

$$\omega_z^2 = \frac{2}{m} U_0 k_0^2 \sin^2(\theta/2) = \frac{4\omega_R}{\hbar} U_0 \tag{4.3}$$

where $\omega_R = E_R/\hbar$ is the frequency associated with the recoil energy $E_R = \hbar^2 k^2/(2m)$, $k = \pi/d$ and $k_0 = 2\pi/\lambda$. If a condensate at a given site populates only the ground states of the harmonic oscillator along z of the respective well (which means that it is confined to zero point oscillations along z), the sum of its kinetic and potential energy is $E = \frac{1}{2}\hbar\omega_z$. This energy consists to equal parts of the potential and the kinetic energy, which thus has the value $E_c = \langle \frac{1}{2} m v^2 \rangle = \frac{1}{4}\hbar\omega_z$.

Neglecting the initial size of the harmonic oscillator ground state, which is a good approximation for expansion times much longer than ω_z^{-1}, as well as the effect of interactions on the expansion, one then finds for the size of the cloud after expansion

$$Z = \sqrt{(vt)^2 + Z_0^2} = \sqrt{\left(\frac{t}{\sqrt{m}} \left(U_0 E_R\right)^{1/4}\right)^2 + Z_0^2}\,, \tag{4.4}$$

where Z_0 is the size of the expanded cloud for $U_0 = 0$. The size after expansion should thus vary approximately as $Z \propto U_0^{1/4}$.

Equation (4.4) has however limited validity: first, it is only valid for large lattice heights, which

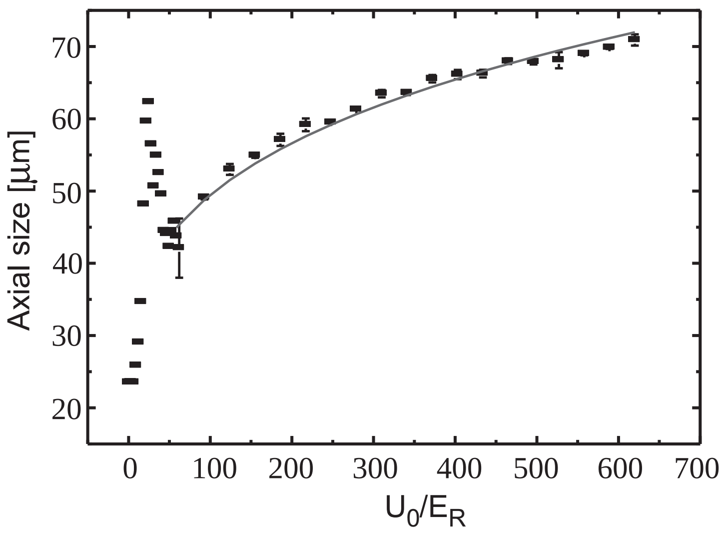

Figure 4.3: Axial size Z of the cloud after 22 ms expansion as a function of the lattice depth U_0. For all data points the lattice was ramped up in $\tau_{\mathrm{ramp}} = 200\,\mathrm{ms}$ and left on for $\tau_{\mathrm{hold}} = 500\,\mathrm{ms}$ before ToF was performed. The full line is the prediction for the U_0 dependence of equation (4.4).

squeeze the atomic cloud enough to make them quasi-2D. Second, the influence of interactions on the axial expansion velocity depends on the lattice height, and neglecting this influence is thus not necessarily a good approximation for all lattice heights.

Figure 4.3 shows experimental values of Z after 22 ms ToF as a function of the lattice height. The clouds were fitted by gaussians, and the plotted axial size is the rms of the gaussian. The curve of all data points was then fitted with the U_0-dependance of equation (4.4). This fit gives $Z_0 = 24\,\mu\mathrm{m}$ and $U_0^{max}/h = 50\,\mathrm{kHz}$, which is comparable to the value obtained by splitting the trap potential in two independent wells.

The "heating bump" Figure 4.3 also shows a sharp peak in the axial size of the cloud in the region $20 < U_0/E_R < 35$. This peak is due to strong heating at these lattice heights. The peak heating rate (measured from the radial size of the cloud after ToF) is $\sim 200\,\mathrm{nK/s}$.

For a long time we could not explain this strong heating by neither technical nor physical effects [3]. However, when changing the mechanical setup to obtain a better stability, the heating disappeared. We now believe that mechanical vibrations (possibly due to a water tube touching a mirror mount) led to parametric excitation of the cloud for specific lattice heights.

d) Lattice height: Comparison of the different measurements

In the following table the results of paragraphs (a)-(c) are summarized:

Method	Calculation	a) Splitting	b) Kapitza-Dirac	c) Expansion
U_0/h	60 kHz	52 kHz	54-66 kHz	50 kHz

Most of the experimental results indicate a lattice height of $U_0/h \approx 50-54\,\mathrm{kHz}$, which is $\approx 20\,\%$ lower than the calculated value. Only two of the measurements performed with the KD-method are of the order of this calculated value. This method is however based on a purely qualitative comparison of imaged and calculated density profiles, and thus the least trustable (which is also indicated by the large difference between the individual values obtained with this method).

In most applications in the following it is more important to give a lower bound on U_0 than an exact estimate. According to the above presented results this lower bound is taken as $U_0/h = 50\,\mathrm{kHz}$.

4.1.3 Axial frequency, atom numbers and dimensionality in the lattice sites

As discussed above, the axial trapping frequency varies with the height of the lattice potential, as well as with the angle between the two beams (equation (4.3)). For the work presented in this thesis we have used several lattice periods, between the minimal value $d_1 = 2.7\,\mu\mathrm{m}$ and the maximal value $d_2 = 5.1\,\mu\mathrm{m}$. The respective oscillation frequencies along z are $\omega_1/2\pi = 4.0\,\mathrm{kHz}$ and $\omega_2/2\pi = 2.1\,\mathrm{kHz}$ for full laser power.

When separating single sites from the lattice, as will be described in section 4.3, one can derive the number of atoms per site through a fitting routine. At the end of such an experimental cycle the BEC atom numbers in the most populated central sites are $N_1 \approx 10^4$ and $N_2 \approx 2 \times 10^4$ respectively.

For these atom numbers, a radial trapping frequency of $\omega_\perp/2\pi = 106\,\mathrm{Hz}$ and the above mentioned axial frequencies, the corresponding chemical potentials were derived by numerically solving the Gross-Pitaevskii equation. This gives $\mu_1/h = 2.2\,\mathrm{kHz}$ and $\mu_2/h = 2.5\,\mathrm{kHz}$, where the $\hbar\omega_{1,2}/2$ zero-point offset is suppressed in the definition of μ.

For the range of lattice periods given above, the condensates in the shortest period lattice are well in the 2D regime with $\mu_1/(\hbar\omega_1) = 0.6$. For the clouds in the longest period lattice this ratio is 1.2. Due to the smooth crossover from 3D to 2D it is however not clear if these different ratios will result in qualitatively - rather than only quantitatively - different properties of the cloud.

4.1.4 Ramping time of the lattice

In most experiments the experimental cycle begins with a cigar shaped 3D condensate, routinely produced as described in chapter 2. The lattice intensity is ramped up only after the end of the evaporation cycle. To chose the duration of this ramp, several time scales of the system need to be considered carefully.

A first time scale is given by the trap frequencies of the magnetic trap. The ramp should be slow compared to these scales, in order not to excite the condensate in the beginning of the ramp. With $\omega_\perp^{-1} \approx 1.5\,\mathrm{ms}$ and $(\omega_z^{(0)})^{-1} \approx 14\,\mathrm{ms}$, it is not difficult to respect this condition.

The second important time scale is related to the band structure of the lattice. To make sure that the condensate populates only the lowest Bloch band at the end of the ramp, the ramping has to be adiabatic with respect to the time scale corresponding to the energy of the band separation. For a condensate that is initially at rest, i.e. has a momentum $q = 0$, it can be shown that for small lattice heights the adiabaticity criterion for loading all atoms in the lowest band is given by [33, 125]

$$\frac{dU_0}{dt} \ll 16\frac{E_R^2}{\hbar}.$$

The recoil energy $E_R = \hbar^2 k^2/(2m)$ depends on the lattice spacing, and is $E_R^{(1)}/h = 80\,\mathrm{Hz}$ for the small period $d_1 = 2.7\,\mu\mathrm{m}$, and $E_R^{(2)}/h = 22\,\mathrm{Hz}$ for the large period $d_2 = 5.1\,\mu\mathrm{m}$. If the lattice is ramped linearly to its maximal height, $U_0/h \approx 50\,\mathrm{kHz}$, the ramping time should be much longer than 13 ms for the small period, and 160 ms for the long period lattice.

In most experiments the lattice potential is ramped to its maximal height in 200 ms, using a linear ramp or a sine-function $P(t) = \sin(\pi t/(2t_0))$, where t_0 is the rise time. With this ramp time we do not see important excitations of the condensates in the lattice sites.

A third time scale is given by the timescale of the tunneling: due to the long lattice period and the large height of the potential barriers, the condensates can be completely isolated from each other - which means that the tunneling times are very large compared to our experimental time scale. The matrix element J for the tunneling of a single particle between neighboring sites scales as $E_R\,(U_0/E_R)^{3/4}\,e^{-2\sqrt{U_0/E_R}}$ [126]. As calculated above, the maximum lattice depth corresponds to $U_0 \approx 625\,E_R$, which leads to $J/h \sim 10^{-18}\,\mathrm{Hz}$. The actual tunneling rate is J times the number of atoms per lattice site. For $\sim 10^4$ atoms per site the tunneling time for a single particle is of the order of $10^{14}\,\mathrm{s}$ and thus negligible on the timescale of the experiment.

4.1.5 Scales of the lattice potential

The following table gives an overview over the most important scales of the lattice derived in sections 4.1.1-4.1.4. As several lattice periods were used in the experiments presented in this manuscript, the table gives the values of the smallest and largest used periods, d_1 and d_2. All numbers correspond to a lattice potential of maximal height $U_0 \approx 50\,\mathrm{kHz}$.

		d_1	d_2
atom number	atom number per site N	$N_1 \sim 10^4$	$N_2 \sim 2\,10^4$
length scales	lattice period d harmonic oscillator length $a_z = \sqrt{\hbar/(m\omega_z)}$ Thomas-Fermi radius $R_\perp$	$d_1 = 2.7\,\mu\mathrm{m}$ $a_z = 120\,\mathrm{nm}$ $R_\perp \sim 5\,\mu\mathrm{m}$	$d_2 = 5.1\,\mu\mathrm{m}$ $a_z = 170\,\mathrm{nm}$ $R_\perp \sim 5\,\mu\mathrm{m}$
energy scales	recoil energy $E_R = \hbar^2 k^2/(2m)$ lattice depth U_0	$E_R/h = 80\,\mathrm{Hz}$ $U_0/h = 50\,\mathrm{kHz}$	$E_R/h = 22\,\mathrm{Hz}$ $U_0/h = 50\,\mathrm{kHz}$
time scales	radial trapping frequency $\omega_\perp$ axial trapping frequency ω_i	$\omega_\perp^{-1} = 1.5\,\mathrm{ms}$ $\omega_1^{-1} = 40\,\mu\mathrm{s}$	$\omega_\perp^{-1} = 1.5\,\mathrm{ms}$ $\omega_2^{-1} = 80\,\mu\mathrm{s}$

4.2 Selecting sites from the lattice

Once the lattice potential is ramped up and the 3D BEC is cut in 20 - 35 independent pancake shaped condensates, one can start the routine for the removal of atoms from selected lattice sites. Since the radial trapping is purely magnetic, the sites can be addressed by an rf-knife, which induces spin-flips to untrapped Zeeman states.

4.2.1 Adding a magnetic field gradient

To selectively address the sites, we have chosen to modify their resonant frequencies for evaporation of atoms by applying a magnetic field gradient b' along z (this method has also been used in [120]). To produce this gradient we use the MOT coils - a pair of coils in anti-Helmholtz configuration, aligned with the z-axis of the magnetic trap, as shown in figure 4.4. These coils

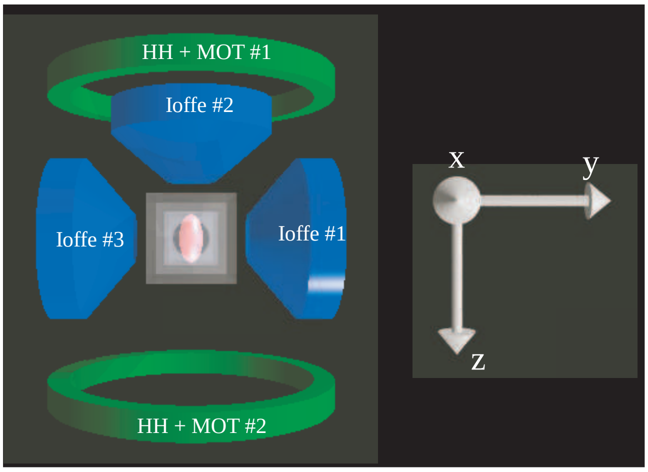

Figure 4.4: Relative position of the Ioffe-Pritchard coils and the MOT coils which produce the magnetic field gradient, seen from above.

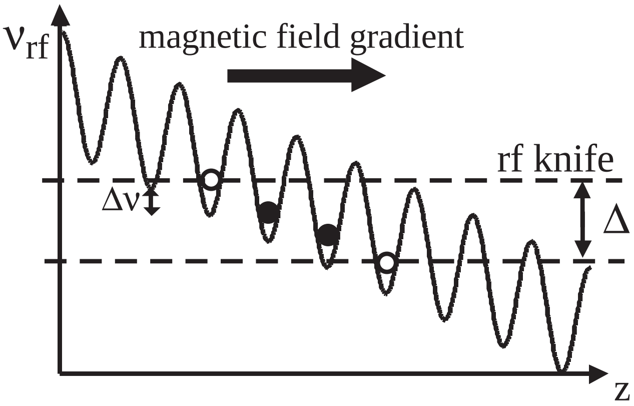

Figure 4.5: A magnetic field gradient along the lattice axis allows us to selectively address the sites by an rf field. The atoms from all the sites are evaporated, except those within a frequency gap Δ.

produce a quadrupole field with the main axis z:

$$\mathbf{B}(x,y,z) = \begin{pmatrix} (b'/2)x \\ (b'/2)y \\ -b'z \end{pmatrix}, \tag{4.5}$$

which added to the Ioffe-Pritchard field gives the following total field:

$$\mathbf{B}(x,y,z) = B_0 \begin{pmatrix} 0 \\ 0 \\ 1 \end{pmatrix} + \begin{pmatrix} (-B' + b'/2)x \\ (+B' + b'/2)y \\ -b'z \end{pmatrix} + \frac{B''}{2} \begin{pmatrix} -xz \\ -yz \\ z^2 - \frac{1}{2}(x^2+y^2) \end{pmatrix} \tag{4.6}$$

The minimum along z of this combined field is shifted to the position b'/B'', where the field is $B = B_0 - b'^2/(2B'')$. If b' is not too large, the atoms can however not follow this displacement, because they are held by the steep lattice walls. So the atoms stay in their original positions in the lattice sites, where the magnetic field varies approximately linearly along z. The resonant

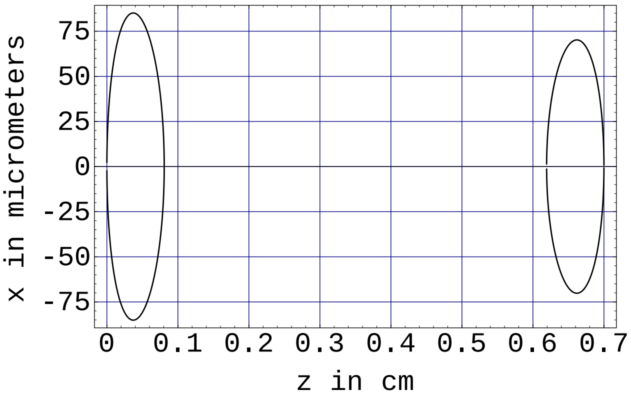

Figure 4.6: Cut through the potential surface $|\boldsymbol{B}| = B_0$ at $y = 0$, where $\boldsymbol{B}$ is given by equation (4.6), $B_0 = 1\,\mathrm{G}$, $B' = 130\,\mathrm{G/cm}$, $B'' = 80\,\mathrm{G/cm}^2$ and $b' = 28\,\mathrm{G/cm}$. Note that the x-axis gives the z-position in cm, while the y-axis gives the x-position in μm.

frequencies for evaporation of two neighboring sites are split by $\delta\nu \approx \mu_\mathrm{B} b' d/(2h)$, where μ_B is the Bohr magneton (figure 4.5).

To obtain the shape of the equipotential lines of the magnetic field at the position of the atoms, one has to calculate $|\boldsymbol{B}(x, y, z)|$ with the field given in equation (4.6). For gradients $b' > (2B_0 B'')^{1/2}$ the magnetic field minimum has a negative value, and the equipotential surface for $|\boldsymbol{B}| = B_0$ corresponds to two distinct surfaces around the zeroes of the field at positions $z_1 \approx B_0/b'$ and $z_2 \approx 2b'/B''$. For a gradient $b' = 28\,\mathrm{G/cm}$, $z_1 \approx 0.04\,\mathrm{cm}$ and $z_2 \approx 0.7\,\mathrm{cm}$, and a cut at $y = 0$ through the equipotential surface $|\boldsymbol{B}| = B_0$ is shown in figure 4.6. To derive the shape of the equipotential surface near the center of the cigar (that is for x,y,$z \ll 100\,\mu\mathrm{m}$) an approximation of $|\boldsymbol{B}(x, y, z)|$ is obtained by an expansion of the square root, where the terms of order z^2 (and higher) and the term in x^4 can be neglected. Setting $|\boldsymbol{B}(x, y, z)| = B_0$, this leads to the following shape in the xz-plane:

$$x^2_\mathrm{evap}(z) = \frac{2b' B_0 z}{(B' + b'/2)^2} \qquad \text{for} \qquad 0 < z \ll 100\,\mu\mathrm{m}. \tag{4.7}$$

Near the center of the cigar the equipotential surfaces correspond thus approximately to a part of an ellipsoid's surface with a center at $z = z_1$ (which corresponds to the left ellipsoid in figure 4.6).

In our experiments we mostly used gradients between $28\,\mathrm{G/cm}$ and $40\,\mathrm{G/cm}$, the latter being a technical limit due to the used power supply. With the range of lattice periods between $d_1 = 2.7\,\mu\mathrm{m}$ and $d_2 = 5.1\,\mu\mathrm{m}$ the frequency splittings range from $\delta\nu_1 = 5\,\mathrm{kHz}$ to $\delta\nu_2 = 13\,\mathrm{kHz}$. These splittings are larger than the chemical potentials of the 2D condensates in all our experiments. They are also larger than the Rabi frequency of the rf transition, which is estimated to $\approx 2\,\mathrm{kHz}$. Therefore these parameters allow us to individually address the lattice sites.

Beside the wanted effect of the gradient field in the z-direction the MOT coils also produce a field gradient of value $b'/2$ in the radial direction. This gradient has an influence on the radial trapping frequencies

$$\omega^2_{x,y} = \frac{\mu_\mathrm{B}}{m}\left(\frac{1}{B_0}\left(B' \pm \frac{b'}{2}\right)^2 - \frac{B''}{2}\right) \approx \frac{\mu_\mathrm{B}}{mB_0}\left(B' \pm \frac{b'}{2}\right)^2,$$

where the sign of the modification is different for the x- and y-direction. For $B' = 130\,\mathrm{G/cm}$ and maximal gradients of $b' = 40\,\mathrm{G/cm}$, the radial frequencies are thus modified by $\pm 15\%$, which leads to an ellipticity $2(\omega_x - \omega_y)/(\omega_x + \omega_y) = 30\,\%$.

Height of the potential wells in the presence of a gradient

When looking closer at figure 4.5, which illustrates the effect of the gradient on the deformation of the potential, one might wonder whether the atoms will spill over the lattice barriers when the slope becomes too large. To estimate this critical slope, one has to look at the combined potential along the z-axis, consisting of the optical lattice plus the gradient:

$$U(z) = U_0 \cos^2(\pi z/d) + \mu_\mathrm{B} b' z + \text{const.} \tag{4.8}$$

The minima of this potential are at the z-positions where its derivative is zero, which is equivalent to the condition:

$$\sin(2\pi z/d) = \frac{\mu_\mathrm{B} b' d}{\pi U_0}. \tag{4.9}$$

With increasing gradient b' neighboring pairs of a minimum and a maximum move towards each other, until they merge when

$$\frac{\mu_\mathrm{B} b' d}{\pi U_0} = 1.$$

At this point the potential barriers between the sites have completely vanished. For the largest lattice period used in our experiments, $d = 5.1\,\mu$m, this situation happens for a gradient of $b' = 220\,$G/cm, which is much larger than the gradients used. For our largest gradient of 40 G/cm, the above factor is 0.18 and the deplacement of the extrema is $\Delta_{z_0} \approx \pm 0.03\ d$, where the positions of the maxima are shifted to larger z-values, and the positions of the minima to lower z-values. The potential difference between a maximum and a minimum is

$$\Delta U/h \approx U_0/h - \frac{\mu_\mathrm{B}}{h}\, b'\, d \cdot (0.5 - 0.06) \approx 38\,\mathrm{kHz},$$

where $U_0/h = 50\,$kHz is the original height of the lattice, when no gradient is applied. The modified barrier $\Delta U/h$ is still very high compared to the chemical potential in the sites and the gradient cannot provoke any spilling of the condensates between the lattice site.

4.2.2 The influence of the gravitational sag

For the above considerations it was intuitively assumed that the atomic cloud is at the center of the magnetic trap. Due to gravity its position is however below the magnetic trap center, and the distance from the center depends on the bias field B_0 of the IP-trap: the value of the gravitational sag is $\Delta_\mathrm{sag}/B_0 \approx 8\,\mu$m/G (see chapter 2). If the gravitational sag is too large, it can prevent selective addressing of the sites, as illustrated in figure 4.7. The system is thereby defined as fully addressable, if magnetic equipotential surfaces exist that allow to fully evaporate the chosen sites without touching the others.

As discussed above, the shape of the equipotential surfaces at the position of the atoms corresponds to the surfaces of ellipsoids. The addressability condition is thus equivalent to the existence of equipotential ellipsoids that allow for all sites to either have their center located inside the ellipsoid, or being located completely outside of the ellipsoid (which is the case in figure 4.7 (b), but not in figure 4.7 (a)). Wether this condition can be fulfilled, depends on the ellipsoid's aspect ratio, the lattice period and the sag. The ideal combination of these parameters is derived in the following.

Selective evaporation can be described as the edges of the evaporational ellipsoid approaching one site after another, depending on the applied rf frequency. In the case of no gravitational sag, the ellipsoid corresponding to the magnetic field B_0 evaporates the central site, and through fine tuning of this magnetic field the neighboring sites can be emptied. The only limit of this principle is the TF-radius of the clouds $R_\perp$, which has to be smaller than the radius of the evaporation

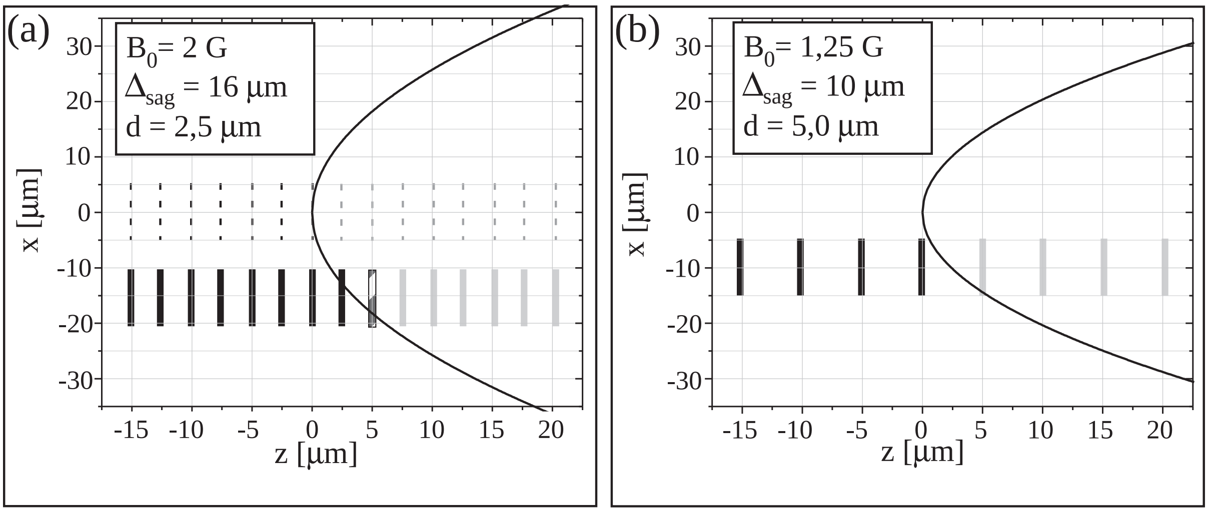

Figure 4.7: Relative position of lattice sites and evaporation ellipses when a gradient of 28 G/cm is applied. Due to the influence of gravity the atoms are not in the radial center of the evaporation ellipses, but below. This limits addressability in the case of small lattice periods and large bias fields: (a) The dotted lines indicate the theoretical position of the atoms without gravity. The full lines indicate the real position for a bias field $B_0 = 2\,\mathrm{G}$ and $d = 2.5\,\mu\mathrm{m}$: More than one site is evaporated for a given rf frequency. (b) Changing the parameters to $B_0 = 1.25\,\mathrm{G}$ and $d = 5\,\mu\mathrm{m}$ allows for single site addressability.

ellipses x_{evap} at a distance d from the evaporated site. For our experimental parameters this constraint can be fulfilled relatively easily, even for small lattice spacings (see figure 4.7 (a), dotted lines).

In the case of a nonzero gravitational sag, addressability is however reduced. An rf-field of frequency B_0/h is then not resonant with the site at the position $z = 0$, but with the site at a position z_0, which is given by $x_{\mathrm{evap}}(z_0) = \Delta_{\mathrm{sag}}$, where Δ_{sag} is the distance of the site's center from the $(x = 0)$ - axis due to the gravitational sag. In figure 4.7 (a) this corresponds approximately to the site at $z_0 = 5\,\mu\mathrm{m}$.

To insure selective addressing of the sites, the center of the z_0 site must be addressed without touching the neighboring sites at the positions $z_0 \pm d$. This leads to the conditions $x_{\mathrm{evap}}(z0+d) > \Delta_{\mathrm{sag}} + R_\perp$ and $x_{\mathrm{evap}}(z0-d) < \Delta_{\mathrm{sag}} - R_\perp$, where $R_\perp \approx 5\,\mu\mathrm{m}$ is the TF-radius of the central sites. The first of these conditions is a stronger constraint, and includes the second one, as the equipotential lines are steeper at the position $z_0 - d$ than at $z_0 + d$. With equation (4.7) this condition can be rewritten as:

$$\frac{2b'B_0 d}{(B'+b'/2)^2} > 2\Delta_{\mathrm{sag}} R_\perp + R_\perp^2 .$$

Therefore one has to work at small bias fields (leading to small gravitational sags and TF-radii), high gradients b' and with a large lattice period. In figure 4.7 two situations with different sets of parameters are shown, one allowing for selective evaporation (b), the other not (a).

4.2.3 Misalignment between QP- and Ioffe-field

While the bias field must be small during the evaporation of the selected sites, it should be larger during the rest of the experimental cycle. This is due to the decrease of the condensate lifetime

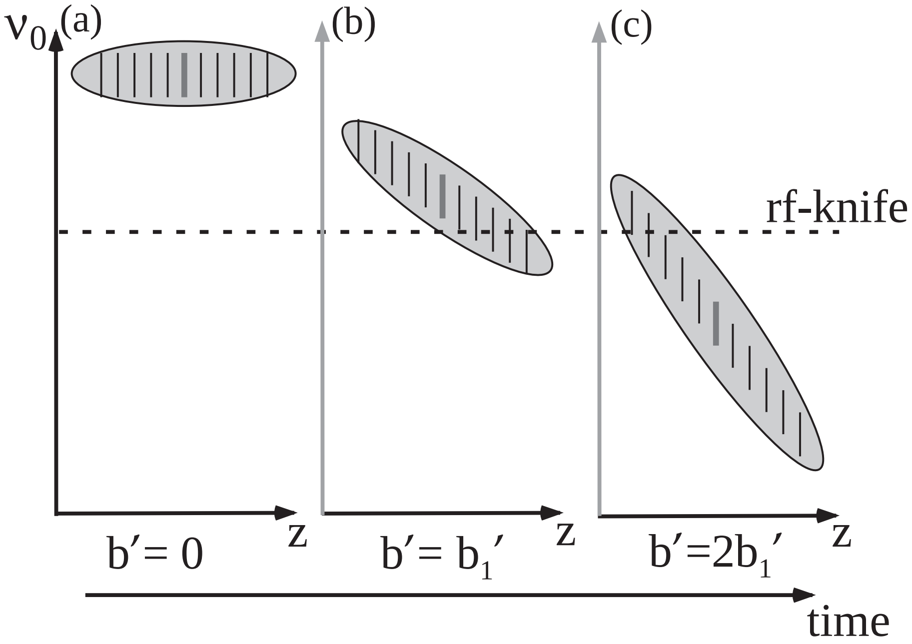

Figure 4.8: The misalignment between the center of the Ioffe-Pritchard-trap and the center of the gradient field leads to a change in the trap bottom ν_0 of all lattice sites when the gradient is ramped up. In this figure the rf knife is placed in a way that when ramping the gradient from 0 (a) to some value b'_1 (b), only the 3 lowest sites are evaporated. When ramping the gradient to the double value $2b'_1$ (c) most sites are evaporated, including the central one.

with decreasing bias field, because of the enhanced 3-body recombination in steeper traps. To this end one can consider to slowly ramp down the bias-field during the ramp of the gradient. In our configuration this happens "automatically", due to a misalignment Δ_z of several hundred micrometers between the center of the MOT-coils and the center of the Ioffe-field in z-direction[2].

When taking into account the misalignment Δ_z in the z-component of the combined magnetic field (equation (4.6)) one gets:

$$B_z = B_0 - b'(z - \Delta_z) + \frac{B''}{2}z^2 = (B_0 + b'\Delta_z) - b'z + \frac{B''}{2}z^2$$

From this equation one can see that the magnetic field at the position $z = 0$ is modified by the amount $b'\Delta_z$. In our setup $\Delta_z < 0$, and the above modification corresponds to a *decreasing* magnetic field with increasing gradient. While ramping up the gradient the trap bottom thus decreases continuously, and reaches its minimal value for the maximal gradient, when the splitting between resonant rf-frequencies is highest, and selective evaporation takes place.

This effect is used to selectively address the sites: instead of scanning the frequency of the rf-knife, as proposed at the beginning of this chapter, the rf-knife is held at a certain value, and the trap bottom of the selected sites is tuned through the "waiting" rf-frequency. This procedure is visualized in figure 4.8. Based on this effect different routines are used to spare one or several sites from evaporation, which will be explained in section 4.3.

In radial direction the misalignment has a less important effect, as one can see from the

---

[2] The exact value varies between $\Delta_z \approx -300\,\mu$m and $\Delta_z \approx -630\,\mu$m for the data sets presented in this manuscript. This variation is due to several changes of one of the Ioffe-coils, which lead to slightly changed positions of the IP-trap's center.

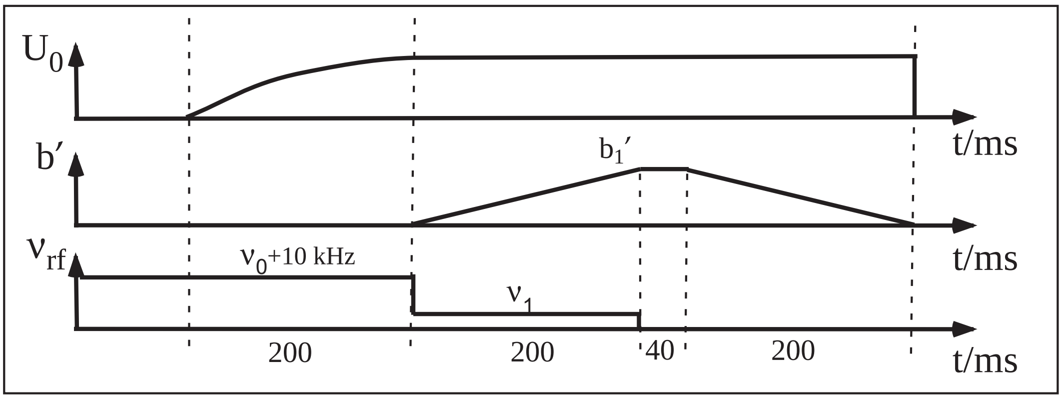

Figure 4.9: Experimental routine for position selective evaporation: after the lattice is ramped up, the rf knife is set to a variable position ν_1. The gradient then drives part of the cigar through the "waiting" rf knife. During the ramp down of the gradient no rf evaporation is performed.

radial components of equation (4.6), when taking into account the misalignment:

$$\begin{aligned} B_x(x) &\approx -B'x + \frac{b'}{2}(x - \Delta_x) = \left(-B' + \frac{b'}{2}\right) x - \frac{b'}{2}\Delta_x \\ B_y(y) &\approx +B'y + \frac{b'}{2}(y - \Delta_y) = \left(+B' + \frac{b'}{2}\right) y - \frac{b'}{2}\Delta_y. \end{aligned}$$

The misalignment $\Delta_{x,y}$ is of the order of $300\,\mu$m in both radial directions[3] and the minimum of the trap is shifted by

$$\delta_{x,y} = \frac{b'\Delta_{x,y}}{2B' + b'} \approx 40\,\mu\text{m},$$

for our trap parameters and maximal gradient $b' = 40\,$G/cm. This shift is smaller by a factor 2.5 than the waist of the beams constituting the lattice, so that the atomic cloud stays in the region of large lattice height. We also did not observe any heating or excitation due to this displacement, which is not astonishing, given that our gradient is never ramped in less than 200 ms to its maximal value, resulting in a radial velocity of $0.15\,\mu$m/ms. This is slow compared to the ratio of the cloud's radial diameter $2R_\perp \approx 10\,\mu$m and the time for a full radial oscillation of $\omega_\perp^{-1} = 1.5\,$ms.

4.3 Experimental results

4.3.1 Experimental routine and preliminary experiments

Our first experimental goal was to prove the general ability of our setup for position resolution, that is to selectively address only some of the lattice sites. To this end we performed a series of experiments, in which more and more sites were evaporated, starting at one end of the cigar.

The experimental routine for these experiments starts with the 200 ms ramp-up of the lattice (see figure 4.9). During the lattice ramp-up the rf-frequency is kept at the value $\nu_0 + 10\,$kHz, where ν_0 is the frequency corresponding to the bottom of the unperturbed Ioffe-Pritchard trap. Directly afterwards the rf-frequency is changed to a variable value $\nu_1 = \nu_0 - b'\Delta_z \pm \delta$. At $\delta = 0$

---

[3] In contrast to the value of Δ_z the values of Δ_x and Δ_y stay nearly unchanged during changes of the mechanical setup.

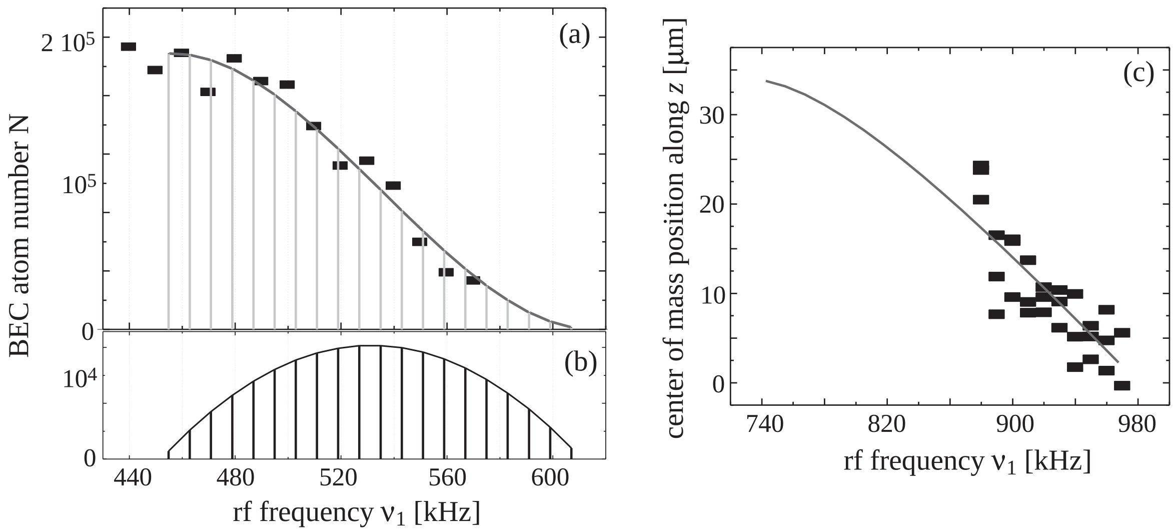

Figure 4.10: (a) BEC atom number N as a function of ν_1. Each data point corresponds to an experiment of the type illustrated in figure 4.9 with $b' = 26\,\mathrm{G/cm}$, $d = 4.4\,\mu\mathrm{m}$, $\nu_0 = 1690\,\mathrm{kHz}$, and $\Delta_z = 630\,\mu\mathrm{m}$. The data is fitted by the spatial integral over the sites, starting at the side of the cigar with the higher trap bottom (full line). From this fit the atom number at each site of the lattice is derived, which leads to the density profile in (b). Figure (c) shows the position of the center of mass as a function of ν_1, with the parameters $b' = 40\,\mathrm{G/cm}$, $d = 4.4\,\mu\mathrm{m}$, $\nu_0 = 2190\,\mathrm{kHz}$ and $\Delta_z = 310\,\mu\mathrm{m}$. The full line is a fit with the expected functional form, where the length of the initial cigar was a free parameter. In this series the rf-knife was scanned only over one half of the cigar.

this value corresponds to the trap bottom of the central site when a gradient b' is applied. For $\delta \neq 0$ the frequency corresponds to sites with higher or lower trap bottom.

Only after the change of the rf frequency the gradient is ramped up in 200 ms to a fixed value b'. During this ramp the trap bottom of all sites decreases continuously, and the larger ν_1, the more sites are emptied (as visualized in figure 4.8). The rf-field is then turned off and the gradient is ramped down in another 200 ms before turning off the lattice and magnetic trap simultaneously to perform a ToF experiment. The atom number of the remaining cloud, as well as the position of its center of mass are derived from the density profile after 22 ms ToF with the usual fitting routine.

Atom number Figure 4.10 (a) shows the number of atoms as a function of the ν_1, in experiments performed with $b' = 26\,\mathrm{G/cm}$, $d = 4.4\,\mu\mathrm{m}$, $\nu_0 = 1690\,\mathrm{kHz}$ (leading to $\nu_\perp = 108\,\mathrm{Hz}$), and $\Delta_z = 630\,\mu\mathrm{m}$. The slope in the atom number thereby varies with the population of the sites that are emptied: at the edges the slope is small because the edge sites of the cigar contain only few atoms. In the center of the curve, corresponding to the largest sites being evaporated, the slope is maximal.

One can fit the data curve with the function describing the successive emptying of the sites when assuming the TF-distribution of the initial cigar-shaped condensate:

$$N = \frac{3N_t}{2L}\int_{-\frac{L}{2}}^{-\frac{L}{2}+nd}\left(1-\frac{z^2}{(L/2)^2}\right)dz\,, \quad \text{and} \quad n\,\epsilon\,\left[1,\frac{L}{d}\right]\,,$$

where n counts the number of sites spared from evaporation. The free parameters in this fit are total atom number N_t after the evaporation routine, and the length of the cigar L, from

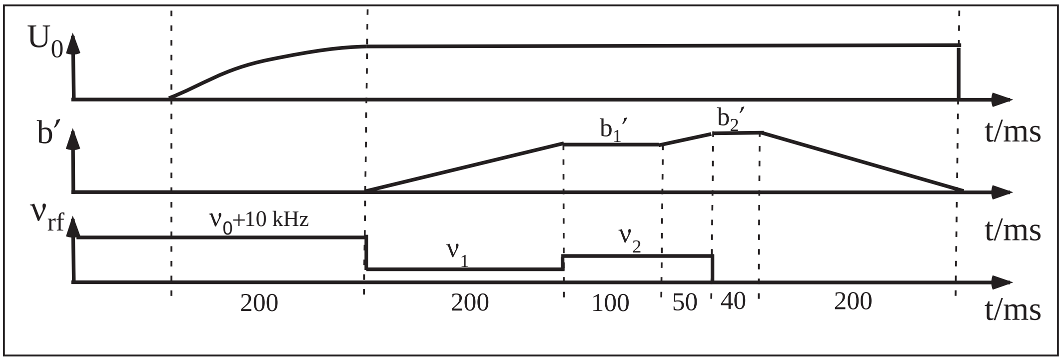

Figure 4.11: Experimental routine for the separation of a single or several 2D condensates. The gradient is ramped to an intermediate value b'_1. During this ramp the "lower" part of the cigar is driven through the rf knife at the value ν_1. The rf frequency is then set to $\nu_2 = \nu_1 + \Delta$, before the gradient is ramped to its final value $b'_2 > b'_1$. This ramp eliminates the sites in the "upper" part of the cigar. This routine spares all sites within the frequency gap Δ.

which the initial chemical potential and the initial atom number N_i (corresponding to the system before the lattice is ramped up) can be calculated.

The fitting routine gives $N_t = 1.9 \cdot 10^5$ and $L = 87\,\mu$m. This TF-length L corresponds to an initial atom number $N_i = 2.0 \cdot 10^5$. This indicates that atom losses are small during the experimental cycle in the lattice. The measured data curve corresponds well to the functional shape of the fit (diamonds+line in figure 4.10 (a)). The experimental data thus reproduces well the distribution of atoms in the different sites, which is shown in figure 4.10 (b).

Axial position The center of mass on the z-axis of the atom distribution in the magnetic trap changes with the number of sites that are spared from evaporation. If only one edge site is spared at the position $z_1 = -L/2$, the center of mass is at $z = -L/2$. When more sites survive, at positions $z_2 = -(L/2) + d$, $z_3 = -(L/2) + 2d$, ..., the center of mass position changes with the function

$$\bar{z}(n) = \frac{\int_{-\frac{L}{2}}^{-\frac{L}{2}+nd} \left(1 - \frac{z^2}{(L/2)^2}\right) z\,dz}{\int_{-\frac{L}{2}}^{-\frac{L}{2}+nd} \left(1 - \frac{z^2}{(L/2)^2}\right) dz} \;, \quad n \,\epsilon \left[1, \frac{L}{d}\right] \;, \tag{4.10}$$

and for the full number of sites the center of mass position is $z = 0$. As the lattice potential and the magnetic trap are switched off simultaneously, this displacement of the center of mass can also be measured in the cloud's position after ToF.

Figure 4.10 (c) shows the axial position of the cloud's center of mass after 22 ms ToF, for slightly different experimental parameters than in figure (a), $b' = 40\,$G/cm, $d = 4.4\,\mu$m, $\nu_0 = 2190\,$kHz and $\Delta_z = 310\,\mu$m. For an atom number $N_i = 2\,10^5$ the expected TF-length is $L = 79\,\mu$m, and the expected frequency split between the sites at the outer edges of the cigar is $Lb'\mu_B/h = 227\,$kHz . Fitting the data with the function (4.10), where L is used as fitting parameter, one finds the result $L = 68\,\mu$m, which differs by $\approx 15\,\%$ from the expected result. The fluctuations in the position are however much larger than those of the atom number. A possible explanation for these large fluctuations is that the magnetic trap might be switched off slightly later than the lattice, due to inductance effects in the coils. The atoms would then acquire a small initial momentum along z, which would be observed in the position after ToF.

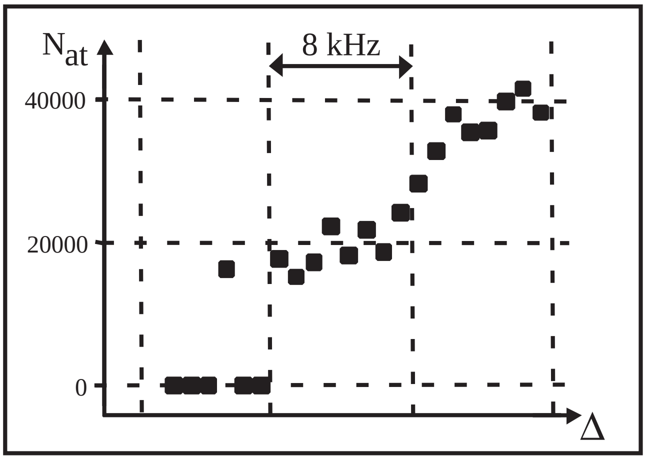

Figure 4.12: Steps in the BEC atom number N_{at} as a function of the frequency gap Δ, corresponding to 0, 1 and 2 sites spared from evaporation. Each data point represents a single measurement.

4.3.2 Steps in the atom number

The experiments described in the previous section proved our general ability for selective evaporation. It is however not very useful for the realization of a single 2D condensate, because the last condensate spared is always a small one at the edge of the cigar, and we are more interested in keeping a large site in the center of the cigar. To this end we performed a slightly modified experimental routine, shown in figure 4.11.

In this routine the rf frequency is set to the value ν_1 corresponding to the trap bottom of the cigar's center when a gradient b_1' is applied. The gradient is then ramped up to this value, and all sites with trap bottoms lower than ν_1 are eliminated. Then the rf frequency is changed to a higher value $\nu_2 = \nu_1 + \Delta$, where $\Delta > 0$ is variable, before the gradient is ramped up even more, to a value b_2'. This second gradient ramp empties all sites that had a resonant frequency larger than the new rf frequency ν_2 before the start of the second ramp. The only sites spared from evaporation are those which had a trap bottom within the frequency range Δ before the second ramp started. For the ramp down of the gradient, the rf amplitude is set to zero.

Figure 4.12 (a) shows the total number of condensed atoms left in the trap as a function of Δ. For these experiments, $d = 5.1\,\mu$m and $b_2' = 22\,$G/cm, resulting in an expected splitting of the resonant rf frequencies of $\delta\nu = 8\,$kHz. The ToF duration was 18 ms and the atomic density distribution was fitted with TF-profiles to extract the atom number. The graph shows an atom number increase in steps of $N_2 = 2 \times 10^4$ every 8 kHz, which is in good agreement with the expected frequency splitting. One can see three clear plateaus corresponding to 0, 1 and 2 sites spared from evaporation. The atom number per site is however only half of its initial value.

Atom losses of the order of 50 %, did not appear when approaching the lattice sites only from one side, as presented in section 4.3.1, where atom losses were $< 5\,\%$. The large losses during the experiments described here might thus be due to partial evaporation of the remaining sites. This is much more likely to happen if the rf ellipses approach the remaining sites from larger frequencies, which was not the case in the experiments presented in section 4.3.1.

Another important source might be 3-body-losses due to the large trap frequencies during the evaporation. When aiming to spare the central sites, the duration of this period at high gradient b' (and thus low B) is $\approx 200\,$ms instead of 40 ms in the case of a rf scan from one end to the other (compare figures 4.9 and 4.11).

For smaller lattice spacings qualitatively similar results were obtained (where in general

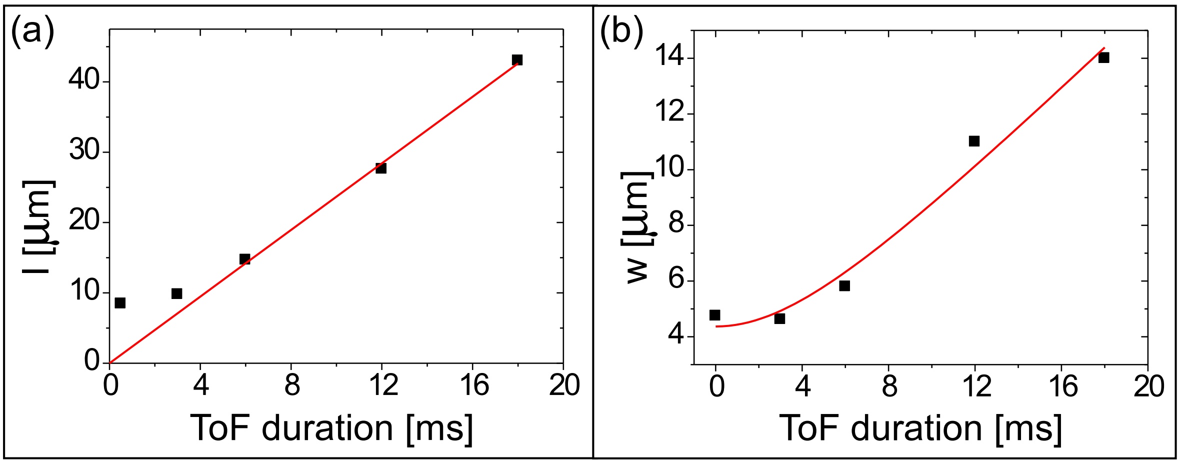

Figure 4.13: Axial (a) and radial (b) expansion of a 2D condensate. ToF expansion is varied from 3 ms to 18 ms. The full lines correspond to a linear (a) and $\sqrt{1+x^2}$ (b) fit of the data.

slightly larger gradients were used). In these cases the expected step size is about 5 kHz and still clearly visible. It is however already comparable to the chemical potential, which reduces addressability and results in some rounding off of the steps.

4.3.3 Expansion properties of the 2D clouds

After the preparation of a single 2D condensate we have performed experiments to characterize its free expansion[4]. In these experiments the clouds were released from a lattice with period $d_2 = 5.1\,\mu$m and imaged after a variable ToF duration. We then extract the axial (l) and the radial (w) rms size of the cloud from gaussian fits to the density distribution.

Axial expansion Due to the tight confinement along z, the observed expansion is predominantly one-dimensional along the axial direction. For short expansion times, $t \leq 3$ ms, the apparent axial size is limited by our imaging resolution, but for longer times it follows the linear scaling $l = vt$, with $v = 2.7$ mm/s (full line in figure 4.13 (a)). This value is only slightly larger than the calculated velocity in the harmonic oscillator ground state along z, $v_g = \sqrt{\hbar\omega_2/(2m)} = 2.1$ mm/s, which would be expected in absence of interactions. The axial expansion thus does not seem to be dominated by the atomic interactions.

Radial expansion It is found that the radial expansion can be described by the empirical law $w = w_0\sqrt{1+(t/t_0)^2}$, with $w_0 = 4.4\,\mu$m and $t_0 = 5.7$ ms (full line in figure 4.13 (b)). The same law describes the radial expansion of a cigar-shaped 3D condensate, with $t_0 = \omega_\perp^{-1}$ [94], where $\omega_\perp^{-1} = 1.5$ ms for our trap. The radial expansion of our 2D gas is slower by a factor of ≈ 4 compared to the 3D case, because the fast axial expansion results in an almost sudden ($\omega_2^{-1} = 76\,\mu$s) decrease of the atomic density, and only a small fraction of the interaction energy is converted into radial velocity.

---

[4] The expansion properties of 2D condensates were also studied by the group of C. Foot [127].

4.3.4 Temperature of the 2D clouds

Precise thermometry at the end of the experimental cycle is difficult, because the thermal cloud is very dilute. To give nevertheless an estimate of the temperature range a lower and an upper bound for the temperature are calculated.

Lower bound During the 500 ms selective evaporation routine, the clouds are heated due to three-body recombination, and the only constant source of cooling is the finite lattice depth. Atoms with an energy larger than U_0 are accelerated away by the magnetic field gradient (figure 4.5). Assuming the largest realistic evaporation parameter $\eta = \Delta U_i/(k_\mathrm{B}T) = 10$ (where $i = 1, 2$, and $\Delta U_1 = h \cdot 44\,\mathrm{kHz}$ and $\Delta U_2 = h \cdot 38\,\mathrm{kHz}$ are the lattice heights in presence of the maximal gradient for lattice periods d_1 and d_2), one gets the lower bounds for the temperature $T^{(1)}_\mathrm{min} = \Delta U_1/(k_\mathrm{B}\eta) \approx 210\,\mathrm{nK}$, and $T^{(2)}_\mathrm{min} = \Delta U_2/(k_\mathrm{B}\eta) \approx 180\,\mathrm{nK}$.

Upper bound To get an upper bound one notes that at the beginning of the experiment the atomic clouds have a condensed fraction certainly above 50%, i.e. the initial number of thermal atoms is smaller than the initial number of condensed atoms: $N^i_\mathrm{th} < N^i$. As we know from the fits of the clouds before and after the experimental cycle, the atom number in the condensate drops by a factor of ≈ 2 during the experimental cycle, and the final number of condensed atoms is thus $N^f \approx N^i/2$, for both lattice periods $d_{1,2}$. The atoms missing must then either be part of the thermal cloud or have left the trap, and the final number of thermal atoms is $N^f_\mathrm{th} < N^i_\mathrm{th} + N^i/2 < 3N^i/2$. The fraction of condensed atoms at the end of the experiment is thus $N^f/(N^f_\mathrm{th} + N^f) > 1/4$, which gives the lower bound for the final condensed fraction. Using the measured number of condensed atoms and integrating the Bose distribution over the density of states in the lattice, one gets the upper temperature bound $T_\mathrm{max} \approx 500\,\mathrm{nK}$.

Since the number of thermal atoms is different at T_max and T_min (where losses in the total atom number are assumed), the two bounds correspond to different condensation temperatures T_c. The estimated temperature range is thus more clearly expressed in units of T_c, and for the small period lattice the cloud's temperature is in the range $0.65 \leq T_1/T_c \leq 0.9$, while for the large period lattice it is $0.55 \leq T_2/T_c \leq 0.9$. For both situations $k_\mathrm{B}T_{1,2} \gtrsim \hbar\omega_{1,2}$, so the thermal clouds are not fully in the 2D regime.

Chapter 5

Detection of phase defects in 2D condensates

The motivation for the production of 2D condensates lies in the coherence properties of such systems, that are very different from the 3D case (see chapter 3). While in a 2D homogeneous system a BEC can only exist at zero temperature, for interacting systems a transition to a superfluid phase exists at a finite T. This is the Kosterlitz-Thouless (KT) transition [38, 42, 43], which is associated with the unbinding of vortex-antivortex pairs. In the low temperature phase of the KT transition, the system is superfluid, but has a fluctuating phase. Part of these phase fluctuations can be described as bound vortex-antivortex pairs. On the high temperature side of the transition the pairs unbind, and the system enters the normal state.

As discussed in chapter 3, in a trapped 2D system Bose-Einstein condensation of an ideal gas occurs at a finite temperature. For interacting gases phase-coherent BECs were predicted and observed at low temperatures [16, 25, 80, 104, 127]. It is however not a priori sure, if the transition to the condensed state is a KT-type, or an "ordinary" BEC-type transition [79, 114]. To answer this question, several experiments have the objective to gain evidence for the existence of a KT-phase through the observation of vortex-antivortex pairs in trapped 2D atomic gases [25, 97, 127].

In this chapter an interferometric method for the detection of phase-defects in 2D ultracold clouds is presented. With this method it was possible to observe nontrivial phase defects in 2D quasi-condensates [5]. Even if these phase defects cannot be unambiguously identified as thermally activated vortices, there are strong indications that this is the most likely interpretation [115].

5.1 Interferometric detection of phase defects

In contrast to the density profile of a Bose-Einstein condensate, which is obtained directly by absorbtion imaging, information about the BEC's phase properties is in general only obtained through relatively elaborate techniques. Only some phase properties result in a distinct modification of the density profile after ToF, and can thus be extracted immediately from the signal obtained by absorption imaging. An example for such a phase configuration is a single vortex, which results in a zero in the cloud's wave function. In rotating clouds the resulting density dips are easily detectable after some time of flight expansion [128].

A more general method to access the phase properties of an atomic cloud relies on interference of the cloud, either with a "copy" of itself [129], or with an independently prepared sample [35]. The interference fringes then give access to the relative phase distributions of the clouds. This is the method used in our experiment for the investigation of the phase properties of the 2D condensates.

5.1.1 Experimental routine

The experiments for the interferometric detection of phase defects start with the preparation of a small array of 2D BECs, as described in chapter 4. This routine consists of selective rf evaporation of the atoms from all sites, except those in a frequency gap Δ. For the experiments presented in this chapter, the frequency gap is chosen to be $\Delta = n \cdot \delta\nu$, where $n = 2, ..., 8$. In the beginning of an experimental series the value of the gap is chosen carefully to contain exactly the wanted number of sites, using the calibration method presented in chapter 4. However, as the lattice might drift with respect to the magnetic trap during the series (which typically has a duration of 2 to 4 hours), this initial calibration might not be valid for all individual experiments. A frequency gap of $\Delta = n \cdot \delta\nu$ might thus contain $(n{\pm}1)$ lattice sites at the end of a series, instead of n. In the following paragraphs the given number of interfering sites[1] is thus always to be read as $\approx n$.

After the routine for selective evaporation the gradient b' is ramped to 0. In some experiments the clouds are then held in the lattice for a variable hold time τ_{hold}, before a time-of-flight (ToF) experiment is performed. In most of the presented experiments they are however released immediately after the end of the gradient ramp-down, and allowed to expand and overlap during a ToF duration of $12 - 18\,\text{ms}$, depending on the lattice period d. The resulting interference pattern is then recorded by absorption imaging along an axis perpendicular to the lattice axis (y), which corresponds to an integration of the pattern along y. The expected pattern for a periodic array of independent BECs with uniform phases consists of straight fringes [3, 35].

Because of the radial imaging, the choice of ToF duration is crucial. First, the optical density of the signal decreases strongly with ToF, due to the fast axial expansion (see chapter 4.3.3). Second, the first harmonic of the interference pattern has a period of $D = ht/(md)$, and the ToF duration t should be long enough to resolve this period well with an imaging resolution of $\approx 5\,\mu\text{m}$. In practice this means that $D \gtrsim 20\,\mu\text{m}$. The ToF duration must thus be chosen compatible with this condition, but as short as possible so that the optical density of the signal stays as high as possible at the same time.

This constraint leads to a situation where the first harmonic of the interference pattern is well resolved, while the higher harmonics are less visible. Each image can thus be approximated as the incoherent sum of the pairwise interferences of nearest-neighbor condensates (see chapter 6). One should note that the contrast of the first harmonic depends on the number of interfering clouds, as also described in detail in chapter 6. As tunneling between the sites is completely suppressed, the phases of the individual sites are not correlated. This reduces the expectation value for the contrast of the first harmonic in the case of more than two sites with uniform phases. For 8 clouds, which is the largest number used in the experiments, the expectation value for the first harmonic fringe contrast is however still $\approx 65\,\%$, and a high contrast should thus be visible in most experiments.

5.1.2 Experimental results

The discussion of the experimental results is organized following the number of sites that are spared from evaporation and allowed to interfere. The most spectacular results were obtained with 4-5 interfering clouds, which is the subject of the first paragraph (a), before interference of only 2 (b), or 6-8 condensates (c), is discussed.

---

[1] In section 4.3.2 the number of sites is calibrated as a function of the fitted atom number or optical density, which is derived from axial absorption imaging. In the experiments presented here, radial imaging was used, which has a less good signal to noise ratio, so that in general it is not possible to relate the number of sites unambiguously to the optical density.

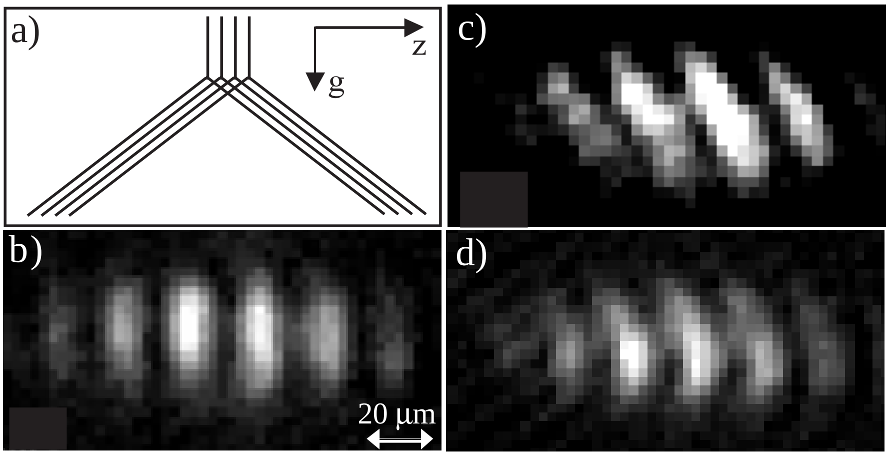

Figure 5.1: Interference of four independent BECs. (a) Four sites are selected from the $2.7\,\mu$m period lattice and allowed to overlap in 12 ms ToF expansion. The resulting interference pattern is observed by absorption imaging along the y-axis. (b) Straight interference fringes with high contrast appear in most experiments. (c)-(d) The observed straight fringes do not always have an angle of 90° to the z-axis. Angles between $\approx 60°$ to 120° with respect to the z-axis were observed (c), as well as slightly curved fringes (d).

a) Four to five interfering clouds

For the interference of a periodic array of condensates with uniform phases one expects an interference pattern consisting of straight fringes, with the period of the first harmonic being $D = ht/(md)$ [3, 35]. In a first series of experiments the lattice period was chosen as small as possible, that is $d = 2.7\,\mu$m. The time of flight duration is 12 ms, leading to a period $D = 20\,\mu$m for the first harmonic.

With these parameters we have in fact observed the expected straight interference fringes in 70 % of 200 images, and an example is shown in figure 5.1 (b). The fringes do not always appear with an angle of 90° to the z-axis, but also with angles between $\approx 60°$ to 120° (figure 5.1 (c)). These angles reflect simple phase gradients in one or some of the interfering clouds, thus indicating small radial velocities. We have also seen slightly curved fringes (figure 5.1 (d)), which we also did not classify as topologically different from straight fringes.

We have however also observed topologically different patterns, which contain a dislocation line along the z-axis of the clouds. The most striking examples for this kind of pattern are “zipper” patterns, where the spatial phase of the interference pattern changes by π across a line parallel to z, and the contrast on both sides of this line is as high as in a “normal” interference

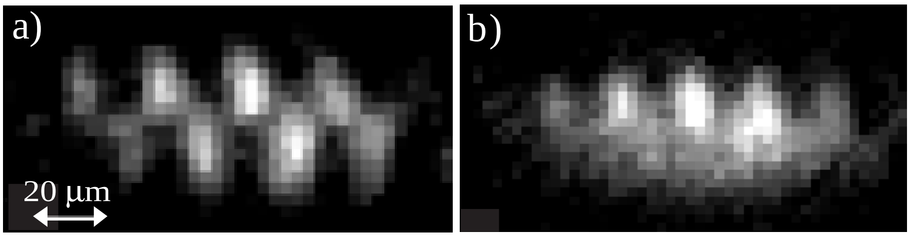

Figure 5.2: Interference patterns of four independent BECs. Dislocation lines in the pattern’s phase (a) or contrast (b) reveal the presence of phase defects in quasi-2D condensates.

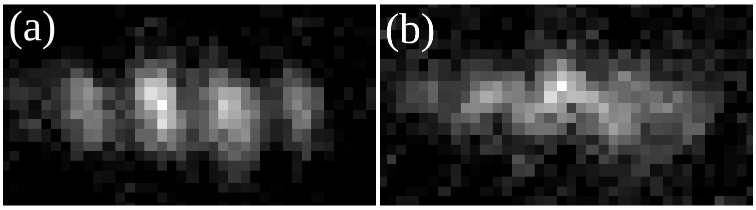

Figure 5.3: Interference of two independent BECs. Two sites are selected from the 2.7 μm period lattice and allowed to overlap in 12 ms ToF expansion. (a) The signal to noise ratio is in general not as good as in the experiments performed with four clouds (figures 5.1 and 5.2). Straight interference fringes are nevertheless clearly detectable. (b) The only type of dislocation line observed with 2 clouds is the "zipper" pattern.

pattern consisting of straight fringes. Such a zipper pattern is shown in figure 5.2 (a). We have also observed a second type of dislocation line, which does not separate zones of different fringe phase, but of different fringe contrast: The contrast is high on one side of the line, and vanishing on the other. Such a "comb" pattern is shown in figure 5.2 (b).

A clear dislocation line (either a "zipper" or a "comb") is clearly distinguishable in $\approx 15\%$ of 200 experiments with four interfering clouds. Another 15 % of images show significantly reduced contrast, or patterns which are hard to classify.

Dependence on the lattice period
The same kind of experiment was performed with a larger lattice period, $d = 5.1\,\mu$m and a ToF duration of $t = 18$ ms. The expected period for the first harmonic is then 16 μm. In this case patterns with a sharp dislocation line appeared in 10 % of 100 images. This number is comparable to that obtained with the smaller lattice period $d = 2.7\,\mu$m, even if in the small period lattice the clouds are deeper in the 2D regime (see chapter 4.1.3).

Letting the clouds equilibrate before performing ToF
Experimental series with an additional hold time τ_{hold} of 200 to 500 ms in the lattice have also been performed. This hold time takes place after the ramp-down of the gradient b', and before the ToF expansion. In these experiments zipper and comb type patterns were observed for all used τ_{hold}. A statistical analysis on the probability of such patterns did not show a significative dependence on the hold time. The existence of phase defects after long equilibration times proves that these defects are not a transient effect provoked by the evaporation routine.

b) Two interfering clouds

We have performed the same kind of interference experiment as described above with only two interfering clouds. In general the signal to noise ratio is not as good as in the case of four clouds, due to the low atom numbers and the fast axial expansion.

Nevertheless straight interference fringes are distinguishable in about ≈ 30 % of 94 images, of which an example is shown in figure 5.3 (a). In only one of the 94 images a zipper-type pattern is distinguishable (figure 5.3 (b)). ≈ 70 % of all images show however too low contrast to be classified in one of these two categories. For this reason the series with only two interfering clouds was not taken into account for the statistical analysis of the observed dislocation events.

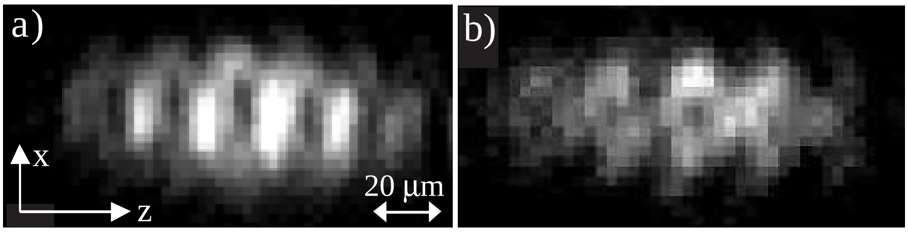

Figure 5.4: Interference of eight independent BECs is observed 12 ms after release from the 2.7 μm period lattice. A new type of pattern appears in these experiments, showing two dislocation lines along z, and over each line the fringe phase changes by π.

c) Seven to eight interfering clouds

When performing interference experiments with 7-8 clouds, the general interpretability of the patterns is more difficult than in the case of only 4-5 interfering clouds. A careful statistic analysis was thus not carried out.

In 3 of the ≈ 20 images one can however spot a new clearly distinguishable structure, that has not been observed in the experiments with less interfering clouds. This structure has two dislocation lines, and the phase of the fringes changes by π across each dislocation line. Two examples of this "braid" structure are shown in figure 5.4.

5.2 Interpretation of the interference pattern

In this section some possible phase configurations are presented, that might be at the origin of a sharp dislocation line in the interference pattern. The phase configuration that is considered in most detail, is that of a centered vortex in one of the interfering clouds. Its effect on the interference pattern is discussed qualitatively in part 5.2.1, while part 5.2.2 shows numerical simulations for an idealized experimental situation.

One should however keep in mind that one cannot unambiguously derive the underlying phase configuration from an integrated interference pattern. This means that even if the presence of a vortex in one of the interfering clouds can explain the observed patterns, there are other phase configurations that lead to patterns of the same visual appearance. Some of these are discussed in section 5.2.3.

5.2.1 Expected pattern for a vortex in one of the clouds

The simplest phase configuration that can explain the appearance of sharp dislocation lines is a vortex in one of the interfering clouds. In fact the appearance of single dislocations - even if not dislocation lines - was observed already in the case of two "radially interfering" BECs, of which one contained a vortex [109, 129–132].

To gain some intuition for this effect in our experimental situation of "axially interfering" clouds, the discussion is first restricted to the case of two interfering condensates (a). In paragraphs (b) and (c) larger numbers of clouds are considered.

a) Interference of two clouds

The integrated interference pattern of two BECs with arbitrary uniform phases, initially separated by a distance d on the z axis, and expanding and overlapping along the z-axis, shows a

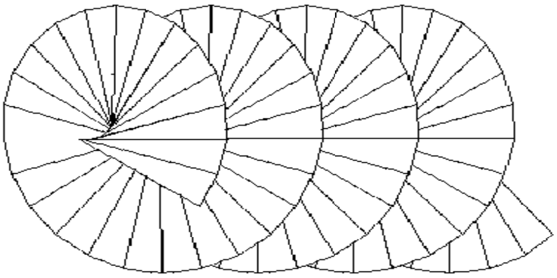

Figure 5.5: Schematic 3-dimensional interference pattern for the "axial" interference of two BECs, of which one contains a centered vortex.

modulation of (see chapter 6)

$$F(z) = 1 + \cos(2\pi z/D + \phi),$$

where $D = ht/(md)$, and ϕ is the relative phase between the two BECs.
We now consider a phase configuration, in which one of the interfering clouds has a uniform phase (chosen as 0), and the other contains a centered vortex, corresponding to a phase winding of 2π in the x-y-plane of the cloud. The phase of the expected interference pattern then depends on the angle θ in the x-y-plane (for an illustration see figure 5.5):

$$\begin{aligned} F(x,y,z) &= 1 + \cos(2\pi z/D + \theta) \\ &= 1 + \left[\cos(2\pi z/D) \cdot \frac{x}{\sqrt{x^2+y^2}} - \sin(2\pi z/D) \cdot \frac{y}{\sqrt{x^2+y^2}}\right] \end{aligned}$$

This interference pattern is recorded by absorption imaging along the y-axis. If one assumes the clouds to have a homogeneous density distribution with radius R in the x-y-plane, the observed signal $A(x,z)$ is proportional to $\int_{-R}^{R} F(x,y,z)\, dy$. This leads to:

$$A(x,z) \propto 2R + \tilde{a}(x)\cos(2\pi z/D), \qquad \text{where} \qquad \tilde{a}(x) = x \cdot \int_{-R}^{R} \frac{1}{\sqrt{x^2+y^2}}\, dy.$$

One can see immediately that the amplitude of the cosine modulation $\tilde{a}(x)$ is 0 on the line $x = 0$. For $x \neq 0$ the amplitude is antisymmetric in x, i.e. $\tilde{a}(-x) = -\tilde{a}(x)$. The phase of the modulation $A(x,z)$ is thus different by π for $x > 0$ and $x < 0$ respectively, and a maximum at $x > 0$ corresponds to a minimum at $x < 0$ and vice versa. The absolute value $|\tilde{a}|$ and the sign of the amplitude $\tilde{a}/|\tilde{a}|$ are plotted as a function of x in figure 5.6 (a) and (b) respectively.

Even if this model does not take into account some features of the experimental situation - in the model the cloud with the vortex has no density dip at $(x,y) = (0,0)$, while a real vortex does - it reproduces the main feature of the observed zipper patterns, which is a dislocation line of vanishing contrast, across which the fringe phase changes by π.

In the case of two interfering BECs this zipper pattern is also the only pattern that can result from a phase configuration containing a centered vortex. This result is confirmed by the simulations presented in section 5.2.2, and agrees with the experimental observations: indeed a zipper pattern is the only kind of dislocation that was observed when letting interfere two clouds (see section 5.1.2(b)).

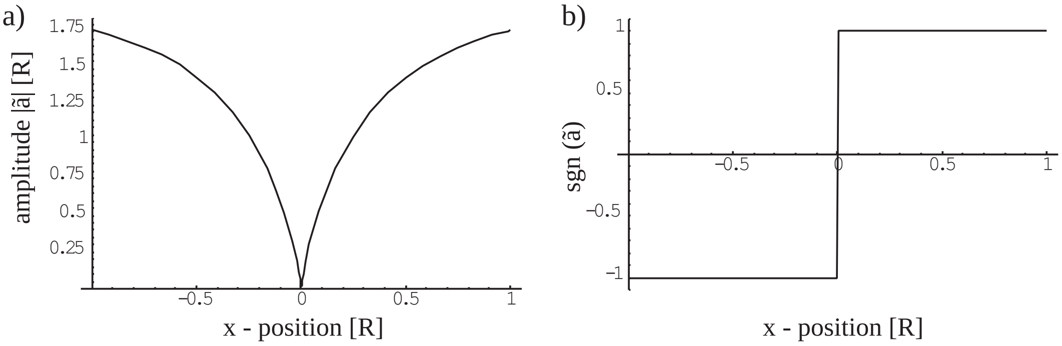

Figure 5.6: Expected absolute value (a) and sign (b) of the amplitude of the interference pattern as a function of the radial position x. One can clearly see the absence of modulation at $x = 0$, which corresponds to the observed dislocation line, and the π-shift in phase from $x < 0$ to $x > 0$.

b) Three or four interfering BECs

To explain the observed "comb" patterns, one needs to assume that more than 2 clouds interfere. Indeed this kind of pattern was only observed in the experiments of 4 to 8 interfering clouds. The general analysis of paragraph (a) cannot be easily extended to larger number of interfering clouds, as in this case the phases of all clouds not containing the vortex are arbitrary. One can however look closer at some instructive examples, where the uniform phases of the BECs have the value 0 or π with respect to an arbitrary reference phase. In figure 5.7 this case is illustrated for 3 interfering BECs, of which one contains a vortex.

In the cases of all phases being set to 0 or π, the analysis of paragraph (a) can be easily extended to the case of three condensates. As we consider only the first harmonic of the interference pattern, this case can be described by the sum of the two pairs of neighboring sites. In the case of a phase difference π between the neighbors, the sign of the amplitude $\mathrm{sign}(\tilde{a}) \equiv \tilde{a}/|\tilde{a}|$ is -1, while it is $+1$ for a phase difference 0.

If the two interfering pairs lead to fringes with a phase difference π, the total first harmonic of the pattern vanishes, while in the case of identic phases its amplitude stays large. The possible combinations shown in figure 5.7 can thus lead to vanishing contrast in both halves of the cloud (a), high contrast in both halves of the cloud, with a phase shift π between the two halves (b) and vanishing contrast in one of the cloud's halves (c)-(d). This last case corresponds to the comb pattern as shown in figure 5.2 (b).

With this model it can be easily explained how a comb pattern can arise when 4 or 5 BECs interfere. In the case of 4 condensates one can for example achieve low contrast in the upper half, compared to perfect contrast in the lower half, when adding one more condensates with a uniform phase 0 to the configuration of figure 5.7(d). In an experiment this difference in contrast might well lead to the appearance of a "comb".

The phase configurations used in figure 5.7 are of course only the limiting cases to the large number of possible combinations if the phases have arbitrary values. In these cases the contrast on one side can be more or less reduced. To obtain an estimate for the probability of a zipper or comb pattern to be clearly distinguishable from straight fringes, one has to perform simulations where arbitrary phases are assigned to the BECs. This kind of simulations and the resulting conclusions are presented in section 5.2.2.

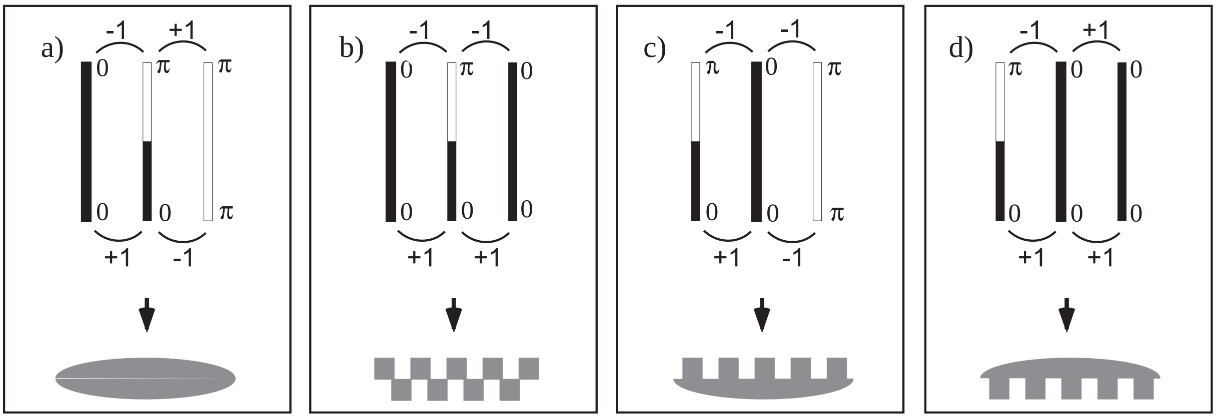

Figure 5.7: Phase configurations for 3 BECs of which one contains a vortex, and the others have uniform phases of value 0 or π compared to an arbitrary reference phase. The expected interference pattern after integration along y can then be a zipper with large contrast on both sides of a dislocation line (b), a comb with vanishing contrast on one side (c)-(d), or show no contrast on both sides (a).

c) Many interfering BECs

Increasing the number of interfering BECs enhances the probability that some of them contain defects. This might be the reason why the braid patterns with two dislocation lines were observed only with more than four clouds. A simple explanation for this kind of pattern consists in assuming that two of the interfering clouds contain a vortex. The probability of this event grows of course with the number of interfering clouds.

However, the interpretation of images also becomes increasingly difficult the more BECs interfere. Also, the effect of a single defect on the interference pattern decreases. As a defect in one of the clouds affects only the interference with the two neighboring BECs, it is likely to be washed out by the contributions of the other pairs.

5.2.2 Simulations of interfering condensates containing phase defects

As shown above, interference of two BECs of which one contains a vortex, always leads to a zipper type pattern. In the case of more than two condensates it is less clear with what probability a phase configuration containing a vortex leads to a visually distinguishable dislocation line, due to the arbitrary uniform phases of the individual condensates. To obtain an estimate for this probability, numerical simulations with different numbers of interfering clouds were performed by Baptiste Battelier [133].

For these simulations the wave function of the system is modeled as the sum of spherical gaussian wave-packets with widths $\sigma = d/8$ and the distance d between two clouds. A phase factor $e^{i\varphi} = (x + iy)/(x^2 + y^2)^{1/2}$, corresponding to a single vortex, is assigned to the wave-function of one arbitrarily chosen cloud, while the other clouds have arbitrary uniform phases. Then a 3D Fourier-transformation of this system is performed, to simulate the ToF-expansion. The resulting 3-dimensional pattern is integrated over the y-axis, and then convolved with a Gaussian of 4 μm width, to account for the absorbtion imaging and the finite imaging resolution.

Statistics of distinguishable zipper and comb patterns:
In the simulations with four clouds about half of 100 simulations with a vortex show clear zipper- or comb-type dislocations. The other half shows weaker dislocations (of a phase shift

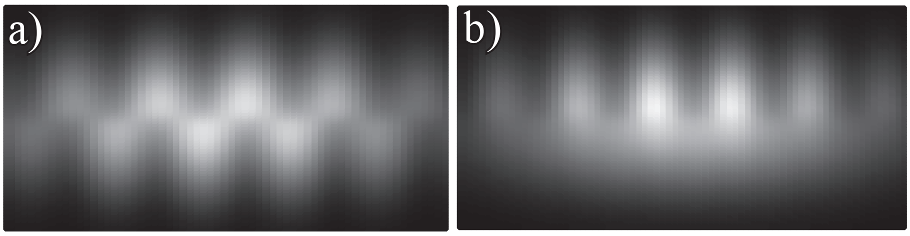

Figure 5.8: Examples of numerical simulations of two (a) and four (b) interfering condensates. In both cases one randomly chosen BEC has a phase factor $e^{i\varphi}$ corresponding to a centered vortex, and the others have randomly chosen uniform phases. For simplicity, the clouds are modeled as gaussian wave packets and interactions are neglected during the expansion. The images are convolved with a gaussian of $4\,\mu$m rms width to simulate the finite imaging resolution.

$< \pi$) which are not easily distinguishable from straight interference fringes, or reduced contrast in both halves of the pattern.

If one assumes that the observed dislocations result from the presence of vortex in one of the interfering clouds, one can use the result of the simulations to estimate the probability that one of the 2D BECs contains such a phase defect. In experiments with ≈ 4 sites $15\,\%$ of all images show a clearly distinguishable comb or zipper pattern. As only in half of all simulations with a single vortex such a clear signature appears, one can conclude that such a phase defect is present in $30\,\%$ of all experiments. Given that the experiments are performed with ≈ 4 sites, this means that $\approx 7.5\,\%$ of all produced 2D BECs contain a vortex.

Examples of simulated patterns:
Examples of numerical simulations for two or four interfering clouds (of which one contains a vortex) are presented in figure 5.8 (a) and (b) respectively. The model used for these simulations does not take into account all of the properties of the experimental situation. So does it not consider any interaction effects during expansion. In spite of its simplicity it seems however to capture the essential features of the experimental findings, which is suggested by the similarity of the simulations presented in figure 5.8 to the experimental images (figures 5.3 (b) and 5.2(a)-(b)). As already stated, this does however not strictly speaking imply that our experimental results prove the presence of vortices, as will be discussed in the following section.

5.2.3 Discussion of other possible phase configurations

Despite the agreement between simulations involving one or several vortices and the observed patterns, one should keep in mind that it is in general not possible to unambiguously deduce the underlying phase configuration from an interference image. This is even less the case when information about one of the spatial directions is missing, due to the integration over a given direction.

Another possible phase configuration that leads to a single dislocation line is for example a dark soliton, where the phase of one of the BECs changes by π across a line parallel to the imaging axis. The explanation how this could lead to a zipper or comb pattern, works along the same argumentation as presented for the vortex in sections 5.2.1(a)-(b), with only small modifications. Correspondingly, the results of simulations performed with either a vortex or a dark soliton phase configuration, are not distinguishable by eye. For the appearance of two dislocation lines could then account two dark solitons, not necessarily in the same cloud. However, while dark solitons were observed to be stable in 1D systems [134], they are expected to decay in vortex-antivortex pairs via the snake instability in 2D systems [135]. Also the energy needed to create a dark soliton in a 2D system is higher than that of a vortex-antivortex pair or single vortex [115]. Note however, that solitons are only another example for possible phase configurations, and one might think of many other possible solutions.

Simultaneous imaging along a second radial direction could make it possible to discriminate between some of these possible phase configurations (e.g. between a vortex and a soliton in one of the clouds). It is planned to provide such simultaneous imaging in future experiments.

5.3 Axial imaging: Possibility for vortex detection in 2D clouds

A clear evidence for vortices could be provided, if a density dip was observed in the axial image of individual 2D condensates. To obtain such images, single condensates were separated from the lattice, and allowed to expand for varying durations between 6 and 20 ms. In the absorption images along the axial direction z however no clear signature of vortices could be spotted.

It might be possible that this method of vortex detection is in general difficult in freely expanding 2D clouds. The following paragraphs discuss some relevant aspects of the problem. However, no exact calculations exist on the expected vortex expansion in this situation.

5.3.1 3D expansion of a quasi-2D gas

So far the expansion of a vortex core in an initially 2D system was studied theoretically only for the case of a purely two-dimensional expansion [72, 94, 95]. In this case the vortex core size increases at the same velocity as the cloud's size, and the vortex is well resolvable by absorbtion imaging after usual ToF durations.

For 3-dimensional free expansion, as in our case, no calculations for initially 2D systems exist. However calculations for 3D systems with different aspect ratios [136] were performed. According to these the relative expansion velocities of a vortex core and the radial cloud diameter depend strongly on the trap geometry. If the initial confinement is a cigar shaped trap, the vortex core size and the radius of the cloud increase nearly at the same velocity, following the expected scaling for the solutions of the Gross-Pitaevskii equation [72, 94, 95]. In the case of a initially pancaked shaped trap, the vortex core size is however expected to increase much faster than the cloud's radius, until the ratio of core size and cloud radius reaches a final value of ~ 0.3. The more the cloud is pancake shaped in the beginning, the faster this value is reached during ToF. Note however, that the numerical calculations in [136] are carried out only for trap anisotropies $\omega_z/\omega_\perp$ up to 2.5, while this parameter in our experimental situation is of the order of $20 - 40$.

The value of ~ 0.3 for the ratio of core size and cloud radius corresponds to the result for a freely expanding noninteracting 3D gas [136]. Accordingly, when using the model simulation described in section 5.2.2 for a single site, the size of the vortex core corresponds to ≈ 0.3 times the cloud's size after the Fourier transformation. When integrating the Fourier-transformed density over the z-axis, thus simulating axial imaging, a density dip is clearly visible. Such an ideal gas model does not however fully correspond to the experimental situation. Even if the influence of the interactions should vanish fast during the axial expansion (see chapter 4.3.3), a more detailed analysis of this regime is needed to gain quantitative insight on the possibility for vortex detection in freely expanding 2D gases.

5.3.2 Experimental difficulties for vortex detection

In rotating 3D systems vortices are readily detected after ToF (see e.g. [128] and part III). Such systems expand however mostly radially, while the 2D clouds in our experiment expand mostly axially (section 4.3.3). This expansion could be a reason why no vortices were detected after expansion of the 2D clouds. Due to the large aspect ratio of the vortex line, a small misalignment with the imaging axis can lead to a significant reduction of the contrast, making the expected density dip much less pronounced[2].

A further difficulty of our specific setup probably lies in the limited addressability of the lattice sites. As discussed in chapter 4.3.2, the finite chemical potential and temperature of the individual 2D BECs do not allow to keep one single site while completely emptying the neighboring ones. Even if the atom number in the neighboring sites is only a fraction of a full site's atom number, the contribution of several sites decreases the contrast of density dips in any of them.

Even if the addressability of our setup might be improved in the future, and the relevance of the other mentioned considerations for our experimental situation is yet to be studied, it becomes clear that axial vortex detection in expanding 2D condensates might be a difficult task. With respect to this problem interferometric detection along a radial direction offers a fundamentally superior signal, because a localized defect affects the appearance of the whole image.

5.4 Probability of thermal vortex configurations

As discussed above, a single vortex in one of the clouds is one of the phase configurations that can explain the observed experimental patterns. As vortex or vortex pair configurations are expected to be observed in a Kosterlitz-Thouless (KT) phase of the 2-dimensional system, it is interesting to confront our experimental parameters with the estimates for the KT transition, as presented in chapter 3.

5.4.1 Probability of a single vortex in a 2D gas

The probability to thermally excite a free vortex in a system is proportional to $\exp[-F_{vx}/(k_\mathrm{B}T)]$, where F_{vx} is the free energy of the vortex. The free energy of a single vortex F_{vx} in a 2D system of radius $R_\perp$ and superfluid density n_s can be estimated to (chapter 3 and [109]):

$$F_{vx}/(k_\mathrm{B}T) \approx \frac{1}{2}\left(n_s\Lambda_\mathrm{dB}^2 - 4\right)\ln\left(\frac{R_\perp}{\xi}\right),$$

where ξ is the healing length.

For the 2D condensates in the short period lattice ($d = 2.7\,\mu$m) the relevant experimental parameters are (see chapter 4): $R_\perp \approx 6\,\mu$m, $\omega_z/(2\pi) \approx 4\,$kHz, $\mu/h \approx 2\,$kHz, and $T \approx 200 - 500\,$nK. For the average superfluid density $\bar{n}_s$ of the parabolic density profile of our clouds this gives $\bar{n}_s\Lambda_\mathrm{dB}^2 \approx 10 - 25$, depending on the assumed temperature, while the free energy for single vortices in uniform systems vanishes for $n_s\Lambda_\mathrm{dB}^2 = 4$. As discussed in chapter 3, the estimate $n_s\Lambda_\mathrm{dB}^2 = 4$ gives only an upper bound for the transition temperature, as it does not include the influence of vortex-vortex interactions. The transition temperature should in fact be significantly smaller when taking into account such interactions.

As the energy of a single vortex is lowered by the surrounding tightly bound vortex-antivortex pairs, the temperature above which the creation of pairs becomes probable also plays an important role. The free energy of tightly bound vortex-antivortex pairs F_{vp} can be estimated to

$$F_{vp}/(k_\mathrm{B}T) \approx \frac{1}{4}n_0(0)\Lambda_\mathrm{dB}^2 - 2\ln\left(\frac{R_\perp}{\xi}\right).$$

For our experimental parameters $\xi \approx 0.2\,\mu$m, $R_\perp \approx 6\,\mu$m, and $\ln(R_\perp/\xi) \approx 3.5$. Depending on our temperature estimates, $F_{vp}/(k_\mathrm{B}T)$ has thus a value between 2.5 (if $T = 200\,$nK) and -3 (if

---

[2] This problem could eventually be overcome in an experimental setup that allows for purely radial expansion of the 2D cloud (e.g. as described in [25]).

$T = 500\,\mathrm{nK}$). The existence of thermally excited tightly bound vortex-antivortex pairs in our system is thus not unlikely (see also figure 3.4).

The presence of only tightly bound pairs is not sufficient to explain our experimental observations. As the distance between the two vortices in such a pair is of the order of ξ, they cannot be resolved by our imaging system. The presence of tightly bound pairs has however a large effect on the energy of loosely bound pairs or single vortices, which is lowered through screening by the tightly bound pairs (see chapter 3.3.2(c)). The presence of tightly bound pairs thus makes the presence of such detectable defects more likely.

5.4.2 Simulations regarding our experiment

The above estimates are not very accurate, as they do not take into account either the position dependent density $n = n(\boldsymbol{r})$ of the system, or the vortex-vortex interaction. These subjects are not easily treated analytically, but might be studied numerically.

In a very recent publication our experiment was the subject of numerical calculations, using ab initio classical field simulations [115]. For our experimental parameters the authors found that indeed vortex-antivortex pairs of different sizes are present in the 2D condensates. Examples of the radial density distribution of such clouds before time of flight expansion are shown in figure 5.9 (b) and (c). In the figures the vortices and antivortices are labelled with a "+" or a "−"-sign respectively. One can clearly see that the distances between the two vortices of a pair varies considerably, and the two defects are not necessarily in regions of the same condensate density. The cloud in figure (b) even has a single vortex in its center. The authors of [115] explain the existence of this vortex by the dissociation of a vortex pair. According to their results such seemingly independent vortices should appear in the higher temperature region of the KT-phase, as the energy cost for the dissociation of a pair is comparable to the cost for the creation of a new pair.

When letting the two clouds interfere, the single vortex in the center of one of the condensates has the biggest effect on the interference pattern. The tighter bound pairs at the edges of the cloud do not have a significant impact on the interference pattern. The shown clouds thus represent possible phase configurations that would lead to a zipper pattern.

5.4.3 The mesoscopic nature of our system

The free energy of a single vortex has a logarithmic dependence on the ratio between the size of the system and the size of the vortex core $R_\perp/\xi$. In the thermodynamic limit $R_\perp \to \infty$, and on one side of the phase transition the cost of a free vortex becomes infinite, while on the other side a large density of free vortices appears.

In the case of a finite system, this ratio stays also finite, and for our trap parameters $\ln(R_\perp/\xi) \approx 3$. This value is not large compared to 1, and this fact underlines the mesoscopic nature of the system. More concretely this means that the phase transition should be replaced by a gradual increase of the average number of free vortices with temperature. For $F_{vx}/k_\mathrm{B}T \sim 1$ the number of free vortices should then show large fluctuations and two condensates produced under identical experimental conditions can have qualitatively different wave functions.

5.5 Conclusion

In this chapter the observation of nontrivial phase defects in quasi-2D BECs was described. This was achieved using an interferometric method. Even if the interference patterns cannot be unambiguously connected to a distinct phase configuration of the clouds, there are strong hints that the presence of vortices is at the origin of the observed patterns. Such indices are the non

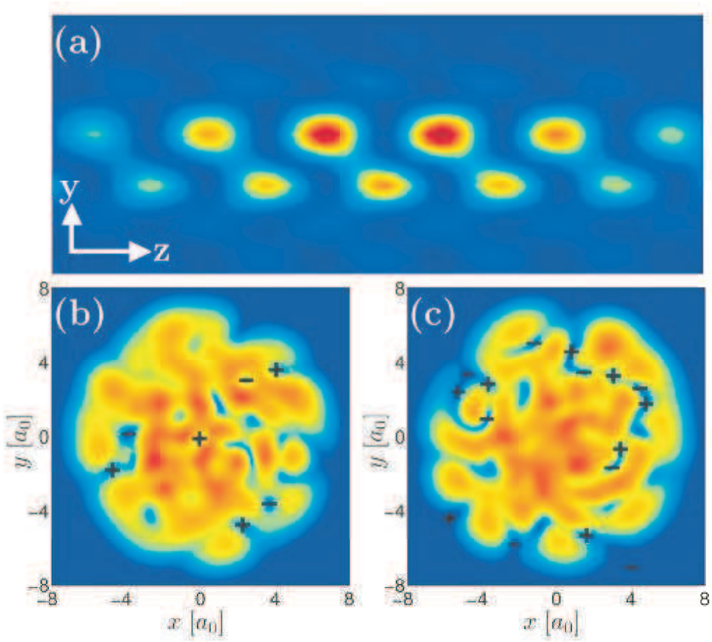

Figure 5.9: Interference pattern (a) produced by two independent clouds (b) and (c) at temperature $T/T_c = 0.93$. The zipper structure in (a) is the telltale signature of the phase singularity associated with the central vortex in (b). Figures (b)-(c) show the density distribution in the x-y plane before time of flight expansion. Figure from [115], color online.

negligible excitation probability for vortex-antivortex pairs in our experimental situation, and recent numerical studies on this subject [115].

Chapter 6

Interference of 30 independent condensates

In the experiments presented in chapters 4 and 5 an optical lattice was used to realize individual 2D condensates. The realization of low-dimensional quantum gases is however only one of the applications of optical lattice potentials [21, 22, 118]. More often atomic gases in optical lattices are used to model solid state systems. This is due to their comparability to an electron gas in a periodic potential, and to the great tunability of a optical lattice system: the lattice height and period can be tuned to (nearly) arbitrary values, and the main parameters of the model system are thus tunable at will.

When using lattice systems to explore properties of corresponding solid state systems, one is less interested in the characteristics of the individual sites, but instead in those of the full sample, including the tunneling connections between the sites. As those are tunable with the lattice height, one can for example gradually drive the transition from a superfluid to an insulator by increasing the lattice height. This way the quantum phase transition to a Mott-insulator could be monitored in an atomic gas trapped in an optical lattice [34, 137–139].

The most commonly used probes of atomic gases in optical lattices are the interference patterns obtained when the gas is released from the lattice, so that the wave packets emanating from different lattice sites expand and overlap. Commonly the appearance of high-contrast interference fringes in the resulting density distribution is associated with the presence of phase coherence between the different lattice sites. Accordingly the disappearance of the fringes is often seen as a sign for the loss of phase coherence [32, 73, 118, 140]. This correlation - even if right under certain circumstances - is however not fundamental. The work presented in this chapter contains a thorough experimental and theoretical study of the interference of a regular array of BECs, which generalizes the previous analysis for two independent condensates [36, 141, 142]. Contrarily to what could be naively expected, it is shown that interference of many BECs with random relative phases can lead to high-contrast fringes [3].

6.1 Experimental routine

The experiments start with an almost pure ^{87}Rb condensate with 3×10^5 atoms, in a Ioffe-Pritchard trap with harmonic trapping frequencies $\omega_\perp/2\pi = 74\,\mathrm{Hz}$ radially, and $\omega_z^{(0)}/2\pi = 11\,\mathrm{Hz}$ axially. A 1D-optical lattice along the z-direction is then superimposed to the magnetic trap. The parameters of the lattice potential are given in chapter 4, and only the most important properties are repeated in the following:
The lattice potential is

$$U(z) = U_0 \cos^2(\pi z/d), \tag{6.1}$$

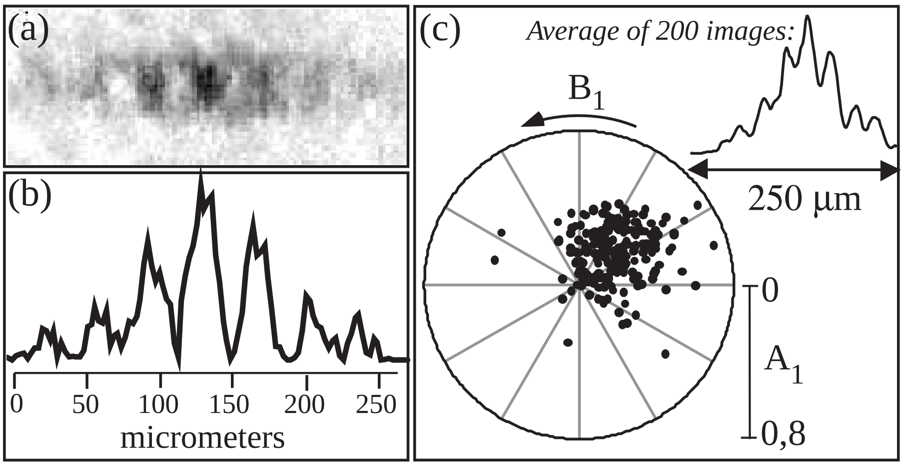

Figure 6.1: Interference of Bose-Einstein condensates with correlated phases: The lattice potential is ramped up in 3 ms, and the clouds are released from the trap without additional hold time, so that their phases do not diffuse away from each other. (a) Absorption image after 22 ms expansion of the clouds. (b) Axial density profile of the cloud, radially averaged over the central 25 μm. (c) Polar plots of the fringe amplitudes and phases (A_1, B_1) for 200 images. Inset: Axial density profiles of the cloud, averaged over the 200 images.

with the lattice depth at full laser power equal to $U_0/h \approx 50\,\mathrm{kHz}$. For the experiments described in this chapter we have used a lattice period of $d = 2.7\,\mu\mathrm{m}$, which corresponds to ~ 30 equally spaced condensates of $\sim 10^4$ atoms in the central sites. At maximum lattice depth the calculated oscillation frequency along z in each lattice site is $\omega_z/(2\pi) = 4\,\mathrm{kHz}$, and the gas at each site is in a 2D regime. The density distribution of each BEC along z is given by a Gaussian with a standard deviation $\ell = \sqrt{\hbar/(2m\omega_z)} = 120\,\mathrm{nm} \ll d$. Thanks to the long lattice period and the large height of the potential barrier between the sites, the condensates can be completely isolated from each other.

In a typical experiment the lattice height is ramped up to $600\,E_R$ (with $E_R/h = 80\,\mathrm{Hz}$) in a variable ramp time τ_{ramp}. This creates ~ 30 condensates separated by the lattice potential. These condensates share their common phase for a short time. However, due to the absence of tunneling they evolve independently in the different wells, where atom number and chemical potential vary due to the magnetic trapping along the z-axis. This results in a fast dephasing of the BECs (see section 6.2.2).

The atoms are hold in the lattice for a variable hold time τ_{hold}, before the optical and magnetic trapping potential are simultaneously switched off. After $t = 22\,\mathrm{ms}$ of free expansion the cloud's density distribution is recorded by absorption imaging along an axis perpendicular to the lattice axis (y).

6.1.1 Fitting routine

A typical example for an interference pattern is shown in figure 6.1(a). From this image the axial density profile is extracted, by averaging the radial density over the central 25 μm. The density profile (see figure 6.1(b)) is fitted with the function

$$Y_{\mathrm{fit}} = [1 + A_1 \cos(B_1 + 2\pi z/D)]\, G(z) \tag{6.2}$$

where $G(z) = A_g \cdot e^{-2(z-z_0)^2/Z_0^2}$ is a Gaussian envelope. This procedure extracts the first harmonic of the modulation of the density distribution. For a series of experiments with identical experimental parameters, the fitting routine consists of two parts:

1. The density profiles of all images are fitted with function (6.2). This attributes values of $A_1^{(i)}$, $B_1^{(i)}$ and $D^{(i)}$ to the individual images i. The found periods $D^{(i)}$ are then averaged.
2. In a second run of the fitting routine the period is fixed to the average value D, and only the amplitude $A_1^{(i)}$ and phase $B_1^{(i)}$ of the fringes are used as free parameters.

The results obtained with this method are presented in the following for phase coherent and incoherent condensates.

6.2 Experimental results

The interference of an array of phase-correlated condensates has been a subjects of thorough studies [32, 118, 140]. The result of this kind of interference is well known: one expects interference fringes with a spacing $D = ht/(md)$, a contrast of $A_1 = 100\,\%$ and a fixed spatial phase B_1. Knowing this we could use experiments with phase coherent condensates to test the stability of our setup, which is the subject of the first paragraph of this section. In the following paragraphs the dephasing between the individual condensates, and interference between completely independent condensates are discussed.

6.2.1 Fringes of correlated BECs

In a first series of experiments the lattice height was ramped up in $\tau_{\mathrm{ramp}} = 3\,\mathrm{ms}$. Without any wait time the BECs were released from the trap. During the short ramp time the phases of the BECs should not completely diffuse away from each other, so that the 30 condensates are still phase correlated. This experiment was repeated 200 times.

When fitting the images with function (6.2), a fringe period of $D = 39.0\,(\pm 2)\,\mu\mathrm{m}$ was found. This is in agreement with the expected value $ht/(md) = 37\,\mu\mathrm{m}$. As described above, the images were then fitted again, with the fringe period set to D. The obtained fringe phases B_1 and amplitudes A_1 are shown in the polar plot in figure 6.1(c).

As one can see from the angular distribution in the polar plot, the fringe phases B_1 are not randomly distributed over the full circle. Their distribution has a standard deviation of $43\,^\circ$, which is significantly smaller than the standard deviation of $\sim 104\,^\circ$ of a random distribution [28]. The stability of the phase can also be quantified in terms of the fringe contrast in the average of the 200 density profiles (inset it figure 6.1(c)). In our experimental situation this averaged density still shows clearly visible fringes, with a contrast $A_1 = 27\,\%$.

Finite distribution of the phase

The stability of the fringe phase is however not perfect, which is due to position fluctuations of the different parts of the experimental setup (magnetic trap, lattice mirrors, camera). To estimate the general stability of the experimental setup we performed a series of 200 experiments under identical conditions. In this series condensates were released from the magnetic trap, without applying the optical lattice. The standard deviation of the position of the BECs after ToF is $\delta z_0 \approx 3.5\,\mu\mathrm{m}$. These fluctuations can be due to either relative position fluctuations of the camera and the magnetic trap, or momentum fluctuations of the BECs caused when the magnetic trap is turned off.

If one supposes them to be due to relative position fluctuations, one can conclude that they result directly in fluctuations of the fitted phase B_1, which is measured with respect to the frame of the image (and not with respect to the center of the gaussian envelope). In this case the width of the fluctuations corresponds to $\delta z_0 \approx D/11$ (for a fringe period $D = 39\,\mu\mathrm{m}$), which results in a standard deviation of the phase of $360\,^\circ/11 \approx 32\,^\circ$. It is thus possible that already relative

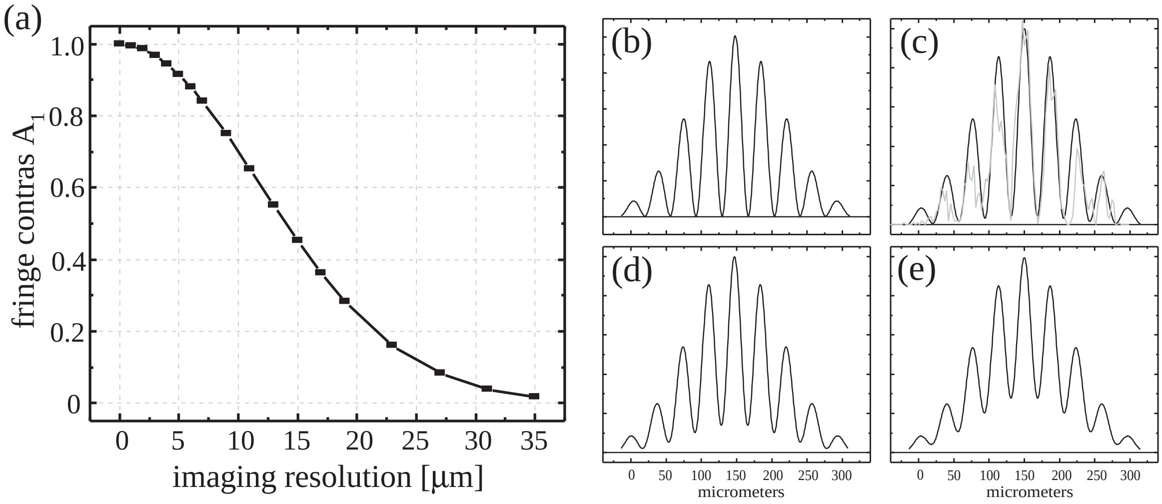

Figure 6.2: Influence of the imaging resolution on the contrast of the imaged interference pattern. (a) Fringe contrast A_1 of an interference pattern with period $D = 38\,\mu$m as a function of the imaging resolution w. (b)-(e) Black lines: Simulations of an interference pattern with 100 % contrast, when imaged with finite imaging resolutions w (equation (6.3)). The imaging resolution is (b) $w = 1\,\mu$m, (c) $w = 5\,\mu$m, (d) $w = 9\,\mu$m, (e) $w = 13\,\mu$m. In figure (c) the experimental data from figure 6.1(b) is added to the graph (grey line).

position fluctuations of the camera and the magnetic trap account for a large part of the finite phase distribution of standard deviation 43 °. Assuming that the relative position fluctuations of the lattice with respect to both the camera and the magnetic trap are of the same order, the width of the phase distribution can be fully explained with the mechanical instabilities of the setup.

Low amplitudes

The mean amplitude A_1 of the 200 observed interference patterns is 0.28 ± 0.13, which is significantly less than the expected 100 %. Of course this "theoretical" contrast is reduced by a finite imaging resolution. The reduction of contrast due to the imaging resolution w can be calculated by convolving the initial periodic function (of perfect contrast) with a gaussian of waist w [143]. When taking into account a finite imaging resolution, one has thus to use a modified fitting function to extract the original contrast:

$$\tilde{Y}_{\text{fit}}(z) = \int Y_{\text{fit}}(z') \cdot e^{-2(z-z')^2/w^2} dz', \quad \text{where} \quad Y_{\text{fit}}(z) = [1 + A_1 \cos(B_1 + 2\pi z/D)]\, G(z) \qquad (6.3)$$

Figure 6.2(a) shows the contrast of the convolved function as a function of the imaging resolution. In figure 6.2(b)-(e) the expected density profiles are shown, for imaging resolutions of 1, 5, 9 and 13 μm from (b) to (e) respectively. The resolution of our imaging system is $w \approx 5\,\mu$m [8], which corresponds to an expected contrast of 91 %.

The imaging resolution can thus not be the only reason for the low average contrast of only 28 %, neither of course can it account for the broad distribution. These must be mainly attributed to the relatively poor quality of the images. In order to keep the phases of the individual BECs constant, the lattice was ramped up in 3 ms, which excited the radial breathing mode and let to a significantly reduced image quality[1].

---

[1] This is the reason for the difference in the visual appearance between figure 6.1(a) and figure 6.4(a).

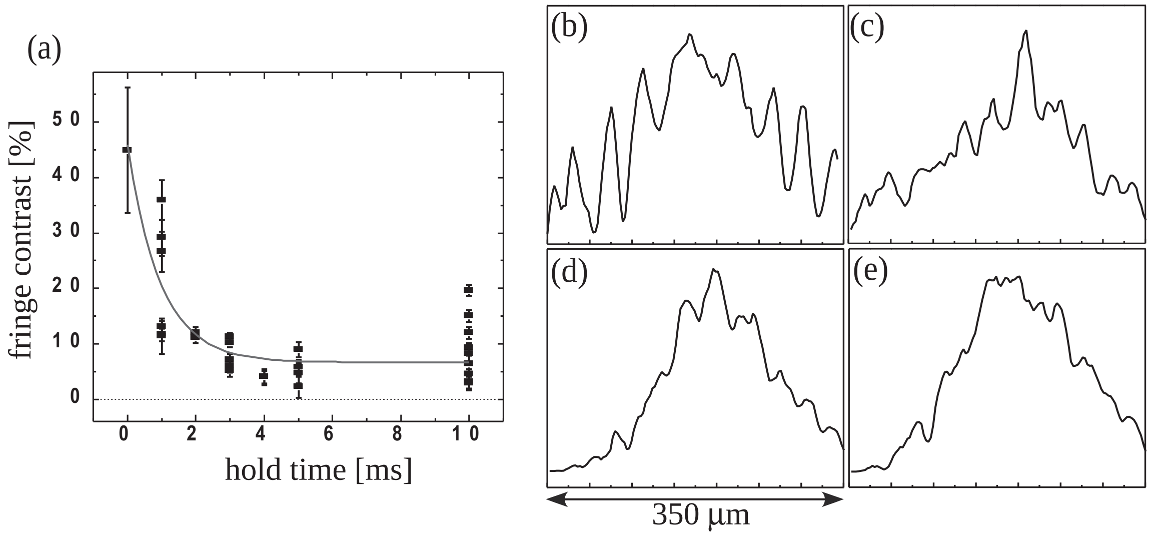

Figure 6.3: Phase diffusion. (a) Average fringe contrast A_1 of 40 consecutively taken images as a function of hold time. The ramp time is $\tau_{\text{ramp}} = 1\,\text{ms}$ for all experiments. (b)-(e) Averages of the density profiles of 40 images taken with identical experimental parameters. The averaged profiles are then fitted with function 6.2 to extract the amplitude of the first harmonic A_1. The hold time and fitted fringe contrast is for figures (b) to (e) respectively: (b) $\tau_{\text{hold}} = 0\,\text{ms}$, $A_1 = 45\,\%$, (c) $\tau_{\text{hold}} = 1\,\text{ms}$, $A_1 = 27\,\%$, (d) $\tau_{\text{hold}} = 2\,\text{ms}$, $A_1 = 12\,\%$, and (e) $\tau_{\text{hold}} = 4\,\text{ms}$, $A_1 = 4\,\%$.

6.2.2 Phase evolution

The evolution of the system from an array of phase coherent condensates to phase independent BECs is due to a dephasing of the individual condensates. The exact time evolution of the relative phases is a complex problem, which has been the subject of several theoretical studies [144–149]. Especially in experiments build for interferometry a great effort is made to control the phase evolution as precisely as possible [28, 30].

For our purposes it is mainly important to obtain a rough time scale of the evolution of the individual condensates' phases. This is necessary to determine the time after which phase coherence has completely vanished, so that one can speak of truly phase independent condensates.

Even in an ideal experiment, with identical external conditions for all sites, there is a limit to phase coherence between the sites, due to the fluctuations in the atom numbers. If these have a Poissonian distribution, the phase diffusion time is of the order of [28]

$$\tau_{\text{diff}} \sim \frac{5h\sqrt{N_{\text{at}}}}{2\mu}, \tag{6.4}$$

where N_{at} is the expectation value for the atom number in an individual site. For our experimental parameters, $N_{\text{at}} \sim 10^4$ and $\mu/h \sim 2\,\text{kHz}$, this fundamental phase diffusion time would be $\tau_{\text{diff}} \approx 125\,\text{ms}$.

However, the independent evolution of the phases in the individual sites can be much faster, due to energy differences between the individual sites. These energy differences can arise from differences in the trapping potential, or the atom number per site, which results in different chemical potentials. This we expect to be the dominant effect for the dephasing of the condensates in the

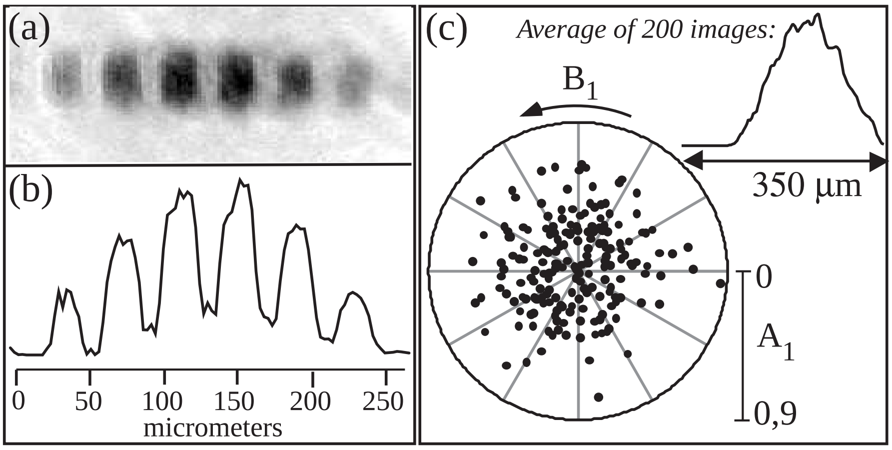

Figure 6.4: Interference of Bose-Einstein condensates with uncorrelated phases. (a) Absorption image after 22 ms expansion of the cloud released from the lattice. The density distribution shows clear interference fringes with a high contrast. (b) Axial density profile of the cloud, radially averaged over the central $25\,\mu$m. (c) Polar plots of the fringe amplitudes and phases (A_1, B_1) for 200 images. Inset: Axial density profiles of the cloud, averaged over the 200 images.

lattice sites: the atom number in the sites are not equal at the moment when tunneling stops, but follow a parabolic distribution. When the lattice is ramped up even more, the individual sites are axially compressed, and the chemical potentials of the individual condensates increase. As these have different atom numbers due to the initial parabolic distribution, the chemical potentials grow to larger values in the central sites than in the edge sites. This difference in chemical potentials leads to independent phase evolutions $\propto \mu t/\hbar$ in the different sites. As the chemical potentials of the trapped condensates are of the order of $\mu/h \sim 1\,$kHz, we expect the phases to diffuse away from each other on a millisecond timescale

Experimental results

For the study of phase diffusion we perform the following series of experiments: The lattice power is ramped up in $\tau_{\text{ramp}} = 1\,$ms, and the atoms are then hold in the lattice for a variable hold time τ_{hold}. For every value of τ_{hold} 40 images are taken, and their axial density profiles are extracted and summed up. The resulting averaged density profile is then fitted with the function $Y_{\text{fit}}(z)$, and the fringe amplitude A_1 is plotted as a function of the hold time (figure 6.3 (a)). In figures 6.3 (b)-(e) the averaged density profiles corresponding to hold times of 0, 1, 2 and 4 ms are shown.

When fitting the decrease of contrast with the hold time with an exponential decay function, $y = y_0 + A \cdot \exp(-\tau_{\text{hold}}/\tau_d)$, one obtains $y_0 = 6.7$, $A = 39\,\%$ and $\tau_d = 0.97$ (full line in figure 6.3(a)). As expected, the phase diffusion time is on the order of a millisecond, $\tau_d \approx 1\,$ms.

6.2.3 Fringes of uncorrelated condensates

For the realization of an array of condensates with uncorrelated phases, the lattice power is ramped up in $\tau_{\text{ramp}} = 200\,$ms, and the atoms are then hold another 500 ms. This slow ramp is chosen to avoid excitations of the radial modes of the BECs.

The images recorded after $t = 22\,$ms of ToF expansion have an average Gaussian envelope of waist $Z_0 = 153\,\mu$m. This is about 15 % larger than the expected waist of $\hbar t/(m\ell) = 133\,\mu$m (see section 6.3.1), where ℓ is the waist of the gaussian that describes the density distribution along z of the atomic clouds in the lattice sites. They commonly show clear interference fringes,

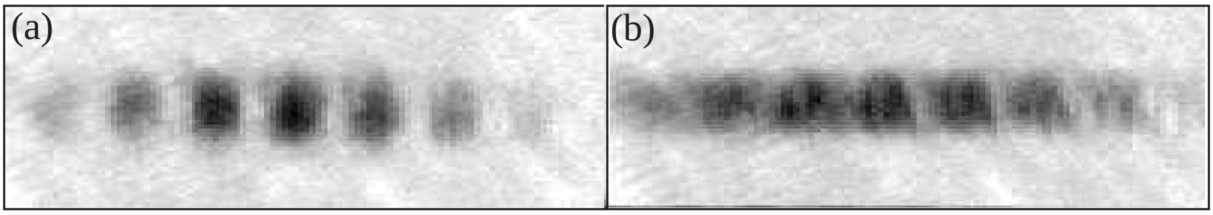

Figure 6.5: Interference of independent condensates, produced in different ways. (a) The lattice is ramped onto a condensate, and cuts it in ≈ 30 individual BECs, which dephase during a hold time of 500 ms. (b) The lattice is ramped onto a thermal cloud, during the evaporation routine. Evaporation is then pursued, until the clouds in the individual sites attain Bose-Einstein condensation. The individual BECs thus never shared a common phase. In both cases absorption imaging is performed after 22 ms ToF.

of which a spectacular example with fringe contrast 85 % is shown in figure 6.4. This result might seem surprising at first sight, as the loss of coherence is generally associated with a loss of fringe contrast [32, 73, 118, 140].

There exists however a distinctive difference to the case of phase coherent condensates: The phases of 200 interference patterns are randomly distributed between 0 and 2π (see figure 6.4(c)). Consequently, no periodic modulation remains visible in the average of the 200 density profiles. Also the distribution of the fringe amplitudes is different: it has the mean value $\langle A_1 \rangle = 0.32$, and the standard deviation $\sigma_{A_1} = 0.18$, which is broader than in the coherent case.

6.2.4 Interference of condensates that never shared a common phase

For the largest lattice height we have performed a second experiment, in which the condensates' phases are not correlated from the beginning. In this type of experiment the lattice is ramped up on the thermal cloud and the evaporation takes place with the lattice already being in place. The condensates are produced independently at the different lattice sites. As this way they "have never seen one another" [150], they never shared a common phase. This experiment is thus a better equivalent to that of two independent interfering laser beams, than the one described in section 6.2.3.

In this series of 100 experiments we observe fringes of significantly lower contrast than when the lattice is ramped onto the condensed cloud. The average value for the contrast of the first harmonic is $\langle A_1 \rangle = 0.15$, and the standard deviation $\sigma_{A_1} = 0.07$. The gaussian density profile along z of the cloud after expansion has an average waist of $185\,\mu$m, which is broader by 20 % when compared to the data presented in section 6.2.3. This can be seen by comparing the data in figure 6.5 (a)-(b), where typical images from the different experimental situation are shown.

This broadening as well as the lower contrast can be explained with the different production process: When the lattice is turned on on a hot cloud, its influence on the atoms becomes significant at a temperature of $T = (h/k_\mathrm{B})\,50\,\mathrm{kHz}$. When the temperature of the cloud is then decreased by evaporative cooling, the atoms get trapped in the edge sites, which would not be populated if the lattice was ramped up on a much smaller BEC. In those edge sites which contain enough atoms, the clouds form condensates. The relevant length scale for this loading mechanism is the diameter of the beams where the intensity is large enough to allow for complete isolation of the sites. The lattice height needed for this is estimated to $\sim 100\,\mathrm{E}_R$ [126], which is equivalent to $U_0/h \sim 8.0\,\mathrm{kHz}$. For our beam profiles the condition $U_0/h \geq 8.0\,\mathrm{kHz}$ is fulfilled within a diameter of $\sim 190\,\mu$m.

The relevant number for the contrast of the observed pattern is the number of interfering sites, as will be discussed in section 6.3.1. According to the above estimate, sites over a length of $\sim 190\,\mu$m are populated, which gives $N_s \approx 70$. Following the argument in section 6.3.1 for large N_s the contrast of the first harmonic scales as $A_1 \propto \sqrt{N_s}$. When ramping the lattice onto the condensed cloud, $N_s \approx 30$, and $\langle A_1 \rangle = 0.32$. For $N_s \approx 70$ one would thus expect an average contrast of $\langle A_1 \rangle = 0.21$. This is still slightly higher than the experimentally found average contrast, and the remaining difference can be explained with the different population distribution of the lattice sites in the two cases. If the lattice is ramped onto a condensed cloud, this distribution is parabolic, and among the 30 populated sites the edge sites contain only a small atom number. If the lattice is ramped onto a thermal cloud, the edge sites contain more atoms, and effectively more "full sites" contribute to the first harmonic.

6.2.5 Phase defects in the 2D BECs

Chapter 5 contains a detailed discussion of the appearance of phase defects in the 2D condensates trapped in the lattice sites. These phase defects were observed in the interference pattern of 2 to 8 interfering clouds. One might thus wonder if similar effects appear when letting interfere 30 BECs released from the lattice. This is not the case, which might be explained either by the absence of phase defects due to a slightly different experimental routine, or a limited ability to detect them. Both possibilities are discussed in the following.

The experimental conditions of the experiments presented here are in principle similar to those of the experiments presented in chapter 5. There are however some differences to the experimental cycle that was used in chapter 5, where a magnetic field gradient was applied along the lattice axis, and then selective evaporation of individual sites was performed. With this routine 500 ms are added to the duration of the experimental cycle, during which the only constant source of cooling is the finite lattice depth. This leads to a significant increase in temperature. As discussed in chapter 5, the condensates have a temperature between 250 and 500 nK after the additional 500 ms, which is near to the condensation temperature. In the experiments with incoherent sources, as presented in this chapter, the total experimental cycle has approximately the same duration, due to the hold time of 500 ms. During this duration however a rf knife is present, which leads to evaporation of atoms with a energy higher than $E_c = h \cdot 12\,\mathrm{kHz}$. With a realistic evaporation parameter $\eta = 5-10$, this leads to an estimated temperature of $60-120\,\mathrm{nK}$.

The appearance of phase defects depends crucially on the temperature of the clouds, as also discussed in chapter 5, and the probability of such defects should be very low for quasi pure BECs. However, no study of the temperature dependance of this phenomenon could be completed so far, and it can not be ruled out completely that even clouds well below the condensation temperature contain phase defects in our experimental conditions.

However, even if the clouds contain phase defects, their detection in the interference image is not very likely. As discussed in section 5.2.2, a phase defect in a single BEC only affects the interference with the two neighboring BECs. The interference with the other sites does not contribute to the first harmonic of the interference pattern, and the effect is likely to be washed out by the contributions of other next-neighbor pairs, which do not contain a defect. The simulations presented in section 5.2.2 show that already with four clouds, only half of 100 simulations with a vortex show clear zipper- or comb-type dislocations. The other half shows weaker dislocations which are not easily distinguishable from straight interference fringes. This effect becomes stronger with an increasing number of interfering sites.

6.3 Theoretical discussion of the results

In this section the experimental results presented above are discussed and described by a theoretical model. The discussion is focused on the novel results for an incoherent array of BECs.

6.3.1 Introduction of the model: N equal condensates

The situation of N_s independent BECs can be modeled with the sum of N_s coherent states, corresponding to the individual condensates. The validity of this ansatz for the interference of independent condensates was shown soon after the first BECs were experimentally achieved[2] [36].

In the following the experiment is modeled as a one-dimensional array of N_s condensates initially localized in $z_n = nd$, $n = 1, \ldots, N_s$. The spatial distribution in z-direction of each condensate is assumed to be a gaussian function with a standard deviation $\ell \ll d$.

The condensates are then allowed to expand and overlap during a time t. The effects of interactions during the expansion are neglected, and the wave function after expansion is supposed to be a sum of coherent states, where the phase of the n-th cloud and the amplitude of its gaussian envelope after expansion are denoted with $\tilde{\varphi}_n$ and α_n. The atom density in z is then [140]:

$$I(z) = \left| \sum_{n=1}^{N_s} \alpha_n \, e^{i\tilde{\varphi}_n} \, e^{-im(z-z_n)^2/(2\hbar t)} \, e^{-(z-z_n)^2/Z_0^2} \right|^2 , \tag{6.5}$$

where $Z_0 = \hbar t/(m\ell)$.
When assuming a long enough expansion time $t \gg 1/\omega_z \approx 40\,\mu$s, so that $\ell, z_n \ll Z_0, \sqrt{\hbar t/m}$, the length of the initial array can be neglected in the gaussian envelope. As a further simplification we suppose that the amplitudes of all initial condensates are equal, and thus $\alpha_n = \alpha$, which leads to:

$$I(z) = \alpha^2 \, e^{-2z^2/Z_0^2} \left| \sum_{n=1}^{N_s} e^{i\varphi_n} \, e^{i2\pi nz/D} \right|^2 , \tag{6.6}$$

with the phase factors $\varphi_n = \tilde{\varphi}_n - m(nd)^2/(2\hbar t)$ and $D = ht/(md)$.
This equation can be rewritten as

$$I(z) = N_s \, \alpha^2 \, e^{-2z^2/Z_0^2} \left[1 + \frac{1}{N_s} \left\{ \left(\sum_{n=1}^{N_s-1} e^{i2\pi nz/D} \sum_{j=n+1}^{N_s} e^{i(\varphi_j - \varphi_{j-n})} \right) + c.\,c. \right\} \right] , \tag{6.7}$$

where $c.\,c.$ denotes the complex conjugate of the term in the parenthesis. As the factor $N_s \, \alpha^2 \, e^{-2z^2/Z_0^2}$ describes only the gaussian envelope, the information about the modulation of $I(z)$ is fully incorporated in the term in the square bracket. This term is a sum of harmonics with periods $D_n = ht/(nmd)$. The function itself is thus necessary periodic with period $D = D_1 = ht/(md)$ and average value 1. Equation (6.7) can thus be written more intuitively as $I(z) = N_s \, \alpha^2 \, e^{-2z^2/Z_0^2} \, F(z)$, where

$$F(z) = \frac{1}{N_s} \left| \sum_{n=1}^{N_s} e^{i(2\pi nz/D + \varphi_n)} \right|^2 = 1 + \sum_{n=1}^{N_s-1} A_n \cos(B_n + 2\pi nz/D), \tag{6.8}$$

and the amplitude A_n and the phase B_n of the n-th harmonic with period D_n are given by the modulus and the argument of the complex Amplitude $\tilde{A}_n$:

$$A_n e^{iB_n} = \tilde{A}_n = (2/N_s) \sum_{j=n+1}^{N_s} e^{i(\varphi_j - \varphi_{j-n})}. \tag{6.9}$$

---

[2] For BECs with large atom numbers this ansatz is equivalent to having each condensate prepared in a Fock state, with the repartition of the atom numbers of the 2 clouds following a Poisson distribution.

A first important result is thus that the interference pattern of an array of incoherent condensates is necessarily periodic, with the period one expects for a coherent array. In the following the contrast of this pattern will be estimated for different situations: a coherent array of N_s condensates (a), the average of $N_s - 1$ experiments with 2 independent condensates (b), and an incoherent array of N_s condensates (c). The two latter cases are explicitly compared in a paragraph (d).

a) Coherent array of N_s condensates

If the N_s condensates have the same phase the weight of the harmonics are growing with the number of pairs contributing to them: $A_n \propto (N_s - n)/N_s$. $F(z)$ is then proportional to the grating function $G_{\text{grat}}(z)$ [140], appearing in the theory of grating diffraction:

$$F(z) = \frac{1}{N_s} G_{\text{grat}}(z) \qquad \text{with} \qquad G_{\text{grat}}(z) = \frac{\sin^2(N_s \pi z/D)}{\sin^2(\pi z/D)} \ . \tag{6.10}$$

The peaks of $F(z)$ are at the positions $z = pD$ (p integer), and have the value $F(z) = N_s$. The width of each peak is $\sim 1/N_s$ and in between the peaks the amplitude is $F(z) \sim 0$.

b) Average of N_s experiments with 2 independent condensates

One could be tempted to estimate the contrast of the pattern resulting from an array of N_s incoherent BECs with the sum of $N_s - 1$ next-neighbor pairs. For this reason an estimate for this situation is given here.
The modulation function for the average of $N_s - 1$ experiments is

$$F(z) = \frac{1}{N_s - 1} \sum_{n=1}^{N_s-1} \left(1 + \cos\left(B_n + \frac{2\pi z}{D}\right)\right) . \tag{6.11}$$

The contrast of all single shots is 100 %, but the spatial phase B_n of the individual patterns are arbitrary. The resulting average pattern is again periodic with period D, and has only a first harmonic modulation with amplitude A_1 and phase B_1.

For the evaluation of expectation value of the averaged pattern's amplitude one sets $1 + A_1 \cos(B_1 + 2\pi z/D) = F(z)$, and with $C = \sum_n(\cos(B_n))$ and $S = \sum_n(\sin(B_n))$ this leads to

$$A_1 \cos\left(B_1 + \frac{2\pi z}{D}\right) = \frac{1}{N_s - 1}\left[C \cos\left(\frac{2\pi z}{D}\right) - S \sin\left(\frac{2\pi z}{D}\right)\right] .$$

From this equation one sees that $A_1 \cos B_1 = C/(N_s - 1)$ and $A_1 \sin B_1 = S/(N_s - 1)$, and thus

$$\langle A_1^2 \rangle = \frac{\langle C^2 + S^2 \rangle}{(N_s - 1)^2} = \frac{1}{N_s - 1}, \tag{6.12}$$

where $\langle C^2 \rangle = \langle S^2 \rangle = (N_s - 1)/2$ can be derived easily when using the definitions of C and S. The average contrast of the pattern thus decreases as $1/\sqrt{N_s - 1}$.

c) Incoherent array of N_s condensates

To estimate the contrast of the interference pattern in the incoherent case, one is interested in the harmonic content of the pattern, $C_n = \langle A_n^2 \rangle$. According to equation (6.9), each A_n results from summing $(N_s - n)$ complex numbers with random phases and moduli $2/N_s$, and the expectation value thus is:

$$\langle A_n^2 \rangle = \frac{4(N_s - n)}{N_s^2} \qquad \text{and} \qquad \langle (F(z) - 1)^2 \rangle = \frac{1}{2} \sum_{n=1}^{N_s-1} \langle A_n^2 \rangle = \frac{N_s - 1}{N_s} \ . \tag{6.13}$$

As expected, the amplitudes A_n of all harmonics decrease with increasing N_s. The number of harmonics does however increase linearly with the number of sites, which compensates for the decreasing weights of the individual harmonics, and keeps the expectation value $\langle (F(z)-1)^2 \rangle$ for the contrast at a high value. The exact shape of $F(z)$ in a period D and the position and values of its extrema vary however randomly from shot to shot, due to the arbitrary phases of the individual condensates. For large N_s the density modulations inside a period D can thus be thought of as noise. This observation, and the result $\langle F(z)^2 \rangle = 2$, which is obtained when using equations (6.8) and (6.13), are reminiscent of the Hanbury-Brown and Twiss correlations for a fluctuating classical field. However, in contrast to the standard Hanbury-Brown and Twiss experiments, in our case the underlying order of the lattice structure leads to a periodic correlation of the noise [151].

Scaling of the minima and maxima with large N_s

One can give an estimate of the expectation value for the maximal and minimal F, $\langle F_{\max} \rangle$ and $\langle F_{\min} \rangle$. This calculation can be done by noticing that for large N_s the probability distribution of F is

$$\rho(F) = e^{-F} \, . \tag{6.14}$$

This result can be proven by noticing from equation (6.8) that $N_s F(z)$ is the square of the distance traveled in a 2D random walk with N_s steps of unit length. One can also check directly from equation (6.8) that the moments of F are $\langle F^n \rangle \approx n!$ for $n \ll N_s$, which proves that the distribution probability of F is indeed $\rho(F) = e^{-F}$. It is also interesting to note that this distribution corresponds to the laser intensity distribution for optical speckle.

To find the expectation value for $F_{\max}$, we note that in a period D the distribution consists of $\sim N_s$ independent values, which is equal to the number of harmonics [151]. Therefore the probability that a point $F_{\max}$ corresponds to the maximum of the N_s independent points is

$$p\left(F_{\max}\right) = \frac{d}{dF_{\max}} \left(\int_0^{F_{\max}} \rho(F)\, dF \right)^{N_s} .$$

Using the distribution (6.14) for F, a short calculation leads to the expectation value

$$\langle F_{\max} \rangle = \sum_{\nu=1}^{N_s} \frac{1}{\nu} \sim \ln N_s \; . \tag{6.15}$$

For the calculation of $\langle F_{\min} \rangle$ an analogue argumentation gives for the probability that a point $F_{\min}$ is the minimum of N_s independent points

$$p\left(F_{\min}\right) = \frac{d}{dF_{\min}} \left(\int_{F_{\min}}^{\infty} \rho(F)\, dF \right)^{N_s} ,$$

which leads to

$$\langle F_{\min} \rangle \sim \frac{1}{N_s} . \tag{6.16}$$

For large N_s the expectation values are thus $\langle F_{\max} \rangle \gg 1$ and $\langle F_{\min} \rangle \ll 1$, and for most single shots $F(z)$ is strongly modulated, with a contrast of almost 100%.

d) Average of N_s 2-sites-experiments vs. one measurement with N_s sites

Comparing the results of equation (6.12) and (6.13), for averaging N_s experiments with two sites and one experiment with N_s sites respectively, one notes that the contrast of the patterns' first harmonic A_1 scales with $N_s^{-1/2}$ in both cases. For the average of N_s experiments with 2 independent condensates this value is equal to the expectation value for the total contrast, as no higher harmonics exist. The contrast of the average thus tends to zero for large N_s. This is not true for an array of N_s condensates, where $\langle (F(z)-1)^2 \rangle$ stays large, because the number of harmonics increases with increasing N_s. If higher harmonics can be resolved, it is thus not a good approximation to estimate the contrast of the interference pattern of N_s condensates with the sum of the patterns of the next-neighbor pairs.

6.3.2 Monte Carlo simulations for incoherent arrays

For a better understanding of the experimental results in the case of arbitrary relative phases we have performed Monte-Carlo simulations. These consist of a calculation of $I(z)$ by assigning sets of random numbers to the phases $\{\varphi_n\}$. The starting point for these simulations is equation (6.5).

a) Large number of equal size condensates

In each realization of a Monte-Carlo "experiment" with a given $\{\varphi_n\}$, the maximum $F_{\max}$ and the minimum $F_{\min}$ value of $F(z)$ are recorded. These values are then averaged over many runs with arbitrary sets of phases $\{\varphi_n\}$. This procedure was carried out for the range $10 \leq N_s \leq 10^4$, where one finds

$$\langle F_{\max} \rangle \sim 1.2 \ln(N_s) \gg 1 \qquad \text{and} \qquad \langle F_{\min} \rangle \sim \frac{0.2}{N_s} \ll 1. \tag{6.17}$$

The scaling of the maximal and the minimal value of F corresponds to the analytic estimates of equations (6.15) and (6.16).

As discussed in section 6.3.1 the exact shape of $F(z)$ and the positions of its extrema are different for each set of random numbers $\{\varphi_n\}$. An example of a simulation with $N_s = 300$ is given in figure 6.6. In this figure it becomes clear that one period can contain several maxima of similar height. The width of the maxima scales with D/N_s.

Due to the completely arbitrary position of the maxima the average of $F(z)$ over many sets of $\{\varphi_n\}$ (corresponding to the average of a large number of images obtained under same experimental conditions) leads to a uniform function $\bar{F} = 1$. This is in agreement with our experimental observations, where the average of 200 density profiles showed no significant modulation (inset in figure 6.4(c)).

b) Comparison of experiment and simulation

For a comparison of the experimental findings, Monte-Carlo studies were then performed with a parabolic distribution for the amplitudes of 30 wave packets, $\alpha_n \propto n(N_s - n)$. The resulting density profiles $I(z)$ were then convolved with a Gaussian of $5\,\mu$m width, which accounts for the finite resolution of the imaging system. The convolved profiles are then fitted in the same way as the experimental data.

When generating 200 density profiles resulting from arbitrary sets of phases φ_n, the fitted fringe phase B_1 is found to be randomly distributed between 0 and 2π. The fringe amplitude has a mean value of $\langle A_1 \rangle^{\text{sim}} = 0.31$ and a distribution of $\sigma_{A_1}^{\text{sim}} = 0.16$. These findings are in remarkable agreement with the experiment, which gave $\langle A_1 \rangle = 0.32$ and $\sigma_{A_1} = 0.18$.

6.3.3 Extensions of the model to other experimental situations

The model derived in the above sections showed remarkable agreement with our experimental findings. To adapt it to the results of other experimental configurations, a few general remarks need to be made. These concern the limits of experimental access to the full interference pattern

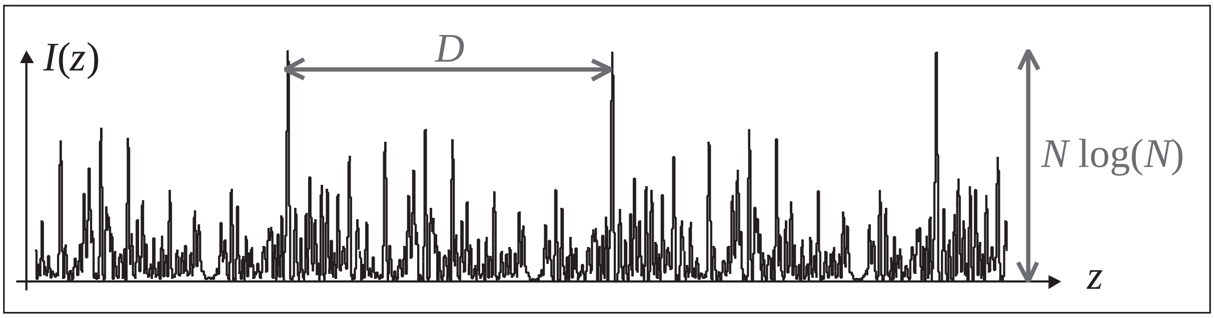

Figure 6.6: Simulation of an interference pattern of an incoherent array of $N_s = 300$ BECs. In principle the harmonic content grows linear with N_s, but due to finite imaging resolution one might not be able to resolve all peaks in a period D, as the width of the peaks varies with $\sim D/N_s$.

due to a finite imaging resolution (a) or to the dimensionality of the pattern (c). Further, an extension of the model to a Mott-insulator state with exactly one atom per site is presented (b).

With these extensions, our model describes well the results of most previous interference experiments, including those where contrast was lost with decreasing phase coherence [21, 34]. There exist however one experimental result, which can not be reconciled with our findings. This result is discussed in section (d).

a) The importance of the imaging resolution

In practice, a large modulation of the interference pattern $F(z)$ can be observed only if the imaging resolution is sufficient to detect a significant fraction of the harmonics. This is a relatively stringent condition for $N_s \gg 1$, as the amplitude of the first harmonic decreases with increasing N_s. In figure 6.6 a Monte-Carlo simulation of 300 condensates with arbitrary phases is shown. Even if the pattern is strongly modulated, it becomes clear that the complexity of such a pattern, consisting of N_s independent peaks with a typical width of $\sim D/N_s$ per period, cannot be resolved with experimental imaging resolutions, which usually are of the order of $5\,\mu$m.

However the experiments presented in this chapter show that the argument of limited imaging resolution is not yet valid in the case of 30 condensates. In practice $N_s = 30$ thus is not "very large" and even the first harmonic is still pronounced. Furthermore most lattice experiments are performed with counter-propagating laser beams, corresponding to much larger "lattice momentum" $\hbar k$. For a similar ToF, the period D is then also larger and many more harmonics are easily resolvable, as the width of the peaks scales with D/N_s.

b) Interference of a Mott insulator state with exactly one atom per site

In the experimental study of the superfluid to Mott insulator transition with cold atoms [21,34], the fringe contrast vanishes in the insulating domain. This observation is used as one of the signatures for the loss of long range phase coherence, which seems in contradiction to our results.

To discuss the significance of the above obtained results for these experiments, one has to extend the analysis to the initial state of a Mott insulator with exactly one atom per lattice site. A thorough study of this situation was published in [83, 151, 152]. For such a system the signal after ToF consists of the set of points $\zeta_1, \ldots, \zeta_{N_s}$ where the N_s atoms are detected, and the harmonic content of this signal is characterized by the real numbers (A_n, B_n) defined as:

$$A_n\, e^{iB_n} \;=\; 2\sum_{j=1}^{N_s} e^{-2i\pi\zeta_j n/D} \quad (\text{for } A_n > 0), \qquad \text{and} \tag{6.18}$$

$$C_n = \langle A_n^2\rangle \;=\; \frac{4}{N_s(N_s-1)}\sum_{j=1}^{N_s}\sum_{i\neq j}\langle e^{-2i\pi(\zeta_j-\zeta_i)n/D}\rangle\ , \tag{6.19}$$

where $\langle ...\rangle$ now denotes a quantum average.

For $n \neq 0$, the average harmonic content is $\langle A_n^2\rangle = 4(N_s - n)/\left[N_s(N_s-1)\right]$. This means that also in the case of a Mott insulator state one should see a strong modulation in the interference pattern, in contrast to what has been observed in [21,34].

However one can reconcile the two findings by noticing that these experiments are performed with 3D systems. When recording the interference pattern by absorbtion imaging, the effect of integration along one axis reduces the content of harmonics, as discussed in the next paragraph.

c) More than one dimension

The arguments presented so far naturally extend into two and three dimensions. In 3D, the function generalizing equation (6.8) is

$$F(\boldsymbol{r}) = 1 + \sum_{\boldsymbol{n}} A_{\boldsymbol{n}} \cos(B_{\boldsymbol{n}} + 2\pi\boldsymbol{n}\cdot\boldsymbol{r}/D), \tag{6.20}$$

where $\boldsymbol{n} = (n_x, n_y, n_z)$ is a triplet of integers. This is a periodic function in x, y, z with period D. A Monte-Carlo analysis for a cubic lattice with $20\times 20\times 20$ sites with random phases shows that $F(\boldsymbol{r})$ is again strongly modulated, with $\langle F_{\max}\rangle \simeq 12$ and $\langle F_{\min}\rangle \ll 1$.

However, in practice it is difficult to obtain experimental access to the 3-dimensional structure of an interference pattern. In most cases 3D patterns are observed by integrating the spatial distribution $I(\boldsymbol{r})$ along a line of observation, here denoted as z. In this case, only the harmonics $(n_x, n_y, 0)$ are observed and the integration over the z-axis gives for the modulation function

$$\langle (F(x,y)-1)^2\rangle \propto \frac{1}{N_z},$$

where N_z is the number of sites along z. The integration along z thus reduces the contrast of modulation by $\sqrt{N_z}$. This effect is similar to that of averaging N_z images of a 2-dimensional experiment (see section 6.3.1 (b)).

This effect is illustrated in figure 6.7. For this figure a 2-dimensional Monte-Carlo simulation with $N_x = N_y = 25$ sites was realized. Figures (a)-(c) show cuts through the 2-dimensional interference pattern at different values of the y-coordinate. In figure 6.7(d) the profile along the x-axis is shown, after the pattern was integrated over y, which reduces the modulation considerably.

The results of this paragraph thus explain the reduction of fringe contrast in the transition from a superfluid to a Mott-insulator state[3], as observed in [21, 34]. There is of course no reduction of contrast due to integration in the case of a coherent 3D array, where the positions of the interference peaks build a perfect lattice. For this reason a non-vanishing contrast of the pattern can be associated with phase coherence in these experiments.

---

[3] This reduction is however only a quantitative effect, and periodic correlations of the particle density are still detectable, as recently confirmed in [83].

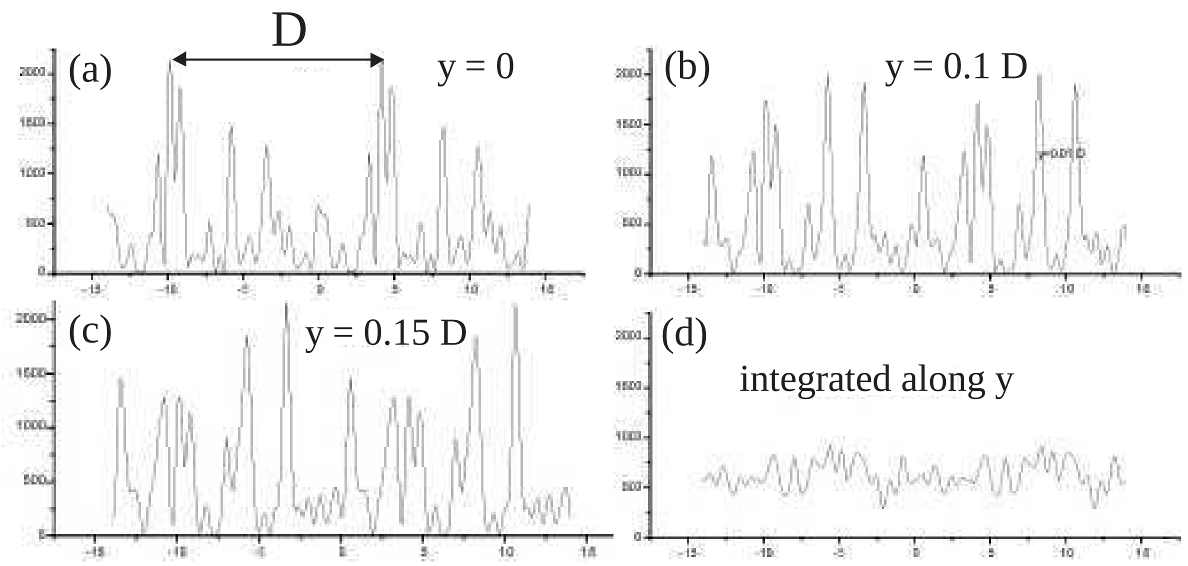

Figure 6.7: Integrating a 2-D pattern along one direction. (a)-(c) Cuts through a 2-D interference pattern in the xy-plane at $y = 0$, $y = 0.1\,D$ and $y = 0.15\,D$ respectively. (d) Integration along y of the same 2D interference pattern.

d) Experiments with a 1D lattice

There exists one other experiment with a 1-dimensional optical lattice, in which a loss of contrast was seen with increasing lattice height [73]. In this experiment some of the experimental parameters are relatively similar to our case: the number of occupied lattice sites is $N_s = 12$, and the atom number per site is $N_{\mathrm{at}} \sim 10^3$.

An important difference to our situation is that this experiment was performed with a red-detuned lattice with period $d = 420\,\mathrm{nm}$. This period is much smaller than the period in our experiment, and a full isolation of the sites could not be achieved. At full lattice height the authors could however reach a regime of low tunneling rates, where they expect significant number-squeezing [73]. The loss of contrast of the interference pattern was thus interpreted as a signature of the onset of number squeezing.

In our experiment we could not find reduced contrast for any of the explored lattice heights. We could however not explore the specific region in which numbers-squeezing becomes significant (which should occur for $20 < U_0/E_R < 100$, as argued in section 6.4), due to the at the time of the experiment unexplained strong heating in that region (see chapter 4.1.2, paragraph "The heating bump"). In the mean time this heating was found to be due to a technical problem, which has now been solved. As the full range of lattice depths is now accessible, it will be an interesting subject for future experiments to complete the study of interference contrast through the region of decreasing tunneling.

6.4 Number squeezing and Mott-Insulator-transition

The last section of this chapter discusses the potential of our experimental system for the realization of strongly number-squeezed states [73, 153] and the observation of the Mott-insulator transition [21, 34, 154]. For simplicity the discussion in this paragraph is restricted to the case of translational invariance, without the quadratic magnetic potential applied along the z-axis.

6.4.1 Number squeezing

Number squeezed states are states with low fluctuations in the atom number $N_{\rm at}$, which means that the atom number in each site has a sub-Poissonian distribution, with a standard deviation $\sigma < \sqrt{N_{\rm at}}$.

In optics the use of squeezed photon number states can lead to an improved sensitivity in interferometric measurements, as discussed in [153]. The arguments presented there also hold for atom interferometers, and squeezed states with large average atom numbers thus promise to be of a great relevance for atom interferometry and precision measurements. A first experimental attempt for their realization in a 1D lattice was published in [73].

In the ground state of the system the squeezing of the atom number on each site depends on the ratio of the tunneling rate $\tilde{t}$ and the effective strength of the repulsive on-site interactions $U_{\rm int}$ [154]. There the tunneling rate is $\tilde{t} = N_{\rm at}J/h$, where J is the matrix element for the tunneling of a single particle between neighboring sites. The on-site interaction energy is $U_{\rm int} \sim \mu/N_{\rm at}$, where μ is the chemical potential.

In our experiment $N_{\rm at} \sim 10^4$, $\mu/h \approx 2\,$kHz, and $U_{\rm int}/h \sim 0.2\,$Hz. For these parameters one can qualitatively distinguish three regimes:

1. $J \gtrsim N_{\rm at}\, U_{\rm int}$: Tunneling rates are large ($\tilde{t} \gtrsim 2 \cdot 10^7\,$Hz), squeezing is negligible and the atom number on each site follows a Poissonian distribution with a standard deviation $\sigma = \sqrt{N_{\rm at}} \sim 100$.
2. $J \sim U_{\rm int}$: This is achieved for $\tilde{t} \sim 2\,$kHz. In this regime squeezing is significant, and σ is reduced to $N_{\rm at}^{1/4} \sim 10$.
3. $J \sim U_{\rm int}/N_{\rm at}$: This condition corresponds to $\tilde{t} \sim 0.2\,$Hz and classifies the regime where the phase transition to a Mott insulator with $\sigma < 1$ occurs [154].

In our setup, the value of J can be tuned across this full range, and according to the above estimates, the formal criterion for the Mott transition is satisfied for $U_0 \sim 100 - 150\, E_R$ [126]. The region of significant number squeezing ($\sigma < N_{\rm at}^{1/4}$), which should occur for intermediate lattice heights is thus in principle accessible. A systematic study of this regime proved however to be difficult at the time of the experiment, due to the strong heating at the corresponding lattice heights (see chapter 4.1.2, paragraph "The heating bump").

6.4.2 The Mott insulator state for systems with large $N_{\rm at}$

The regime of the Mott-insulator state is reached at a lattice height where the matrix element for the tunneling of a single particle becomes comparable to the on-site interactions per particle [138, 154]. As stated above, the formal criterion for the transition is satisfied for $U_0 \sim 100 - 150\, E_R$. The corresponding tunneling rate is of the order of 0.2 Hz.

Translational invariance

A first condition to achieve a Mott-insulator state, is that the assumed translational invariance must be insured to a sufficient level. In practice the potential energies at different lattice sites must be matched to better than the calculated bandwidth $J/h \sim 10^{-5}\,$Hz. For our magnetic trap, which has an axial frequency of $\omega_z/(2\pi)$, this condition is fulfilled only up to a length of a few nanometers.

Already the absence of translational invariance makes thus an observation of the Mott-insulator transition impossible in our system. It is however not fully out of scope to reach such a regime, by reducing both the axial trapping frequency, and the lattice spacing.

Relevant time scales

There exists however a more general limit to Mott-insulator states with large atom numbers per site. This limit is due to the low interaction energy per particle $U_{\text{int}} = \mu/N_{\text{at}}$, which decreases with increasing atom number, as discussed in the following.

First, the feasibility of a Mott-insulator state relies on the capacity to ramp up the lattice potential slowly compared to the tunneling times. This is necessary for a permanent redistribution of the atoms, until the perfect Mott-state is achieved. Once the final lattice height is reached, it is essential that the tunneling rate $\tilde{t}$ remains higher than the rate of any decoherence processes. Otherwise the occupation numbers in the various sites will rapidly decorrelate from each other due to losses, and after some time they will follow independent Poisson distributions, similar to those obtained in a system of fully independent condensates ($J = 0$).

For these two reasons the experimental ramp time of the lattice, and the hold time after the ramp is completed, should be longer than $\tilde{t}^{-1} \gtrsim 5\,\text{s}$. This poses practical problems, as this time is comparable to the lifetime of the condensate. Under these conditions one may question the relevance of the concept of a Mott insulating state for large numbers of atoms, which implies small values of the tunneling matrix element J.

6.5 Conclusion

In the first sections of this chapter the interference of a 1D periodic array of independent condensates prepared in a deep optical lattice potential was studied. It was shown that most “single shot” realizations of this system lead to a strongly modulated interference pattern after expansion. This effect was explained with a simple model that can easily be extended to 3D lattices.

The general resume of these results is that an underlying periodic structure of the system is sufficient to result in periodic correlations in the interference pattern. This means that even if the structure of the pattern in one period corresponds to arbitrary noise, this arbitrary structure is periodically repeated. The spatial correlations of the noise reveal thus the underlying order of the system. This effect has been also studied for other systems, such as correlated pairs of fermions [151,155], and recently also for a 3-dimensional Mott-insulator with a large number of sites [83,151,152].

In the last section the possibilities of our setup for the observation of number squeezed states and the Mott-insulator transition were discussed. It was found that the experimental realization of a Mott-insulator with large atom numbers per site will be difficult due to the very low tunneling rates at which this transition should occur. The regime of number squeezed states should however be accessible in our experiment, and the study of this regime is an interesting subject for future experiments.

Part III

Fast rotating condensates in quartic potentials

Contents

Introduction

In part II of this manuscript thermal vortices played a major role as the main ingredients to the understanding of the Kosterlitz-Thouless phase transition in a homogeneous 2-dimensional system. The average angular momentum of these systems is however zero, even if individual experimental measurements can show a non-zero angular momentum.

In part III the situation is different. In the systems described here large angular momenta are transferred to the condensate. Experimentally this is achieved by loading the BECs into an elliptic potential, whose main axes rotate around the z-axis. This stirring routine is stopped after typically 300 ms, and the system equilibrates in the axial symmetric magnetic potential. Due to the constraints on the velocity field of a BEC, rotation is only possible around vortex lines, where the wave function's phase has a singularity and the density vanishes. In the regime of *fast rotation* the angular momentum per particle corresponds to many of such vortex lines, which arrange themselves in a triangular lattice. Such vortex lattices have been realized and studied in several groups [128, 156–159].

The nucleation of vortex lattices is not unique to gaseous Bose-Einstein condensates. They have been observed in other systems that are described by macroscopic wave functions, such as fast rotating liquid ^{4}Helium. In this case the limit of fast rotation involves a dramatic change of the system's properties: for large rotation frequencies the superfluidity of the system disappears, and the system enters the normal state [160]. A similar effect occurs for type-II superconductors placed in a magnetic field, which loose their superconductivity when the field exceeds a critical value [37]. The similar behavior of these two systems can be explained by a profound analogy of their theoretical descriptions.

This analogy of rotating neutral particles and charged particles in a magnetic field leads to predictions for novel quantum states in harmonically trapped fast rotating bosonic gases. In these systems it is expected that a "fractional quantum Hall effect (FQHE)- regime" exists for rotation frequencies just below the trapping frequency, which is a bosonic analogue to the known regime for charged particles in magnetic fields [44]. The experimental search of this regime has motivated several groups to perform fast rotation experiments, and the lowest Landau level regime was already reached experimentally [1, 161]. In purely harmonic traps further progress in the direction of the FQHE-regime is however experimentally difficult, as for large particle numbers this regime requires an extraordinary control of the rotation frequency.

For this reason different trapping geometries have been proposed. These can be classified in two main categories: (i) using potentials that contain a component that is steeper than harmonic, so that the rotation frequency of the cloud is not limited, and (ii) rotating the sites of a 1D-optical lattice, and exploring the properties of the bulk-system. For the experiments presented here the first method was applied by adding a radial quartic potential to the harmonic potential provided by the Ioffe-Pritchard trap. The chapters of part III describe experimental results obtained with this anharmonic potential, as well as calculations concerning the spectrum of the eigenstates and the condensation temperature for a fast rotating gas in such a potential.

The chapters of part III

- **Chapter 7** gives an introduction to the properties of quantized vortices and vortex lattices in rotating BECs. In a second section the analogy of fast rotating bosons and charged particles in a magnetic field is developed. Due to this analogy a "bosonic FQHE-regime" exists in fast rotating bosonic gases, and it is discussed how this regime can be reached experimentally.

- **Chapter 8** presents experimental results of a rotating condensate in a quadratic plus a quartic potential. This potential is realized by focusing a blue-detuned laser onto the BEC. Due to the steep walls of the quartic potential it is possible to reach rotation frequencies of the order of (or even exceeding) the harmonic trapping frequency. The modifications in the energy spectrum arising from the anharmonic term are discussed in a first section, before the experimental routine and results are presented. One of the experimental results is that the vortex visibility decreases strongly at rotation frequencies $\Omega \sim \omega_\perp$, and several possible explanations for this effect are given.

- **Chapter 9** contains a calculation of the condensation temperature of a fast rotating cloud in the quadratic+quartic potential. It is shown that the semiclassical result is valid in this case, as well as in the purely harmonic case. This chapter generalizes the results of Stringari [162] to a quadratic+quartic trap. The obtained condensation temperatures exclude one of the hypotheses of chapter 8, which is that the presence of a thermal cloud is the reason for the vanishing vortex contrast at large rotation frequencies.

- **Chapter 10** presents experimental results concerning the eigenmodes of a fast rotating condensate in a quadratic+quartic potential. The radial monopole mode is studied in detail, at different rotation frequencies. It is found that unlike in a harmonic potential the frequency of this shape oscillation depends on the rotation frequency of the BEC. The shape of the monopole mode also differs from the case of a harmonic potential. Such possible modifications of the system's eigenmodes might be useful for probing new quantum states of the system [163]. This chapter was published in [2].

Chapter 7

Introduction to rotating condensates and the quantum Hall effect

The velocity field of a BEC is given by the gradient of its wave-function's phase, and is thus irrotational by construction. Nevertheless angular momentum can be transferred to a condensate, and the rotation of the fluid is possible through the nucleation of vortices. Such vortices are lines or rings of vanishing density, where the wave function's phase has a singularity and the curl around the singularity is nonzero. In cold atomic gases vortices have been observed since 1999, when in the group of Eric Cornell vortices were first nucleated through phase imprinting [156]. Since then a method using an optical stirrer, the so-called"spoon"-potential, first introduced by Madison *et al.* [128], was used in most of the experiments where vortices in atomic BECs were observed [157–159, 164].

For a singly charged and centered vortex in a harmonically trapped BEC the angular momentum per particle is $\hbar$. If the angular momentum per particle increases, more and more vortices are nucleated in the condensate, which arrange themselves in a triangular lattice. For angular momenta per particle $L_z \gg \hbar$ the condensate contains many vortices - BECs with more than hundred vortices were observed [165] - and the coarse grained average of the velocity field is identical to that of a rigid body with angular frequency Ω [160]. As the properties of single vortices and vortex lattices in atomic BECs are thoroughly discussed in the literature (see e.g. [62, 160], as well as in the manuscripts of my predecessors on the experiment [8, 9]), section 7.1 is restricted to a short overview of their most prominent features.

The regime of "fast" rotation, where many vortices are present in the condensate, is in the focus of this chapter. In a harmonic trap with radial frequency $\omega_\perp$ the limit of this regime corresponds to a rotation frequency $\Omega = \omega_\perp$. At this rotation frequency the trapping force is compensated by the centrifugal force, and the gas is not trapped anymore. Due to the Coriolis force this situation is analogue to that of charged particles in a uniform magnetic field, where the single particle states organize in highly degenerate Landau levels separated by $2\,\hbar\omega_\perp$. This regime is thus analogue to the situation of the quantum Hall effect (QHE) [40,41,166–168]. This analogy and its consequences are discussed in sections 7.2 and 7.3 .

7.1 Rotating condensates: vortices and vortex lattices

As shown in chapter 1.3, the velocity field $\boldsymbol{v}$ of an interacting Bose-Einstein condensate (or superfluid in general) is irrotational at any point where the phase of the wave function is not singular,

$$\boldsymbol{\nabla} \times \boldsymbol{v} = 0.$$

This is due to the nature of the velocity field, which is itself a gradient field:

$$\boldsymbol{v} = \frac{\hbar}{m}\boldsymbol{\nabla}\varphi, \tag{7.1}$$

where φ is the phase of the condensate wave function $\Psi = \sqrt{n}\, e^{i\varphi}$.

The irrotational character of the velocity field implicates that the circulation C around each closed path C vanishes, if the velocity field has no singularity in the enclosed area S_C. This follows immediately from Stokes' theorem:

$$\mathsf{C} = \oint_C \boldsymbol{v} \cdot d\boldsymbol{\ell} = \int_{S_C} (\boldsymbol{\nabla} \times \boldsymbol{v})\ d^2S = 0.$$

The possible motions of a condensate are thus more restricted than those of a classical fluid. The only rotational motion is in fact possible around lines where the phase of the wave function has a singularity. The condensate density on such lines is zero, and the lines correspond to quantized vortices, which must either extend to infinity ("vortex lines") or have the form of closed loops ("vortex rings"). The general properties of straight vortex lines in 3D condensates are discussed in the next sections.

7.1.1 General properties of vortices

Quantized phase and circulation

In the case of a phase singularity inside the closed loop C, the circulation of the velocity field is not necessarily zero, and with $\boldsymbol{v} = (\hbar\boldsymbol{\nabla}\varphi)/m$, it can be calculated to

$$\mathsf{C} = \oint_C \boldsymbol{v} \cdot d\boldsymbol{\ell} = \frac{\hbar}{m}\triangle\varphi,$$

where $\triangle\varphi$ is the variation of the phase along C. The value of $\triangle\varphi$ must be equal to $2\pi q$ (where q is an integer), as the condensate wave function is single valued. This means that the allowed values for the circulation are quantized,

$$\mathsf{C} = q\frac{h}{m},$$

and the integer q is called *vortex charge*.

Velocity field, energy and angular momentum

The equations verified by the velocity field of a vortex are analogue to those verified by a magneto-static field $\boldsymbol{B}$ in vacuum, and vortices are in this analogy the equivalent of an electric current line [160]. Correspondingly a vortex can be understood as the source of the velocity field (like a current is the source of the magnetic field), and the velocity field has the form given by the Biot-Savart law. In the case of a straight vortex line along z, the velocity field is in cylindric coordinates

$$\boldsymbol{v}(r, \theta, z) = \frac{q\hbar}{mr}\boldsymbol{u}_\theta, \tag{7.2}$$

where $r = x^2+y^2$ and $\boldsymbol{u}_\theta$ is the unit vector in angular direction. This velocity field is orthoradial, and its modulus is inversely proportional to the distance of the vortex line, and the velocity diverges thus towards the line.

In spite of this divergence the energy of a vortex stays finite. This is due to the finite core size of a vortex, which is of the order of the healing length ξ for a singly charged vortex, and grows with the vortex charge. The energy of a vortex can thus be approximated by a sum of two terms, of which one takes into account the energy of the vortex core, and the other the kinetic energy of the atoms outside the core region [109]. The first one of these terms can be neglected if the radial size of the system $R_\perp$ is much bigger than the vortex core. Under this assumption the energy of a centered vortex line in a condensate with radial symmetry and density profile $n(\boldsymbol{r})$ is

$$E_{vx} = \int_\xi^{R_\perp} d^2r \int dz \, \left(n(\boldsymbol{r}) \frac{mv^2}{2} \right). \tag{7.3}$$

Using $v = q\hbar/(mr)$ one finds that for a cylindric condensate of uniform density n_0, radius $R_\perp$ and length L, the energy has a logarithmic dependance

$$E_{vx} = L \, \frac{\pi q^2 \hbar^2}{m} \int_\xi^{R_\perp} \frac{n_0}{r} \, dr = L \, n_0 \, \frac{\pi q^2 \hbar^2}{m} \ln \left(\frac{R_\perp}{\xi} \right).$$

The angular momentum along z per particle of a centered vortex is

$$L_z = m(\boldsymbol{r} \times \boldsymbol{v}) \cdot \boldsymbol{u}_z = q\hbar.$$

The angular momentum does not depend on the radius; it is the same for all particles in the cloud. The given value is however only valid for a centered vortex, and the angular momentum per particle is lower if the vortex line is decentered [62].

7.1.2 Vortex lattices

For an angular momentum per particle $L_z \gg \hbar$ in principle two kinds of situation are possible for the condensate: either the nucleation of multiply charged vortices with charge $q \gg 1$, or the nucleation of many singly charged vortices with the same sense of rotation. It is not a priori clear which solution is favored, and this question is discussed in the following paragraphs.

Rotation frequency of a condensate

In harmonic traps a uniform distribution of singly charged vortices is energetically favored over the nucleation of multiply charged vortices, and multiply charged vortices are not dynamically stable [109].

A uniform distribution of vortices is in fact the distribution that leads to the best approximation of the velocity field of solid body rotation, which is for a system with total angular momentum $L_z^{(\mathrm{tot})}$:

$$\boldsymbol{v} = \boldsymbol{\Omega} \times \boldsymbol{r}, \qquad \text{and} \qquad \Omega = \frac{L_z^{(\mathrm{tot})}}{Nm\langle r^2 \rangle}, \tag{7.4}$$

where $\langle r^2 \rangle$ denotes the average value of $r^2 = x^2 + y^2$. In case of a superfluid solid body rotation is not possible, but it can be approached by a uniform distribution of the vortices. This was first suggested by Feynman [169]. For a large number of vortices, one can look at the coarse grain average of the velocity field, on a scale which is larger than the size of a single vortex. This is equivalent to replacing the point-like vorticity of the individual vortices by a diffuse and uniform vorticity [162]. In this limit the velocity field corresponds to solid body rotation, with $v = \Omega r$.

Density profile of the rotating condensate

In the case of uniform distribution of the vortices, the density profile of the cloud is given by [162]:

$$n(\boldsymbol{r}) = \frac{1}{g} \left(\mu - U(\boldsymbol{r}) + \frac{1}{2} m \Omega^2 r^2 \right). \tag{7.5}$$

This profile is equivalent to the usual Thomas-Fermi profile (see chapter 1.2.3), with a correction for the centrifugal term. In a harmonic potential the radial trapping frequency $\omega_\perp$ is thus replaced by $(\omega_\perp^2 - \Omega^2)^{1/2}$. In potentials steeper than harmonic the density at the center of the trap can become zero under certain conditions, and lead to a more complex trap geometry, which is not simply connected but has a hole in the center. In this case the hole can contain many quanta of circulation, and a stable "giant vortex" phase exists, contrary to the harmonic case.

Uniform distribution of the vortices

The circulation of the velocity field around a closed loop is equal to the quantum of circulation h/m times the number of vortices N_{vx} enclosed by the loop:

$$2\pi r(\Omega r) = N_{vx}\frac{h}{m} = \pi r^2 n_{vx}\frac{h}{m},$$

where n_{vx} is the vortex surface density $n_{vx} = N_{vx}/(\pi r^2)$. From the above equation one can deduce the relation between the rotation frequency of the condensate and the vortex surface density:

$$\Omega = \frac{h n_{vx}}{2m}. \tag{7.6}$$

In the limit of a uniform distribution of vortices one can also find a simple relation between the angular momentum per particle L_z and the number of vortices N_{vx}. To this end one writes the angular momentum per particle as

$$L_z = \frac{\int n(\boldsymbol{r}) m\Omega r^2 \; d^3\boldsymbol{r}}{\int n(\boldsymbol{r}) \; d^3\boldsymbol{r}} = m\Omega\langle r^2\rangle = \frac{h n_{vx}}{2}\langle r^2\rangle, \tag{7.7}$$

where expression (7.6) was used for the rotation frequency. This leads to the relation

$$N_v = \frac{L_z}{\hbar}\frac{R_\perp^2}{\langle r^2\rangle},$$

and $R_\perp^2/\langle r^2\rangle = 2$ for a cylindric condensate, and 2/7 for a harmonically trapped condensate of cylindric symmetry.

Lattice structure

The uniform repartition of vorticity in the cloud can in principle lead to different configurations of the individual vortices, ranging from a disordered vortex liquid to a crystal structure. It was shown by Tkachenko in 1966 that the triangular lattice has the lowest energy of all possible configurations [170]. Some experimental examples of such triangular vortex lattices are shown in figure 7.1 (a)-(c).

In small vortex lattices however the limited size of the cloud has an influence on the geometry, and structures that correspond better to the circular shape of the cloud are preferred. A result of the limited size is thus that some vortex arrangements are energetically more favorable than others. In our experiment a very common structure contains 7 vortices, consisting of a central vortex plus 6 vortices forming a hexagonal structure (figure 7.1 (a)). A similar structure exists for 19 vortices, consisting of the central vortex, a hexagon of 6, and a second hexagon of 12 vortices (figure 7.1 (b)).

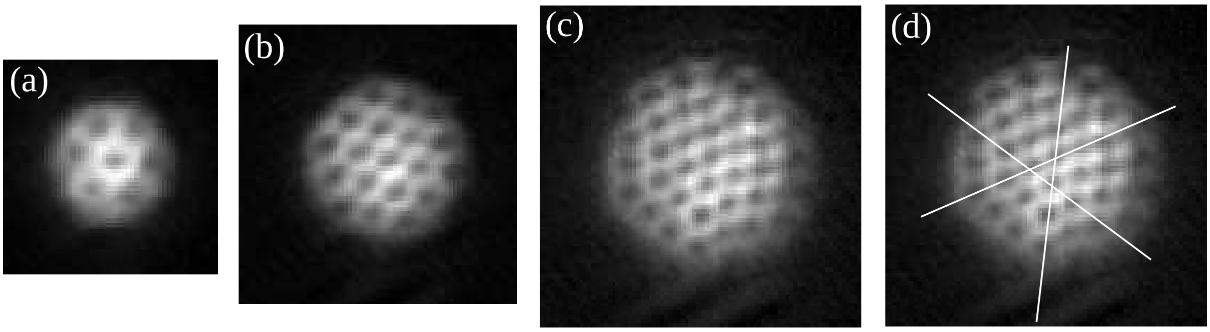

Figure 7.1: Vortex lattices obtained with our experimental setup, containing 7 (a), 19 (b), and approximately 40 (c) vortices. Figure (d) contains the same experimental data as figure (c), but straight lines are added to indicate the triangular lattice structure. In the center of the cloud the vortices are very well aligned on a triangular lattice, but at the edges the structure clearly deviates, to adjust better to the circular shape of the condensate.

7.1.3 Measuring the rotation frequency of a condensate with a vortex lattice

As shown above one can attribute a rotation frequency to a BEC with a given angular momentum per particle L_z through relation (7.7). For our experimental setup it is especially important to possess possibilities to determine this effective rotation frequency Ω_{eff} of the cloud (see chapter 8). This is due to the excitation routine used in our experiments, which consists in adding a rotating elliptic potential. The stirring frequency Ω_{stir} of this potential is well controlled, but as the condensate relaxes from elliptic to circular shape after the stirring phase - and thus changes its moment of inertia - the rotation frequency is not conserved, and Ω_{eff} can be different from Ω_{stir}. The rotation frequency (and thus the angular momentum) can be measured by different methods. These methods consist in

(a) fitting the density profile of the cloud, and determine Ω through equation (7.5),

(b) determining the vortex surface density, which is related to Ω by equation (7.6), and

(c) measuring the energy splitting of the two quadrupole modes m_{+2} and m_{-2}, which depends on the angular momentum of the BEC [171].

So far already the first two methods were presented. The third method was published by Chevy *et al.* [171]. The principle of this method relies on the splitting of the two quadrupole modes m_{+2} and m_{-2}. For a nonrotating cloud these modes are degenerate and have the frequency $\sqrt{2}\omega_\perp$ (see chapter 1.4.2). For a rotating cloud their frequencies are split by

$$m_{+2} - m_{-2} = \frac{2\langle L_z \rangle}{m\langle r^2 \rangle} = 2\Omega. \tag{7.8}$$

where the second equality is valid in the case of a condensate containing a large vortex lattice, so that diffuse vorticity can be assumed. Measuring the frequencies of these modes thus gives access to the rotation frequency of the BEC.

7.2 Rotating Bosons and the quantum Hall effect

The quantum Hall effect in semiconductors is based on the 2-dimensionality of the system. For this reason the following discussion of the analogy between such fermionic systems and rotating bosons in a harmonic trap is also restricted to the 2D case. Furthermore the 2D-trap is supposed to be rotational symmetric, i.e. $\omega_x = \omega_y = \omega_\perp$.

7.2.1 Analogy of rotating neutral particles to electrons in magnetic fields

Classical analogy

For rotating neutral particles in a harmonic trap a surprising analogy arises when the rotation frequency Ω approaches the trapping frequency $\omega_\perp$. At this frequency the expulsive centrifugal force $F_{\text{cen}} = m\Omega^2 r\hat{\boldsymbol{u}}_{\boldsymbol{r}}$ (where $\hat{\boldsymbol{u}}_{\boldsymbol{r}}$ is the radial unit vector) compensates exactly the trapping force of the harmonic oscillator $F_{ho} = -m\omega_\perp^2 r\hat{\boldsymbol{u}}_{\boldsymbol{r}}$. The only force acting on the atoms is then the Coriolis force $F_C = -2m\ (\boldsymbol{\Omega} \times \boldsymbol{v})$. The Coriolis force is mathematically analogue to the Lorentz force $F_L = Q\ (\boldsymbol{v} \times \boldsymbol{B})$ which acts on a particle of charge Q, that moves with a velocity $\boldsymbol{v}$ in a magnetic field $\boldsymbol{B}$.
Mathematically a *neutral* particle rotating with $\Omega = \omega_\perp$ in a harmonic trap thus behaves like a particle of *charge* Q moving in a magnetic field of strength $B = 2m\Omega/Q$. Due to this analogy it was suggested that a bosonic analogue to the fractional quantum Hall effect (FQHE) might be observable in systems of rotating bosons [40, 41, 172–174].

Quantum mechanical analogy

The analogy between neutral particles rotating in an harmonic potential $U(\boldsymbol{r})$ and charged particles in a magnetic field can also be seen from a similarity in the respective Hamilton operators. The Hamiltonian in the rotating frame is obtained by the transformation

$$H = H_0 - \Omega L_z,$$

where $H_0 = \boldsymbol{p}^2/(2m) + U(\boldsymbol{r})$ is the Hamiltonian in the laboratory frame.
The Hamiltonian in the rotating frame is thus

$$H = \frac{\boldsymbol{p}^2}{2m} + U(\boldsymbol{r}) - (\boldsymbol{\Omega} \times \boldsymbol{r}) \cdot \boldsymbol{p} = \frac{[\boldsymbol{p} - m(\boldsymbol{\Omega} \times \boldsymbol{r})]^2}{2m} + U(\boldsymbol{r}) - \frac{m}{2}\ (\boldsymbol{\Omega} \times \boldsymbol{r})^2. \tag{7.9}$$

For $\Omega = \omega_\perp$ the last term in equation (7.9) cancels the transverse part of the harmonic potential. The resulting hamiltonian shows a clear analogy to the hamiltonian of a charged particle in a homogeneous magnetic field $\boldsymbol{B}$, where the vector potential $\boldsymbol{A} = (\boldsymbol{B} \times \boldsymbol{r})/2$ is replaced by $\boldsymbol{\Omega} \times \boldsymbol{r}$.

7.2.2 Landau levels for rotating particles

The single particle energy spectrum of a 2D harmonic oscillator, with radial frequencies $\omega_x = \omega_y = \omega_\perp$ is

$$E(n_x, n_y) = \hbar\omega_\perp\,(n_x + n_y + 1) = \hbar\omega_\perp\,(n + 1)\,,$$

where n_x and n_y are the quantum numbers of the excitation energy in the respective direction, $n_i = 0, 1, ...,$ and $n = n_x + n_y$. All levels with equal n are degenerate.
The corresponding wave functions are

$$|n_x, n_y\rangle \propto P_{n_x}\ P_{n_y} e^{-(x^2+y^2)/(2a_{\text{ho}}^2)},$$

where P_{n_x} and P_{n_y} are the Hermite polynomials of order n_x and n_y, and a_{ho} is the harmonic oscillator length. Due to the degeneracy of the states $|n_x, n_y\rangle$ with $n_x + n_y = n$ it is useful to change the system of basis functions to the functions $|n, m_z\rangle$, where $n = n_x + n_y$ and m_z indicates the angular momentum along z. This is equivalent to a transformation from cartesian to polar coordinates, and m_z can take values from $-n$ to n, while $n + m_z$ has to stay even [64].
For these quantum numbers the energy spectrum becomes in the rotating frame

$$E(n, m_z, \Omega) = \hbar\omega_\perp(n + 1) - \hbar\Omega m_z. \tag{7.10}$$

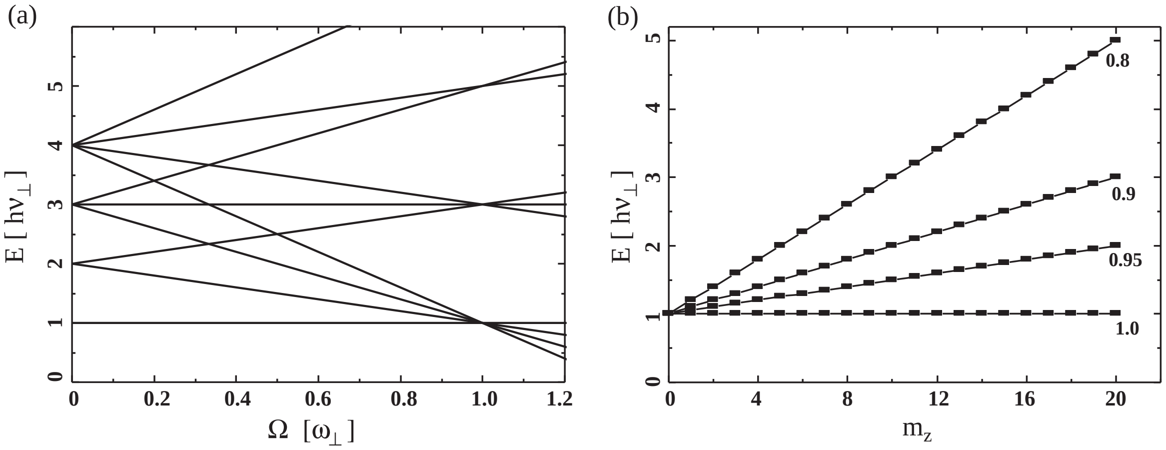

Figure 7.2: Landau levels for a single particle in a rotating harmonic trap. (a) Construction of the Landau levels. For $\Omega \to \omega_\perp$ the levels organize into the Landau levels, which are separated by the energy $2\hbar\omega_\perp$. In the figure all states with $n = 1, ..., 4$ are plotted, and one can see see the first three Landau levels ($n_L = (n - m_z)/2 = 0$, 1 and 2 from bottom to top) arising at $\Omega = \omega_\perp$. (b) The Lowest landau level $|n_L = 0, m_z\rangle$ for different rotation frequencies $\Omega/\omega_\perp$ =1, 0.95, 0.9 and 0.8 from the bottom to the top.

In a rotating system the levels are shifted by a quantity proportional to their angular momentum m_z. For $\Omega = \omega_\perp$ again a strongly degenerate spectrum arises:

$$E(n, m_z, \Omega = \omega_\perp) = \hbar\omega_\perp(n - m_z + 1). \tag{7.11}$$

As $n + m_z$ is an even number, and $-n \leqslant m_z \leqslant n$, the possible energy levels are $(2n_L + 1)\hbar\omega_\perp$, with $n_L = 0, 1, 2, ...$ Each of these levels n_L consists of all states $|n, m_z\rangle$ with $n - m_z = 2n_L$ and is infinitely degenerate. This behavior is illustrated in figure 7.2 (a). The levels n_L correspond to the famous Landau levels that appear for a charged particle in a homogeneous magnetic field. The level of smallest energy ($n_L = 0$ and $n = m_z$) is the well-known *Lowest Landau level* (LLL), which is of some importance in the interpretation of the fractional quantum Hall effect.

7.2.3 Short introduction to the quantum Hall effect in fermionic systems

The integer quantum Hall effect: a fermionic effect

The integer quantum Hall effect was first observed by von Klitzing [175] in a 2D semiconductor. The system consists of a thin homogeneous film of a semiconducting material, containing N free electrons. A magnetic field $\boldsymbol{B}$ is applied perpendicular to the film. The single particle states then organize in a spectrum of infinitely degenerate energy levels, the Landau levels. These Landau levels are spaced by the energy $\hbar\omega_c$, where $\omega_c = eB/m$ is the cyclotron frequency.

The infinite degeneracy of the levels is only possible in an infinite homogeneous system. In a finite system it can be shown that the number of states per Landau level is equal to the number of magnetic flux quanta N_ϕ traversing the system [176]:

$$N_\phi = \frac{SB}{h/e} \ ,$$

where S is the surface of the system, and h/e is the flux quantum. For the description of the

QHE the filling factor

$$\nu_f = \frac{N}{N_\phi} \propto \frac{1}{B}. \tag{7.12}$$

is introduced.

At low temperatures the distribution of the electrons is governed by the Pauli principle. For a given magnetic field B the Fermi sea fills the lowest Landau levels completely, up to a level n_L, and partially the level $n_L + 1$. Increasing the B-field increases the number of states in each of the Landau levels, and the level $n_L + 1$ is emptied gradually. For the specific B fields, which correspond to integer values of the filling factors ν_f, exactly the ν_f lowest levels (with $n_L = 0, ..., \nu_f - 1$) are filled. These states have remarkable transport properties [175, 176], and they are at the origin of the famous plateaus of the resistance as a function of B [175].

The integer quantum Hall effect relies thus on the statistic properties of fermions, because the gradual filling of the Landau levels relies on the fact that not more than one electron can occupy a specific quantum state. Unlike for the fractional quantum Hall effect, up to now no equivalent behavior has been suggested for neutral bosonic particles.

The fractional quantum Hall effect

Some years after the observation of the equally spaced plateaus in the resistance of some 2D semiconductors, which were explained by the Landau level structure created through the magnetic field, additional plateaus were discovered by Störmer and Tsui in 1982 [45]. These plateaus correspond to fractional values of the filling factor: $\nu_f = 1/3, 2/3, 2/5, ...$

Laughlin found that some of these states belong to a new family of wave functions, the so-called Laughlin-functions [44]. These are the states with

$$\nu_f = \frac{1}{2p+1},$$

where p is an integer. An example for such a wave function is the function describing the state with a filling factor $\nu_f = 1/3$

$$\Psi(z_1, ..., z_N) = \prod_{i<j} (z_i - z_j)^3 \; e^{-\sum |z_i|^2/(4\ell^2)}, \tag{7.13}$$

where $z_j = x_j + i\,y_j$ are the complex coordinates of the particle j in the 2D plane, ℓ is the magnetic length $\ell = (\hbar/eB)^{1/2}$, and the power 3 is the inverse of the filling factor. This wave function describes a remarkable state of the N particle system, which is strongly correlated, incompressible and has a particular excitation spectrum [44].

Due to the emergence of strongly correlated states in the theoretical treatment of the physics of the fractional quantum Hall effect, this effect can only be understood by the collective behavior of the electron gas. This is contrary to the physics of the integer quantum Hall effect, in which the transport properties of the individual electrons at the surface of the Fermi sea play the most important role.

7.3 Bosonic systems in the LLL

As the fractional quantum Hall effect does not rely on the fermionic properties of the electrons, the question has been asked, if for the FQHE a "bosonic twin to the electronic brother" might exist in rotating Bose-Einstein condensates [41, 177]. The theoretical activity around this question has largely evolved during the last years [40, 41, 167, 174, 178–182], inspired by the experimental progress that was made in the control of fast rotating condensates containing large vortex lattices [157, 161].

7.3.1 2-dimensionality

The system in which one might hope to achieve the equivalent to the FQHE in a rotating Bose gas must by 2-dimensional, i.e. its temperature and chemical potential must be smaller than $\hbar\omega_z$. The wave function can then be written as a product function

$$\Psi(\boldsymbol{r}) = \psi(x, y)\chi(z), \qquad \text{where} \qquad \chi(z) = \frac{1}{(\sqrt{\pi}a_z)^{1/2}} e^{-z^2/(2a_z^2)}, \tag{7.14}$$

and $a_z = (\hbar/(m\omega_z))^{1/2}$ is the harmonic oscillator length along z. This situation is discussed in chapter 3. It was experimentally achieved in combined magnetic and optical traps [16, 25, 26], the sites of 1-dimensional optical lattices [3, 5, 73, 117, 118] and in a fast rotating Bose-Einstein condensate [24]. In the latter the effective radial trap frequency $\tilde{\omega}_\perp$ is weakened due to the centrifugal force, to

$$\omega_\perp \to \frac{\omega_\perp}{\gamma}, \qquad \text{where} \qquad \gamma = \frac{1}{\sqrt{1 - \Omega^2/\omega_\perp^2}}.$$

Increasing the rotation frequency Ω thus reduces the 2D chemical potential

$$\mu = 2\hbar\frac{\omega_\perp}{\gamma} \left(Na/\ell_z\right)^{1/2}$$

(see equation 3.12), where $\ell_z = \sqrt{2\pi}a_z$ and a is the 3D scattering length. For large enough Ω the condition for 2-dimensionality $\mu < \hbar\omega_z$ can be fulfilled.

The next paragraphs discuss some of the expected phenomena for a 2D Bose gas rotating at a fast rotation frequency $\Omega \sim \omega_\perp$.

7.3.2 The mean field quantum Hall regime

The first step to a different regime occurs at the rotation frequency for which all particles populate states belonging to the LLL. The wave function is then completely restricted to the LLL, which results in interesting properties of the system. This situation arises if the chemical potential μ and the temperature $k_{\mathrm{B}}T$ are smaller than the spacing between the Landau levels. For the chemical potential this leads to:

$$2\hbar\frac{\omega_\perp}{\gamma} \left(Na/\ell_z\right)^{1/2} < 2\hbar\omega_\perp \qquad \Leftrightarrow \qquad \gamma > \left(Na/\ell_z\right)^{1/2}. \tag{7.15}$$

Note that in the case of bosons the number of atoms N in the LLL can be much larger than the number of states N_l in the LLL, which is not the case for a fermionic system. The filling factor $\nu_f = N/N_l$ can thus be larger than 1. In the case of large filling factors, $\nu_f \gg 1$ the system is still described by a mean field wave function, and has not entered the FQHE-regime. This situation is called *mean field quantum Hall regime.*

The wave function of the system is then a sum of LLL-states ϕ_{m_z} (where $m_z \geqslant 0$):

$$\Psi_{LLL} = \sum_{m_z} a_{m_z}\phi_{m_z} = \sum_{m_z} a_{m_z} \frac{(x + iy)^{m_z}}{\sqrt{\pi m_z!}} e^{-(x^2+y^2)/2a_\perp^2} \tag{7.16}$$

where a_{m_z} is the complex amplitude of the respective state. Even if this wave function belongs to a 2D system, its states are denoted by a single quantum number (m_z), which means that the dynamics of the system is effectively 1-dimensional [183].

Despite this distinct difference of a system restricted to the LLL compared to a “normal” 2D system, the transition from one regime to the other does not coincide with striking differences of the experimentally observed clouds. There are however some differences between the two situations, and one of the observable effects of the LLL regime is the saturation of the vortex core size.

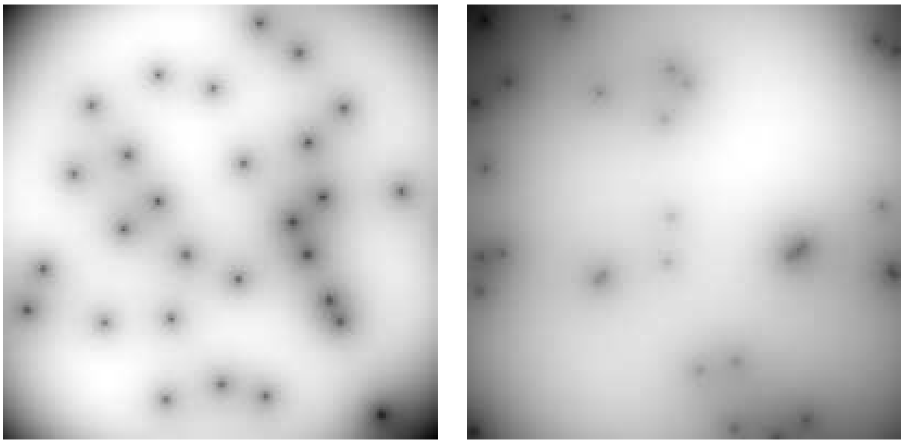

Figure 7.3: Zeroes of the LLL-polynomial. (a) Zeroes of a polynomial of the form of equation (7.16) for a random set of $m_z = 30$ coefficients a_{m_z}. The coefficients are randomly chosen from a gaussian distribution. The figure shows the logarithm of the density distribution, $\log(|\Psi_{LLL}|^2)$, to make the positions of the zeroes more visible. (b) The corresponding density plot, where not the coefficients of the polynomial, but the zeroes z_i are chosen randomly with a gaussian distribution. Comparing the two distributions, one clearly sees the antibunching of the vortex positions in (a).

Saturation of the vortex core size

Outside of the LLL-regime, the size of the vortex core is of the order of the healing length,

$$\xi = \sqrt{\frac{\hbar^2}{m\mu}} = \frac{\sqrt{\gamma}a_\perp}{\sqrt{2}} \left(\frac{Na}{\ell_z}\right)^{-1/4},$$

where $a_\perp = \sqrt{\hbar/(m\omega_\perp)}$ is the size of the harmonic oscillator in radial direction.
The distance d_{vx} between two vortices is

$$d_{vx} = \frac{1}{\sqrt{n_{vx}}} = \sqrt{\pi}a_\perp \left(1 - \frac{1}{\gamma^2}\right)^{-1/4},$$

as the vortex surface density increases like $n_{vx} = 2m\Omega/h$. The vortex core size and the intervortex spacing become of the same order for $\gamma \sim (Na/\ell_z)^{1/2}$, which is the same limit as that of the mean field quantum Hall regime.

One might wonder if for even larger values of γ the vortex core size can become larger than the intervortex spacing. This is not the case, because the vortex size saturates at d_{vx} for very large values of γ [184]. This effect was experimentally observed in [185].

Vortices in an ideal gas in the LLL

As a side-remark on the special properties of a system without interactions in the LLL, one might look back at the wave function of such a system, equation (7.16). This wave function is Gaussian times a complex polynomial of order m_z, and thus has m_z complex zeroes z_i. Integrating the phase of Ψ_{LLL} around one of the zeroes gives 2π.

A system described by the LLL wave function (7.16) thus necessarily contains vortices, if it does not populate only the $m_z = 0$ state. This might not seem surprising at first sight, given that the Landau level structure appears due to a fast rotation of the system. Note however that the LLL wave function of equation (7.16) is a sum of single particle states, and an eigenfunction of the hamiltonian of an ideal gas in the LLL. An ideal gas can thus contain vortices, which is contrary to a sometimes encountered belief, that vortices are a proof for the superfluidity of a system.

To get some insight on the distribution of these LLL-vortices, one needs to look at the statistical properties of the roots of the LLL-polynomial. This polynomial belongs to the class of Weyl-polynomials for a complex variable ζ

$$P(\zeta) = \sum_{m=0}^{m_{\max}} a_m \frac{\zeta^m}{\sqrt{m!}} \ ,$$

where the a_m are independent random complex numbers with the same gaussian probability distribution. Those polynomials were studied by Hannay and Leboeuf [186–188], who showed that the roots of such polynomials are *not* randomly distributed. Instead their position distribution shows anti-bunching. To illustrate this anti-bunching, figure 7.3 (a) shows a distribution of the zeros for a LLL-polynomial of order 30, where the coefficients a_{m_z} are randomly chosen with a gaussian distribution. For comparison the positions of the roots are chosen randomly (but also with a gaussian distribution) in figure 7.3 (b).

Also note that the states with different m_z correspond to circular density distributions, where the distance of the density maximum from $z = 0$ increases with m_z. In the case of an ideal gas, and macroscopic population of the LLL-modes, the vortices can be understood as the points of destructive interference of the macroscopically populated LLL modes. The observed interference is thus reminiscent of the interference of a 1D array of BECs [3, 35].

7.3.3 The fractional quantum Hall regime

For rotation frequencies very close to the trap frequency (i.e. very large γ), filling factors $\nu_f < 1$ can be reached, which corresponds to the situation of the fractional quantum Hall effect (FQHE) for fermions. To estimate the conditions for this regime one should note that for a gas that only populates LLL-modes, the number of occupied states in the LLL is equal to the number of vortices $N_l = N_{vx}$. The filling factor is thus

$$\nu_f = \frac{N}{N_{vx}}.$$

With the vortex surface density n_{vx} one obtains

$$N_{vx} = n_{vx}\pi r^2 = \sqrt{\gamma^2 - 1}\left(\frac{Na}{\ell_z}\right)^{1/2} ,$$

and a filling factor $\nu_f < 1$ is reached for

$$\gamma > \left(\frac{N\ell_z}{a}\right)^{1/2} . \tag{7.17}$$

This condition is a much stronger constraint than the condition to be fully in the LLL (equation (7.15)), as in most experiments only the quasi-2D regime is reached, which is defined by $\ell_z \gg a$ (see chapter 3).

Laughlin wave function for Bosons

For fractional filling factors $\nu_f < 1$ the equivalent to the Laughlin wave functions for fermions ($\nu_f = 1/(2p + 1)$, see equation (7.13)) corresponds to $\nu_f = 1/(2p)$ for bosonic systems. Except of the change in the exponent, which is $1/\nu_f = 2p$ instead of $1/\nu_f = 2p+1$, the bosonic and the fermionic wave function are equivalent, and in the bosonic case the wave function with the lowest exponent is

$$\Psi_{1/2}(z_1, ..., z_N) = \prod_{i<j}(z_i - z_j)^2 \; e^{-\sum |z_i|^2/(4\ell^2)}. \tag{7.18}$$

The change in the exponent is of course necessary, as the bosonic wave function must be symmetric instead of antisymmetric. One can show that in the case of an interaction potential $\delta(r)$ the function $\Psi_{1/2}$ is an exact eigenstate of the N-body hamiltonian of the LLL [41,174].

For the detection of this particular state it was proposed to perform a time of flight experiment, and study the correlations in the density [151]. This should reveal the specific distribution of the atoms in the system [183].

Melting of the vortex lattice

For filling factors $\nu_f > 1/2$ no exact solutions are known. For small systems of 5 to 20 particles the hamiltonian was diagonalized numerically, and for these numbers a new region of distinct behavior was found [40,41,167,179,181]: while for filling factors $\nu_f \gtrsim 8$ the system is still in the mean field quantum Hall regime, exotic states which have an analogue in the fermionic FQHE, were found numerically for $1/2 < \nu_f \lesssim 8$. These states have remarkable statistical properties, and are highly correlated.

A question of special interest regarding this regime concerns the experimental signature of the transition between the mean field and the correlated state regime. In [178] Sinova *et al.* studied the quantum fluctuations of the vortex positions for diminishing ν_f. They showed that for $\nu_f \sim 8$ the vortex lattice melts due to the quantum uncertainty in the positions of the individual vortices. This approximative value of the filling factor where mean field theory breaks down is confirmed by a study of Cooper *et al.* [40]. The authors of this work show that the gaps in the excitation spectrum of the incompressible states disappear for $\nu_f \sim 6$.

Comparing these different studies, it becomes clear that for an experimental observation of the distinct properties of the FQHE regime, filling factors smaller than ~ 8 need to be achieved. In the next section the experimental conditions are discussed, under which such small ν_f can be realized. Note however that so far only filling factors larger than 100 were achieved experimentally [1,24].

7.3.4 How to reach the regime of the FQHE in a dilute Bose gas

To reach the regime of the fractional quantum Hall effect, according to the above considerations several conditions must be fulfilled:

1. **Be 2D.** The QHE is an effect that is based on the 2-dimensionality of the system. For dilute Bose-gases the confinement must thus be strong enough in the z-direction to freeze the motion in this direction. An example for the realization of such a potential by an optical lattice is given in part II of this manuscript.

2. **Be in the LLL.** To achieve a situation in which the system is restricted to the LLL the chemical potential and the temperature of the cloud must be smaller than the energy distance to the next Landau level, which is $2\hbar\omega_\perp$. Note that in a pancake shaped trap this condition is harder to fulfill than the 2-dimensionality.

3. **Have sufficient LLL-states of energy $< 2\hbar\omega_\perp$.** To achieve filling factors $\nu_f < 1$, the number of LLL-states within the energy range $[0, 2\hbar\omega_\perp]$ must be larger than the atom number of the system N. In the case of a completely flat LLL this is automatically the case. Note however that for this situation the condensate must rotate exactly at the

harmonic trapping frequency, and is then not confined anymore. This is experimentally not possible. The FQHE regime can however also be attained if the energy of the LLL states increases slightly with m_z (see figure 7.2 (b)). The corresponding condition is then (equation 7.10 for $m_z = n = N$)

$$\frac{1}{2}\left(1 - \frac{\Omega}{\omega_\perp}\right) \leqslant N^{-1}.$$

For atom numbers of the order of $N = 10^4$ this signifies that an extraordinary precision on the rotation frequency of the system is needed.

Until this day no experiment has fulfilled all of these requirements. While some experiments have attained the 2D regime in optical potentials [5,25,26], there is usually no rotation involved in these experiments.

Two groups have so far attained the regime of the LLL by different methods. The group of Eric Cornell achieved the LLL-regime by rotating at a frequency very near to the trapping frequency ($\Omega \approx 0.99\omega_\perp$) [24]. In experiments of our group the LLL-regime was also reached [1]. This was achieved by adding a quartic potential to the harmonic trap, as described in chapter 8.

No experiment has however been near to fulfilling condition 3, concerning the number of states in the LLL compared to the atom number N. Due to the relatively large atom numbers of the order of $10^4 - 10^5$ the rotation frequency must be extremely well controlled, and for current experimental setups this seems not feasible to the required accuracy of $1 - \Omega/\omega_\perp \sim 10^{-4}$.

A possible solution to this problem is to rotate the sites of a 1D optical lattice, as described in chapter 4. In this case each individual site contains a much smaller atom number than a standard BEC, and the FQHE-regime can be reached more easily. In this case one would need to look for a signature of this regime in the bulk system (including many lattice sites), as small atom numbers usually represent a serious limit to the imaging quality. Some proposals concerning such multi-layer geometries were made by Schoutens *et al.* [189,190].

7.4 Conclusion

The notion of "fast rotation" of a BEC is defined by a large angular momentum per particle, $L_z \gg \hbar$. As has been discussed in this chapter, two regimes of fast rotation exist in harmonic traps. These regimes are separated by comparing the atom number to $\Omega/\omega_\perp$, i.e. the ratio of the rotation frequency and the harmonic trapping frequency. This situation is illustrated schematically in figure 7.4. For intermediate rotation frequencies the system stays a Bose-Einstein condensate, containing a large triangular vortex lattice. The velocity field of a large vortex lattice gives a good coarse grain imitation of a solid body rotation. This description stays right even for rotation frequencies so close to $\omega_\perp$, that the system populates only states of the LLL. For rotation frequencies even closer to $\omega_\perp$, the number of states in the LLL becomes larger than the number of atoms, and this situation gives rise to new phenomena closely related to the physics of the fractional quantum Hall effect.

The FQHE-regime was not reached so far by any experiment. One of the main problems is that in a harmonic trap the system becomes unstable for $\Omega \to \omega_\perp$. We have thus chosen to work with a potential containing a small quartic term, that allows fast rotation at $\Omega = \omega_\perp$. Even if the modification of the potential alters the system properties, it should in principle allow to explore the same regimes as a purely harmonic potential, included the mean field quantum Hall and the FQHE-regimes. This situation is discussed in chapter 8, where also experimental results obtained with the quadratic+quartic potential are presented.

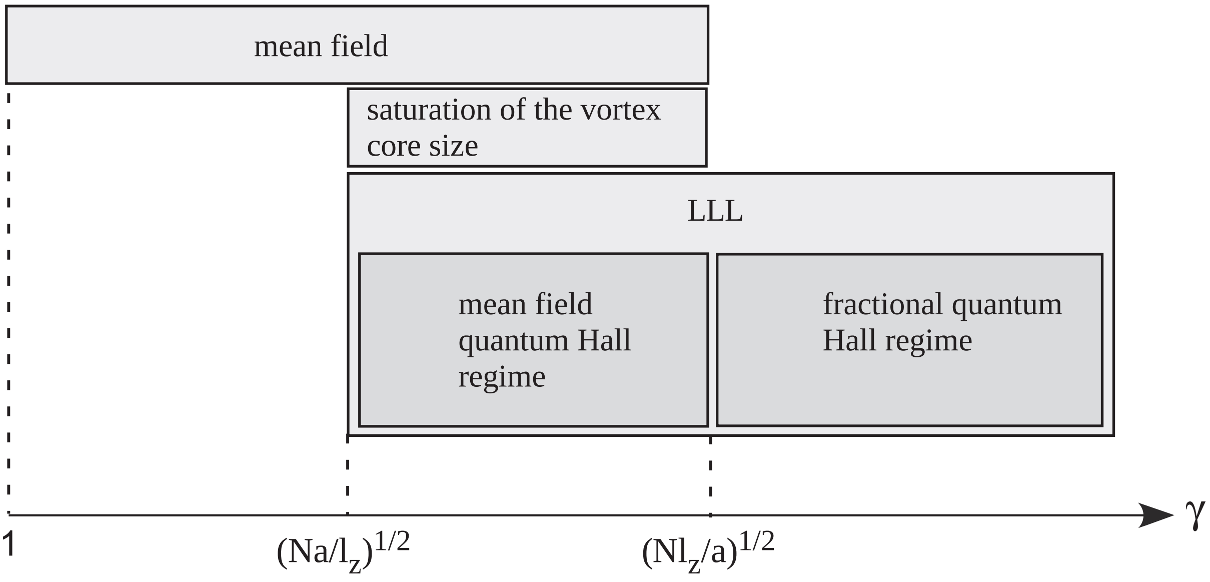

Figure 7.4: Schematic overview of the different regimes for fast rotating condensates. The parameter $\gamma = \left(\sqrt{1 - \Omega^2/\omega_\perp^2}\right)^{-1}$ gives a measure for the rotation frequency as compared to the trap frequency. The mean field description stays valid for intermediate rotation frequencies, where the system populates only states of the LLL, but the number of atoms is much larger than the number of LLL-states. For rotation frequencies even closer to $\omega_\perp$, the number of states becomes comparable to the atom number, and a regime of strongly correlated states is reached, which is an analogue to the FQHE-regime for fermions.

Chapter 8

Fast rotation of a BEC in a quartic potential

To achieve the regime of the FQHE it is necessary to rotate at frequencies Ω very close to the harmonic trapping frequency. For the stirring mechanism used in our experiment, an elliptic red detuned "spoon" potential, this is not possible in a harmonic trap, due to the resonant excitation of the dipole mode for $\Omega \sim \omega_\perp$, which destabilizes the trap [191]. For this reason we have chosen to work with an additional anharmonic potential, which contains an additional quartic term in the radial confinement.

This quartic terms alters the structure of the Landau levels, and the energy spectrum for the quadratic+quartic case is calculated in the first section of this chapter. Section 8.2 presents experimental results for fast rotating condensates in the anharmonic potential. This section was published in [1].

8.1 Rotating bosons in anharmonic traps

The anharmonic potential was created experimentally by adding a far blue detuned laser beam to the harmonic trap, which is described in section 8.2. The total radial potential is well approximated by

$$U(r) = \frac{m}{2}\omega_\perp^2 r^2 + \frac{k}{4} r^4,$$

where k classifies the strength of the quartic term, and is given by the experimental parameters. In our experimental situation $k = 2.6 \cdot 10^{-11}\ \mathrm{J\,m^{-4}}$ and $\omega_\perp/(2\pi) \approx 65\,\mathrm{Hz}$, and the nonrotating BEC has a radius of $\sim 5\,\mu\mathrm{m}$. For this radius and experimental parameters the quadratic term is a hundred times larger than the quartic term, so that the confinement is essentially harmonic for a cloud at rest. For a rotating cloud this is however not the case. The influence of the quartic term on the shape of the Landau levels of a fast rotating cloud is described in the following section, while the corresponding experiments are presented in section 8.2.

8.1.1 The lowest Landau level in an anharmonic trap

In spite of the modification of the potential by the quartic term, it might also be possible to reach the LLL regime in this situation for fast rotation frequencies. It is thus interesting to look at the structure of the LLL for a single particle in the quadratic+quartic confinement described above.

For the calculation of the energy levels in the quadratic+quartic case it is useful to introduce a new radial quantum number n_m which labels the excitation in the xy-plane of a state with a given angular momentum m_z. To visualize this labeling, the energies of the states $|m_z, n_m\rangle$ are

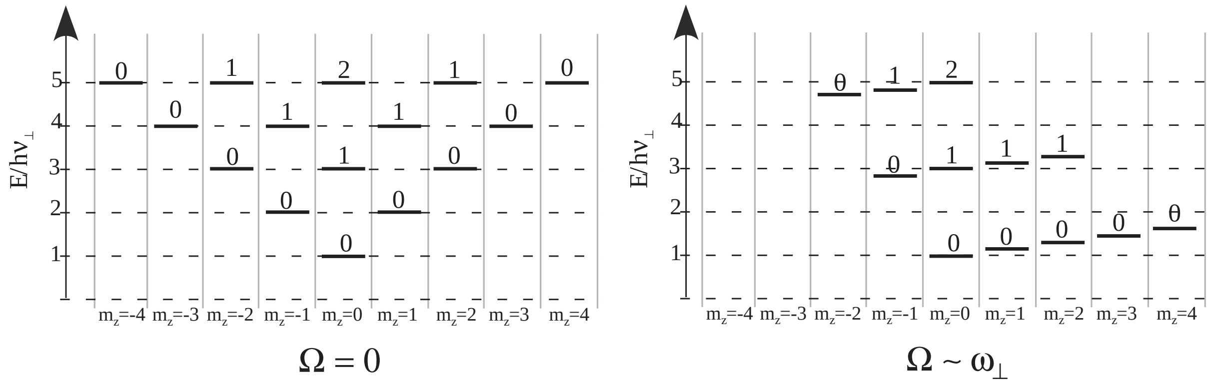

Figure 8.1: Single particle levels in a 2D harmonic oscillator. The energy of a state can be characterized by two quantum numbers: m_z labels the angular momentum along z and n_m characterizes the excitation in the xy-plane for a given m_z. Here each state is labeled with its quantum number n_m. The energies of the states $|m_z, n_m\rangle$ are shown for a nonrotating system ($\Omega = 0$) and a system rotating with a frequency slightly below the harmonic trapping frequency $\Omega \lesssim \omega_\perp$.

shown in figure 8.1 for the case of a purely harmonic confinement, which is not rotating (left) or rotating at a frequency slightly smaller than the trapping frequency (right)[1].

In the case of quadratic+quartic confinement, one can then find the energy of a state with a given m_z through a perturbative treatment of the quartic term. To this end the eigenfunctions in the xy-plane are written as $\Psi(r,\phi) = \psi(r)e^{im_z\phi}$. Applying the 2D-Hamiltonian in cylindric coordinates to this ansatz gives the following equation for the radial function $\psi(r)$:

$$-\frac{\hbar^2}{2m}\left(\frac{\partial^2}{\partial r^2}\psi + \frac{1}{r}\frac{\partial}{\partial r}\psi\right) + \left(\frac{\hbar^2 m_z^2}{2mr^2} + \frac{m}{2}\omega_\perp^2 r^2 + \frac{k}{4}r^4\right)\psi = E_\perp(m_z, n_m)\ \psi, \tag{8.1}$$

where the second bracket on the left hand side corresponds to an effective m_z-dependant potential $U_{\text{eff}}(m_z)$.
Equation (8.1) can be written as

$$\left(H_0 + \frac{k}{4}r^4\right)\psi = E_\perp(m_z, n_m)\ \psi,$$

where H_0 is the Hamiltonian of the purely harmonic confinement with frequency $\omega_\perp$. For $n_m = 0$ and $m_z \geq 0$ the eigenfunctions $\psi^{(0)}_{(m_z,0)}$ of the unperturbed Hamiltonian H_0 are (see section 7.3.2):

$$\psi^{(0)}_{(m_z,0)} \propto \frac{r^{m_z}}{\sqrt{\pi|m_z|!}}\, e^{-r^2/(2a_\perp^2)},$$

where $a_\perp = \sqrt{\hbar/(m\omega_\perp)}$ is the radial harmonic oscillator length. The eigenenergies corresponding to these exact solutions are

$$E_\perp^{(0)}(m_z, 0) = \hbar\omega_\perp(|m_z| + 1).$$

This energy dependence is shown in the left part of figure 8.1.
In first order perturbation theory the eigenenergies of the hamiltonian $H = H_0 + kr^4/4$ are then calculated as

$$E_\perp^{(1)}(m_z, 0) = E_\perp^{(0)}(m_z, 0) + \frac{1}{4}\frac{\int \psi^{(0)*} kr^4 \psi^{(0)}\, d^2r}{\int \psi^{(0)*}\psi^{(0)}\, d^2r},$$

---

[1] In the notation of section 7.2.2 the quantum number n_m is given by $n_m = (n - |m_z|)/2$.

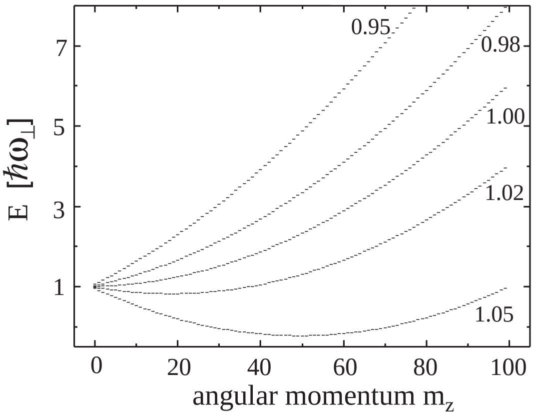

Figure 8.2: Rotating in a quadratic + quartic potential. The structure of the lowest Landau level is modified due to the quartic term as compared to figure 7.2. The individual curves show the energy of the states of the LLL, with $0 < m_z < 100$, and correspond to rotation frequencies $\Omega/\omega_\perp = 1.05$, 1.02, 1.00, 0.98 and 0.95 from the bottom to the top.

which leads to the energy spectrum:

$$E_\perp^{(1)} = \hbar\omega_\perp(|m_z|+1) + \frac{\hbar^2 k}{4m^2\omega_\perp^2}\left(|m_z|+1\right)\left(|m_z|+2\right).$$

One can show that the validity condition for this result is given by:

$$|m_z| \ll \frac{m^2\omega_\perp^3}{k\hbar},$$

which corresponds to $|m_z| \ll 500$ for our experimental parameters.
In the rotating frame one has then to add the term $-m_z\hbar\Omega$, and this gives in first order approximation:

$$E_\perp^{(\mathrm{rot})}(m_z,0) = \hbar\omega_\perp(|m_z|+1) + \frac{\hbar^2 k}{4m^2\omega_\perp^2}\left(|m_z|+1\right)\left(|m_z|+2\right) - m_z\hbar\Omega. \tag{8.2}$$

This energy dependence of the states of the lowest Landau level ($m_z \geq 0$ and $n_m = 0$) is plotted in figure 8.2 for five different rotation frequencies $\Omega/\omega_\perp$ =0.95, 0.98, 1.00, 1.02 and 1.05. One can clearly see the influence of the quartic term: in the case $\Omega = \omega_\perp$ the LLL is not degenerate, but the energy of its states increases significantly with m_z. This effect becomes more important for states with high angular momentum m_z, as the radii of the corresponding orbits increase with m_z, and the wave function extends more and more into an area where the quartic term is important.

8.1.2 Spacing of the Landau levels

For the calculation of states with arbitrary n_m one has to look first for the minimum of the effective potential $U_{\mathrm{eff}}(m_z, r)$. Treating the quartic term again as a small perturbation (which amounts to neglecting terms in k^2), one gets the position of this minimum:

$$r_\mathrm{q} = r_0 - \frac{k r_0^3}{4m\omega_\perp^2}, \qquad \text{where} \qquad r_0 = a_\perp\sqrt{|m_z|},$$

and r_0 is the minimum for the purely harmonic case with $k = 0$. The effective harmonic frequency ω_e at this minimum is then calculated through $m\omega_e^2 = \partial^2/\partial r^2(U_{\text{eff}})$ at the position $r = r_{\text{q}}$, which leads to

$$\omega_e \approx \left(2 + \frac{27}{16}\frac{\hbar k}{m^2\omega_\perp^3}|m_z|\right)\omega_\perp$$

The energy of the excited states in this effective potential are calculated as

$$E_\perp(m_z, n_m) \approx U_{\text{eff}}(m_z, r = r_q) + (n_m + \frac{1}{2})\,\hbar\omega_e\ .$$

which gives

$$E_\perp(m_z, n_m) \approx E_\perp^{(1)}(m_z, 0) + n_m\,\hbar\omega_\perp\left(2 + \frac{27}{16}\frac{\hbar k}{m^2\omega_\perp^3}|m_z|\right) \approx E_\perp^{(1)}(m_z, 0) + 2n_m\hbar\omega_\perp, \qquad (8.3)$$

and the second approximation holds because of $\hbar k|m_z|/(m^2\omega_\perp^3) \ll 1$. The splitting between levels with equal m_z thus remains $\approx 2\hbar\omega_\perp$, as in the harmonic case.

To answer the question if the LLL-regime can be reached in a quadratic+quartic trap, one must thus look at the number of states in an energy interval of width $2\hbar\omega_\perp$. The increase in the energy of the states of the LLL with increasing m_z limits the number of states in this energy interval even at $\Omega = \omega_\perp$. Note however that this number must be limited in any case, as only a system of infinite size can have an infinitely degenerate LLL. In this respect the addition of a quartic potential is similar to rotating in a harmonic trap, but at $\Omega < \omega_\perp$. In both cases the relevant number is the number of states in an energy interval of width $2\hbar\omega_\perp$, and this can be tuned either by approaching $\Omega/\omega_\perp \to 1$ in the harmonic case, or by rotating at $\Omega \sim \omega_\perp$ and diminishing the quartic term in a combined quadratic+quartic potential.

Ideal rotation frequency in the quadratic+quartic case

The relevant parameter for the FQHE-regime is the LLL-filling factor, $\nu_f = N/N_l$, which is the ratio of the atom number and the number of LLL-states in an energy interval of width $2\hbar\omega_\perp$. In the purely quadratic case ν_f decreases if $\omega_\perp - \Omega$ approaches 0.

From figure 8.2 one can see that in the quadratic+quartic case the number N_l can be increased by rotating at a frequency Ω larger than $\omega_\perp$. This is due to the negative slope in the m_z-dependence of the energy $E_\perp(m_z, 0)$ for small m_z. From equation (8.2) one can derive that the LLL-state with the smallest energy has the quantum number

$$m_{z0} \approx \frac{2\hbar(\Omega - \omega_\perp)}{ka_\perp^4},$$

and due to the approximately quadratic dependence $E_\perp(m_z) - E_\perp(m_{z0}) \propto (m_z - m_{z0})^2$ the number of states in the energy-interval $[E_\perp(m_{z0}, 0), \hbar\omega_\perp]$ is $N_l \approx 2m_{z0}$.

The number m_{z0} is limited due to the fact that the states of the first Landau level have the same energy dependence in m_z as those in the LLL. If one sets the condition $E_\perp(m_{z0}, 1) \geq E_\perp(0, 0) = \hbar\omega_\perp$, one gets a bound on the rotation frequency:

$$\hbar(\Omega - \omega_\perp) \leq \sqrt{2\hbar\omega_\perp ka_\perp^4}.$$

For our experimental parameters this is equivalent to $\Omega \leq 1.06\,\omega_\perp$, and for the "ideal" rotation frequency, $\Omega \approx 1.06\,\omega_\perp$, the number of levels is $N_l = 2 \cdot (8\hbar\omega_\perp/(ka_\perp^4))^{1/2} \approx 130$.

This situation can be compared to rotation at $\Omega = \omega_\perp$, where the number of states in the energy interval $[\hbar\omega_\perp, 3\hbar\omega_\perp]$ can be evaluated to $N_l = (8\hbar\omega_\perp/(ka_\perp^4))^{1/2} \approx 65$. In our case a rotation at the slightly higher frequency $\Omega = 1.06\,\omega_\perp$ thus decreases the filling factor by a factor 2, for else identical parameters.

Of course the above calculation also shows that the highest reachable N_l for the strength of our quartic potential is much smaller than typical atom numbers of our system. The possibility to reach fractional filling factors is thus very restricted. The results of the previous paragraphs show however that the presence of the quartic term does not prevent the possibility to reach the regime of the mean field quantum Hall effect, where only states of the LLL are populated. The following section presents experimental results of fast rotating condensates in this regime.

8.2 Fast rotation of an ultra-cold Bose gas

This section was published in: V. Bretin, S. Stock, Y. Seurin and J. Dalibard, Fast rotation of an ultra-cold Bose gas, Phys. Rev. Lett. ***92****, 050403 (2004) [1].*

The fast rotation of a macroscopic quantum object often involves a dramatic change of its properties. For rotating liquid ^{4}He, superfluidity is expected to disappear for large rotation frequencies [160]. A similar effect occurs for type-II superconductors placed in a magnetic field, which loose their superconductivity when the field exceeds a critical value [37]. For the last few years it has been possible to set gaseous Bose-Einstein condensates into rotation, by nucleating in the gas quantized vortices which arrange themselves in a triangular lattice [128,156–159]. The theoretical investigation of these fast rotating gases has led to several possible scenarios depending on the confinement of the gas: nucleation of multiply charged vortices [184,192–197], melting of the vortex lattice [178], or effects closely connected to Quantum Hall physics [40,41,166–168].

Consider a condensate transversely confined by a harmonic potential with frequency $\omega_\perp$. For an angular momentum per particle $L_z \gg \hbar$, the condensate contains many vortices [165] and the coarse grained average of the velocity field is identical to that of a rigid body with angular frequency Ω [160]. The limiting case $\Omega = \omega_\perp$ corresponds to $L_z = \infty$ and is thus singular. This can be understood in the frame rotating at frequency Ω, where the trapping force is compensated by the centrifugal force and only the Coriolis force remains. The physics of this situation is analogous to that of charged particles in a uniform magnetic field and one expects to recover for weak interactions an energy spectrum with Landau levels separated by $2\,\hbar\omega_\perp$. However the absence of confinement in a harmonic trap rotating at $\Omega = \omega_\perp$ makes this study experimentally delicate [191]. The Boulder group recently reached $\Omega = 0.99\ \omega_\perp$ using evaporative spin-up [161].

In the present paper, following suggestions in [192,192–195] we study the rotation of a Bose-Einstein condensate in a trap whose potential is well approximated by a superposition of a quadratic and a small quartic potential:

$$V(\boldsymbol{r}) \simeq \frac{1}{2}m\omega_z^2 z^2 + \frac{1}{2}m\omega_\perp^2 r_\perp^2 + \frac{1}{4}k r_\perp^4 \qquad (k > 0)\ . \tag{8.4}$$

where $x^2 + y^2 = r_\perp^2$. We can thus explore with no restriction the domain of rotation frequencies Ω around $\omega_\perp$. For $\Omega/\omega_\perp < 0.95$ we observe a regular vortex lattice. This lattice gets disordered when Ω increases. For $\Omega > \omega_\perp$ the number of detectable vortices is dramatically reduced although we have a clear evidence that the gas is still ultra-cold and in fast rotation. We conclude by proposing some possible explanations for this behavior.

Our ^{87}Rb condensate is formed by radio-frequency evaporation in a combined magnetic+laser trap. The pure magnetic trap provides a harmonic confinement along the 3 directions with the frequencies $\omega_\perp^{(0)}/2\pi = 75.5$ Hz and $\omega_z/2\pi = 11.0$ Hz. We superimpose a blue detuned laser (wavelength 532 nm) propagating along the z direction to provide the quartic term in the

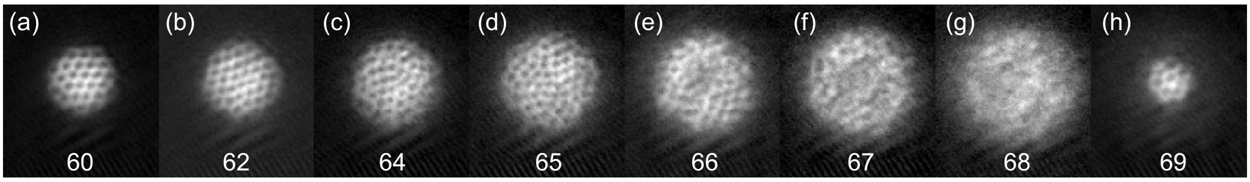

Figure 8.3: Pictures of the rotating gas taken along the rotation axis after 18 ms time of flight. We indicate in each picture the stirring frequency $\Omega_{\mathrm{stir}}^{(2)}$ during the second stirring phase ($\omega_\perp/2\pi = 64.8$ Hz). The vertical size of each image is 306 μm.

confinement. The potential created by the laser is

$$U(r_\perp) = U_0 \exp\left(-\frac{2r_\perp^2}{w^2}\right) \simeq U_0 - \frac{2U_0}{w^2} r_\perp^2 + \frac{2U_0}{w^4} r_\perp^4 \; . \tag{8.5}$$

The laser's waist is $w = 25$ μm and its power is 1.2 mW. The first term U_0 ($\sim k_B \times 90$ nK) in the right hand side of (8.5) is a mere shift of the energy scale. The second term is a correction of the transverse trapping frequency; from the oscillation frequency of the center-of-mass of the condensate, we infer for the combined magnetic-laser trap $\omega_\perp/2\pi = 64.8\,(3)$ Hz [2]. The last term in (8.5) corresponds to the desired quartic confinement, with $k = 2.6\,(3) \times 10^{-11}$ $\mathrm{J\,m^{-4}}$.

We start the experimental sequence with a quasi-pure condensate that we stir using an additional laser beam, also propagating along z [128]. This laser stirrer creates an anisotropic potential in the xy plane which rotates at a frequency Ω_{stir}. To bring the condensate in rotation at a frequency close to $\omega_\perp$, we use two stirring phases. First we choose $\Omega_{\mathrm{stir}}^{(1)} \simeq \omega_\perp/\sqrt{2}$, so that the stirring laser resonantly excites the transverse quadrupole mode $m = +2$ of the condensate at rest [164]. The duration of this first excitation is 300 ms and we then let the condensate relax for 400 ms in the axisymmetric trap. This procedure sets the condensate in rotation, with a vortex lattice containing typically 15 vortices.

We then apply the laser stirrer for a second time period, now at a rotation frequency $\Omega_{\mathrm{stir}}^{(2)}$ close to or even above $\omega_\perp$. For the condensate with 15 vortices prepared during the first phase, the transverse quadrupole mode is shifted to a higher frequency and can now be resonantly excited by a stirrer rotating at $\Omega_{\mathrm{stir}}^{(2)} \sim \omega_\perp$ [159, 198]. The second stirring phase lasts for 600 ms. It is followed by a 500 ms period during which we let the condensate equilibrate again in the axisymmetric trap. At this stage the number of trapped atoms is 3×10^5.

We find that this double nucleation procedure is a reliable way to produce large vortex arrays and to reach effective rotation frequencies Ω_{eff} around or above $\omega_\perp$. It has one drawback however: the effective rotation frequency Ω_{eff} of the gas after equilibration might differ significantly from the rotation frequency $\Omega_{\mathrm{stir}}^{(2)}$ that we apply during the second stirring phase. The stirring phase injects angular momentum in the system, and the rotation frequency of the atom cloud may subsequently change if the atom distribution (hence the moment of inertia) evolves during the final equilibration phase.

The rotating atom cloud is then probed destructively by switching off the confining potential, letting the cloud expand during $\tau = 18$ ms and performing absorption imaging. We take simultaneously two images of the atom cloud after time of flight (TOF). One imaging beam is parallel to the rotation axis z and the other one is perpendicular to z [199]. Fig. 8.3a-h shows images taken along the z axis and obtained for various $\Omega_{\mathrm{stir}}^{(2)}$ around $\omega_\perp$. When $\Omega_{\mathrm{stir}}^{(2)}$ increases, the increasing centrifugal potential weakens the transverse confinement. This leads to an increasing radius in the xy plane. As it can be seen from the transverse and longitudinal density profiles of Fig. 8.4, obtained for $\Omega_{\mathrm{stir}}^{(2)}/2\pi = 66$ Hz, the gas after TOF has the shape of a flat pancake.

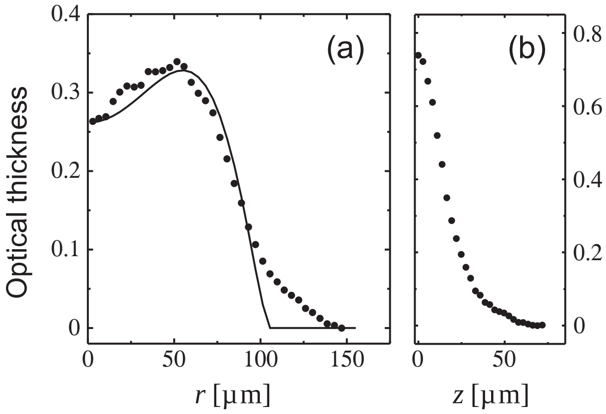

Figure 8.4: Optical thickness of the atom cloud after time-of-flight for $\Omega_{\mathrm{stir}}^{(2)}/2\pi = 66$ Hz. (a) Radial distribution in the xy plane of Fig. 8.3e. Continuous line: fit using the Thomas-Fermi distribution (8.6). (b) Distribution along the z axis averaged over $|x| < 20$ μm (imaging beam propagating along y).

The limit of our method for setting the gas in fast rotation is shown on the image (h) at the right of Fig. 8.3. It corresponds to $\Omega_{\mathrm{stir}}^{(2)}/2\pi = 69$ Hz, far from the quadrupole resonance of the condensate after the first nucleation. In this case we could not bring the gas in the desired fast rotation regime.

For the pictures (e,f) obtained with $\Omega_{\mathrm{stir}}^{(2)}/2\pi = 66$ and 67 Hz, the optical thickness of the cloud has a local minimum in the center; this indicates that the confining potential in the rotating frame, $V_{\mathrm{rot}}(\boldsymbol{r}) = V(\boldsymbol{r}) - m\Omega_{\mathrm{eff}}^2 r_\perp^2/2$, has a Mexican hat shape. The effective rotation frequency Ω_{eff} thus exceeds $\omega_\perp$. The striking feature of these images is the small number of visible vortices which seems to conflict with a large value of Ω_{eff}. The main goal of the remaining part of this Letter is to provide more information on this puzzling regime.

In order to analyze quantitatively the pictures of Fig. 8.3, we need to model the evolution of the cloud during TOF. For a pure harmonic potential ($k = 0$), a generalization of the analysis of [94] to the case of a rotating condensate shows that the expansion in the xy plane is well described by a scaling of the initial distribution by the factor $(1+\omega_\perp^2\tau^2)^{1/2}$ [109,200]. We assume here that this is still approximately the case for a condensate prepared in a trap with a non zero quartic term $kr_\perp^4/4$.

We have analyzed 60 images such as those of Fig. 8.3, assuming an initial Thomas-Fermi distribution:

$$n(\boldsymbol{r}) = \frac{m}{4\pi\hbar^2 a}\left(\mu - V_{\mathrm{rot}}(\boldsymbol{r})\right) , \tag{8.6}$$

where $a = 5.2$ nm is the scattering length characterizing the atomic interactions and μ the chemical potential. The optical thickness for the imaging beam propagating along z, proportional to the column atomic density in the xy plane, varies as $(\alpha + \beta r_\perp^2 + \gamma r_\perp^4)^{3/2}$, where α, β, γ can be expressed in terms of the physical parameters of the problem[2]. An example of the fit, which takes μ and Ω_{eff} as adjustable parameters, is given in Fig. 8.4a. The agreement is correct, though not as good as for condensates confined in purely harmonic traps. This may be a consequence of the approximate character of the scaling transform that we use to describe the TOF evolution. The resulting values for Ω_{eff} as a function of $\Omega_{\mathrm{stir}}^{(2)}$ are given in Fig. 8.5. We find $\Omega_{\mathrm{eff}} \simeq \Omega_{\mathrm{stir}}^{(2)}$ for stirring frequencies ≤ 68 Hz. Note that for $\Omega_{\mathrm{stir}}^{(2)}/2\pi = 68$ Hz (image Fig. 8.3g) the quality of

---

[2] Such a simple formula could not be obtained for the column density along y, hence the absence of a fitting function in Fig. 8.4b.

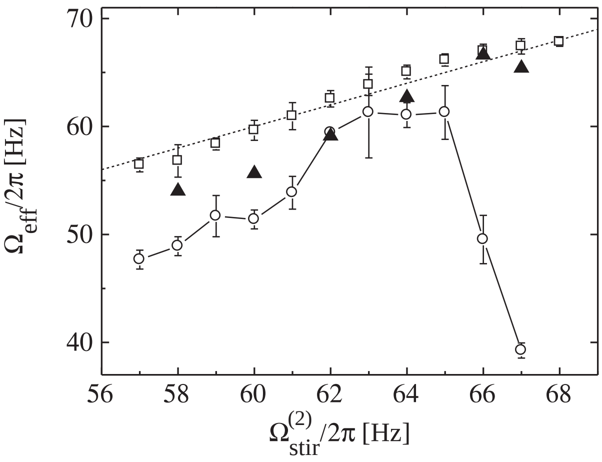

Figure 8.5: Effective rotation frequency Ω_{eff} as a function of the stirring frequency $\Omega^{(2)}_{\text{stir}}$. □: values deduced from the fit using the Thomas-Fermi distribution (8.6). ○: values obtained by measuring the vortex density in the TOF pictures. ▲: values obtained using surface wave spectroscopy. The bars indicate standard deviations.

the fit is comparatively poor due to local inhomogeneities of the atom cloud.

From the value of μ given by the fit, we recover the atom number [192]. For $\Omega/(2\pi) = 67$ Hz, the Thomas-Fermi distribution (8.6) corresponds to a nearly spherical atom cloud before TOF (diameter 30 μm in the xy plane and length 34 μm along z).

A second determination of the effective rotation frequency Ω_{eff} of the condensate is provided by the vortex surface density after TOF. This is measured manually by counting the number of vortices in a test surface of a given area (typically 25% of the whole area of the condensate). Assuming that the vortex pattern is scaled by the same factor as the condensate density, we deduce the vortex density n_v before TOF, hence the rotation frequency $\Omega_{\text{eff}} = \pi\hbar n_v/m$ [165]. For $\Omega^{(2)}_{\text{stir}} < \omega_\perp$, the value of Ω_{eff} deduced in this way and plotted in Fig. 8.5 is in fair agreement with the one deduced from the fit of the images[3]. On the contrary, for $\Omega^{(2)}_{\text{stir}}/2\pi = 66 - 68$ Hz the number of distinguishable vortices is much too low to account for the rotation frequencies determined from the fits of the TOF images. In this regime the vortex lines are not detectable neither in the images taken perpendicular to the z axis (not shown here), contrarily to what happens for lower stirring frequencies [199, 201].

In order to gather more information on the rotational properties of the gas, we now study the two transverse quadrupole modes $m = \pm 2$ of the gas. We recall that these two modes have the same frequency for a non rotating gas, due to symmetry. For a rotating gas in the hydrodynamic regime, the frequency difference $\omega_{+2} - \omega_{-2}$ is proportional to the ratio between the average angular momentum of the gas and its moment of inertia, which is nothing but the desired effective rotation frequency Ω_{eff} [198]. The strength of this approach is that it does not make any assumption on the expansion during TOF.

To study these quadrupole modes, we briefly illuminate the rotating gas using the laser stirrer, now with fixed axes [171]. This excites a superposition of the modes $m = \pm 2$ with equal amplitudes. We then let the cloud evolve freely in the trap for an adjustable duration and perform the TOF analysis. From the time variation of both the ellipticity of the cloud in the xy plane and the inclination of its eigenaxes, we deduce $\omega_{\pm 2}$, hence the effective rotation

---

[3] This value for Ω_{eff} is systematically slightly below the one derived from the cloud's radius as also found in [165].

frequency $\Omega_{\rm eff} = (\omega_{+2} - \omega_{-2})/2$. The corresponding results are plotted in Fig. 8.5. They are in good agreement with the results obtained from the fits of the images: $\Omega_{\rm eff} \simeq \Omega_{\rm stir}^{(2)}$. Consequently they conflict with the rotation frequency derived from the vortex surface density when $\Omega_{\rm stir}^{(2)}/2\pi = 66 - 68$ Hz.

To explain the absence of visible vortices in the regime $\Omega_{\rm stir}^{(2)}/2\pi = 66-68$ Hz, one could argue that the rotating gas might be relatively hot, hence described by classical physics. However all experiments shown here are performed in presence of radio-frequency (rf) evaporative cooling. The rf is set 24 kHz above the value which empties the trap and it eliminates all atoms crossing the horizontal plane located at a distance $x_{\rm ev} \sim 19$ μm below the center (one-dimensional evaporation). From evaporative cooling theory [60, 202] we know that the equilibrium temperature T of the rotating gas is a fraction of the evaporation threshold $V_{\rm rot}(x_{\rm ev}) \sim 30$ nK for $\Omega_{\rm eff}/2\pi = 67$ Hz. This indicates that T is in the range of $5 - 15$ nK, well below the critical temperature at this density (180 nK for an estimated density 3×10^{13} cm^{-3})[4]. This low temperature is also confirmed by the small decay rates of the quadrupole modes (~ 20 s^{-1}), characteristic of $T \ll T_c$.

The estimated temperature T is of the order of μ, since the Thomas-Fermi law (8.6) gives $\mu/k_{\rm B} = 8\,{\rm nK}$ for $\Omega/(2\pi) = 67\,{\rm Hz}$. It is also similar to the splitting between Landau levels $2\hbar\omega_\perp/k_B = 6.3\,{\rm nK}$, so that only the first two or three levels are appreciably populated. For each Landau level, the rf evaporation eliminates states with an angular momentum $L_z/\hbar > (x_{\rm ev}/a_{\rm ho})^2 \sim 200$, where $a_{\rm ho} = \sqrt{\hbar/(m\omega_\perp)}$.

A first possibility to interpret our data consists in assuming that the gas shown in Fig. 8.3e-g is rotating, that it is in the degenerate regime, but that it cannot be described by a single macroscopic wave function. A theoretical analysis along this line, involving the formation of composite bosons, has been proposed in [203]. We note however that such a fragmentation is usually expected when the number $N_{\rm lev}$ of single particle levels in an energy band of width μ is comparable with the atom number, while we have here $N_{\rm lev}/N \lesssim 10^{-2}$.

A second explanation is that the vortices are strongly tilted or bent for $\Omega \geq \omega_\perp$, so that they do not appear as clear density dips in the images of Fig. 8.3e-g. The distortion of the vortex lattice could result from (i) a strong increase of the cristallization time, (ii) a distortion due to the residual static anisotropy of the trap, (iii) an increase of the fragility of the vortex lattice. To check for possibility (i), we have increased $\tau_{\rm eq}$ from 500 ms to 2 s without noticing any qualitative change in the atom distribution (for larger $\tau_{\rm eq}$ the gas slows down significantly). Concerning option (ii), the Boulder group has shown for $\Omega = 0.95\,\omega_\perp$ that a static anisotropy of $\sim 4\%$ may reduce considerably the vortex visibility [201]. However the residual anisotropy of our trap is $< 1\%$ and this effect should be limited. Finally if option (iii) is valid, the vortex lattice should be visible only at ultra-low temperatures that cannot be reached in our experiment. A recent theoretical study [204] seems to favor this hypothesis: when looking for the ground state of the system using imaginary time evolution of the Gross-Pitaevskii equation, it was found that much longer times were required for $\Omega \gtrsim \omega_\perp$ to reach a well ordered vortex lattice.

To summarize we have presented in this Letter a direct evidence for a qualitative change in the appearance of a degenerate Bose gas, confined in a quadratic + quartic potential, when it is rotated around and just above the trapping frequency. The predicted existence of giant vortices in this type of potential [184, 192–197], remains to be investigated. Another extension of the present work consists in transposing the experimental scheme to a 2D geometry, where the motion along z would be frozen. For $\Omega \sim \omega_\perp$ the situation would then be the bosonic analog of the situation leading to the quantum Hall effect.

---

[4] The rotation of the gas is crucial for establishing a link between the evaporation radius and the temperature. For a gas at rest, the evaporation threshold is $V(x_{\rm ev})$ instead of $V_{\rm rot}(x_{\rm ev})$, which corresponds to a much higher temperature (100-200 nK).

Chapter 9

Condensation temperature in a quadratic+quartic potential

In the chapter 8 experiments with a fast rotating condensate in a nonharmonic potential were presented. This potential is well approximated by a 3-dimensional harmonic potential plus a radial quartic term. The results obtained for the rotating cloud in this potential are especially interesting for rotation frequencies near and above the radial trapping frequency: for rotation frequencies approaching $\omega_\perp$ the vortex contrast diminishes, and it nearly vanishes for even faster rotation $\Omega \sim 1.05\,\omega_\perp$ [1]. To explain this phenomenon, several possible explanations were proposed. One of these possibilities is the presence of a large fraction of thermal atoms which blurs the image. Other possibilities include fragmentation of the condensate or excitation of the vortex lines.

To be able to exclude the - scientifically less interesting - hypothesis of a large thermal cloud, one needs to calculate the condensation temperature T_c for a fast rotating condensate in a quadratic+quartic trap. This chapter is devoted to this calculation, as well as some general results concerning the physics of a fast rotating bosonic gas.

For rotating ideal gases in harmonic traps the condensation temperature was already calculated by Stringari in 1999 [162]. In this work he showed that the condensation temperature of a rotating system can be obtained by rescaling the radial trapping frequency to $\tilde{\omega}_\perp = (\omega_\perp^2 - \Omega^2)^{1/2}$. This result is recovered in section 9.1 with an approach taking into account the emergence of Landau levels due to the fast rotation. Section 9.2 generalizes the Landau level approach to a quadratic+quartic potential and a rotation frequency $\Omega = \omega_\perp$. In this situation it is also possible to find an analytical solution within the semiclassical approach, and the semiclassical result is compared to the exact calculation. In 9.3 the case of arbitrary rotation frequencies is then treated by numerical integration of the semiclassical integral.

9.1 Condensation temperature of a rotating gas in a harmonic trap

The problem of a rotating gas in a harmonic trap was studied by Stringari in [162]. One of the results of this work concerns the ideal gas condensation temperature T_c, which was recovered through a rescaling of the radial trapping frequency $\omega_\perp$ to $\tilde{\omega}_\perp = \sqrt{\omega_\perp^2 - \Omega^2}$, where Ω is the rotation frequency of the gas. This approach takes into account the weakening of the potential due to the centrifugal force, and for a fixed number of atoms the condensation temperature T_c

is related to the result for a nonrotating gas $T_c^{(0)}$ by

$$T_c(\Omega) = T_c^{(0)} \left(1 - \frac{\Omega^2}{\omega_\perp^2}\right)^{1/3} . \tag{9.1}$$

The change in T_c is most dramatic for $\Omega \to \omega_\perp$, where the system becomes untrapped, and T_c tends to zero.

9.1.1 Semiclassical calculation of T_c

In a semiclassical treatment of the harmonically trapped rotating gas the effective potential has the following shape in the rotating frame:

$$U_{\rm rot}(r,z) = \frac{m}{2}\omega_z^2 z^2 + \frac{m}{2}\left(\omega_\perp^2 - \Omega^2\right) r^2, \tag{9.2}$$

and the density of states is

$$\rho(\epsilon) = \frac{\epsilon^2}{2\hbar^3\bar{\omega}^3} \quad , \qquad \text{with} \qquad \bar{\omega}^3 = \left(\omega_\perp^2 - \Omega^2\right)\omega_z .$$

The ideal gas condensation temperature is calculated through the relation

$$N = \int_0^\infty \frac{\rho(\epsilon)}{e^{\;\epsilon/(k_{\rm B}T)} - 1}\, d\epsilon, \tag{9.3}$$

which gives for the above density of states

$$N = \zeta(3)\,\frac{(k_{\rm B}T/\hbar)^3}{\left(\omega_\perp^2 - \Omega^2\right)\omega_z} = \zeta(3)\,\frac{(k_{\rm B}T/\hbar)^3}{\left(\omega_\perp + \Omega\right)\left(\omega_\perp - \Omega\right)\omega_z} \ , \tag{9.4}$$

and $\zeta(3) \approx 1.2$. In the next section this result is recovered by an exact summation over the single particle states. This approach takes into account the emergence of Landau levels for the single particle states of a fast rotating gas.

9.1.2 The LLL formalism

As discussed in chapter 8.1.1, the eigenstates of a system in a potential of cylindrical symmetry can be labeled by 3 quantum numbers n_z, n_m, m_z, where $n_z = 0, 1, ...$ is the vibrational quantum number along z, $n_m = 0, 1, ...$ characterizes the excitation energy in the xy-plane for a state with a given m_z, and m_z is the angular momentum along z.

For the rotating harmonic potential (9.2) the eigenenergies are then

$$E_{\rm rot}(n_z, m_z, n_m) = (n_z + \frac{1}{2})\,\hbar\omega_z + (2n_m + |m_z| + 1)\,\hbar\omega_\perp - m_z\,\hbar\Omega. \tag{9.5}$$

In this equation one sees appear the Landau level structure for the transverse motion for $\Omega \to \omega_\perp$. The Landau levels are spaced by the energy $\hbar(\omega_\perp + \Omega)$, and the lowest Landau level contains states of angular momentum $m_z = 0, 1, 2, ...$, the first Landau level states with $m_z = -1, 0, 1, ...$, and so on. Two adjacent states within a Landau level are separated by the energy $\hbar(\omega_\perp - \Omega)$ (see figure 9.1 (a)).

The exact ansatz for the relation between the condensation temperature and the atom number is

$$N = \sum_{n_z, m_z, n_m}{}' \left(e^{E_{\rm rot}(n_z,m_z,n_m)/(k_{\rm B}T)} - 1\right)^{-1}, \tag{9.6}$$

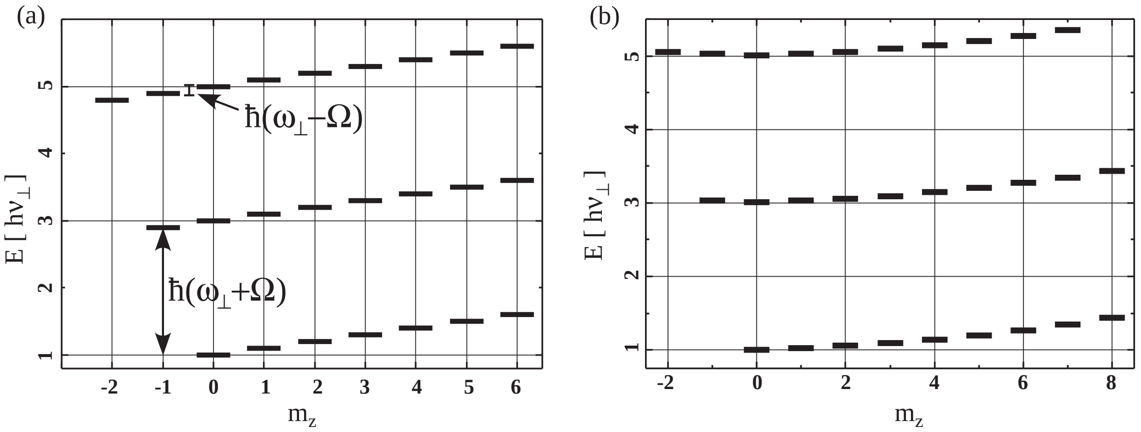

Figure 9.1: Single particle states of fast rotating condensates. a) Landau levels in a harmonic trap for $\Omega = 0.9\ \omega_\perp$. (b) In a quadratic+quartic trap the structure of the Landau levels is modified as compared to the purely harmonic case. In this graph $\Omega = \omega_\perp$, and the strength of the quartic term is larger by a factor 10 as compared to the experimental case, to make the quadratic variation more visible.

where the sum excludes the ground state $n_z = m_z = n_m = 0$, which is indicated by the $'$. This sum can be calculated numerically, and the result is similar to the one of the semiclassical approach (9.4).

This is easily understood when using the eigenenergies E_{rot} of equation 9.5 in the sum. These eigenenergies are equal to those of a nonrotating 3D harmonic oscillator with frequencies ω_z, $(\omega_\perp + \Omega)$ and $(\omega_\perp - \Omega)$ (see figure 9.1 (a)). These frequencies also appear in the result of the semiclassical approach, equation (9.4).

9.2 Results for the combined quadratic + quartic potential

The results for the harmonic case are now extended to the situation of a quadratic+quartic potential, where the quartic term constitutes a small modification to the purely harmonic confinement. This corresponds to the experimental situation of chapter 8, of which the most important properties are summarized in the following.

9.2.1 Experimental situation

The external trapping potential is well described by a 3D harmonic trap plus a radial quartic term:

$$U(\boldsymbol{r}) = \frac{1}{2}m\omega_z^2 z^2 + \frac{1}{2}m\omega_\perp^2 r^2 + \frac{1}{4}kr^4 \qquad \text{where} \qquad k = 2.6\cdot 10^{-11}\,\mathrm{J\,m^{-4}}, \tag{9.7}$$

$r^2 = x^2 + y^2$, and the harmonic trapping frequencies are $\omega_\perp/2\pi = 64.8\,\mathrm{Hz}$ and $\omega_z/2\pi = 11.0\,\mathrm{Hz}$. The atom number is $N \sim 3\cdot 10^5$, and a nonrotating cloud has a Thomas-Fermi radius of $\sim 5\,\mu\mathrm{m}$. For this radius the quartic term constitutes only a small deviation to the harmonic potential, but it becomes increasingly important with increasing radial rotation frequency. For a cloud rotating at a frequency $\Omega = \omega_\perp$ the effective potential $U_{\mathrm{rot}}(\boldsymbol{r})$ finally becomes purely quartic in radial direction:

$$U_{\mathrm{rot}}(\boldsymbol{r}) = \frac{m}{2}\omega_z^2 z^2 + \frac{m}{2}\tilde{\omega}_\perp^2 r^2 + \frac{1}{4}kr^4, \qquad \text{with} \qquad \tilde{\omega}_\perp^2 = \omega_\perp^2 - \Omega^2. \tag{9.8}$$

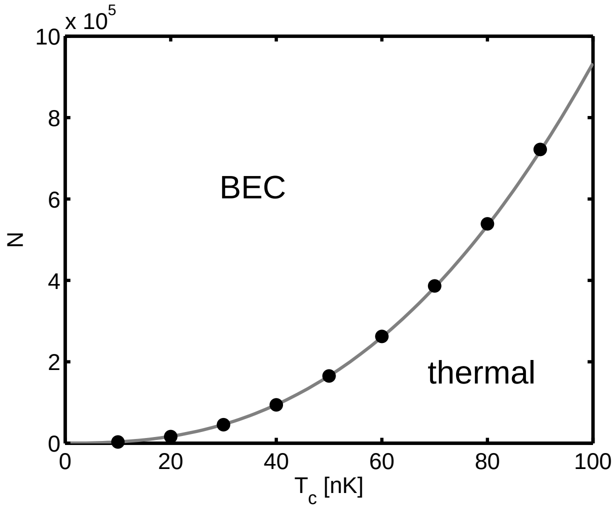

Figure 9.2: Rotation at $\Omega = \omega_\perp$ in a quadratic + quartic potential. The relation between the atom number N and the BEC transition temperature T_c is calculated with the semiclassical approach (equation (9.9), full line) and compared to the evaluation of the sum (9.6) with the eigenenergies of equation (9.10) (dots).

The faster the cloud is rotating, the larger is thus the influence of the quartic term.

9.2.2 Semiclassical approach at $\Omega = \omega_\perp$

For a quadratic+quartic potential it is not possible to analytically calculate the condensation temperature for arbitrary rotation frequencies. For $\Omega = \omega_\perp$ the potential becomes however purely quartic in the rotating frame, as the harmonic confinement is cancelled by the centrifugal force. In this case the analytic calculation becomes possible, and the density of states is

$$\rho(\epsilon) = \frac{2m\epsilon^{3/2}}{3\hbar^3\omega_z\sqrt{k}} \, .$$

The relation between atom number and condensation temperature is then calculated through equation (9.3), which gives for the above density of states

$$N = \frac{\sqrt{\pi}}{2}\zeta(5/2)\,\frac{m(k_{\mathrm{B}}T_c)^{5/2}}{\hbar^3\omega_z\sqrt{k}}, \tag{9.9}$$

where $\zeta(5/2) \approx 1.34$.
A generalization of this result to arbitrary rotation frequencies is given in section 9.3, where T_c is calculated numerically as a function of Ω.

9.2.3 Energy levels in the quadratic+quartic case

For the calculation of the radial energy levels in the quadratic+quartic case the eigenfunctions in the xy-plane are written as $\Psi(r,\phi) = \psi(r)e^{im_z\phi}$, and a perturbational approach leads to the following spectrum for the states $m_z, n_m = 0$ (see section 8.1.1):

$$E_\perp(m_z, 0) = \hbar\omega_\perp(|m_z| + 1) + \frac{\hbar^2 k}{4m^2\omega_\perp^2}\,(|m_z| + 1)\,(|m_z| + 2)\, .$$

This result is valid for $|m_z| \ll \frac{m^2\omega_\perp^3}{k\hbar}$, which is ~ 500 for our experimental parameters.
For a calculation of T_c at $\Omega \sim \omega_\perp$ this validity range should be sufficient. This can be derived by noticing that for our experimental parameters the condensation temperature of a nonrotating cloud in the purely quadratic potential is $\approx 100\,\mathrm{nK}$, and T_c for a cloud rotating at $\Omega \sim \omega_\perp$ in the quartic potential is certainly smaller. Setting $T^{(\max)} = 100\,\mathrm{nK}$, and $k_\mathrm{B}T^{(\max)} = \hbar^2 k/4m_z^2\omega_\perp^2\,(|m_z|+1)\,(|m_z|+2)$ gives $m_z^{(\max)} \sim 260$, and for these values the above energy dependence is valid.
The result for arbitrary n_m is also calculated in section 8.1.1 (equation 8.3):

$$E_\perp(m_z, n_m) \approx E_\perp(m_z, 0) + 2n_m\hbar\omega_\perp,$$

9.2.4 Evaluation of the sum for $\Omega = \omega_\perp$

In the rotating frame one has to add the term $-m_z\hbar\Omega$, and for $\Omega = \omega_\perp$ this leads to

$$E_\mathrm{rot}(n_z, m_z, n_m) = (n_z+\frac{1}{2})\,\hbar\omega_z+(|m_z|-m_z+2n_m+1)\,\hbar\omega_\perp+\frac{\hbar^2 k}{4m^2\omega_\perp^2}(|m_z|+1)\,(|m_z|+2). \quad (9.10)$$

These energy levels are plotted in figure 9.1 (b).

Analog to the harmonic case the relation between the atom number and the condensation temperature is then calculated by evaluating the sum (9.6) with the energy of equation (9.10). The numerical result of this sum is plotted in figure 9.2 (dots). It is in good agreement with the result of the semiclassical calculation (9.9), which corresponds to the full line in figure 9.2.

Physical analogue to the situation

In the case of $m_z \gg 1$, the spectrum of equation (9.10) varies approximately with m_z^2:

$$E_\mathrm{rot}(n_z, m_z, n_m) \approx (n_z + \frac{1}{2})\,\hbar\omega_z + (2n_m + 1)\,\hbar\omega_\perp + \frac{\hbar^2 k}{4m^2\omega_\perp^2}m_z^2. \quad (9.11)$$

This energy spectrum has the same structure as that of a particle of mass m^* confined in two dimensions by the harmonic potentials of frequencies ω_z and $2\omega_\perp$, and moving freely in the third direction along a segment of length L. The correspondence is obtained by defining the effective mass m^* through

$$\frac{(2\pi)^2\hbar^2}{2m^*L^2} = \frac{\hbar^2 k}{4m^2\omega_\perp^2}\ . \quad (9.12)$$

In the semiclassical approach the relation between the atom number and the critical temperature of such a system is

$$N \approx \frac{\sqrt{m^*}L(k_\mathrm{B}T)^{5/2}}{2\hbar^3\omega_z\omega_\perp} = \frac{2\pi}{\sqrt{2}}\frac{m(k_\mathrm{B}T)^{5/2}}{\hbar^3\omega_z\sqrt{k}}.$$

This equation is analogue to the semiclassical result for the rotation at $\Omega = \omega_\perp$ in the quadratic+quartic potential.

9.3 Numerical solution for the quartic potential

The agreement between the semiclassical results and the results obtained by summing explicitly over the single particle states shows that the semiclassical approach is valid for fast rotating condensates, in harmonic traps, as well as in a quadratic+quartic trap when rotating exactly at the trapping frequency. In particular the modification of the energy spectrum due to the

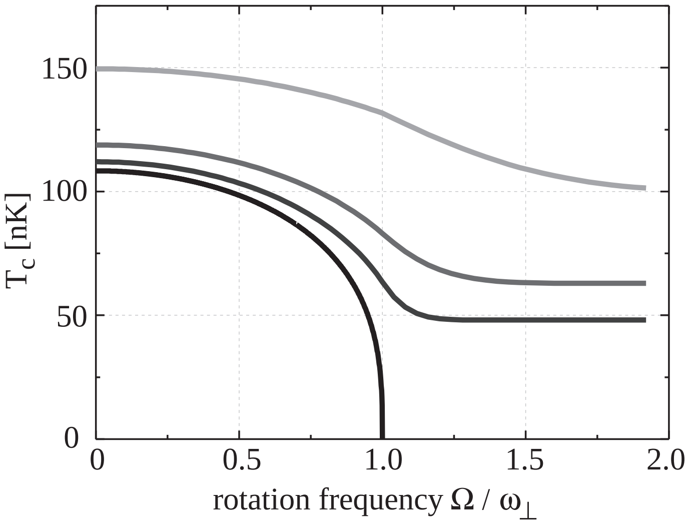

Figure 9.3: The condensation temperature as a function of the rotation frequency $\Omega/\omega_\perp$ for different strengths of the quartic term. From bottom to top: $k = 0$, $k = 2.6\,10^{-11}\mathrm{J/m}^4$, $k = 10^{-10}\mathrm{J/m}^4$, and $k = 10^{-9}\mathrm{J/m}^4$.

appearance of the strongly degenerate Landau levels does not invalidate the semiclassical approach. The semiclassical approach is now used in the following to numerically calculate the condensation temperature T_c for clouds rotating at arbitrary Ω.

In the semiclassical approach the relation between the total atom number of the system and the condensation temperature is given by

$$N = \frac{1}{(2\pi\hbar)^3} \int \frac{1}{e^{\beta E} - 1}\, d^2r\; dz\; d^3p = \frac{1}{(2\pi\hbar)^3} \int \left(\sum_{n=1}^{\infty} e^{-n\beta E} \right) d^2r\; dz\; d^3p,$$

where $\beta = (k_\mathrm{B}T)^{-1}$, and $E = p^2/(2m) + U_\mathrm{rot} - \mu$, and μ is the chemical potential. Using the gaussian integral the integration over p and z leads to

$$N = \frac{m(k_\mathrm{B}T)^2}{\hbar^3\omega_z} \int_0^\infty g_2\left(e^{-\beta(U_\perp(r)-\mu)}\right)\, r\; dr, \tag{9.13}$$

where g_2 is the polylogarithm function defined by $g_2(z) = \sum_n (z^n/n^2)$, and

$$U_\perp(r) = \frac{m}{2}\tilde{\omega}_\perp^2 r^2 + \frac{1}{4}kr^4$$

is the radial component of U_rot.
For a condensate the chemical potential is $\mu = \min(U_\perp(r))$, which leads to

$$\mu_1 = 0 \quad \text{for} \quad \Omega \leqslant \omega_\perp \qquad \text{and} \qquad \mu_2 = -\frac{m^2(\Omega^2 - \omega_\perp^2)^2}{4k} \quad \text{for} \quad \Omega \geqslant \omega_\perp.$$

Using this result and substituting $t = r^2$ the energy in the exponent of equation (9.13) becomes for the respective cases:

$$E_1 = \frac{k}{4}(t + \frac{m\tilde{\omega}_\perp^2}{k})^2 - \frac{m^2\tilde{\omega}_\perp^4}{4k} \qquad \text{and} \qquad E_2 = \frac{k}{4}(t + \frac{m\tilde{\omega}_\perp^2}{k})^2.$$

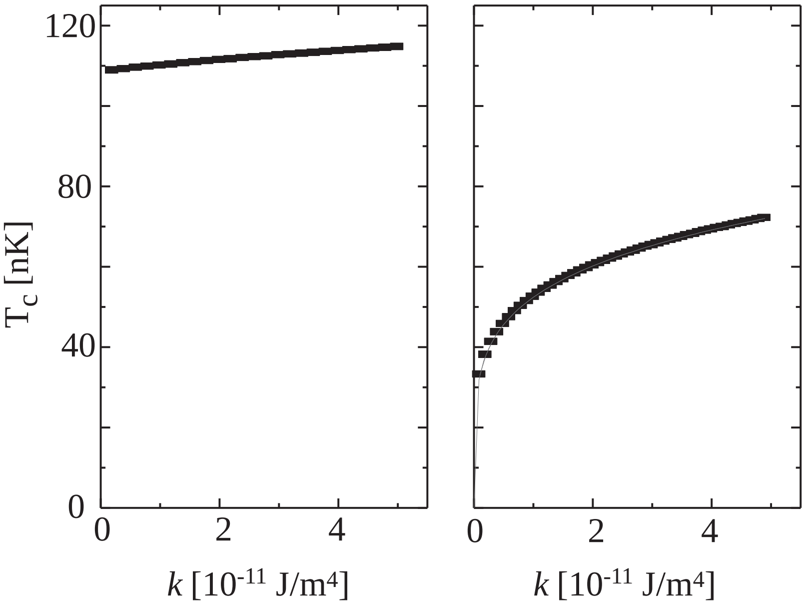

Figure 9.4: The condensation temperature T_c as a function of the strength of the quartic potential, which is described by the parameter k. Left: $\Omega = 0$, i.e. the cloud is not rotating. Right: $\Omega = \omega_\perp$. For a nonrotating cloud T_c is only slightly changed by a small quartic term. For cloud rotating at $\Omega = \omega_\perp$ the condensation temperature depends dramatically on the quartic confinement. One can also clearly see that independent of the value of the quartic term the condensation temperature is in general significantly decreased for a fast rotating cloud.

Using these results in equation (9.13), one gets the integrals of the simple form

$$N_1 = \frac{m(k_\mathrm{B}T)^{5/2}}{\hbar^3\omega_z\sqrt{k}} \int_0^\infty g_2\left(e^{-(u+v)^2+v^2}\right) du, \qquad \text{for } \Omega \le \omega_\perp, \tag{9.14}$$

and

$$N_2 = \frac{m(k_\mathrm{B}T)^{5/2}}{\hbar^3\omega_z\sqrt{k}} \int_0^\infty g_2\left(e^{-(u+v)^2}\right) du, \qquad \text{for } \Omega > \omega_\perp, \tag{9.15}$$

where $u = r^2\sqrt{k/(4k_\mathrm{B}T)}$ and $v = m\tilde{\omega}_\perp^2(4k\,k_\mathrm{B}T)^{-1/2}$.
This integral is solved numerically, and the solutions for T_c are plotted as a function of $\Omega/\omega_\perp$ in figure 9.3 for different strengths of the quartic potential k. For $k = 0$ the solution corresponds to the solution calculated by Stringari (equation (9.1)).

Cuts through these plots at $\Omega = 0$ and $\Omega = \omega_\perp$ are shown in figure 9.4. For a nonrotating cloud our quartic potential has a rather small influence of the condensation temperature. As expected its influence on a fast rotating cloud is more dramatic: without the quartic potential no condensation can occur at $\Omega = \omega_\perp$, while in presence of the quartic term T_c decreases only by a factor ~ 2 compared to the nonrotating case.

9.4 Relevant results for the experimental situation

The most important results for the experiments described in chapter 8 are the values of T_c for fast rotation frequencies $\Omega \sim \omega_\perp$. For $N = 3 \cdot 10^5$ atoms, $\omega_z/(2\pi) = 11.0\,\mathrm{Hz}$ and $\omega_\perp/(2\pi) = 64.8\,\mathrm{Hz}$

the condensation temperature is $T_c = 63\,\mathrm{nK}$ for $\Omega = \omega_\perp$, and $T_c = 57\,\mathrm{nK}$ for the highest explored rotation frequency $\Omega/(2\pi) = 68\,\mathrm{Hz} = 1.05\,\omega_\perp$.

At these rotation frequencies the gas has a temperature of $T \sim 10\,\mathrm{nK}$ due to evaporative cooling. For all used rotation frequencies the gas is thus well in the degenerate regime.

9.5 Conclusion

According to the results of this chapter the presence of a large fraction of thermal atoms in the experimental situation of [1] and chapter 8 can be excluded. Therefore, the most likely explanation of the reduced visibility of the vortex cores is an excitation of the vortex lines. This conclusion is supported by recent numerical calculations of Ionut Danaila [205]. In these simulations the ground state of the system is approximated using imaginary time evolution of the Gross-Pitaevskii equation. It was found that for $\Omega \gtrsim \omega_\perp$ much longer imaginary times (corresponding to very low temperatures) were needed to reach a well ordered vortex lattice of high imaging contrast. In the investigation of the 3D structure of vortex configurations and its effects on the imaging contrast of the vortices, it was found that strong excitations of the vortex lines are present at the experimental temperatures. These excitations significantly decrease the contrast of the vortex cores in axial imaging.

Chapter 10

Monopole in fast rotating BECs

This chapter was published in:
S. Stock, V. Bretin, F. Chevy, and J. Dalibard, Shape oscillation of a rotating Bose-Einstein condensate, Europhys. Lett. ***65*** *594 (2004) [2].*

Shape oscillation of a rotating Bose-Einstein condensate

The investigation of rotating gases or liquids is a central issue in the study of superfluids [37,160]. During the recent years, several experiments using rotating atomic Bose-Einstein condensates have provided a spectacular illustration of the notion of quantized vortices [128,156–158]. Depending on the rotation frequency of the gas, a single vortex or a regular array of vortices can be observed experimentally. When the rotation frequency is increased to a very large value, a new class of phenomena is predicted, in connection with quantum Hall physics [40,41,166–168, 183,206,207]. For a gas confined in a harmonic potential, the fast rotation domain corresponds to stirring frequencies Ω of the order of the trapping frequency $\omega_\perp$ in the plane perpendicular to the rotation axis (hereafter denoted z). From a classical point of view, the transverse trapping and centrifugal forces compensate each other for this stirring frequency, and the motion of the particles in the xy plane is only driven by Coriolis and interatomic forces. This situation is similar to that of an electron gas in a magnetic field, since Lorentz and Coriolis forces have the same mathematical structure.

In order to approach the regime of fast rotation two paths are currently being explored. The first approach is implemented in a pure harmonic potential and is based on evaporative spin-up, i.e. the selective removal of particles with low angular momentum [208]. The stirring frequency Ω can then be raised close to $\omega_\perp$ ($\Omega = 0.993\,\omega_\perp$ was reached in [24]). The second approach, which is followed here, consists in adding to the quadratic confinement a small positive quartic potential, which ensures that the particles will remain confined even when Ω exceeds $\omega_\perp$ [192–196, 209]. We have recently proven that this method can be successfully implemented and we have mechanically stirred a rubidium Bose-Einstein condensate up to $\Omega \simeq 1.05\,\omega_\perp$ [1].

All experiments performed so far (including the present one) are still deeply within the mean field regime, characterized by a number of vortices N_v well below the number of particles N. Nevertheless in order to prepare for future investigations of possible quantum-Hall-like states, one must design proper tools of investigation, such as the study of the eigenmodes of the rotating gas. Possible examples are the transverse quadrupole modes, which allow for a measurement of the z component of the angular momentum [1], and the Tkachenko oscillations of the vortex lattice, recently observed in [208]. Here we report on the experimental and theoretical study of the lowest transverse monopole mode of an ultra-cold gas of rubidium atoms in the fast rotation regime.

In a trap with axial symmetry along the z-axis, excitations can be characterized by their angular momentum along z (quantum number m_z) [210]. Here we are interested in excitations carrying no angular momentum ($m_z = 0$). In the limit $\omega_z \ll \omega_\perp$ which is of interest here, it is possible to identify $m_z = 0$ "transverse monopole" modes, which mostly affect the atom distribution in the xy plane. For a non-rotating condensate the lowest frequency for these $m = 0$ transverse modes is $\omega_{\mathrm{mp}} \simeq 2\,\omega_\perp$ (transverse breathing mode) [71, 211]. In the present work we show experimentally that the relation $\omega_{\mathrm{mp}} \simeq 2\,\omega_\perp$ remains valid for large rotation frequencies (as predicted by [212]), as long as the quartic term in the confinement is not significant. We also explore the region $\Omega \sim \omega_\perp$, where the quartic term plays an essential role. We compare the measured monopole frequency with that derived from a simple hydrodynamic model of an infinite, cylindrical condensate. Finally we discuss the structure of the mode, which exhibits a very particular behavior in the range $\Omega \gtrsim \omega_\perp$.

Our ^{87}Rb Bose-Einstein condensate contains 3×10^5 atoms. It is produced by radio-frequency evaporation in a Ioffe-Pritchard magnetic trap, to which we superimpose a far-blue detuned laser beam. The magnetic trap provides a harmonic confinement with cylindrical symmetry along the z axis, with $\omega_z/2\pi = 11.0$ Hz and $\omega_\perp^{(0)}/2\pi = 75.5$ Hz. The laser beam adds a negative quadratic and a positive quartic potential in the xy plane. The quadratic term decreases the trap frequency $\omega_\perp$ by $\sim 15\%$. The quartic term allows to explore rotation frequencies around and slightly above the trapping frequency $\omega_\perp$. It reads $kr^4/4$, with $r^2 = x^2 + y^2$ and $k = 2.6(3) \times 10^{-11}$ J/m^4. The oscillation frequency of the condensate center-of-mass (dipole motion) in the xy plane is $\omega_{\mathrm{dp}}/2\pi = 65.6$ (± 0.3) Hz. Because of the quartic component of the trapping potential, ω_{dp} is slightly larger than $\omega_\perp$, even for an arbitrarily small amplitude of the dipole motion. The condensate has indeed a finite radius $R_c \simeq 6.5\,\mu$m and therefore explores regions of space where the contribution of the quartic term is significant. Using a perturbative treatment of the quartic term we infer that $\omega_{\mathrm{dp}} - \omega_\perp \simeq 2kR^2/(7\,m\omega_\perp^2)$, so that $\omega_\perp/(2\pi) = 64.8$ (± 0.3) Hz.

The procedure for setting the gas in rotation at a frequency $\Omega \sim \omega_\perp$ has been described in detail in [1]. We apply an additional laser beam creating a rotating anisotropy in the xy plane for two successive phases, with respective durations of 300 ms and 600 ms. During the first phase the rotation at frequency $\Omega \sim \omega_\perp/\sqrt{2}$ resonantly excites the transverse quadrupole mode, and vortices subsequently penetrate the condensate. After a 400 ms relaxation period we apply the second stirring phase at the final desired frequency. This phase is followed by a 500 ms relaxation period. By measuring the transverse size of the condensate, we have checked that it is then rotating at a frequency close to the stirrer frequency Ω (within 2%) for the regime of interest $\Omega \leq 1.05\,\omega_\perp$. In particular, for $\Omega \lesssim \omega_\perp$ we observe large vortex arrays involving up to ~ 50 vortices. During the stirring and relaxation periods, we apply radio frequency (r.f.) evaporative cooling. The r.f. is set 24 kHz above the value which removes all particles from the trap. Assuming $\Omega = \omega_\perp$, so that the transverse confinement is purely quartic, this gives a trap depth $U_0 \sim 40$ nK, hence a temperature $T \lesssim 10$ nK.

We then excite the transverse monopole mode(s) of the gas by changing for a period τ_0 the intensity of the laser creating the quartic potential from I to I'. We choose $\tau_0 = 2\,$ms, which is short compared to the oscillation period of the monopole oscillation $2\pi/\omega_{\mathrm{mp}} = 7.5$ ms. We then wait for an adjustable duration τ before performing a time-of-flight expansion and absorption imaging. The images are taken along the rotation axis z so that we have access to the column density in the xy plane.

Typical results are shown in figure 10.1 for $\Omega/2\pi = 62, 64, 66$ Hz. Each image corresponds to a destructive measurement of the atom density after a duration $\tau = 25, \ldots, 32$ ms and a 18 ms time-of-flight. In order to check that the oscillation is in the linear regime, we explored values between 0 and 4 for the ratio I'/I: we found that the frequency ω_0 is (within experimental uncertainties) independent of the excitation strength $|I - I'|/I$, and that the amplitude of the oscillation varies linearly with this strength. We have also varied the duration of the time-of-

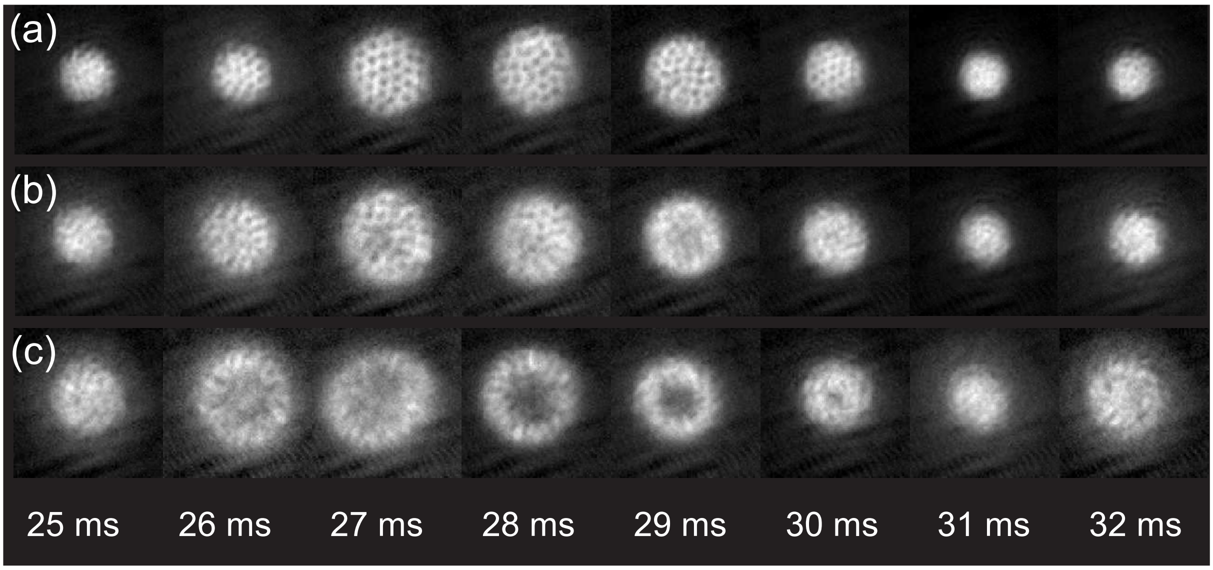

Figure 10.1: Series of images of the condensate for various waiting times τ after excitation. Row a) corresponds to a rotation frequency $\Omega/(2\pi) = 62$ Hz, row b) to $\Omega/(2\pi) = 64$ Hz and row c) to $\Omega/(2\pi) = 66$ Hz.

flight between 6 and 18 ms. We thus verify that all features reported here are independent of this duration, which corresponds to a mere scaling of the initial spatial density distribution.

We have taken similar sequences of images for various stirring frequencies Ω, with τ varying from 0 to 40 ms by steps of 1 ms. We extract from these images the transverse size $R(\tau)$ of the gas. The variations of $R(\tau)$ are well fitted by a single sinusoidal function, with frequency ω_{mp}. The characteristic lifetime of the excitation is larger than 100 ms, so that its decay is negligible during the 40 ms period. The variations of ω_{mp} as a function of Ω are plotted in figure 10.2. An obvious feature of this plot is that ω_{mp} varies very weakly for Ω except in the vicinity of $\omega_\perp$. We now discuss in more details three relevant domains of this graph.

(1) For a non rotating gas ($\Omega = 0$) we find $\omega_{\mathrm{mp}}/(2\pi) = 130.6\ (\pm 1.5)$ Hz, which is close to the well known result[1] $\omega_{\mathrm{mp}} \simeq 2\omega_\perp = 2\pi \times 129.6\,(\pm 0.6)$ Hz.

(2) When the gas rotates at a frequency Ω not too close to $\omega_\perp$, the effect of the quartic potential remains small. In these conditions we find that the monopole frequency ω_0 stays approximately constant. At first sight this may seem a surprising result. For a rotating gas in a pure harmonic potential, the transverse confinement is reduced due to the centrifugal force. In the calculation of the equilibrium shape of the gas, the trapping frequency $\omega_\perp$ is thus replaced by the weaker value $(\omega_\perp^2 - \Omega^2)^{1/2}$. One might have expected that a similar replacement should be done also for the monopole frequency; this is clearly not the case. For a cigar-shaped condensate in the hydrodynamic regime, it was proven in [212] that ω_0 stays equal to $2\omega_\perp$ when Ω varies. In the case of an ideal gas described by classical mechanics, the equality $\omega_{\mathrm{mp}} = 2\,\omega_\perp$ also holds for any Ω as a consequence of the combined action of centrifugal and Coriolis forces.

(3) When the rotation frequency Ω approaches $\omega_\perp$, the contribution of the quartic term becomes more important and the monopole frequency ω_{mp} deviates significantly from $2\omega_\perp$. As shown in figure 10.2, this deviation reaches ~ 8 % for $\Omega/(2\pi) = 68$ Hz, i.e. $\Omega/\omega_\perp \simeq 1.05$. We have also plotted in figure 10.2 the prediction of a theoretical treatment of the monopole mode in the quartic + quadratic trap, neglecting the harmonic confinement along the z-direction.

---

[1] As for the dipole mode there is actually a small correction ($\sim 1\%$) to this relation due to the presence of the quartic potential $kr^4/4$.

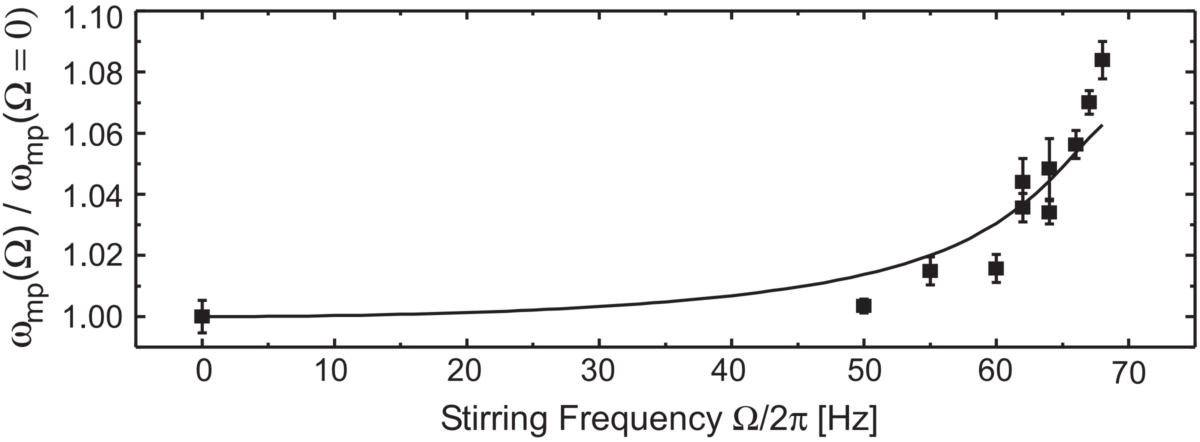

Figure 10.2: Transverse monopole frequency $\omega_{\mathrm{mp}}(\Omega)$ normalized by $\omega_{\mathrm{mp}}(\Omega = 0)$ as a function of the stirring frequency Ω. For a non rotating condensate ($\Omega = 0$) we measure $\omega_{\mathrm{mp}}(0)/(2\pi) = 130.6$ Hz. The vertical bars indicate the error given by the fitting routine.

The agreement between these predictions and the experimental data is satisfactory, given the difference in geometry between the experiment and the model.

The starting point of our theoretical treatment is the set of equations for rotational hydrodynamics [212], which we write in the laboratory frame:

$$\begin{aligned} \partial_t \rho &= -\boldsymbol{\nabla} \cdot (\rho \boldsymbol{v}) && (10.1) \\ \partial_t \boldsymbol{v} &= -\boldsymbol{\nabla}((U + g\rho)/m + v^2/2) + \boldsymbol{v} \times (\boldsymbol{\nabla} \times \boldsymbol{v}) \ , && (10.2) \end{aligned}$$

where ρ and $\boldsymbol{v}$ are the density and velocity field of the atom distribution. $U = m\omega_\perp^2 r^2/2 + kr^4/4$ stands for the trapping potential and $g = 4\pi\hbar^2 a/m$ characterizes the strength of the atomic interactions (a is the scattering length). As explained in [212–214] these equations are valid when one is interested in a phenomenon whose characteristic length scale is larger than the distance between vortices.

The eigenmodes are obtained by linearizing (10.1-10.2) around the rotating equilibrium solution

$$\boldsymbol{v}_{\mathrm{eq}} = \boldsymbol{\Omega} \times \boldsymbol{r} \qquad g\rho_{\mathrm{eq}} = \mu - U - U_{\mathrm{cen}} \ , \tag{10.3}$$

where μ is the chemical potential and $U_{\mathrm{cen}} = -m\Omega^2 r^2/2$ the centrifugal potential. We eliminate the velocity field to get a closed equation for the density variation $\delta\rho$, assuming an oscillation at frequency ω:

$$-\boldsymbol{\nabla} \cdot (\rho_{\mathrm{eq}} \boldsymbol{\nabla}[\delta\rho]) = \frac{m}{g} (\omega^2 - 4\Omega^2) [\delta\rho] \ . \tag{10.4}$$

In absence of a quartic term the eigenfrequencies for the $m = 0$ modes are

$$\omega_n^2 = 4\Omega^2 + 2n(n+1)(\omega_\perp^2 - \Omega^2) \ , \qquad n \text{ positive integer,} \tag{10.5}$$

and the corresponding eigenmodes are polynomials of degree n with respect to r^2. For $n = 1$, we recover in particular $\omega_1 \equiv \omega_{\mathrm{mp}} = 2\,\omega_\perp$.

When Ω approaches $\omega_\perp$, all transverse modes $m = 0$ become degenerate. Such a macroscopic degeneracy is reminiscent of the degeneracy of the energy levels of a single particle in a uniform magnetic field, leading to the well known Landau level structure [215]. An equivalent degeneracy occurs, still at the single particle level, for an isotropic 2D harmonic oscillator of frequency $\omega_\perp$,

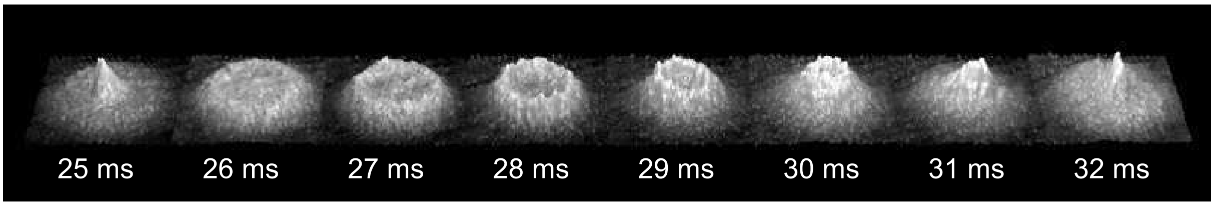

Figure 10.3: Time evolution of the density profile of the oscillating cloud, for $\Omega/2\pi = 68$ Hz.

considered in a frame rotating[2] at frequency $\Omega = \omega_\perp$. However we emphasize that our result here holds not for a single particle spectrum, but for the eigenmodes of a $N-$body system treated in the mean-field approximation. The occurrence of such a macroscopic degeneracy raises interesting questions concerning the linear response of the rotating system to an arbitrary excitation.

When the quartic potential is present, the above degeneracy is lifted. We set $x = r/R$ in (10.4) with $R = (4\mu/k)^{1/4}$, to get the dimensionless eigenvalue equation for the $m = 0$ modes:

$$-\frac{1}{x}\frac{d}{dx}\left(x(1-\epsilon x^2 - x^4)\,\frac{d[\delta\rho]}{dx}\right) = \Lambda(\epsilon)\,[\delta\rho] \qquad \text{where} \qquad \epsilon = \frac{mR^2}{2\mu}(\omega_\perp^2 - \Omega^2)\ . \tag{10.6}$$

For each Ω, i.e. for each ϵ, we are interested in the lowest eigenvalue $\Lambda_0(\epsilon)$ of the hermitian operator in the left hand side of (10.6). We can then deduce the frequency of the lowest transverse monopole mode which is plotted as a continuous line in figure 10.2:

$$\omega_{\rm mp}^2 = 4\Omega^2 + \frac{\mu\Lambda_0(\epsilon)}{mR^2}\ . \tag{10.7}$$

The quantity $\Lambda_0(\epsilon)$ is an increasing function of ϵ which we calculate numerically using a variational method with polynomial trial functions. Just at the critical rotation $\Omega = \omega_\perp$, $\epsilon = 0$ and we get $\Lambda(0) \simeq 11.5$. The slow rotation limit corresponds to $\epsilon \gg 1$, in which case $\Lambda(\epsilon) \simeq 8\epsilon$; we then recover the result $\omega_{\rm mp} = 2\omega_\perp$.

This analysis also explains the periodic apparition of a hole at the center of the density profile for $\Omega \sim \omega_\perp$, as observed in figure 10.1. The stationary density profile (10.3) varies as r^4 around the origin, whereas the mode $\delta\rho$ varies as r^2 in this region. The curvature of the density profile is therefore dominated by the phase of the perturbation.

For $\Omega \geq \omega_\perp$ and a relatively strong excitation ($I'/I = 4$), we observe that the time evolution of the mode structure becomes asymmetric (see figure 10.3; this asymmetry is also slightly visible in the last row of figure 10.1). It consists of a periodic entering positive density wave, which starts on the edge of the condensate and gradually moves to the center in a time period $\sim \pi/\omega_\perp$. A possible interpretation of this unusual structure is that two (or more) transverse modes $m = 0$ are simultaneously excited with a non-zero relative phase. Since these modes have similar frequencies (cf. Eq. (10.5)) the initial phase difference between them stays nearly constant, and this can give rise to the observed phenomenon.

To summarize we have presented in this paper a detailed study of the transverse monopole mode of a fast rotating degenerate Bose gas. We have shown that the non-harmonic character of the potential (which is essential for the confinement of the gas) has a clear influence on the mode frequency. We have also given a simple analysis of this mode for an infinitely long condensate which is in good agreement with the experimental data.

---

[2] In a frame rotating at angular velocity Ω the single particle Hamiltonian becomes $H' = H - L_z$. Therefore all the levels of the 2D harmonic oscillator with an angular momentum m equal to the ecitation number n have an energy $n\hbar(\omega_\perp - \Omega)$ that goes to zero when $\Omega = \omega_\perp$.

Theoretical studies have shown that the addition of a quartic term in the harmonic potential may lead to the formation of a "giant vortex", i.e. a vortex with a circulation larger than the single quantum h/m [184,193–196,216]. The large hole appearing at the center of the condensate during the monopole oscillation when $\Omega \gtrsim \omega_\perp$ should not be confused with such a giant vortex. We are dealing here with a transient state of the condensate, while the predicted giant vortex state is a stationary state of the system, for an appropriate angular momentum. Another example for a transient large core in a condensate is provided by an experiment recently performed in Boulder, in which a hole pierced in a rotating condensate confined in a purely quadratic trap was shown to persist for a long time [161].

We now briefly discuss some perspectives opened by this work. First we recall that the nature of the gas when the rotation frequency Ω is around or above $\omega_\perp$ is still unclear. The detailed study of [1] showed that the number of visible vortices is not sufficient to account for the measured rotation frequency of the gas. Two classes of explanation have been proposed to account for this finding. Either the fast rotating gas cannot be described anymore by a single macroscopic wave function [203], or the vortices are still present but they are distorted and do not show up clearly in the images of the condensate. We hope that the present experimental measurement of the transverse mode frequency can be used to discriminate between these two hypotheses. In principle a generalization of the above theoretical treatment to a condensate in a 3D trap is possible, and the quantitative predictions of such a model could be compared with the experimental findings.

From the experimental point of view a natural extension of the present work is to switch to a two-dimension geometry, using a strong confining potential along the rotation axis. Vortices then become point objects and the predicted properties of the system depend on the ratio between the atom number N and the number of vortices N_v. When N is large, the Bose-Einstein condensate presents a regular vortex array, as already observed in [24]. The array is expected to melt when N decreases to a value of the order of N_v [178] (see also [168]). For $N < N_v$ the quantum Hall regime for particles should emerge. It is an interesting problem to determine the signature of these various regimes on the eigenmodes of the system. For the monopole mode considered here and for a pure harmonic confinement, it has been predicted in [72, 95] that the frequency ω_{mp} of the breathing motion of a 2D gas remains strictly equal to $2\,\omega_\perp$ for any equilibrium state. This does not hold anymore in presence of the quartic term, and thus the deviation of ω_{mp} from $2\,\omega_\perp$ can in principle be used to monitor the emergence of new quantum phases in the rotating gas.

Conclusion and outlook

The experimental results presented in this thesis can be arranged in two categories, according to the experimental methods that are used: the coherence properties of our BECs are probed through interference experiments, while for probing rotational properties it is necessary to transfer angular momentum to the clouds. These two classes of experiments require different experimental tools, which are added to the basic setup for the respective experiments.

In the experiments presented in part II a 1D optical lattice is superimposed to the magnetic trap. Depending on the lattice period, this lattice potential cuts the 3D-BEC in $\approx 15 - 30$ pancake shaped clouds.

The first experimental result in part II is the demonstration of a novel method for the production of individual 2D condensates (chapter 4). These 2D BECs are separated from the array of BECs in the sites of the optical lattice by a adding a magnetic field gradient along the lattice axis and evaporating the sites selectively. With this method not only single 2D BECs, but any wanted number can be spared from evaporation. This is especially useful for probing the phase properties of the clouds by letting interfere two or more 2D BECs.

Using this interferometric detection method, nontrivial phase defects were observed in the 2D clouds (chapter 5). The experimental signal - a dislocation line in the interference pattern - may result from the presence of single vortices and vortex-antivortex pairs in the clouds. Even if other scenarios cannot be excluded, it is argued why vortices represent the most likely explanation, and the presented results might be the first step in the observation of the Kosterlitz-Thouless transition in interacting 2D systems.

In another series of experiments larger arrays of ~ 30 condensates were let to interfere (chapter 6). It is shown that even for completely independent clouds the interference pattern shows a large periodic modulation. This experimental result is explained by a simple analytic model. Especially for experiments where interference contrast is used as a probe for a special state of the system, such as atom number squeezed states or the Mott insulator, our results are important, as they show that the interference pattern has to be interpreted carefully.

For the experiments presented in part III the 3D condensate is subjected to a different optical potential: to the rotating “spoon”-potential, that allows to set the cloud into rotation. With a second optical potential a radial quartic term is added to the harmonic potential of the Ioffe-Pritchard trap. In such a potential the rotation frequency can exceed the harmonic trapping frequency, as the cloud is kept trapped by the steep quartic walls. It was thus possible to reach a fast rotation regime, with rotation frequencies up to and even slightly higher than the harmonic trapping frequency (chapter 8). At such high rotation frequencies the visibility of the vortex lattice was significantly decreased. Most probably this phenomenon is due to the excitations of the vortex lines, which are easily excited at rotation frequencies $\Omega \sim \omega_\perp$.

To exclude however the more trivial explanation of a thermal cloud as a possible reason for the reduced vortex visibility, calculations for the condensations temperature of a fast rotating cloud in the quadratic+quartic potential are presented in chapter 9. These calculations generalize

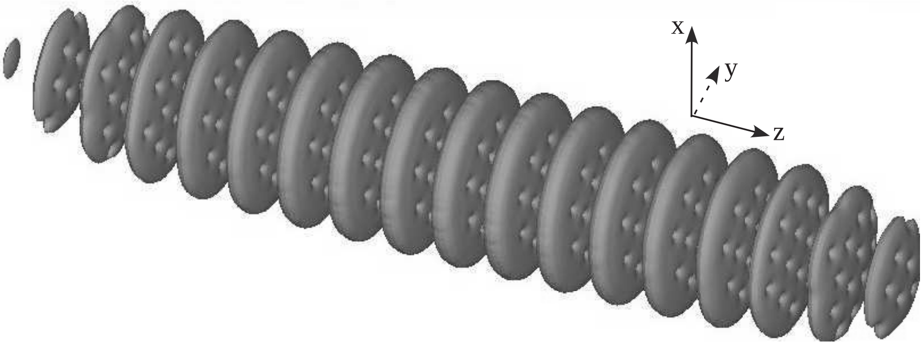

Figure 10.4: Simulation of a 1D array of rotating Bose-Einstein condensates [217].

the work for the purely harmonic case by Stringari [162] to a quadratic+quartic potential. The obtained results clearly exclude the presence of a large fraction of thermal atoms under the experimental conditions of chapter 8.

To get more insight into the specific properties of a cold atomic gas, it can be useful to study the low-lying eigenmodes of the system. For the fast rotating cloud in the quadratic+quartic potential the monopole mode was studied, and it was found that its frequency and shape depends on the rotation frequency of the BEC (chapter 10), unlike in a purely harmonic trap.

Outlook: Rotating BECs in 1D lattices

A somehow natural extension to the experiments presented in this manuscript lies in the simultaneous use of more than one of the presented experimental tools. For example one could dynamically nucleate single vortices or vortex lattices in the 2D clouds trapped in the sites of the optical lattice (see figure 10.4). When using also an additional quartic potential, it could be possible to enter the regime of fast rotation ($\Omega \sim \omega_\perp$) in each of the 2D-clouds.

In these combinations new experimental regimes could then become observable, of which some are listed below, arranged by an increasing rotation frequency:

1. **A slowly rotating, only slightly elliptic spoon-potential** would energetically favor vortices of positive sign, and split possibly present vortex-antivortex pairs in the 2D clouds [114]. As tightly bound vortex-antivortex pairs are not resolvable by our imaging system, the such increased number of free vortices would strongly enhance the probability to interferometrically detect phase defects, and make a systematic study of their temperature dependence easier.

   In the Kosterlitz-Thouless picture the binding energy of such vortex-pairs depends on temperature. With increasing temperature slower rotation frequencies should thus be sufficient for splitting the pairs. This dependency could be used to probe the crossover from the quasi-condensates to the thermal gas.

2. **For rotation frequencies large enough to nucleate single vortices** in the 2D clouds, interesting theoretical proposals have been made, concerning the Kelvon excitations of the vortex line [218–221]. In each of the 2D clouds the vortex is only a point-like defect, and one can only speak of a vortex "line" if tunneling between the sites is possible. For some tunneling strengths the vortex line can experience Kelvon excitations.

3. **Fast rotating 2D condensates in a 1D optical lattice** might prove to be a promising system for the observation of FQHE-physics in rotating bosonic systems. For this regime

> the experimental challenge consists in producing as many vortices as the system has atoms, while having enough atoms for a good imaging quality. As usual vortex number are of the order of ~ 100 the FQHE-regime could be reached in the individual sites of the lattice, if those contain a comparable number of atoms. The system properties should then be probed for all sites simultaneously, allowing for reasonable image qualities. Proposals for the detection of the FQHE-regime in such a "bulk" system have been made by Cooper *et al.* [189, 190].

The experimental tools now present on the experimental setup (and the knowledge concerning their use) allow thus in principle to explore the paths towards several longstanding experimental goals.

Annex

Annex 1: Interference of an array of independent Bose-Einstein condensates

Annex 2: Observation of Phase Defects in Quasi-2D Bose-Einstein Condensates

References

Bibliography

[1] V. Bretin, S. Stock, Y. Seurin, and J. Dalibard, Fast rotation of an ultra-cold Bose gas, Phys. Rev. Lett. **92**, 050403 (2004).

[2] S. Stock, V. Bretin, F. Chevy, and J. Dalibard, Shape oscillations of a rapidly rotating Bose-Einstein condensate, Eur. Phys. Lett. **65**, 594 (2004).

[3] Z. Hadzibabic, S. Stock, B. Battelier, V. Bretin, and J. Dalibard, Interference of an Array of Independent Bose-Einstein Condensates, Phys. Rev. Lett. **93**, 180403 (2004).

[4] S. Stock, B. Battelier, V. Bretin, Z. Hadzibabic, and J. Dalibard, Bose-Einstein condensates in fast rotation, Laser Phys. Lett. **2**, 275 (2005).

[5] S. Stock, Z. Hadzibabic, B. Battelier, M. Cheneau, and J. Dalibard, Observation of Phase Defects in Quasi-2D Bose-Einstein Condensates, Phys. Rev. Lett. **95**, 190403 (2005).

[6] Y. Castin, Z. Hadzibabic, S. Stock, J. Dalibard, and S. Stringari, Seeing zeros of random polynomials: quantized vortices in the ideal Bose gas, Phys. Rev. Lett. **96**, 040405 (2006).

[7] D. Guéry-Odelin, *Dynamique collisionnelle des gaz d'alcalins lourds : du refroidissement évaporatif à la condensation de Bose-Einstein*, PhD thesis, Laboratoire Kastler Brossel, Département de Physique de l'Ecole normale supérieure (disponible sur le serveur http://tel.ccsd.cnrs.fr), 1998.

[8] F. Chevy, *Dynamique d'un condensat de Bose-Einstein*, PhD thesis, Laboratoire Kastler Brossel, Département de Physique de l'Ecole normale supérieure (disponible sur le serveur http://tel.ccsd.cnrs.fr), 2001.

[9] V. Bretin, *Rotations d'un condensat de Bose-Einstein*, PhD thesis, Laboratoire Kastler Brossel, Département de Physique de l'Ecole normale supérieure (disponible sur le serveur http://tel.ccsd.cnrs.fr), 2004.

[10] T. Lahaye, *Refroidissement par évaporation d'un jet atomique guidé magnétiquement*, PhD thesis, Laboratoire Kastler Brossel, Département de Physique de l'Ecole normale supérieure (disponible sur le serveur http://tel.ccsd.cnrs.fr), 2005.

[11] E. A. Cornell and C. E. Wieman, Nobel Lecture: Bose-Einstein condensation in a dilute gas, the first 70 years and some recent experiments, Rev. Mod. Phys. **74**, 875 (2002).

[12] W. Ketterle, Nobel lecture: When atoms behave as waves: Bose-Einstein condensation and the atom laser, Rev. Mod. Phys. **74**, 1131 (2002).

[13] M. H. Anderson, J. R. Ensher, M. R. Matthews, C. E. Wieman, and E. A. Cornell, Observation of Bose-Einstein Condensation in a Dilute Atomic Vapor, Science **269**, 198 (1995).

[14] K. B. Davis, M.-O. Mewes, M. R. Andrews, N. J. van Druten, D. S. Durfee, D. M. Kurn, and W. Ketterle, Bose-Einstein Condensation in a Gas of Sodium Atoms, Phys. Rev. Lett. **75**, 3969–3973 (1995).

[15] F. Schreck, L. Khaykovich, K. L. Corwin, G. Ferrari, T. Bourdel, J. Cubizolles, and C. Salomon, Quasipure Bose-Einstein condensate immersed in a Fermi sea, Phys. Rev. Lett. **87**, 080403 (2001).

[16] A. Görlitz, J. M. Vogels, A. E. Leanhardt, C. Raman, T. L. Gustavson, J. R. Abo-Shaeer, A. P. Chikkatur, S. Gupta, S. Inouye, T. Rosenband, and W. Ketterle, Realization of Bose-Einstein Condensates in Lower Dimensions, Phys. Rev. Lett. **87**, 130402 (2001).

[17] S. Dettmer, D. Hellweg, P. Ryytty, J. J. Arlt, K. Stengstock, D. S. Petrov, G. V. Shlyapnikov, H. Kreutzmann, L. Santos, and M. Lewenstein, Observation of phase fluctuations in elongated Bose-Einstein condensates, Phys. Rev. Lett. **87**, 160406 (2001).

[18] I. Shvarchuck, C. Buggle, D. S. Petrov, K. Dieckmann, M. Zielonkowski, M. Kemmann, T. G. Tiecke, W. von Klitzing, G. V. Shlyapnikov, and J. T. M. Walraven, Bose-Einstein Condensation into Nonequilibrium States Studied by Condensate Focusing, Phys. Rev. Lett. **89**, 270404 (2002).

[19] S. Richard, F. Gerbier, J. H. Thywissen, M. Hugbart, P. Bouyer, and A. Aspect, Momentum spectroscopy of 1D phase fluctuations in Bose-Einstein condensates, Phys. Rev. Lett. **91**, 010405 (2003).

[20] B. L. Tolra, K. M. O'Hara, J. H. Huckans, W. D. Phillips, S. L. Rolston, and J. V. Porto, Observation of reduced three-body recombination in a correlated 1D degenerate Bose gas, Phys. Rev. Lett. **92**, 190401 (2004).

[21] T. Stöferle, H. Moritz, C. Schori, M. Köhl, and T. Esslinger, Transition from a Strongly Interacting 1D Superfluid to a Mott Insulator, Phys. Rev. Lett. **92**, 130403 (2004).

[22] B. Paredes, A. Widera, V. Murg, O. Mandel, S. Fölling, J. I. Cirac, G. V. Shlyapnikov, T. W. Hänsch, and I. Bloch, Tonks-Girardeau gas of ultracold atoms in an optical lattice, Nature **429**, 277 – 281 (2004).

[23] T. Kinoshita, T. Wenger, and D. S. Weiss, Observation of a one-dimensional Tonks-Girardeau gas, Science **305**, 1125–1128 (2004).

[24] V. Schweikhard, I. Coddington, P. Engels, V. P. Mogendorff, and E. A. Cornell, Rapidly rotating Bose-Einstein condensates in and near the Lowest Landau Level, Phys. Rev. Lett. **92**, 040404 (2004).

[25] D. Rychtarik, B. Engeser, H.-C. Nägerl, and R. Grimm, Two-Dimensional Bose-Einstein Condensate in an Optical Surface Trap, Phys. Rev. Lett. **92**, 173003 (2004).

[26] N. L. Smith, W. H. Heathcote, G. Hechenblaikner, E. Nugent, and C. J. Foot, Quasi-2D confinement of a BEC in a combined optical and magnetic potential, Journal of Physics B **38**, 223–235 (2005).

[27] L. Pricoupenko, H. Perrin, and M. O. (edt.), *Quantum gases in low dimensions*, EDP Science, Les Ulis, 2004.

[28] Y. Shin, M. Saba, T. A. Pasquini, W. Ketterle, D. E. Pritchard, and A. E. Leanhardt, Atom Interferometry with Bose-Einstin Condensates in a Double-Well Potential, Phys. Rev. Lett. **92**, 050405 (2004).

[29] M. Albiez, R. Gati, J. Fölling, S. Hunsmann, M. Cristiani, and M. K. Oberthaler, Direct Observation of Tunneling and Nonlinear Self-Trapping in a Single Bosonic Josephson Junction, Phys. Rev. Lett. **95**, 010402 (2005).

[30] T. Schumm, S. Hofferberth, L. M. Andersson, S. Wildermuth, S. Groth, I. Bar-Joseph, J. Schmiedmayer, and P. Krüger, Matter wave interferometry in a double well on an atom chip, Nature Physics **1**, 57 (2005).

[31] S. Gupta, K. W. Murch, K. L. Moore, T. P. Purdy, and D. M. Stamper-Kurn, Bose-Einstein Condensation in a Circular Waveguide, Phys. Rev. Lett. **95**, 143201 (2005).

[32] I. Bloch, Quantum gases in optical lattices, Physics World, April 2004, pp. 25-29.

[33] O. Morsch and M. Oberthaler, Bose-Einstein condensates in optical lattices, Rev. Mod. Phys. , (submitted).

[34] M. Greiner, O. Mandel, T. Esslinger, T. W. Hänsch, and I. Bloch, Quantum phase transition from a superfluid to a Mott insulator in a gas of ultracold atoms, Nature **415**, 29 (2002).

[35] M. R. Andrews, C. G. Townsend, H.-J. Miesner, D. S. Durfee, D. M. Kurn, and W. Ketterle, Observation of interference between two Bose condensates, Science **275**, 637–641 (1997).

[36] Y. Castin and J. Dalibard, Relative phase of two Bose-Einstein condensates, Phys. Rev. A **55**, 4330–4337 (1997).

[37] M. Tinkham, *Introduction to superconductivity*, McGraw-Hill, 1996.

[38] J. M. Kosterlitz and D. J. Thouless, Ordering, metastability and phase transitions in two dimensional systems, J. Phys. C: Solid State Phys. **6**, 1181–1203 (1973).

[39] J. M. Kosterlitz, The critical properties of the two-dimensional xy model, J. Phys. C: Solid State Phys. **7**, 1046 (1974).

[40] N. R. Cooper, N. K. Wilkin, and J. M. F. Gunn, Quantum phases of vortices in rotating Bose-Einstein condensates, Phys. Rev. Lett. **87**, 120405 (2001).

[41] B. Paredes, P. Fedichev, J. I. Cirac, and P. Zoller, $\frac{1}{2}$-anyons in small atomic Bose-Einstein condensates, Phys. Rev. Lett. **87**, 010402 (2001).

[42] D. J. Bishop and J. D. Reppy, Study of the Superfluid Transition in Two-Dimensional ^{4}He Films, Phys. Rev. Lett. **40**, 1727 (1978).

[43] A. I. Safonov, S. A. Vasilyev, I. S. Yasnikov, I. I. Lukashevich, and S. Jaakola, Observation of quasicondensate in two-dimensional atomic hydrogen, Phys. Rev. Lett. **81**, 4545 (1998).

[44] R. B. Laughlin, Fractional quantization (Nobel lecture), Rev. Mod. Phys. **71**, 863 (1999).

[45] H. L. Stormer, D. C. Tsui, and A. C. Gossard, The fractional quantum Hall effect, Rev. Mod. Phys. **71**, S298 (1999).

[46] A. Einstein, Quantentheorie des einatomigen idealen Gases, Sitzungsbericht Preuss. Akad. Wiss., Bericht 22 , 261–267 (1924).

[47] A. Einstein, Quantentheorie des einatomigen idealen Gases. II, Sitzungsbericht Preuss. Akad. Wiss., Bericht 1 , 3–14 (1925).

[48] A. Einstein, Zur Quantentheorie des idealen Gases, Sitzungsbericht Preuss. Akad. Wiss., Bericht 3 , 18–25 (1925).

[49] F. London, The λ -phenomenon of liquid helium and the Bose-Einstein degeneracy, Nature **141**, 643 (1938).

[50] S. Jochim, M. Bartenstein, A. Altmeyer, G. Hendl, S. Riedl, C. Chin, J. H. Denschlag, and R. Grimm, Bose-Einstein Condensation of Molecules, Science **302**, 2101 (2003).

[51] M. Greiner, C. A. Regal, and D. S. Jin, Emergence of a molecular Bose-Einstein condensate from a Fermi gas, Nature **426**, 537 (2003).

[52] M. W. Zwierlein, C. A. Stan, C. H. Schunck, S. M. F. Raupach, S. Gupta, Z. Hadzibabic, and W. Ketterle, Observation of Bose-Einstein Condensation of Molecules, Phys. Rev. Lett. **91**, 250401 (2003).

[53] T. Bourdel, L. Khaykovich, J. Cubizolles, J. Zhang, F. Chevy, M. Teichmann, L. Tarruell, S. J. J. M. F. Kokkelmans, and C. Salomon, Experimental Study of the BEC-BCS Crossover Region in Lithium 6, Phys. Rev. Lett. **93**, 050401 (2004).

[54] S. Chu, The manipulation of neutral particles (Nobel lecture), Rev. Mod. Phys. **70**, 685 (1998).

[55] C. N. Cohen-Tannoudji, Manipulating atoms with photons (Nobel lecture), Rev. Mod. Phys. **70**, 707 (1998).

[56] W. D. Phillips, Laser cooling and trapping of neutral atoms (Nobel lecture), Rev. Mod. Phys. **70**, 721 (1998).

[57] H. F. Hess, Evaporative cooling of magnetically trapped and compressed spin-polarized hydrogen, Phys. Rev. B **34**, 3476 (1986).

[58] K. B. Davis, M.-O. Mewes, M. A. Joffe, M. R. Andrews, and W. Ketterle, Evaporative Cooling of Sodium Atoms, Phys. Rev. Lett. **74**, 5202–5205 (1995).

[59] K. B. Davis, M.-O. Mewes, and W. Ketterle, An Analytical Model For Evaporative Cooling of Atoms, Appl. Phys. B **60**, 155–159 (1995).

[60] O. J. Luiten, M. W. Reynolds, and J. T. M. Walraven, Kinetic Theory of evaporative cooling of a trapped gas, Phys. Rev. A **53**, 381 (1996).

[61] C. J. Pethick and H. Smith, *Bose-Einstein Condensation in Dilute Gases*, Cambridge University Press, Cambridge, UK, 2002.

[62] L. Pitaevskii and S. Stringari, *Bose-Einstein Condensation*, Oxford University Press, Oxford, 2003.

[63] V. Bagnato, D. E. Pritchard, and D. Kleppner, Bose-Einstein condensation in an external potential, Phys. Rev. A **35**, 4354 (1987).

[64] C. Cohen-Tannoudji, B. Diu, and F. Laloë, *Quantenmechanik, Bd. 2*, Walter de Gruyter, Berlin, 1999.

[65] N. N. Bogoliubov, On the theory of superfluidity, J. Phys. (USSR) **11**, 23 (1947).

[66] W. Ketterle, D. S. Durfee, and D. M. Stamper-Kurn, Making, probing and understanding Bose-Einstein condensates, Bose-Einstein condensation in atomic gases, Proceedings of the International School of Physics Enrico Fermi, Course CXL, pages 67–176, IOS Press, Amsterdam, 1999.

[67] S. Stringari, Collective excitations of a trapped Bose-condensed gas, Phys. Rev. Lett. **77**, 2360–2363 (1996).

[68] P. Öhberg, E. L. Surkov, I. Tittonen, S. Stenholm, M. Wilkens, and G. V. Shlyapnikov, Low-energy excitation of a trapped Bose-condensed gas, Phys. Rev. A **56**, R3346 (1997).

[69] S. Stringari, Dynamics of Bose-Einstein condensed gases in highly deformed traps, Phys. Rev. A **58**, 2385 (1998).

[70] D. S. Jin, J. R. Ensher, M. R. Matthews, C. E. Wieman, and E. A. Cornell, Collective Excitations of a Bose-Einstein Condensate in a Dilute Gas, Phys. Rev. Lett. **77**, 420 (1996).

[71] F. Chevy, V. Bretin, P. Rosenbusch, K. Madison, and J. Dalibard, The transverse breathing mode of an elongated Bose-Einstein condensate, Phys. Rev. Lett. **88**, 250402 (2002).

[72] L. P. Pitaevskii and A. Rosch, Breathing mode and hidden symmetry of trapped atoms in two dimensions, Phys. Rev. A **55**, R853 (1997).

[73] C. Orzel, A. K. Tuchman, M. L. Fenselau, M. Yasuda, and M. A. Kasevich, Squeezed states in a Bose-Einstein condensate, Science **291**, 2386 (2001).

[74] S. Inouye, T. Pfau, S. Gupta, A. P. Chikkatur, A. Görlitz, D. E. Pritchard, and W. Ketterle, Observation of phase-coherent amplification of atomic matter waves, Nature **402**, 641–644 (1999).

[75] M. Kozuma, Y. Suzuki, Y. Torii, T. Sugiura, T. Kuga, E. W. Hagley, and L. Deng, Phase coherent amplification of matter waves, Science **286**, 2309–2312 (1999).

[76] I. Bloch, T. W. Hänsch, and T. Esslinger, An atom laser with a cw output coupler, Phys. Rev. Lett. **82**, 3008 (1999).

[77] E. W. Hagley, L. Deng, M. Kozuma, J. Wen, K. Helmerson, S. L. Rolston, and W. D. Phillips, A Well-Collimated Quasi-Continuous Atom Laser, Science **283**, 1706–1709 (1999).

[78] T. Lahaye, J. M. Vogels, K. Guenter, Z. Wang, J. Dalibard, and D. Guery-Odelin, Realization of a magnetically guided atomic beam in the collisional regime, Phys. Rev. Lett. **93**, 093003 (2004).

[79] D. S. Petrov, M. Holzmann, and G. V. Shlyapnikov, Bose-Einstein Condensation in Quasi-2D Trapped Gases, Phys. Rev. Lett. **84**, 2551 (2000).

[80] D. S. Petrov, D. M. Gangardt, and G. V. Shlyapnikov, Low-dimensional trapped gases, J. Phys. IV **116**, 5–44 (2004).

[81] R. H. Brown and R. Q. Twiss, Correlation between photons in two coherent beams of light, Nature **177**, 27 (1956).

[82] R. H. Brown and R. Q. Twiss, A New Type of Interferometer for Use in Radio Astronomy, Phil. Mag **45**, 663 (1954).

[83] S. Fölling, F. Gerbier, A. Widera, O. Mandel, T. Gericke, and I. Bloch, Spatial quantum noise interferometry in expanding ultracold atom clouds, Nature **434**, 481 (2005).

[84] P. Kapitza, Viscosity of liquid helium below the λ-point, Nature **141**, 74 (1938).

[85] J. F. Allen and A. D. Misener, Flow of liquid helium II, Nature **141**, 75 (1938).

[86] F. London, On the Bose-Einstein Condensation, Phys. Rev. **54**, 947 (1938).

[87] A. J. Leggett, Superfluidity, Rev. Mod. Phys. **71**, S318 (1999).

[88] H. J. Metcalf and P. van der Straten, *Laser Cooling and Trapping*, Springer, New York, 1999.

[89] D. Guéry-Odelin, J. Söding, P. Desbiolles, and J. Dalibard, Is Bose-Einstein condensation of atomic cesium possible?, Europhys. Lett. **44**, 25 (1998).

[90] T. Weber, J. Herbig, M. Mark, H.-C. Nägerl, and R. Grimm, Bose-Einstein Condensation of Cesium, Science **299**, 232–235 (2003).

[91] J. Dalibard and C. Cohen-Tannoudji, Laser cooling below the Doppler limit by polarization gradients: simple theoretical models, J. Opt. Soc. Am. B **6**, 2023 (1989).

[92] C. Cohen-Tannoudji, *Piégeage non dissipatif et refroidissement évaporatif*, 1996/97, Cours du Collège de France, available online on http://www.phys.ens.fr/cours/college-de-france/index.html.

[93] W. Paul, Electromagnetic traps for charged and neutral particles, Rev. Mod. Phys. **62**, 531 (1990).

[94] Y. Castin and R. Dum, Bose-Einstein condensation in time dependent traps, Phys. Rev. Lett. **77**, 5315–5319 (1996).

[95] Y. Kagan, E. L. Surkov, and G. V. Shlyapnikov, Evolution of a Bose gas under variations of the confining potential, Phys. Rev. A **54**, R1753–R1756 (1996).

[96] D. Hellweg, L. Cacciapuoti, M. Kottke, T. Schulte, K. Sengstock, W. Ertmer, and J. J. Arlt, Measurement of the Spatial Correlation Function of Phase Fluctuating Bose-Einstein Condensates, Phys. Rev. Lett. **91**, 010406 (2003).

[97] Y. Colombe, E. Knyazchyan, O. Morizot, B. Mercier, V. Lorent, and H. Perrin, Ultracold atoms confined in rf-induced two-dimensional trapping potentials, Europhys. Lett. **67**, 593 (2004).

[98] N. D. Mermin and H. Wagner, Absence of Ferromagnetism or Antiferromagnetism in One- or Two-Dimensional Isotropic Heisenberg Models, Phys. Rev. Lett. **17**, 1133 (1966).

[99] P. C. Hohenberg, Existence of Long-Range Order in One and Two Dimensions, Phys. Rev. **158**, 383 (1967).

[100] N. D. Mermin, Crystalline Order in Two Dimensions, Phys. Rev. **176**, 250 (1968).

[101] W. Kane and L. Kadanoff, Long-Range Order in Superfluid Helium, Phys. Rev. **155**, 80 (1967).

[102] V. Berezinskii, Destruction of long-range order in one-dimensional and 2-dimensional systems having a continuous symmetry group, 1 - classical systems, Sov. Phys. JETP-USSR **32**, 493 (1971).

[103] V. Berezinskii, Destruction of long-range order in one-dimensional and 2-dimensional systems having a continuous symmetry group, 2 - quantum systems, Sov. Phys. JETP-USSR **34**, 610 (1972).

[104] V. Bagnato and D. Kleppner, Bose-Einstein condensation in low-dimensional traps, Phys. Rev. A **44**, 7439 (1991).

[105] J. O. Andersen, U. A. Khawaja, , and H. T. C. Stoof, Phase Fluctuations in Atomic Bose Gases, Phys. Rev. Lett. **88**, 070407 (2002).

[106] T.-L. Ho and M. Ma, Quasi 1 and 2d Dilute Bose Gas in Magnetic Traps: Existence of Off-Diagonal Order and Anomalous Quantum Fluctuations, J. Low Temp. Phys. **115**, 61 (1999).

[107] M. L. Bellac, *Des phénomènes critiques aux champs de jauge*, InterEditions/Editions du CNRS, France, 1988.

[108] M. Kardar, *MIT lecture notes: Statistical mechanics of fields*, 2004, available online on http://web.mit.edu/8.334/www/lectures/index.html.

[109] Y. Castin and R. Dum, Bose-Einstein condensates with vortices in rotating traps, Eur. Phys. J. D **7**, 399–412 (1999).

[110] V. N. Popov, *Functional Integrals in Quantum Field Theory and Statistical Physics*, Reidel, Dordrecht, 1983.

[111] N. Prokof'ev, O. Ruebenacker, and B. Svistunov, Critical Point of a Weakly Interacting Two-Dimensional Bose Gas, Phys. Rev. Lett. **87**, 270402 (2001).

[112] D. R. Nelson and J. M. Kosterlitz, Universal Jump in the Superfluid Density of Two-Dimensional Superfluids, Phys. Rev. Lett. **39**, 1201 (1977).

[113] D. J. Thouless, *Topological Quantum Numbers in Nonrelativistic Physics*, World Scientific, New York, 1998.

[114] T. P. Simula, M. D. Lee, and D. A. W. Hutchinson, Transition from Bose-Einstein Condensate to Berezinskii-Kosterlitz-Thouless Phase, cond-mat/0412512 (2004), to appear in Philosophical Magazine Letters.

[115] T. P. Simula and P. B. Blakie, Thermal activation of vortex-antivortex pairs in quasi-2D Bose-Einstein condensates, cond-mat/0510097 (2005).

[116] M. Holzmann, G. Baym, J.-P. Blaizot, and F. Laloë, The Kosterlitz-Thouless-Berezinskii transition of homogeneous and trapped Bose gases in two dimensions, cond-mat/0508131 (2005).

[117] S. Burger, F. S. Cataliotti, C. Fort, P. Maddaloni, F. Minardi, and M. Inguscio, 2D Bose-Einstein condensation in an optical lattice, Europhys. Lett. **57**, 1 (2002).

[118] M. Köhl, H. Moritz, T. Stöferle, C. Schori, and T. Esslinger, Superfluid to Mott insulator transition in one, two, and three dimensions, J. Low. Temp. Phys. **138**, 635 (2005).

[119] H. Ott, E. de Mirandes, F. Ferlaino, G. Roati, V. Türck, G. Modugno, and M. Inguscio, Radio Frequency Selective Addressing of Localized Particles in a Periodic Potential, Phys. Rev. Lett **93**, 120407 (2004).

[120] D. Schrader, I. Dotsenko, M. Khudaverdyan, Y. Miroshnychenko, A. Rauschenbeutel, and D. Meschede, A neutral atom quantum register, Phys. Rev. Lett. **93**, 150501 (2004).

[121] R. Grimm, M. Weidenmüller, and Y. B. Ovchinnikov, Optical dipole traps for neutral atoms, cond-mat/9902072 (1999).

[122] P. L. Kapitza and P. A. M. Dirac, Proc. Cambrigde Philos. Soc. **29**, 297 (1933).

[123] S. Altshuler, L. M. Frantz, and R. Braunstein, Phys. Rev. Lett. **17**, 231 (1966).

[124] P. L. Gould, G. A. Ruff, and D. E. Pritchard, Diffraction of atoms by light: the near-resonant Kapitza-Dirac effect, Phys. Rev. Lett. **56**, 827 (1986).

[125] J. Denschlag, J. Simsarian, H. Häffner, C. McKenzie, A. Browaeys, D. Cho, K. Helmerson, S. L. Rolston, and W. D. Phillips, A Bose-Einstein condensate in an optical lattice, J. Phys. B **35**, 3095 (2002).

[126] Y. Castin, *Les limites du refroidissement laser dans les mélasses optiques à une dimension*, PhD thesis, Laboratoire Kastler Brossel, Département de Physique de l'Ecole normale supérieure, 1992.

[127] G. Hechenblaikner, J. M. Krueger, and C. J. Foot, Properties of quasi-two-dimensional condensates in highly anisotropic traps, Phys. Rev. A **71**, 013604 (2005).

[128] K. W. Madison, F. Chevy, W. Wohlleben, and J. Dalibard, Vortex formation in a stirred Bose-Einstein condensate, Phys. Rev. Lett. **84**, 806–809 (2000).

[129] F. Chevy, K. Madison, V. Bretin, and J. Dalibard, Interferometric detection of a single vortex in a dilute Bose-Einstein condensate, Phys. Rev. A **64**, 031601(R) (2001).

[130] E. L. Bolda and D. F. Walls, Detection of Vorticity in Bose-Einstein Condensed Gases by Matter-Wave-Interference, Phys. Rev. Lett. **81**, 5477 (1998).

[131] J. Tempere and J. T. Devreese, Fringe pattern of interfering Bose-Einstein condensates with a vortex, Solid State Commun. **108**, 993 (1998).

[132] S. Inouye, S. Gupta, T. Rosenband, A. P. Chikkatur, A. Görlitz, T. L. Gustavson, A. E. Leanhardt, D. E. Pritchard, and W. Ketterle, Observation of vortex phase singularities in Bose-Einstein condensates, Phys. Rev. Lett. **87**, 080402 (2001).

[133] B. Battelier, PhD thesis, Laboratoire Kastler Brossel, Département de Physique de l'Ecole normale supérieure, (to be published).

[134] S. Burger, K. Bongs, S. Dettmer, W. Ertmer, K. Sengstock, A. Sanpera, G. V. Shlyapnikov, and M. Lewenstein, Dark Solitons in Bose-Einstein Condensates, Phys. Rev. Lett. **83**, 5198 (1999).

[135] D. L. Feder, M. S. Pindzola, L. A. Collins, B. I. Schneider, and C. W. Clark, Dark-soliton states of Bose-Einstein condensates in anisotropic traps, Phys. Rev. A **62**, 053606 (2000).

[136] F. Dalfovo and M. Modugno, Free expansion of Bose-Einstein condensates with quantized vortices, Phys. Rev. A **61**, 023605 (2000).

[137] K. Sheshadri, H. R. Krishnamurthy, R. Pandit, and T. V. Ramakrishnan, Superfluid and Insulating Phases in an Interacting-Boson Model: Mean-Field Theory and the RPA., Europhys. Lett. **22**, 257 (1993).

[138] D. Jaksch, C. Bruder, J. I. Cirac, C. W. Gardiner, and P. Zoller, Cold Bosonic Atoms in Optical Lattices, Phys. Rev. Lett. **81**, 3108 (1998).

[139] J. Hecker-Denschlag, J. E. Simsarian, H. Häffner, C. McKenzie, A. Browaeys, D. Cho, K. Helmerson, S. L. Rolston, and W. D. Phillips, A Bose-Einstein Condensate in an optical lattice, J. Phys. B **35**, 3095–3110 (2002).

[140] P. Pedri, L. Pitaevskii, S. Stringari, C. Fort, S. Burger, F. S. Cataliotti, P. Maddaloni, F. Minardi, and M. Inguscio, Expansion af a Coherent Array of Bose-Einstein Condensates, Phys. Rev. Lett. **87**, 220401 (2001).

[141] J. Javanainen and S. M. Yoo, Quantum Phase of a Bose-Einstein Condensate with an Arbitrary Number of Atoms, Phys. Rev. Lett. **76**, 161–164 (1996).

[142] M. Naraschewski, H. Wallis, A. Schenzle, J. I. Cirac, and P. Zoller, Interference of Bose condensates, Phys. Rev. A **54**, 2185–2196 (1996).

[143] E. Hecht, *Optics*, Addison-Wesley, Reading, 1989.

[144] M. Lewenstein and L. You, Quantum Phase Diffusion of a Bose-Einstein Condensate, Phys. Rev. Lett. **77**, 3489–3493 (1996).

[145] J. Javanainen and M. Wilkens, Phase and phase diffusion of a split Bose-Einstein condensate, Phys. Rev. Lett. **78**, 4675–4678 (1997).

[146] A. J. Leggett and F. Sols, Comment on 'Phase and Phase Diffusion of a Split Bose-Einstein Condensate', Phys. Rev. Lett. **81**, 1344 (1998).

[147] J. Javanainen and M. Wilkens, Reply to Leggett et al, Phys. Rev. Lett. **81**, 1345 (1998).

[148] J. A. Dunningham, M. J. Collett, and D. F. Walls, Quantum state of a trapped Bose-Einstein condensate, Phys. Lett. A **245**, 49 (1998).

[149] C. Menotti, J. R. Anglin, J. I. Cirac, and P. Zoller, Dynamic splitting of a Bose-Einstein condensate, Phys. Rev. A **63**, 023601 (2001).

[150] P. W. Anderson, The Lesson of Quantum Theory, pages 23–34, Elsevier, Amsterdam, 1986.

[151] E. Altman, E. Demler, and M. D. Lukin, Probing many-body states of ultracold atoms via noise correlations, Phys. Rev. A **70**, 013603 (2004).

[152] R. Bach and K. Rzazewski, Correlation functions of cold bosons in an optical lattice, Phys. Rev. A **70**, 063622 (2004).

[153] C. M. Caves, Quantum-mechanical noise in an interferometer, Phys. Rev. D **23**, 1693 (1981).

[154] W. Zwerger, Mott-Hubbard transition of cold atoms in optical lattices, J. Opt. B **5**, S9–S16 (2003).

[155] M. Greiner, C. A. Regal, J. T. Stewart, and D. S. Jin, Probing Pair-Correlated Fermionic Atoms through Correlations in Atom Shot Noise, Phys. Rev. Lett. **94**, 110401 (2005).

[156] M. R. Matthews, B. P. Anderson, P. C. Haljan, D. S. Hall, C. E. Wieman, and E. A. Cornell, Vortices in a Bose-Einstein Condensate, Phys. Rev. Lett. **83**, 2498 (1999).

[157] J. R. Abo-Shaeer, C. Raman, J. M. Vogels, and W. Ketterle, Observation of Vortex Lattices in Bose-Einstein Condensates, Science **292**, 476–479 (2001).

[158] E. Hodby, G. Hechenblaikner, S. A. Hopkins, O. M. Maragò, and C. J. Foot, Vortex nucleation in Bose-Einstein condensates in an oblate, purely magnetic potential, Phys. Rev. Lett. **88**, 010405 (2002).

[159] P. C. Haljan, I. Coddington, P. Engels, and E. A. Cornell, Driving Bose-Einstein condensate vorticity with a rotating normal cloud, Phys. Rev. Lett. **87**, 210403 (2001).

[160] R. J. Donnelly, *Quantized vortices in helium II*, Cambridge University Press, Cambridge, 1991.

[161] P. Engels, I. Coddington, P. C. Haljan, V. Schweikhard, and E. A. Cornell, Observation of long-lived vortex agregates in rapidly rotating Bose-Einstein condensates, Phys. Rev. Lett. **90**, 170405 (2003).

[162] S. Stringari, Phase diagram of quantized vortices in a trapped Bose-Einstein condensed gas, Phys. Rev. Lett. **82**, 4371 (1999).

[163] M. A. Cazalilla, Surface modes of ultra-cold atomic clouds with very large number of vortices, Phys. Rev. A **67**, 033613 (2003).

[164] K. W. Madison, F. Chevy, V. Bretin, and J. Dalibard, Stationary States of a Rotating Bose-Einstein Condensate: Routes to Vortex Nucleation, Phys. Rev. Lett. **86**, 4443 (2001).

[165] C. Raman, J. R. Abo-Shaeer, J. M. Vogels, K. Xu, and W. Ketterle, Vortex nucleation in a stirred Bose-Einstein condensate, Phys. Rev. Lett. **87**, 210402 (2001).

[166] T.-L. Ho, Bose-Einstein condensates with large number of vortices, Phys. Rev. Lett. **87**, 060403 (2001).

[167] N. Regnault and T. Jolicoeur, Quantum Hall fractions in rotating Bose-Einstein condensates, Phys. Rev. Lett. **91**, 030402 (2003).

[168] U. R. Fischer, P. O. Fedichev, and A. Recati, Vortex liquids and vortex quantum Hall states in trapped rotating Bose gases, Jour. Phys. B: Atomic, molecular and optical physics **37**, S301 (2002).

[169] R. P. Feynman, Progress in Low Temperature Physics, volume 1, page 17, North-Holland, Amsterdam, 1955.

[170] V. K. Tkachenko, On Vortex Lattices, Sov. Phys. JETP **22**, 1282 (1966), Zh. Eksp. Teor. Fiz 49, p. 1875 (1965).

[171] F. Chevy, K. Madison, and J. Dalibard, Measurement of the angular momentum of a rotating Bose-Einstein condensate, Phys. Rev. Lett. **85**, 2223 (2000).

[172] N. R. Cooper and N. K. Wilkin, Composite fermion description of rotating Bose-Einstein condensates, Phys. Rev. B **60**, R16279 (1999).

[173] B. Mottelson, Yrast Spectra of Weakly Interacting Bose-Einstein Condensates, Phys. Rev. Lett. **83**, 2695 (1999).

[174] N. K. Wilkin and J. M. F. Gunn, Condensation of composite bosons in a rotating BEC, Phys. Rev. Lett. **84**, 6 (2000).

[175] K. von Klitzing, The quantized Hall effect (Nobel lecture), Rev. Mod. Phys. **58**, 519 (1986).

[176] D. R. Yennie, Integral quantum Hall effect for nonspecialists, Rev. Mod. Phys **59**, 781 (1987).

[177] Z.-B. Chen, B. Zhao, and Y.-D. Zhang, Quantum Hall effect in a rotating Bose-Einstein condensate : an atomic twin of the electronic brother ?, cond-mat/0211187 (2002).

[178] J. Sinova, C. B. Hanna, and A. H. MacDonald, Quantum melting and absence of Bose-Einstein condensation in two-dimensional vortex matter, Phys. Rev. Lett. **89**, 030403 (2002).

[179] B. Paredes, P. Zoller, and J. I. Cirac, Fermionizing a small gas of ultracold bosons, Phys. Rev. A **66**, 033609 (2002).

[180] J. Sinova, C. B. Hanna, and A. H. MacDonald, Measuring the condensate fraction of rapidly rotating trapped boson systems : off-diagonal order from the density profile, Phys. Rev. Lett. **90**, 120401 (2003).

[181] N. Regnault and T. Jolicoeur, Quantum Hall fractions for spinless bosons, Phys. Rev. B **69**, 235309 (2004).

[182] T. Nakajima and M. Ueda, Energy gaps and roton structure above the $\nu = \frac{1}{2}$ Laughlin state of a rotating dilute Bose-Einstein condensate, Phys. Rev. Lett. **91**, 140401 (2003).

[183] N. Read and N. R. Cooper, Free expansion of lowest Landau level states of trapped atoms: a wavefunction microscope, Phys. Rev. A **68**, 035601 (2003).

[184] U. R. Fischer and G. Baym, Vortex states of rapidly dilute rotating Bose condensed gases, Phys. Rev. Lett. **90**, 140402 (2003).

[185] I. Coddington, P. C. Haljan, P. Engels, V. Schweikhard, S. Tung, and E. A. Cornell, Experimental studies of equilibrium vortex properties in a Bose-condensed gas, Phys. Rev. A **70**, 063607 (2004).

[186] E. Bogomolny, O. Bohigas, and P. Leboeuf, Distribution of roots of random polynomials, Phys. Rev. Lett. **68**, 2726 (1992).

[187] J. H. Hannay, Chaotic analytic zero points: Exact statistics for those of a random spin state, J. Phys. A: Mathematical and general **29**, L101 (1996).

[188] P. Leboeuf, Random analytic chaotic eigenstates, J. Stat. Phys. **95**, 651 (1999).

[189] N. R. Cooper, F. J. M. van Lankvelt, J. W. Reijnders, and K. Schoutens, Density profiles for atomic quantum Hall states, cond-mat/0409146 (2004).

[190] N. R. Cooper, F. J. M. van Lankvelt, J. W. Reijnders, and K. Schoutens, Quantum Hall states of atomic Bose gases: density profiles in single-layer and multi-layer geometries, cond-mat/0508031 (2005).

[191] P. Rosenbusch, D. Petrov, S. Sinha, F. Chevy, V. Bretin, Y. Castin, G. Shlyapnikov, and J. Dalibard, Critical rotation of a harmonically trapped Bose gas, Phys. Rev. Lett. **88**, 250403 (2002).

[192] A. L. Fetter, Rotating vortex lattice in a Bose-Einstein condensate trapped in combined quadratic and quartic radials potentials, Phys. Rev. A **64**, 063608 (2001).

[193] E. Lundh, Multiply quantized vortices in trapped Bose-Einstein condensates, Phys. Rev. A **65**, 043604 (2002).

[194] K. Kasamatsu, M. Tsubota, and M. Ueda, Giant hole and circular superflow in a fast rotating Bose-Einstein condensate, Phys. Rev. A **66**, 053606 (2002).

[195] G. M. Kavoulakis and G. Baym, Rapidly rotating Bose-Einstein condensates in anharmonic traps, New Journal of Physics **5**, 51.1–51.11 (2003).

[196] A. Aftalion and I. Danaila, Three-dimensional vortex configurations in a rotating Bose Einstein condensate, Phys. Rev. A **68**, 023603 (2003).

[197] A. D. Jackson, G. M. Kavoulakis, and E. Lundh, Phase diagram of a rotating Bose-Einstein condensate with anharmonic confinement, Phys. Rev. A **69**, 053619 (2004).

[198] F. Zambelli and S. Stringari, Quantized vortices and collective oscillations of a trapped Bose-Einstein condensate, Phys. Rev. Lett. **81**, 1754 (1998).

[199] P. Rosenbusch, V. Bretin, and J. Dalibard, Dynamics of a single vortex line in a Bose-Einstein condensate, Phys. Rev. Lett. **89**, 200403 (2002).

[200] E. Lundh, C. J. Pethick, and H. Smith, Vortices in Bose-Einstein-condensed atomic clouds, Phys. Rev. A **58**, 4816 (1998).

[201] P. Engels, I. Coddington, P. C. Haljan, and E. A. Cornell, Nonequilibrium effects of anisotropic compression applied to vortex lattices in Bose-Einstein condensates, Phys. Rev. Lett. **89**, 100403 (2002).

[202] W. Ketterle and N. J. van Druten, Advances in Atomic, Molecular, and Optical Physics, volume 37, pages 181–236, Academic Press, San Diego, 1996.

[203] E. Akkermans and S. Ghosh, Composite bosons description of rapidly rotating Bose-Einstein condensates, cond-mat/0307418 (2003).

[204] A. Aftalion and I. Danaila, private communication (october 03).

[205] I. Danaila, Three-dimensional vortex structure of a fast rotating Bose-Einstein condensate with harmonic-plus-quartic confinement, Phys. Rev. A **72**, 013605 (2005).

[206] G. Baym and C. J. Pethick, Vortex core structure and global properties of rapidly rotating Bose-Einstein condensates, Phys. Rev. A **69**, 043619 (2004).

[207] L. O. Baksmaty, S. J. Woo, S. Choi, and N. P. Bigelow, Vortex lattices: from the hydrodynamic to the quantum hall regime, cond-mat/0310567 (2003).

[208] I. Coddington, P. C. Haljan, V. Schweikhard, and E. A. Cornell, Observation of Tkachenko oscillations in rapidly rotating Bose-Einstein condensates, Phys. Rev. Lett. **91**, 100402 (2003).

[209] M. Tsubota, K. Kasamatsu, and A. Tsunehiko, Dynamics of quantized vortices in superfluid helium and rotating Bose-Einstein condensates, Recent Res. Devel. Physics **4**, 631 (2003).

[210] F. Dalfovo, S. Giorgini, L. P. Pitaevskii, and S. Stringari, Theory of Bose-Einstein condensation in trapped gases, Rev. Mod. Phys. **71**, 463 (1999).

[211] C. Fort, M. Prevedelli, F. Minard, F. S. Cataliotti, L. Ricci, G. M. Tino, and M. Inguscio, Europhys. Lett. **49**, 8 (2000).

[212] M. Cozzini and S. Stringari, Macroscopic dynamics of a Bose-Einstein condensate containing a vortex lattice, Phys. Rev. A **67**, 041602 (2003).

[213] A. Sedrakian and I. Wasserman, Kinetics of Bose Condensation, Phys. Rev. A **63**, 063605 (2001).

[214] F. Chevy and S. Stringari, Kelvin modes of a fast rotating Bose-Einstein condensate, Phys. Rev. A **68**, 053601 (2003).

[215] L. D. Landau and E. M. Lifshitz, *Quantum Mechanics, Course of Theoretical Physics, Vol.3, Chap. 15*, Butterworth-Heinemann, Stoneham, MA, 1981.

[216] M. Tsubota, K. Kasamatsu, and A. Tsunehiko, Dynamics of quantized vortices in superfluid helium and rotating Bose-Einstein condensates, Recent Res. Devel. Physics **4**, 631 (2003).

[217] I. Danaila and A. Aftalion, private communication (2004).

[218] J.-P. Martikainen and H. T. C. Stoof, Quantum fluctuations of a vortex in an optical lattice, Phys. Rev. Lett. **91**, 240403 (2003).

[219] J.-P. Martikainen and H. T. C. Stoof, Vortex-Line Solitons in A Periodically Modulated Bose-Einstein Condensate, Phys. Rev. Lett. **93**, 070402 (2004).

[220] J.-P. Martikainen and H. T. C. Stoof, Quantum theory of a vortex line in an optical lattice, Phys. Rev. A **69**, 053617 (2004).

[221] J.-P. Martikainen and H. T. C. Stoof, Spontaneous squeezing of a vortex in an optical lattice, Phys. Rev. A **70**, 013604 (2004).